Efficient Network Interfaces for Tuneable-Cavity-Coupled Diamond Spin Qubits

Gareth Siôn Jones

Mansfield College

University of Oxford

A thesis presented for the degree of

Doctor of Philosophy

Michaelmas 2024-2025

Acknowledgements

I am deeply grateful to Prof. Jason M. Smith for his unwavering guidance, invaluable insights, and steadfast support throughout my journey as a scientist. His mentorship has shaped my academic and personal growth in countless ways. I extend heartfelt thanks to Matt (Zhin) Mai and Dr Andrew Kirkpatrick, who taught me nearly everything I know about optics. Their patience, expertise, and encouragement were instrumental, and I am lucky to count them, along with Xingrui Cheng, Eugenio Picheo, and the entire Photonic Nanomaterials Group, among my friends. My gratitude also goes to Robin Scales, whose friendship and intellectual camaraderie have been a constant source of inspiration. I am deeply appreciative of Dr Clara Barker and Prof. Thorsten Hesjedal for their invaluable assistance and guidance in thin-film growth, and to Prof. Susie Speller for providing access to the growth facilities. Dr Jarrod Lewis's expertise in XRD analysis was indispensable, as was the generous support of Prof. Richard Todd and David (Zonghao) Guo for sharing their ceramic knowledge and helping with target development. Special thanks to Dr Phani Karamchad for continued guidance with SEM work. I am also grateful to Prof. Adrian Taylor for facilitating the funding which allowed me to complete this work. I am very appreciative to my thesis examiners, Dr Greg Mazur and Prof. Michael Strain, for their thorough inspection of my thesis, and detailed discussion during examination. Finally, and most importantly, I owe an immeasurable debt of gratitude to my mother, Sheila Mary Matthews. Her unconditional support and love made all of this possible.

Declaration

I, [author name], declare that ...

Signature *Date*

Abstract

To enable the transformative potential of quantum information processing, it is essential to develop robust quantum networks capable of sharing quantum states via entanglement swapping. A highly efficient network node is critical for coupling qubit states into quantum channels. The nitrogen-vacancy (NV) centre in diamond is a promising qubit candidate but suffers from a low branching ratio of photons coupling into the zero-phonon line (ZPL). Embedding the NV centre in a resonant cavity can enhance this coupling, but existing open-air cavity designs lack mechanical stability. This work reports the first monolithic Fabry-Pérot microcavities fabricated in diamond membranes. By employing focused ion beam milling to form convex features and enclosing the diamond with distributed Bragg reflector (DBR) mirrors, we achieve a mechanically robust cavity structure. Addressing the challenge of tunability, we introduce a novel method using the strong electro-optic material $Sr_{0.75}Ba_{0.25}Nb_2O_6$ (SBN). SBN, synthesised via pulsed laser deposition, can alter the cavity optical path length under an applied electric field. We characterise the microstructure, optical properties, and electro-optic response of SBN, proposing a fabrication method for freestanding, releasable membranes suitable for optical integration. A numerical model incorporating these material properties examines the potential impact on cavity resonance tuning. Prototype cavities in this work are currently limited by anomalous absorption in one DBR mirror. However, improving the mirror coatings and integrating the SBN layer is expected to enable substantial Purcell enhancement and cavity tunability. This approach provides a significant advancement towards efficient and scalable quantum network nodes.

Intellectual Property Resulting from this Work

1. Freestanding Strontium Barium Niobate Membranes for Quantum Optics and Low Temperature Optoelectronics - Patent Pending

Publications

Cited in this thesis

1. Kirkpatrick, A., **GSJ**, et al *"Deterministic Laser-Writing of Nitrogen-Vacancy Centres in High Purity Diamond"*, Manuscript submitted for review (2025)
2. Cheng, X, **GSJ**, et al, *"Laser Activation of Single Group-IV Colour Centres in Diamond"*, Nat. Commun. 16 (2025)

Not cited in this thesis

1. Montenegro, V., **GSJ**, Bose, S., Bayat, A., *"Sequential Measurements for Quantum-Enhanced Magnetometry in Spin Chain Probes"*, Phys. Rev. Lett, 129, 120503 (2022)
2. **GSJ**, Bose, S., Bayat., A, *"Remote Quantum Sensing with Heisenberg Limited Sensitivity in Many Body Systems"*, arXiv:2003.02308, 2020

Conference Presentations

1. **2024** - 34th International Conference on Diamond and Carbon Materials - Talk - Dresden, Germany
2. **2024** - Quantum Computing and Simulation Hub Update Forum - Talk - Oxford, United Kingdom

3. **2022** - Quantum Computing and Simulation Hub Update Forum - Poster Presentation - Oxford, United Kingdom
4. **2022** - Photon 2022 - Poster - Nottingham, United Kingdom

Software

1. **PyLumerical** : A wrapper package for creating and simulating optical structures by FDTD in the Lumerical Software. https://www.github.com/png-oxford/PyLumerical. Documentation at https://www.readthedocs.org/PyLumerical. Manuscript in preparation.

Table of Contents

List of Figures

List of Tables

List of Abbreviations

BSE . . . . . Backscattered Electrons

DBR . . . . . Distributed Bragg Reflector

EBSD . . . . . Electron Backscatter Dispersion

EDX . . . . . Electron Dispersive X-Ray

EO . . . . . Electro-Optic

FDTD . . . . . Finite Difference Time Domain

FIB . . . . . Focussed Ion Beam

FP . . . . . Fabry-Pérot

IPF . . . . . Inverse Pole Figure

NV . . . . . Nitrogen Vacancy

PFM . . . . . Piezoresponse Force Microscopy

PLD . . . . . Pulsed Laser Deposition

PSB . . . . . Phonon Sideband

SAl . . . . . Strontium Aluminate

SBN . . . . . Strontium Barium Niobate

SEM . . . . . Scanning Electron Microscope

STO . . . . . Strontium Titanate

XRD . . . . . X-Ray Diffraction

ZPL . . . . . Zero-Phonon Line

1 | Introduction

Quantum information processing (QIP) promises a transformative paradigm for quantum mechanical simulation of complex systems [1, 2], acceleration of solutions to classically hard problems such as prime number factoring [3], and advancements in provably secure encryption methods [4, 5]. To fully realise the potential of QIP, once the requirements for fault tolerance are satisfied [6–9], it will be essential to enable spatial transmission of quantum information over metropolitan and global distances via a quantum internet [10–12].

A quantum network comprises three fundamental hardware elements: the quantum node, channel, and repeater [10]. The node functions as the quantum information processor, and networking requires entanglement sharing between nodes and qubit transmission through free-space or optical telecommunications fibre channels. However, the capacity of a quantum channel to maintain coherent quantum state transmission diminishes exponentially with channel length [13]. To preserve the fidelity of entanglement over extended distances, repeater protocols are necessary [14, 15].

1.1 Spin-System Requirements for Quantum Networking

There are numerous potential spin-systems which may be viable platforms for quantum networking, including cold atoms, atomic vapours, and solid state defects. To be a viable platform, the spin system must meet several demanding requirements to ensure quantum coherence, efficient light-matter interaction, and interoperability with photonic systems.

In order to preserve entanglement, the spin coherence time T_2 should exceed the communication and gate operation times, and for quantum memories over long range, ideally this coherence time would extend to milliseconds or even seconds. This places a requirement on the material host of spins, especially in the solid state, since these materials must be isotropically pure and with low magnetic field noise from other impurities.

Quantum networking requires photons to transmit information. Therefore the spin system must have an optically addressable transition, ideally one which is spin-selective, a zero-phonon line (ZPL) fraction for indistinguishable single-photon emission, and narrow linewidths near the Fourier transform limit corresponding to long photon coherence times. To transfer quantum states of entangle distance qubits, the optically addressable transition should be spin selective to allow for spin-photon entanglement. This often involves a Λ-type three-level system. For long-distance communication through optical fibre, ideally the photons will be emitted in the telecoms spectral region, or in a waveband which can be readily converted to telecoms.

To enhance photon emission and therefore entanglement generation rates, the spin-system should be compatible with photonic structures such as solid immersion lenses or optical microcavities to enhance rates by photon routing or Purcell enhancement. In addition, since a large-scale quantum network will require many identical nodes, it is important that the spin-system platform is amenable to scalable fabrication techniques such as ion implantation, chemical vapour deposition growth, deterministic placement, etc.

1.1.1 Solid State Defects

Solid state defects in wide bandgap materials are well established as excellent photon sources for quantum networking. These defects can be naturally occurring or engineered in a variety of materials. Diamond is the leading host of color centres for quantum networking applications due to its nearly nuclear spin-free environment, high Debye temperature, and wide bandgap. The Nitrogen Vacancy (NV) centre in diamond is the most widely studied solid state defect, with millisecond-scale coherence times at room temperature [16] and coherence times extending to seconds at cryogenic temperatures [17], with nuclear spin coherence exceeding one second [18, 19].

However, a significant limitation for NV centres in quantum networking is their poor Debye-Waller factor. A crucial requirement for quantum networking is the generation of indistinguishable photons for entanglement generation [20]. Any two photons are distinguishable if they differ in any degree of freedom that could allow them to be told apart. This includes differences in arrival time, frequency or spectral shape, spatial mode or propagation direction, polarisation, or optical path. Any variation in these properties can encode *which-photon* information inhibiting the generation of entangled states, as is discussed in Section 2.1.1.1. Therefore, it is highly desirable to work with systems with a far higher Debye-Waller factor.

Within diamond, a large number of defect centres have been shown to have promise for quantum networking. Aside from the NV centre, Group IV defects show increasingly impressive potential. Since group IV defects possess inversion symmetry, which suppresses phonon coupling, their Debye-Waller factors are much larger than that of the NV centre.

However, diamond possesses a spin-triplet ground state which is orbitally non-

degenerate, which means that the spin degrees of freedom are decoupled from orbital motion, making them less sensitive to phonons and crystal strain. As a result, NVs exhibit exceptional spin coherence times. In contrast, the group IV defects possess orbitally degenerate ground states with strong spin-orbit coupling. This orbital component couples strongly to phonons, especially at cryogenic temperatures, causing fast dephasing and orbital relaxation, leading to shorter spin coherence times.

Therefore, there remains a trade-off for building quantum networks with defects in diamond. For longer distance communications, the long spin coherence times of the NV centre are favourable. However, they require integration into optical microstructures to enhance entanglement rates. On the other hand, group IV defects may be preferable for shorter distance network links due to their short coherence times but large Debye-Waller factors.

Aside from diamond, there are a range of different host materials for defect centres and a variety of defect types. The properties of these defects are summarised in Table 1.1. From a fabrication perspective, any silicon based technology is likely to be the most preferable option for scaling up a technology, due to the extremely mature fabrication ecosystem for Si. Excitingly, color centres observed in Si are gaining increasing research and industrial interest, particularly the T centre [21–23]. An added benefit of these defects is that they naturally emit photons in the telecoms band, negating the need for frequency conversion. Defects in silicon carbide (SiC) are gaining traction for the same reasons [24]. On the other hand, diamond is a difficult platform to scale up the fabrication, due to a lack of potential for large scale single-crystal wafer growth. Any diamond based node would be limited in dimensions to a few millimeters, at significant cost per node.

Quantum dots are very well established single photon sources [25]. However,

due a combination of their low Debye-Waller factors and short coherence times, they are unlikely to be a leading quantum network platform. 2D materials such as hexagonal boron nitride (hBN) [26] are exciting new emerging hosts of defect centres, but currently it seems that such defects are limited by short coherence times also.

Whilst rare-earth defects [27] may possess T_2 times comparable to diamond based defects, the Debye-Waller factors of rare-earth ions tend to be low due to their 4f-4f optical transitions, which are parity-forbidden and weakly coupled to phonons. In addition, because of these weak transitions, the emission rates are low, so the photon flux is much lower than other single photon emitters. This would further reduce entanglement generation rates.

In terms of coherence times and Debye-Waller factor, diamond is still the leading candidate host material, with the NV centre still the most widely studied and adopted defect. In the future, it is quite feasible that a different material platform, such as Si or SiC, are adopted for easier scalability. At present however, defects in these materials are less mature. For example, spin-photon and long distance entanglement has been shown with NV centres in diamond, but not in Si, and whilst having been shown in SiC [28], this is not yet maturely developed. Therefore, at present, diamond based defects are still the primary defects of interest.

1.2 The NV-Centre in Diamond

NV centres are still currently the leading candidate solid state defect for establishing long range quantum networks. Importantly, NV centres can be deterministically generated with a laser-writing process into these membranes with high repeatability and positioning accuracy [29, 30], and micron-thick diamond membranes provide an exceptionally pure environment, reducing excited state dephas-

Table 1.1: **Comparison of figures of merit of different solid state defects for quantum networking**

Material	Defect	λ (nm)	DW Factor	T_2
Diamond	NV	637	$2-4\%$	1 ms - 1s
	SnV	620	$50-60\%$	250 μs
	SiV	737	$70-80\%$	~ 1 ms
	GeV	602	$60-70\%$	$\sim 50\mu$s
	MgV	550	$20-50\%$	Unknown
	PbV	520	$20-30\%$	$\sim 1\mu$s
Si	T	1326	$30-40\%$	~ 1 ms
	C	1550	$10-20\%$	Spin-0 (no T_2)
	G	970	30%	Spin-0 (no T_2)
	W	1218	Unknown	Unknown
	V_2	$1018-1078$	$10-20\%$	100μs
SiC	V_{Si}^- (4H-SiC)	860-920	$5-10\%$	$1-2$ ms
	V_{Si}^- (6H-SiC)	$860-950$	5%	$100-1000$ μs
	VV^0 (4H-SiC)	$1070-1130$	$10-20\%$	$1-5$ ms
	VV^0 (6H-SiC)	$1100-1170$	$10-20\%$	$1-2$ ms
Quantum Dots	InAs/GaAs (SA)	$900-1000$	$5-10\%$	$\sim 1\mu$s
	InGaAs/GaAs	$900-1000$	$5-10\%$	$\sim 1\mu$s
	GaAs	$780-820$	$10-20\%$	~ 10 ns to $\sim 10\mu$s
	CdSe	620	$10-20\%$	$10-100$ ns
	PbS/PbSe	$1000-2000$	10%	10 ns
	Perovskites	$510-540$	$10-20\%$	~ 100 ps to ~ 1 ns
2D Materials	hBN	$580-700$	$40-70\%$	~ 100 ns
	WSe_2	$720-850$	$10-20\%$	$10-100$ ps
	MoS_2	$650-750$	10%	$10-100$ ps
	$MoSe_2$ / WS_2	$750-800$	10%	100 ps
	CrSBr	$720-800$	Unknown	$10-100$ ps
Rare-Earth	Er^{3+}	$1530-1540$	$10-50\%$	1 ms
	Eu^{3+}	$580-590$	$10-20\%$	10 ms - 1 s
	Pr^{3+}	$610-620$	$10-30\%$	100 ms - 1 s
	Tm^{3+}	$780-800$	$5-15\%$	100 ms
	Nd^{3+}	$880-890$	$5-10\%$	1 ms
	Yb^{3+}	$980-1000$	$5-10\%$	1 ms

ing and spectral diffusion.

The poor Debye-Waller factor of NV centres is a challenge which requires a technological solution. For NV centres, two emitted photons can be distinguishable through: temporal mismatches due to different emission times or excited-state lifetimes; spectral differences such as shifts in zero-phonon line (ZPL) frequencies from strain or electric field variations (Stark effect); and phonon sideband contributions. Spatial distinguishability can also arise if the photons are collected from different optical paths or locations on the sample, and polarisation differences can emerge due to varying dipole orientations or crystal axes.

Many of these challenges can be mitigated directly: temporal distinguishability can be mitigated by temporal mode matching schemes; spectral mismatch can be compensated by Stark shifting or external optical correction; and polarisation mismatches can largely be minimised by virtue of the fact that NV centres in single crystal diamond grown along the same lattice orientation largely share the same dipole orientation. However, phonon contributions are a more challenging issue. Any photons generated which are accompanied by lattice vibrations can be distinguished, therefore only photons at an energy within the zero-phonon-line region of its spectrum can be free of this source of distinguishibility. Unfortunately, most NV centre emission couples to vibrational states in the phonon sideband (PSB), with only $\sim 4\%$ of free-space emission occurring in the ZPL. This can be significantly enhanced however through both cooling the NV centre to cryogenic temperatures. By cooling the NV centre, thermal coupling mechanisms contributing to inhomogeneous spectral broadening are mitigated, and therefore the likelihood of photon emission being accompanied by phonons is diminished substantially. In Figure 1.1, the optical spectra of an NV centre in bulk single crystal diamond, excited with a 532 nm continuous wave laser, is shown. At room temperature, the ZPL is broad, and ZPL coupling efficiency is nascently around

$2 \sim 4\%$. Whilst cooling the NV to 4 K inhibits thermally-dependant spectral broadening mechanisms giving a much narrower ZPL linewidth, phonon modes provide homogeneous broadening which are not removed by cooling, and so the ZPL coupling efficiency remains at around 4%.

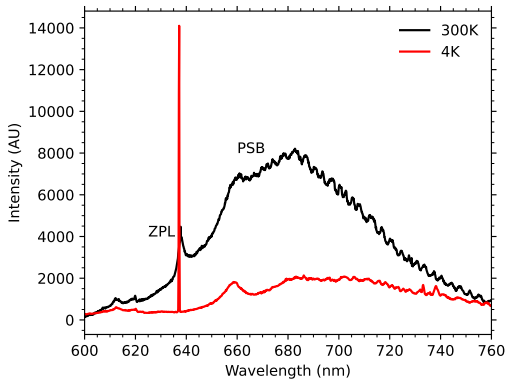

Figure 1.1: **Comparison of optical spectra of NV centre at room and cryogenic (4K) temperature**

Nonetheless, even when the NV centre is cooled, the contribution of the phonon sideband to the optical emission is still substantial. This can be improved further by exploiting Purcell enhancement, by embedding the NV centre within a resonant cavity. Fabry-Pérot (FP) cavities have proven effective in improving ZPL emission from NV centres [31–34]. Placing a diamond membrane within an open-access cavity facilitates coupling to transform-limited optical transitions, and the cavity can be brought onto resonance with the emitter by adjusting one of the cavity mirrors via a piezoelectric actuator, enabling resonant mode tuning as needed. Consequently, recent advances in networked quantum technologies frequently adopt this cavity approach [35–38]. However, these structures often lack mechanical robustness due to the air gap and suffer losses at the air-diamond interface [34]. Therefore, to scale the technology up, advancing toward monolithic FP structures, where the diamond is completely enclosed by DBR mirrors, is highly desirable.

This shift introduces a significant technical challenge: monolithic cavities lack the straightforward post-fabrication tunability of open-cavity systems. Fabrication errors as small as hundreds of picometers can cause a mismatch between the cavity resonance and the ZPL. Since coupling the cavity and mirror prevents positional adjustments for tuning, developing a method to tune the resonance of monolithic FP cavities to the ZPL post-fabrication is critical. Addressing this challenge is the primary goal of this project.

1.3 Monolithic Quantum Optical Device for Efficient Network Coupling

The are numerous methods available to generate NV centres in diamond, as are explained in more detail in Section 2.3. In the photonic nanomaterials group at Oxford University, a well established and highly promising technological advance has been made in recent years, facilitating the deterministic creation of NV centres by applying laser pulses to diamond to form Frenkel defects [29, 30]. Following either a thermal anneal or laser diffusion pulse train, these defects can form NV centres with a lateral precision of some tens of nanometers.

This advancement offers an exciting prospect of creating a diamond device with an extremely high density of qubits, each of which could act as individual emitters or combine to form more complex graph states. Not withstanding the spatial separation between neighbouring NVs required to mitigate crosstalk, if a single crystal diamond membrane of dimensions 4 mm^2 was filled with deterministically created NV centres by laser writing, based on the positioning accuracy of this approach, in principle a device containing 10^6 qubits could be produced, far exceeding any physical qubit amount necessary for implementing quantum error

correcting codes. For integration to a quantum network, each NV centre would need to be coupled to a resonant optical microcavity with a dynamically tuneable interface. For this task, it is evident that open-access cavities would be far too cumbersome to scale to so many qubits.

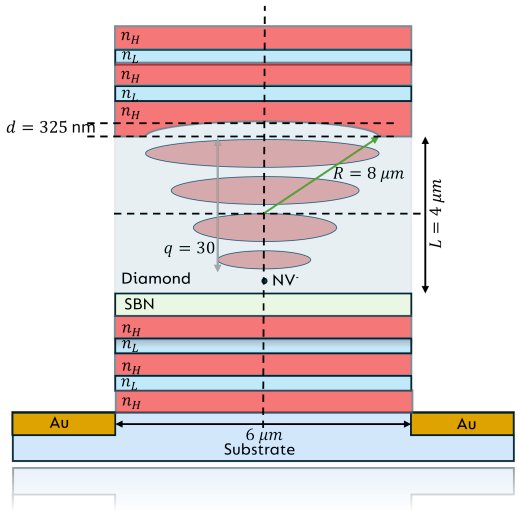

Figure 1.2: **Cross-section of intended integrated photonic quantum network node:** A cavity is formed by milling a convex feature into a diamond membrane, and coating each side with DBR mirrors. Between the diamond and the planar mirror, a tuneable electro-optic material(SBN) is bonded. An NV centre is formed in the diamond membrane by laser writing. The cavity structure sits on a substrate with electrodes to provide resonant mode tuning.

A proposed integrated-photonics quantum optical device for efficiently coupled dense arrays of NV centres to a quantum network is shown schematically in Figure 1.2. An NV^- centre sits within a thin diamond membrane, having been formed by laser writing. A convex feature is formed into the diamond membrane, and each side of the diamond is coated with distributed Bragg reflector (DBR) mirrors to form a resonant cavity. Between the diamond and the planar DBR mirrors is an electro-optic material which is used to tune the resonant mode of the cavity (Section 1.3.1). The device sits on a substrate, and electrodes are fabricated either side of the diamond to tune the resonant mode of the cavity. More electrodes can

be fabricated to also provide electronic control of the NV centre.

The proposed monolithic cavity structure would consist of a $4\ \mu m$ thick high-purity (< 5 ppb nitrogen and < 1 ppb boron concentration) diamond membrane, which could support a longitudinal mode index of q=30 which provides high Q-Factors (Section 4.1.2). The intended cavity radius of curvature is $8\ \mu$m with a cavity feature depth of ~ 325 nm. For high finesse, the planar cavity mirrors should offer a reflectivity of R_{plan}=0.9999 and the featured mirrors should provide R_{feat}=0.9950. A summary table of the design requirements is given in Table 1.2, and the impact of these parameters is discussed further in Section 4.1.2.

Table 1.2: **Summary of geometric requirements of proposed cavity device.**

L	$4\ \mu m$
RoC	$8\ \mu m$
depth	325 nm
R_{plan}	0.9999
R_{feat}	0.9950

1.3.1 Candidate Materials for Cavity Tuning

Finding an appropriate candidate approach/material capable of facilitating cavity tuning is itself a significant challenge. Multiple approaches may initially come to mind, but after experimenting with and/or modelling multiple different approaches, we find that many approaches ultimately fail to be viable. In principle, if a strong piezoelectric material is bonded to the diamond, the physical cavity length could be adjusted by applying a bias voltage, and the cavity resonance could be tuned. However, this would require very large bias fields to achieve very limited cavity tuning; a problem which would be compounded at cryogenic temperatures as the crystal lattice of the piezoelectric would become much stiffer. In addition, straining the piezoelectric material to a sufficient degree would potentially dete-

riorate the interface between the piezoelectric layer and the bonded diamond and DBR mirror. Therefore, this approach is not feasible.

Another way the physical cavity length could be modified would be by spin coating and baking a polymer layer between the diamond and DBR mirrors. The polymer could then be cured by UV radiation under a microscope, which would cause cross-linking and consequently shrinking of the polymer, allowing for cavity tuning. However, this approach is limited by only being able to work once, rather than in situ, and there are significant challenges in preventing prior polymerisation during the mirror growth, which typically requires temperatures of several hundreds of degrees Celsius.

1.3.1.1 Phase-Change Materials

Rather than changing the physical length of the cavity, the optical path length can be modified by introducing a hybrid material with a modifiable refractive index. In principle, this could be achieved using phase-change materials (PCMs), which possess a modifiable refractive index when the crystal structure of the PCM is modified by heating / laser irradiation. These are typically chalcogens or alloys of chalcogens, such as GeTe or Gb2Sb2Te5 (GST). However, in practice all known PCMs have optical losses via absorption substantially higher than what would be required to form a good cavity [39], with extinction coefficients in the visible spectrum typically between $1 \leq \kappa \leq 2$. Even more modern families of PCMs known to be exceptionally low loss by comparison (Sb_2S_3 and Sb_2Se_3) are still too absorbing at visible wavelengths [40].

We initially embarked upon an investigation of the suitability of Sb_2Se_3 for cavity tuning, and synthesised this material onto Si substrates by RF Sputtering. We measured the optical reflectivity by ellipsometry and modelled both the refractive

index and extinction coefficients for Sb_2Se_3 in both the amorphous and crystalline phases. We confirmed that the material absorption in the visible spectrum (Figure 1.3), our bandwidth of interest, is still fairly large with $\kappa > 1$. As we discuss in Section 4.1.4.1, this significantly exceeds what is required for integration into an optical microcavity.

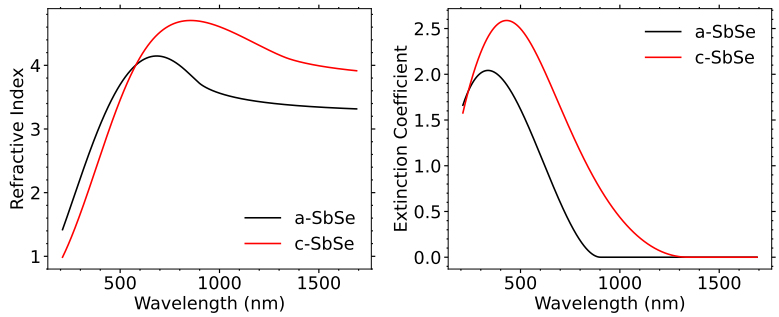

Figure 1.3: **Measured refractive index (a) and extinction coefficient (b) of Sb_2Se_3** grown by RF Sputtering, in the amorphous and crystalline phases.

1.3.1.2 Electro-Optic Materials

The most sensible approach to monolithic cavity tuning may be to introduce a strong electro-optic material at the diamond-mirror interface, whose refractive index can be modified in response to an applied static electric field. There are many known electro-optically active materials, but for most the magnitude of this effect is small. Given the short optical path length of the proposed device, a large refractive index shift is required. Therefore, a careful review of the possible candidate electro-optic materials is required.

The figure of merit for linear EO materials is the Pockels Effect, which quantifies the degree to which the cations and anions within the material shift relative to each other in response to an applied electric field, modifying the local electric dipole moments within the crystal, in units of pm/V. As is discussed in Section 4.2.2, the Pockels effect is described by a tensor r_{ij}. For lithium niobate ($LiNbO_3$), the most

widely used EO material, the largest Pockels tensor coefficient is r_{33}=33 pm/V. This is considered large for many planar optical modulators, but in practice the change in refractive index is very small - for a bias field of magnitude 10^7 MV/m, the relative change in refractive index for $LiNbO_3$ would be $\sim 10^{-4}$, and therefore unfeasibly large bias fields would be required to provide a large resonance wavelength tunability. However, there are many other materials which are known to exhibit an electro-optic response

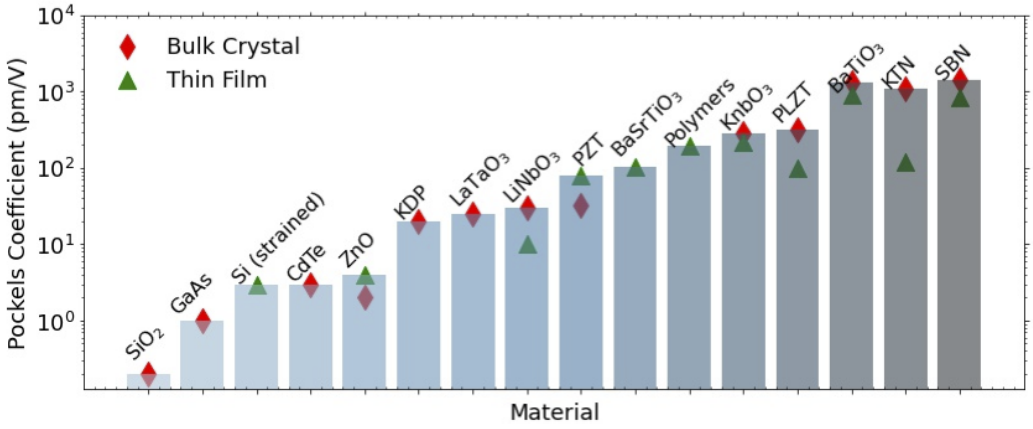

Figure 1.4: **Comparison of literature values for the Pockels effect in thin film form for different known EO materials.** Figure modified and updated from IBM Research [41]. This is not an exhaustive list of all known electro-optic materials, but a summary of the most widely studied ones which have demonstrated a strong Pockels effect and/or have been synthesised in thin-film.

Ferroelectric materials and perovskites are the most widely studied materials which exhibit an electro-optic response, but many semiconductor alloys such as GaAs also display a modest Pockels effect, as well as certain 2D materials and polymers. The vast majority of these materials however possess modest Pockels coefficients which would not provide a sufficient amount of tunability required for cavity tuning, and most of these materials have only demonstrated even this modest electro-optic response in bulk, not in thin-film. There are however a few materials which

possess a sufficiently large Pockels effect, in both bulk and thin-film. The maximum Pockels coefficient of the most widely studied of these materials is shown in Figure 1.4.

In thin-film form, barium titanate ($BaTiO_3$ / BTO) has the highest reported Pockels coefficient of r_{42}=923 pm/V [42]. This large coefficient was attained after substantial optimisations over a more than a decade, and can seemingly only be acquired under very precisely controlled molecular beam epitaxy. Without extraordinarily well controlled deposition conditions, the reported Pockels effect is typically much smaller, at for example r_{42}=148 pm/V [43]. Therefore, producing $BaTiO_3$ of a sufficient quality for cavity tuning is prohibitive. However, strontium barium niobate ($Sr_xBa_{1-x}Nb_2O_6$ / SBN) is also known to be a very strong electro-optic material, previously measured at 844 pm/V in thin-film form [44]. Importantly, this large coefficient was demonstrated following thin-film growth by Pulsed Laser Deposition (PLD), without the need for such rigorous optimisation. While the tetragonal phase of BTO is difficult to maintain following the growth procedure, it is far simpler for SBN, and it is therefore much simpler to grow SBN in a phase preferable for a high electro-optic coefficient. Fo this reason, SBN is a much more preferable material choice, and was the chosen material for this work. Since thin films of SBN are not sold commercially, and very few research groups continue to work with the material, it was required that we grow SBN in-house by PLD.

1.4 Aim of this Work

The intended long-term application of the present work is to progress towards the creating a scalable platform for quantum communications based on electronic and nuclear spins in diamond coupled to an optical network, with cavity coupled

colour centres such as the NV centre and other group IV vacancies forming the light-matter interface. There are three specific intended outcomes of the present work: (i) fabricate a prototype monolithic Fabry-Pérot microcavity in diamond membranes, and characterise the optical response; (ii) develop a means to provide resonant mode tunability; (iii) build the necessary scientific understanding of each component in the cavity design necessary for a fully integrated device.

1.5 Overview of This Thesis

This review is structured as follows: In **Section 2**, there is a review of various methods for generating entanglement, and further purifying and sharing over a distributed network. A discussion follows regarding the specific case of quantum networks formed using solid state emitters such as the NV centre, optical cavity microstructures, and background information on SBN. This work required a very broad range of experimental techniques to fabricate and characterise the photonic devices in this work; these techniques are detailed in **Section 3**. To build the requisite understanding of the cavity design, materials selection, device integration, and materials characterisation, substantive theoretical analyses were required; the background information on these theoretical explorations is given in **Section 4**. In **Section 5**, the fabrication of convex cavity features in diamond by focussed ion beam (FIB) milling is detailed, and prototype monolithic Fabry-Pèrot optical microcavities in diamond are optically characterised for the first time. In **Section 6**, the deposition and microstructural characterisation of thin-film SBN by PLD is thoroughly detailed. Finally, the optical and electro-optic properties of the fabricated SBN are detailed in **Section 7**, before the thesis concludes in **Section 8**.

2 | Literature Review

In this chapter, a broad review of the literature apropos to the present work is presented. A historical overview of the progress towards realising quantum networks is provided, followed by a review of some key experimental milestones with NV centres as the basis of a quantum network node. The NV centre is briefly explored, followed by an overview of coupling to optical microcavities. Finally, the relevant literature of strontium barium niobate is explored, introducing key information which is further explored in later chapters in this thesis.

2.1 Generating, Preserving, and Sharing Entangled States

The vision of a quantum internet is to revolutionise communication by enabling quantum data exchange between any two points on Earth. Operating alongside the classical internet, it aims to connect quantum processors, unlocking capabilities unattainable with classical systems alone [10, 11]. While the full potential of a quantum internet is still unfolding, several transformative applications have already emerged, including secure communication [4, 5], precise clock synchronisation [45], and efficient remote access to quantum computers [46]. These applications leverage the unique properties of quantum bits (qubits), which differ fundamentally from classical bits. Unlike classical bits, which are either 0 or 1, qubits can exist in a superposition of both states and can exhibit entanglement, creating strong correlations over vast distances. Qubits cannot be copied, and any interference can be detected, making them ideal for secure communication.

However, transmitting qubits over long distances presents significant challenges.

Figure 2.1: **A quantum network aims to connect distant quantum processors over metropolitan and ultimately global distances.**

Traditional methods like signal amplification or repetition are ineffective due to the no-cloning theorem [47]. This necessitates new technologies, such as quantum repeaters, to enable a functional quantum internet. Rapid experimental advancements have brought early quantum networks within reach. The building blocks for a quantum network are entanglement generation schemes, and the distribution of entanglement over a channel, employing purification, swapping, memory, and repeaters. These elements of a quantum network are described here, with specific reference to experimental milestones.

2.1.1 Entangled State Generation

For two arbitrary quantum systems A and B with respective Hilbert spaces H_A and H_B, the joint Hilbert space of the two systems is given by the Kronecker product between the two: $H_A \otimes H_B$. The combined state of the two systems is the Kronecker product of their respective states $|\psi\rangle_{AB} = |\psi\rangle_A \otimes |\psi\rangle_B$. States which can be represented in this way are known as *product states*, and are separable into their respective states. However, not all states of a combined system are

separable. For a basis $\{|i\rangle_A\}$ for H_A and $\{|j\rangle_B\}$ for H_B, a general combined state representation is a summation over the eigenbases:

$$|\Psi\rangle_{AB} = \sum_{ij} c_{ij} |i\rangle_A \otimes |j\rangle_B \tag{2.1}$$

If there exists eigenvectors $[c_i^A]$, $[c_j^B]$ such that $c_{ij} = c_i^A c_j^B$, the combined state can be separated into two eigenstates $|\Psi\rangle_A = \sum_i c_i^A |i\rangle_A$ and $|\Psi\rangle_B = \sum_j c_j^B |j\rangle_B$. However, if there exists eigenvectors $[c_i^A]$, $[c_j^B]$ such that for at least one pair of coordinates c_i^A c_j^B, $c_{ij} \neq c_i^A c_j^B$, the combined state cannot be separated into it's individual bases. Such inseparable states are said to be *entangled*. Entangled states allow for non-local correlations between different quantum systems, and are a critical building block of quantum networks.

The preparation of entangled quantum states is crucial to the realisation of scalable quantum information processors, as well as studying fundamental questions of the foundations of quantum mechanics, such as whether quantum mechanics can be described by a local hidden variable model [48–51]. This has attracted substantial research activity, and numerous methods for generating entangled states have been proposed and demonstrated. Among the earliest demonstrations of entangled EPR pair [52] generation was reported by Wu and Shaknov in 1950 [53], with the polarisation states of photons emitted during positronium annihilation being shown to be entangled with one another. This is a high energy experiment, and so is not useful for practical application in scalable quantum technologies. However, we now benefit from a range of different possible approaches to generating suitably entangled states, following a flurry of experimental activity aiming to both verify Bell's inequalities [48], and to close the detection and locality loopholes [54–63].

One of the earliest methods for generating entanglement used the atomic cascade

effect in a beam of calcium [54–57]. When a calcium atom is exposed to laser light, it can undergo a two-step transition involving spontaneous emission. Specifically, the atom transitions from the $4p^2S_0$ state to the $4s4p^1P_1$ state, and then to the $4s^{21}S_0$ state. In this process, two visible photons are emitted, with their polarisations becoming correlated. This correlation arises because the photons share an intermediate state, allowing for two possible pathways. The resulting entangled state of the photon pair is $|\Psi\rangle = \frac{1}{\sqrt{2}}(|HH\rangle + |VV\rangle)$, where H and V denote horizontal and vertical polarisation, respectively.

Spontaneous parametric down-conversion (SPDC) is a nonlinear optical process also proposed for generating entanglement, where a high-energy photon (pump photon) splits into two lower-energy photons (signal and idler) while conserving energy and momentum [64–68]. This occurs when a pump laser passes through a nonlinear crystal, such as lithium niobate, enabling photon splitting described by the annihilation of a photon in mode κ by an operator $\hat{\alpha}_k$ and the creation of two photons in modes κ_1 and κ_2 via $\hat{\alpha}^\dagger_{\kappa_1}\hat{\alpha}^\dagger_{\kappa_2}$. This process produces entangled photon pairs in states such as $|\Psi\rangle \propto \frac{1}{\sqrt{2}}(|HH\rangle + |VV\rangle)$ or $|\Psi\rangle \propto \frac{1}{\sqrt{2}}(|HV\rangle + |VH\rangle)$ where H and V denote horizontal and vertical polarisation. Alternatively, the photons can be entangled in frequency or direction. SPDC can generate entanglement with [64, 65] or without [58] post-selection, with the latter used in a key experiment addressing the locality loophole [59].

Allowing two or more atoms to interact with the same electromagnetic mode in a resonant cavity provides a well-established method for generating entanglement [69–73]. Cirac and Zoller originally proposed this to prepare a singlet state of two spin-$1/2$ particles with wavefunction $|\Psi\rangle = \frac{1}{\sqrt{2}}(|\uparrow_1\rangle|\downarrow_2\rangle - |\downarrow_1\rangle|\uparrow_2\rangle)$. First, atom 1 is prepared in its excited state $|\uparrow_1\rangle$ and sent through a cavity in the vacuum state $|0\rangle$. After it exits, atom 2, prepared in $|\downarrow_2\rangle$, is sent in a different direction. The Jaynes-Cummings interaction Hamiltonian conserves excitation number

$a^\dagger a + |\uparrow\rangle\langle\uparrow|$, so $|\downarrow\rangle|0\rangle$ remains unchanged, while $|\uparrow\rangle|0\rangle$ and $|\downarrow\rangle|1\rangle$ experience vacuum Rabi oscillations [74, 75]. The atomic velocity $\nu_i = L/t_i$, determined by cavity length L and interaction time t_i, controls these oscillations. If ν_1 is set for $1/4$ of a Rabi oscillation, the system state becomes $|\Psi\rangle = \frac{1}{\sqrt{2}}(|\uparrow_1\rangle|0\rangle - |\downarrow_1\rangle|1\rangle)$. As atom 2 crosses the cavity $|0\rangle|\downarrow_2\rangle$ remains unchanged, and ν_2 is set for $|1\rangle|\downarrow_2\rangle$ to complete half a Rabi cycle, yielding $|\Psi\rangle = \frac{1}{\sqrt{2}}(|\uparrow_1\rangle|\downarrow_2\rangle - |\downarrow_1\rangle|\uparrow_2\rangle)|0\rangle$. This prepares a singlet state while leaving the cavity in the vacuum state, ready for reuse. Extensions include continuous N-atom entanglement in high-Q optical cavities [70], demonstrated experimentally in optical [71] and superconducting cavities [72], and quantum memory using superpositions of Fock states [73].

A complete survey of entanglement generation methods is beyond the scope of this review, since the focus here is limited to the specific case of creating a network of entangled solid-state spins in diamond. For this reason, we focus primarily here on entanglement heralding (detailed in Section 2.1.1.1). Other well established methods include: the use of linear traps of cold ions, interacting with laser beams [12, 60, 76–78]; entangling distant atoms by interference of polarised photons [79]; repeat-until-success linear optics distributed quantum computing [80]; optical generation of matter qubit graph states [81]; photons emitted from decay cascade of the bi-exciton in a quantum dot [82]; and giant optical Faraday rotation induced by a single-electron spin in a quantum dot [83].

2.1.1.1 Heralding Entanglement

Cabrillo, et al, showed that the generation of entangled pairs need not require the control of an effective interaction between two atoms, but rather may be 'heralded' through interference and state projection following a measurement [84]. They proposed using two three-level atoms with a Λ level structure, based at distant locations from one another. These atoms may decay from an excited state

level due to spontaneous emission, consequently producing a single photon. If a detector is placed at half the distance between the atoms, and after some time, the detector registers the arrival of a photon, so long as the as source of the photon caqnnot be distinguished, they showed that an entangled state can be generated. This has the distinct advantage that since the atoms are spatially separated, there is no interaction between them, and therefore fewer decoherence channels are introduced as multi-qubit channels are created. Further, since in this approach entanglement is not generated through the dynamic state evolution of a prepared system, but rather is projected, the challenging preparation and maintenance of a prior entangled state is not required. Consequently, this approach lends itself much better to potential scalability, and provides the basis for the primary entanglement scheme targeted for quantum networking. This scheme is described in detail in the remainder of this section.

The scheme of [84] depends upon the concept of *path erasure*, in which a detector measures the arrival of a photon, but does not have any information regarding from which atom the photon was excited. This places two stringent requirements on the qubit system: i.) the emitted photons from each qubit must be coherent and indistinguishable; and ii.) there should be no trace of the photon emission identifiable to each qubit.

The aim of the entanglement heralding process is to begin with two initially uncorrelated states, and finish with a maximally entangled state. In the simplest case of a two qubit state, the physical setup for such a system is shown in Figure 2.2. Here, we have two matter qubits, each with a λ-level structure, with two ground states $|0\rangle$ and $|1\rangle$, and an excited state $|e\rangle$. These atoms may spontaneously emit a photon, which will be incident on a distant beamsplitter and subsequently detected by two different single photon detectors. With the assumption that that the system is ideal (hence there is no photon loss), and the further assumption that

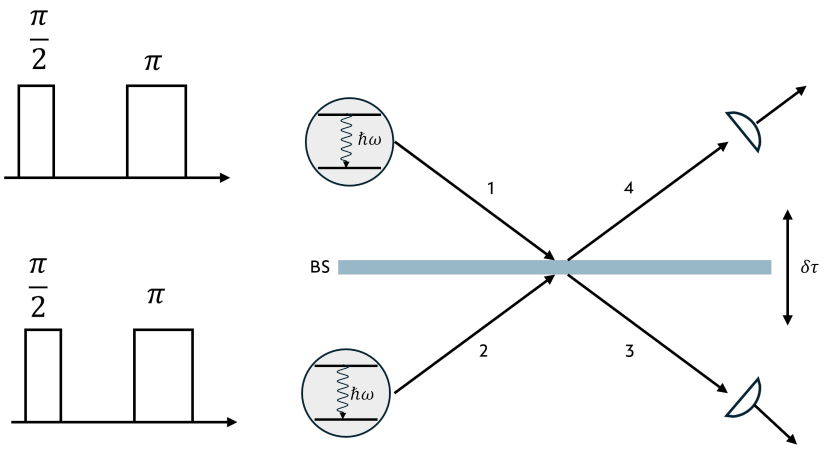

Figure 2.2: **Entanglement generation via projective measurement:** Optical transitions are driven in two different λ-level matter systems, resulting in a spin-dependent photon emission in each system. These photons interfere upon a beam-splitter and are subsequently detected. Due to path erasure, the detectors have no way of distinguishing the source of each arriving photon, and hence entanglement between the distant qubits is heralded by a projective measurement of each photon at the detector stage

the detectors can count the number of incident photons, due to the presence of the beam splitter, if precisely one photon is detected, there is no way for the detector to determine the photon's source. The procedure for generating entangled states by projective measurement is explained in detail in [85].

Starting in the ground state, a $\pi/2$ pulse applied to both qubits initialises each into the state $|+\rangle \equiv \frac{1}{\sqrt{2}}(|0\rangle + |1\rangle)$. Therefore the combined product state of both qubits is $|\Psi\rangle = \frac{1}{\sqrt{2}}(|00\rangle + |01\rangle + |10\rangle + |11\rangle)$. Next, a π rotation in the form of a laser pulse applied to the $|1\rangle \rightarrow |e\rangle$ transition brings the state of each qubit to $|+\rangle \equiv \frac{1}{\sqrt{2}}(|0\rangle + |e\rangle)$, and therefore the state of the system to $|\Psi\rangle = \frac{1}{\sqrt{2}}(|00\rangle + |0e\rangle + |e0\rangle + |ee\rangle)$. After some sufficient relaxation time, the states $|e\rangle$ will relax, and may or may not emit a photon in the process. The state $|00\rangle$ has no excitation, and so no photons will be emitted, and neither detector will click. On the other hand, the state $|ee\rangle$ produces two photons, and so both detec-

tors will click. Neither of these scenarios are useful for generating entanglement, since these could have been generated directly, and in the case of the former, no detection event will occur. However, the states $|0e\rangle$ and $|e0\rangle$ both produce only one photon, and so only one detector clicks. Due to path erasure, the detector has no way of determining from where the the photon emerged.

After each matter qubit has emitted a photon, but before it's arrival to the beamsplitter, with post-selection on a single photon the state of the system interacts with the vacuum state of the electromagnetic field $|\text{vac}\rangle$

$$|\Psi\rangle = \left(\frac{|0e\rangle + |e0\rangle}{\sqrt{2}}\right)|\text{vac}\rangle \tag{2.2}$$

So long as the photons incident to the beamsplitter are indistinguishable, they interfere destructively at the beamsplitter due to the Hong-Ou-Mandel (HOM) effect, leading to zero coincidence counts at the detectors (i.e. both photons go to the same detector). Creation operators can be used to describe the photon interaction at the beamsplitter. The beamsplitter maps the photon modes $a^\dagger$ and $b^\dagger$ onto output modes $c^\dagger$ and $d^\dagger$. In terms of these operators, the interaction of the incoming photons at the beamsplitter is:

$$\left(\frac{|01\rangle\, a^\dagger + |10\rangle\, b^\dagger}{\sqrt{2}}\right)|\text{vac}\rangle \tag{2.3}$$

After the beamsplitter, the photon channels are transformed as:

$$a^\dagger \to \frac{ic^\dagger + d^\dagger}{\sqrt{2}} \qquad\qquad b \to \frac{c^\dagger + id^\dagger}{\sqrt{2}} \tag{2.4}$$

....where the phase i denotes reflection. When the photon passes through the beamsplitter, the state of the system transforms as

$$|\Psi\rangle = \frac{1}{\sqrt{2}} \left([|01\rangle + i\,|10\rangle]\, c^\dagger + [i\,|01\rangle + |10\rangle]\, d^\dagger \right) \tag{2.5}$$

If a projective measurement of a photon has been made at the left detector, the projection operator $|0\rangle\langle 0|$ has been applied to the state $|\Psi\rangle$ such that

$$|0\rangle\langle 0|\Psi\rangle = \frac{|01\rangle + i\,|10\rangle}{\sqrt{2}} \tag{2.6}$$

Therefore, the qubits have been projected into a maximally entangled state. Of course, for a detection event at the right detector would yield the state
$|\Psi\rangle = \frac{i|01\rangle + |10\rangle}{\sqrt{2}}$

The above heralding scheme makes the assumption of an ideal apparatus, and no photon loss through the system. In practice, this is an unrealistic assumption, and false detection events are common. In response to this, Barrett and Kok introduced the 'double heralding' procedure [20]. Here, following the first measurement run, the qubit states are flipped, and the steps from the resonant excitation onwards are repeated. Only when a single photon is registered in two successive rounds of the heralding process is entanglement confirmed. Now the final state is of the system is a maximally entangled Bell state $|\Phi^\pm\rangle$, protected from photon loss:

$$|\Psi\rangle = \frac{|01\rangle \pm |10\rangle}{\sqrt{2}} = \left|\Phi^\pm\right\rangle \tag{2.7}$$

To achieve large scale quantum networks, it is crucial to maximise the probability of successful entanglement generation, by preserving entanglement in the event

that an entangled link is broken, whilst attempting to create new entangled links. One way this may be achieved is by 'brokering' [86], where an extra 'broker' qubit is at each physical system node, and entanglement is passed deterministically onto the neighbouring broker before further entanglement operations begin.

Aside from the prospect of heralding entanglement over a spatially separated network, the measurement-based entanglement scheme provides an important means for realising Raussendorf and Briegel's measurement-based-quantum-computing paradigm [87]. In this approach, a quantum state is associated with a graph state [88, 89], with each node in the graph containing a qubit, and each vertex connecting nodes performing some unitary operation which modifies the phase of the $|11\rangle$ component of the system. This operation can be achieved with the same parity projection protocol of the heralding procedure, which can mimic the controlled-phase operation. In addition, higher dimensional cluster states can be formed in this way [90, 91].

Impact of Photon Distinguishability

The heralded entangled state of Equation 2.7 can only be achieved if the incoming photons are indistinguishable. To see this, consider the case where two emitters are distinguishable in their frequency. Now, the post-selected single-photon emission is frequency dependent, with

$$|\psi\rangle = \frac{1}{\sqrt{2}}\left(|0\rangle\,|e\rangle\,\hat{a}^{\dagger}(\omega_1) + |e\rangle\,|0\rangle\,\hat{b}^{\dagger}(\omega_2)\right)|0\rangle\,, \tag{2.8}$$

where the photon frequencies $\omega_1 \neq \omega_2$. At the beamsplitter, the creation operators a and b are now transformed as:

$$\hat{a}^\dagger(\omega_1) \rightarrow \frac{1}{\sqrt{2}}(\hat{c}^\dagger(\omega_1) + i\hat{d}^\dagger(\omega_1))$$
$$\hat{b}^\dagger(\omega_2) \rightarrow \frac{1}{\sqrt{2}}(i\hat{c}^\dagger(\omega_2) + \hat{d}^\dagger(\omega_2)) \tag{2.9}$$

So the output from the beamsplitter is:

$$|\psi\rangle = \frac{1}{2}\left[\hat{c}^\dagger(\omega_1)\,|0\rangle\,|e\rangle + i\hat{c}^\dagger(\omega_2)\,|e\rangle\,|0\rangle + i\hat{d}^\dagger(\omega_1)\,|0\rangle\,|e\rangle + \hat{d}^\dagger(\omega_2)\,|e\rangle\,|0\rangle\right]|\text{vac}\rangle\,. \tag{2.10}$$

Since the photons are distinguishable, there is no quantum interference. The environment could, in principle, determine the source photon's origin, preventing the spins from forming a coherent superposition. After tracing out the photons, the reduced spin state is:

$$\rho_{AB} = \text{Tr}\left(|\psi\rangle\langle\psi|\right) = \frac{1}{2}\left(|0\rangle\,|e\rangle\langle 0|\langle e| + |e\rangle\,|0\rangle\langle e|\langle 0|\right), \tag{2.11}$$

This is a classical mixture, not an entangled state.

The strict requirement of photon indistinguishability is not actually as strict as was initially thought though. Kok *et al* proposed a simple linear optics setup which was able to attain deterministic entanglement for certain combinations of central energies and linewidths by adjusting the frequency of the probing photons [92] and with injecting squeezed light [93]. However, this does not mitigate the need for high quality photon generation completely, and practical quantum networks should still aim for sources as spectrally indistinguishable as possible.

2.1.2 Purification, Swapping, Memories, and Repeaters

Entanglement is key to building quantum networks but it is difficult to generate over long distances, making preservation methods essential. Quantum repeaters offer a solution by segmenting the network and performing purification and entanglement swapping at intermediate nodes. This process enhances the entanglement step by step, allowing it to span greater distances [13, 14, 94].

Entanglement purification and distillation increases the fidelity of shared entangled states, turning imperfect pairs into fewer near-perfect ones using local operations and classical communication (LOCC). For example, given n entangled pairs, highly entangled pairs are distilled by projecting onto a "typical subspace," improving fidelity as more pairs are used [95, 96]. Similarly, states like $|\Phi^+\rangle$ can be purified from noisy mixtures via operations such as polarising beam splitters (PBS), as demonstrated by Pan et al. [97].

Entanglement swapping extends entanglement by linking two distant nodes (e.g., Bob and Claire) via an intermediary (Alice). Alice's measurement transforms separate entangled states into a shared one between the distant nodes, effectively teleporting the entanglement [98, 99]. Meanwhile, quantum repeaters use these methods to scale networks efficiently, overcoming the exponential challenges of direct transmission. They divide the channel into smaller segments, purify locally, and use swapping to extend entanglement. This approach requires quantum memories to temporarily store states, which can be implemented using atomic ensembles, nuclear spins, or NV centers, depending on the network architecture [13, 100–103].

By combining purification, swapping, and quantum memories, quantum repeaters achieve scalable, long-distance quantum communication with polynomial resource

scaling, as opposed to exponential [14]. Comprehensive reviews of these techniques are available for further details [100–102, 104–106].

2.2 Experimental Milestones in Networked QIP

Early promising experiments in heralding entanglement, sharing with a quantum repeater, and storing in memory, were based on the protocol detailed by Duan, Lukin, Cirac, and Zoller (DLCZ) [13]. This extends the Cabrillo and Barrett and Kok protocols to atomic ensembles and linear optics, allowing for greatly enhanced coupling to light due to the collective enhancement of the ensemble with parametric gain. When a photon is detected by one of two photodetectors following a beam splitter, entanglement is heralded, and can be swapped when one half of the entangled pair of ensembles is read out and mixed onto an optical beam splitter with its counterpart from the other ensemble.

Much of the early experimental progress towards the realisation of networked quantum information processors implemented the DLCZ protocol, particularly with ensembles of caesium atoms. For example, using caesium ensembles in a magneto-optical trap (MOT), entanglement was heralded over a distance of 2.8 m, whilst being capable of storage in memory for 1μs [107]. This approach was later modified for two photons using $^{171}\mathrm{Yb}^{+}$ atoms in radio-frequency ion traps, rather than with atomic ensembles [108], which marked an important milestone, since single-atom quantum memories allow conditional quantum gates to be implemented through photonic channels [109]. However, the entanglement success rate was very low, at around thirty per one-billion attempts, and so in order to realise sufficient attempt rates, this approach would need to be combined with a cavity. This improvement was in fact implemented with ^{87}Rb atoms trapped in an optical dipole trap and held at the centre of a high-finesse optical cavity [110],

resulting in a 2% probability of successfully generating an entangled state.

The first significant experiment demonstrating the appropriateness of NV centres for generating, preserving, and manipulating entangled states for a quantum network emerged from the Hanson group in 2012 [111]. Here, a two-qubit parity measurement was performed on an ancillary electron spin of an NV centre, heralding entanglement between two nuclear spins in diamond (Figure 2.3a). The nuclear spin qubits were provided by the ^{14}N Nitrogen $I{=}1$ NV nuclear spin $|N\rangle$ and the surrounding $I{=}1/2$ ^{13}C carbon nuclear spin $|C\rangle$, and the qubit basis states $|\uparrow\rangle$ and $|\downarrow\rangle$ were encoded in the $m_I{=}0$ ($m_I{=}+1/2$) and $m_I{=}+1$ ($m_I{=}-1/2$) for the states $|N\rangle$ ($|C\rangle$). A high fidelity ($99 \pm 1\%$) parity measurement projected the nuclear spins into maximally entangled states, and a Bell state was created by first forming a maximal superposition between the two qubits and then applying the parity measurement. The resulting Bell state demonstrated reasonable fidelity ($90 \pm 3\%$), with the imperfection being due to imperfect microwave π pulses. This significant result constituted the first violation of Bell's inequalities with solid-state spins.

The entanglement heralded here was of course localised to the same diamond crystal, and so for practical application in a quantum network was not so useful. This was addressed in 2013, with heralded entanglement generated between two electron spin qubits in diamond, held at cryogenic temperature over a distance of three metres [112]. By generating spin-photon entanglement at each node, a later joint projective measurement of the photons projected the qubits into the Bell states $|\Psi^+\rangle$ or $|\Psi^-\rangle$ with fidelity $73 \pm 4\%$ and $64 \pm 5\%$ respectively, and probability 99.98% and 91.80%. At low temperature, the fine structure of the NV spectrum is visible, revealing six discrete energy levels. These levels are sensitive to strain on the local lattice, which may be a problem for generating indistinguishable photons, since this may induce large variations in photon frequency

(Figure 2.3b). To mitigate this, optical transition frequencies were tuned via the DC stark effect. Meanwhile, photo-ionisation was mitigated with repumping of the NV centre with a green laser. Overall, the success probability of the protocol was found to be around 10^{-7}, corresponding to an entanglement event occurring once every ten minutes for a 20 kHz attempt rate.

Entanglement heralding alone is not sufficient for building large scale quantum networks, and purification and swapping schemes must be implemented to preserve the entangled states. The first major step in this direction for diamond qubits was taken in [113], where a qubit state was teleported between two experimental stations, named Alice and Bob, over a distance of 3 metres, mediated by an additional qubit in Alice's node from a ^{14}N nuclear spin. Compared to the previously discussed work [112], the photon collection efficiency was enhanced through applying an anti-reflection coating to the diamond substrate. Both the spectral stability of the NV centre optical transitions and the charge state initialisation was improved by resonantly pre-pumping the NV^0 state zero-phonon line. As a result of these improvements, the entanglement generation rate was boosted to $1/250$ s^{-1}, and state fidelity from F=0.73 to F=0.87. A Bell state fidelity of 0.93 ± 0.02 was achieved with high fidelity single shot readout of the electron and nuclear spins. As a further enhancement, the ideal state of the third qubit was mapped onto a qubit eigenstate such that the readout directly yielded the teleportation fidelity. This 'feed-forward' technique allowed for the realisation of a teleportation fidelity of 0.77 ± 0.03, establishing diamond spin qubits as a prime candidate for the realising quantum networks.

Entanglement distillation, along with a combination of storage and processing, was later realised in a network of distant nodes over a distance of two metres [114] (Figure 2.3c), opening the door to exploring multipartite entanglement on extended quantum networks. A remote, highly entangled state was distilled using

only local operations and classical communication (LOCC) from a number of lower-quality states. By combining optimised readout and real-time feedback, Bell states were distilled with a measured fidelity $F = 0.65$.

In 2021, the Hanson group reported the first realisation of a multi-node quantum network with NV centres [115], combining real-time heralding and feed-forward operations. Two main quantum networks protocols were established. First, a three qubit Greenberger-Horne-Zeilinger (GHZ) state was established across the nodes, Alice, Bob, and Charlie. Subsequently, the generated entanglement was swapped via a Bell state measurement on one of Bob's qubits. Bob has an additional ^{13}C nuclear spin to be used as a memory qubit. Each node experiences different conditions, noise, spectra, etc, and therefore must be individually phase stabilised. This is resolved in the paper with a hybrid-phase stabilisation scheme in which the effective interferometer for each link is decomposed into three independently addressable interferometers, and each being stabilised separately with unbalanced heterodyne phase detection. The resulting measured Bell state fidelity was greater than 0.8 for both links, with an entanglement generation rate of 9 Hz and 7 Hz for A-B and B-C respectively. Bob's carbon spin stored the states for a time limited by the dephasing time $T_2^* = 11.6$ ms, corresponding to 2000 entanglement generation attempts and thus greater memory robustness in the presence of dephasing errors [116]. GHZ states were generated at a rate of about $1/90$ s, and fidelity of around $F{=}0.538$, the swapping fidelity was measured as $F{\sim}0.551$ over all outcomes, with a heralding rate of around $1/40$ s. As a consequence of this work, advanced multi-node protocols and larger entangled states may be explored by, for instance, extending the local registers at the nodes, and interfacing the NV photons with telecom fibre, paving the way to near-term quantum network tests over larger distances.

Most recently, the Hanson group expanded on the short-range qubit network of [115],

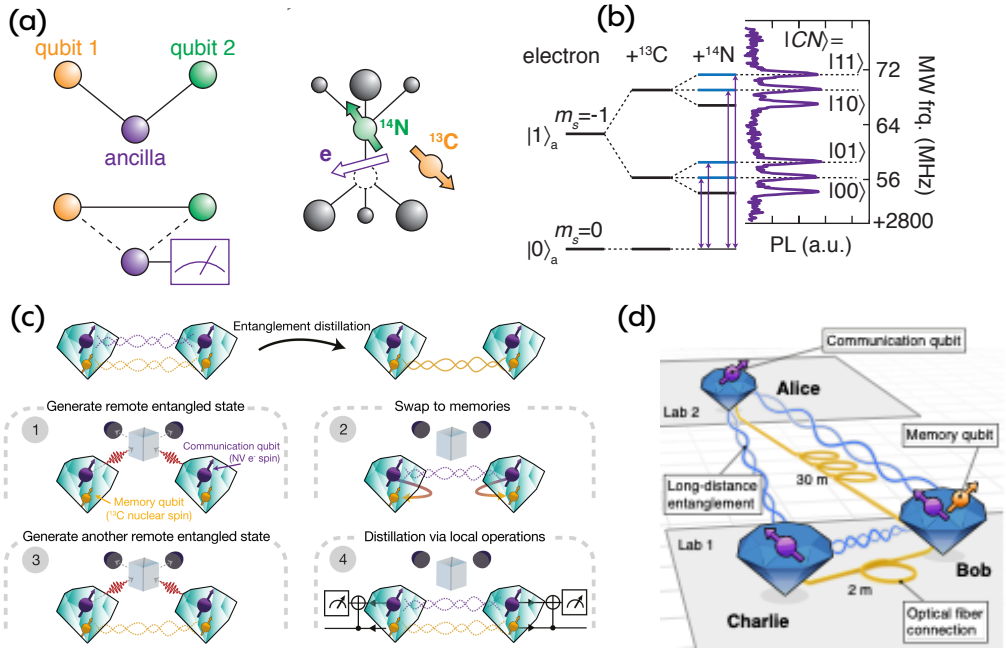

Figure 2.3: **Measurement based entanglement using NV defects in diamond (a)** Two qubits are allowed to interact with an ancillary qubit to which both qubits couple. Subsequent readout of the ancilla can project the qubits in a maximally entangled state without direct interaction between the qubits, as demonstrated in [111]. In this case the spins of a ^{14}N nucleus and surrounding ^{13}C of an NV centre act as qubits, while the NV electron spin is used as an ancilla. Figure reproduced from [111]. **(b)** The energy level and photoluminescence (PL) spectrum for the m_S=0 to m_S= − 1 electron spin transition reveals six resonances due to the hyperfine interactions with the ^{13}C and ^{14}N spins, allowing transitions between the electron m_S=0 to m_S= − 1 for the four different two-qubit states [111]. Figure reproduced from [111]. **(c) Entanglement distillation:** A remote highly entangled state (right) is distilled by LOCC from several lower-quality states (left) that are shared between remote qubits [114]. Each network node has a communication qubit (purple) and a memory qubit (yellow). Remote spin-photon entanglement is generated between the communication qubits, and following interference on a beamsplitter, the optical mode is detected (1). The entangled state is then swapped onto the memory qubits (2), and another round of entangled state generation follows (3). Finally, a state of higher fidelity is distilled by LOCC (4). Figure reproduced from [114]. **(d) Multi-particle diamond-based quantum network** Three nodes, labeled Alice, Bob, and Charlie, contain a communication qubit. Bob has an additional nuclear spin qubit (orange). Remote entanglement can be generated between the nodes via fibre connections, which allows for entanglement to be shared between all nodes. Figure reproduced from [115].

extending the link to network nodes separated metropolitan distances up to 10 km combined with a midway heralding station via 25 km of optical fibre[117]. To mitigate photon loss over such distances, they employed quantum frequency conversion to the telecom L-band and implemented a phase-stabilised architecture, enabling the use of a loss-resilient single-photon entangling protocol. This setup allowed for the reliable delivery of predefined entangled states between the nodes, regardless of the heralding detection pattern. The probability of successful heralding for entanglement creation was optimised using a loss-resilient single-photon entangling protocol and quantum frequency conversion to telecom wavelengths. This resulted in an entanglement generation rate of 0.48 Hz with a success probability per attempt of 7.2×10^{-6} for a 20 ns window, and an entanglement fidelity $> 90\%$.

Table 2.1: **Summary table of entanglement generation success and rates with NV centres in a diamond quantum network. NR: not-reported**

Attempt Rate	Success Prob.	Ent. Gen. Rate	Ent. Fidelity	Ref.
20 KHz	10^{-7}	1 per 600 secs	69 ± 5 and 58 ± 6	[112]
100 KHz	10^{-7}	1 per 250 secs	0.87	[113]
NR	6.40×10^{-9}	1 per hour	0.92 ± 0.03	[61]
NR	NR	0.05 per sec	0.96 (0.65 distilled)	[114]
NR	NR	6 or 39 per sec	0.81 or 0.60	[118]
NR	5×10^{-5}	NR	0.53	[115]

2.3 Colour Centres in Diamond

To realise truly scalable and integrable quantum network nodes, a well-controlled matter-based qubit with an optical interface is required. Simple networks based on photon-mediated entanglement have so far been implemented with atoms [108, 110, 119], trapped ions [120], semiconductor quantum dots [121, 122], and defect centres in diamond [111–115]. Diamond colour centres have emerged as one

of the most promising candidates, and recently a multi-node quantum network with diamond-based network nodes was implemented [115]. Diamond is a host of hundreds of optically active colour centres, including silicon (SiV), germanium (GeV), tin (SnV), and nitrogen (NV) centres. Of these defects, the NV centre is the most well studied and established. Diamond possesses a combination of almost nuclear spin free environment, high Debye temperature, and wide band gap, allowing for NV^- coherence times of approximately 1 ms at room temperature [16] and 1 s at cryogenic temperatures [17], with nuclear spin coherence times greatly exceeding 1 s [18, 19]. Satisfying the DiVincenzo criteria [123], NV spins can be readily initialised, manipulated, and readout with high fidelity [124]. NV defects are also very readily integrable with photonics systems due to the spin dependent optical transitions, providing a means for the development of on-chip networks, and for controlling the interface between network photons and NV nodes with optical cavities.

To successfully implement the path erasure protocol, photon indistinguishability is an important consideration. This requires that emitted photons from nodes must leave no trace of their origin from, for example, lattice vibrations. To satisfy the requirement that the nodes leave no trace of their emission, photons must not couple to vibrational degrees of freedom, but rather must be emitted into the zero-phonon-line. In addition, the photon must be Fourier transform limited, such that the lifetime extends over the spontaneous emission lifetime. This requires a low decoherence environment, and therefore operation at cryogenic temperatures.

Despite the many advantages of NV centres as quantum network nodes, there are some limitations which at first glance impede their ability to readily generate indistinguishable photons for entanglement. First, the Debye-Waller factor / free-space branching ratio into the zero-phonon-line accounts for only approximately $2 - 4\%$ of the overall photon emission, with the remaining photons being

mediated by phonons, hence limiting the rate at which indistinguishable photons can be generated. In addition, due to the low defect symmetry, the NV centre is highly susceptible to spectral diffusion: the NV^- gets photo-ionised to NV^0 under resonant excitation at 637 nm, and therefore the charge state can be unstable.

2.3.1 Generating an NV Centre

Nitrogen-vacancy (NV) centres in diamond are formed when a lattice vacancy pairs with a substitutional nitrogen impurity along a crystal axis. These defects can be introduced during chemical vapour deposition (CVD) growth through delta doping or post-growth by electron irradiation, ion implantation, or laser writing, typically followed by thermal annealing. The development of scalable quantum computing nodes requires precise control over NV centre properties, including spatial positioning, orientation, charge stability, optical coherence, and spin coherence times, all of which are highly sensitive to the local lattice environment. Minimising damage to the diamond lattice during fabrication is critical for meeting these requirements.

Ion implantation allows post-growth defect introduction, with depth controlled by ion beam energy and lateral precision influenced by material properties [125]. However, the probability of implanting a single atom follows a Poisson distribution, with a 37% success rate. Deterministic implantation, achievable via secondary electron detection [126] or pre-impact ion detection in traps [127], improves precision but increases complexity. While annealing mitigates lattice damage [128–131], implanted NV centres often exhibit broad linewidths (>1 GHz), higher strain, and reduced coherence times (50 μs) compared to those formed from native nitrogen [132–134].

NV centres can also be formed using native nitrogen through high-energy electron

irradiation, which induces vacancies which experience less strain compared to ion implantation [135]. Subsequent diamond membrane processing further enhances optical coherence. Delta doping during plasma-enhanced CVD (PE-CVD) introduces nitrogen gently, minimising lattice disruption and providing excellent depth control [136]. Nitrogen doping during growth, followed by activation through electron irradiation [137, 138], carbon implantation [136], or laser writing [29], can result in NV centres with long coherence times (~ 1 ms) [136].

2.3.2 Generating an NV Centre by Femtosecond-Pulsed Laser Writing

A promising alternative to defect creating through implantation and thermal annealing involves laser writing, where Frenkel defects are created using femtosecond laser pulses, followed by thermal annealing to convert defects into NV centers [29]. This process minimises lattice damage by allowing vacancies to heal during annealing, resulting in NV centers with lifetime-limited zero-phonon line (ZPL) transitions at cryogenic temperatures. Coherence times range from 400 to 900 μs [30]. Laser writing offers high positional accuracy, with initial arrays in optical grade diamond achieving a precision of ~ 200 nm laterally and ~ 700 nm in depth. Further refinement, involving real-time fluorescence monitoring and laser annealing, improves accuracy to ~ 35 nm laterally and ~ 200 nm in depth [30]. However, this enhanced precision often comes at the cost of reduced coherence times, which may be mitigated by using higher-purity diamond and compromising on spatial positioning. Recently, we demonstrated an extension of this method, deterministically generating NV centres in electronic grade diamond using a MHz laser writing system [139]. Excitingly, this method can also be extended to other defects, such as the SnV centre [140].

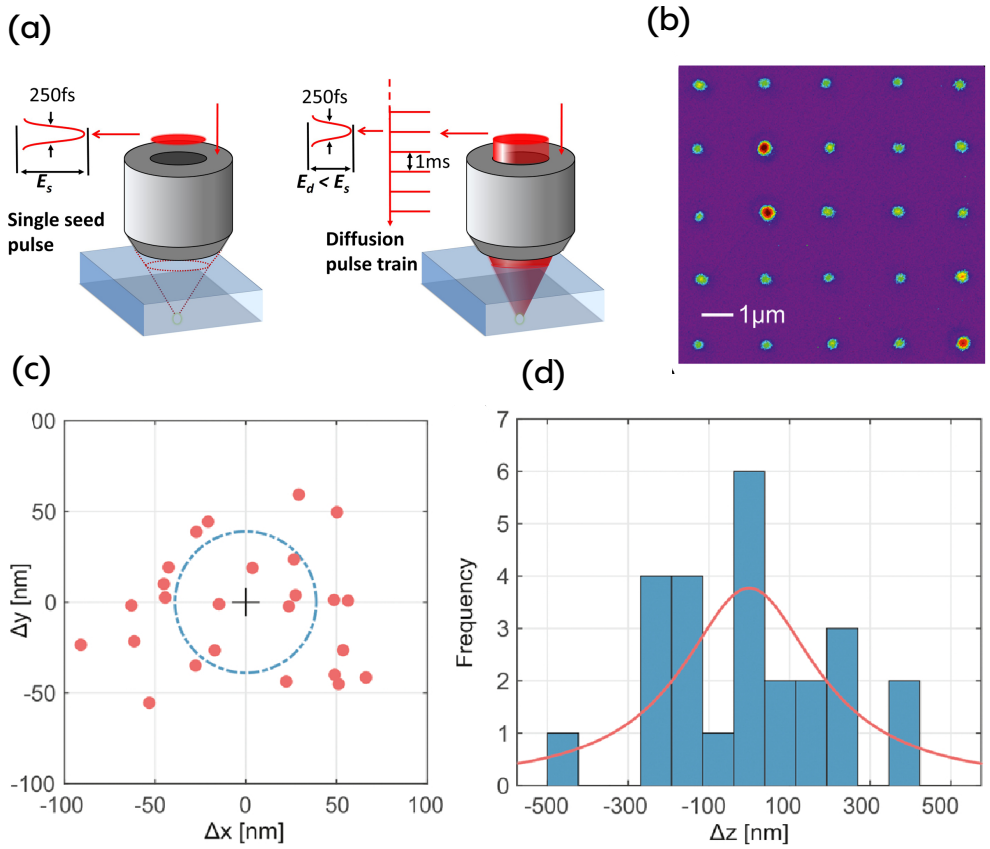

Figure 2.4: **Deterministic laser writing of NV centres: (a)** Schematic diagram of the laser-writing process of [29, 30]. A seed pulse generates vacancies in the crystal, and a subsequent lower energy pulse train locally anneals the diamond. **(b)** Fluorescence image of a high-yield 5x5 array of NV centres produced on a 2 μm square grid. **(c)** High positioning accuracy of NV centre generation in the image plane (~ 35) nm, with the dashed circle denoting a deviation parameter for a fitted Gaussian function. **(d)** Histogram of depth positioning accuracy, with an accompanying Lorentzian best-fit. Figure modified and reproduced from [29].

In [29], an array of NV centres in < 5 ppb N-concentration diamond was created after forming seed pules by a femtosecond laser, followed by a thermal anneal for activation of the Frenkel defects. Due to the Poissonian nature of the thermal diffusion through a lattice, only around 30% of the a-priori created Frenkel defects were annealed to single photon emitters. However, since the volume of Nitrogen impurities was small, the contribution of nuclear spin induced decoherence

was correspondingly small, and therefore the measured spin coherence times of these NV centres was quite large 700 μs, extending to 3 ms with dynamic decoupling [141].

A femtosecond laser pulse train in and of itself can diffuse the vacancy around the lattice, and form an NV centre. This is challenging since the region in which diffusion is possible is limited by the diffraction limited spot size of the focussed laser beam. However, with spectral feedback, it is possible to deterministically generate NV centres, by monitoring the fluorescence of the plasma formed during laser irradiation to the lattice, and turning off the laser pulse train once there is evidence that an NV centre has been formed (Figure 2.5). Fabrication by this method is made easier by having a fairly large natural abundance of nitrogen atoms in the diamond lattice (e.g. of order 1 ppm), since there are more nitrogen impurities within the diffraction limited spot size of a laser fabrication system (typically a few hundred nm).

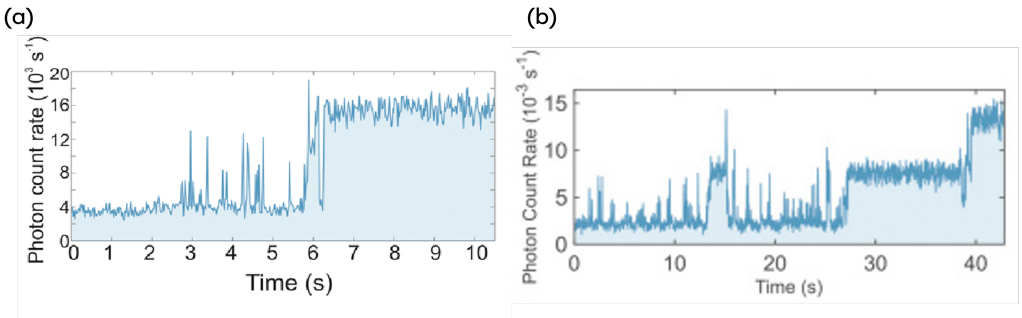

Figure 2.5: **Spectral signature of NV creation during laser diffusion:** the deterministic generation of NV centres in diamond by laser diffusion is facilitated through in-situ spectral monitor of the fluorescence emitted from the laser treated region. The formation of a single NV centre is evident when a stable high fluorescence is seen (a). A vacancy can be diffused away causing the pstable peak to diminish (b). Two sequential peaks, also seen in (b), indicate the formation of two emitters.

However, with such large nitrogen concentration, coherence times can suffer due

to greater presence of nuclear spins. Further refinement, involving real-time fluorescence monitoring and laser annealing, improves accuracy to ~ 35 nm laterally and ~ 200 nm in depth [30]. To mitigate the reduced coherence time, it is desirable then to laser write defects into high purity electronic grade diamond. This comes at the cost of spatial position accuracy and is technologically more demanding since fewer nitrogen atoms will reside within the diffraction limited laser spot. Recently however, we demonstrated the deterministic generation of NV centres in electronic grade diamond using a MHz laser writing system [139]. Excitingly, this method can also be extended to activating other defects, such as the SnV centre [140].

2.3.3 Diamond Membranes

NV centres can be subject to significant line broadening due to charge noise caused by their close proximity to fluctuating charges at the surface, leading to random fluctuations in the spectral frequency of the NV emission [142]. A reliable method for generating NV centres is therefore required, and it is crucial that the NV is embedded into high-purity, single-crystalline diamond [143, 144] to reduce opportunities for excited state dephasing and spectral diffusion. Single crystal, CVD grown diamond membranes [145] have been shown to reliably produce PLE linewidths of around 1 GHz with implanted nitrogen, substantially lower than in nano-crystalline materials [146], and smaller than the 2.87 GHz ground state spin-triplet splitting of the NV, an essential requirement for quantum information processing [147]. Typically, a diamond membrane may be formed using CVD growth in conjunction with mechanical polishing and chemical etching [148–152], although a recent approach combining electron irradiation, high temperature annealing, and inductively coupled plasma reactive ion etching (ICP/RIE) formed micro-metre-scale membranes which contained individually resolvable NV cen-

tres with dephasing widths < 100 MHz and spectral diffusion widths < 250 MHz [135]. The ultra-thin form factor of diamond membranes means they can be incorporated into a Fabry-Pèrot microcavity [35, 135, 146, 153–155], to enhance photon emission into the ZPL.

2.3.4 NV Centres in Optical Micro-Cavities

The efficiency of photon emission into the zero-phonon line of an NV centre is naturally limited to around 4%, inhibiting the ability to produce suitable indistinguishable photons for entanglement swapping. However, by placing the NV centre into an optical microcavity designed to be on resonance with the ZPL, due to Purcell enhancement [156], the photonic density of states in the ZPL can be significantly enhanced, allowing for a substantially higher potential rate of entanglement generation than nascent NV centres.

A number of resonant optical structures have been explored for enhancing the spontaneous emission of solid state emitters, including micro-ring resonators [157], photonic crystal cavities (PCCs) [147, 158–161], hybrid nanodiamonds [162–165], and Fabry-Pèrot (FP) microcavities [153, 166–169]. Nanobeam cavities, microring resonators, and photonic crystal cavities are all appealing resonant structures for enhancing the optical density of states of coupled emitters, since they are quasi-two-dimensional and therefore can possess small mode volumes and correspondingly high Purcell enhancement. However, despite having successfully been coupled to NV centres, they are not the most optimal resonant structure for this defect since the both the NV ZPL linewidth and charge state stability of the NV^- is strongly dependent on the surface chemistry of the diamond [170, 171]. Therefore it is necessary to ensure that the NV centre is sufficiently far away from the diamond surface, e.g. a few μm, which places a lower bound on the required cavity path length. For this reason, Fabry-Pèrot structres are preferable.

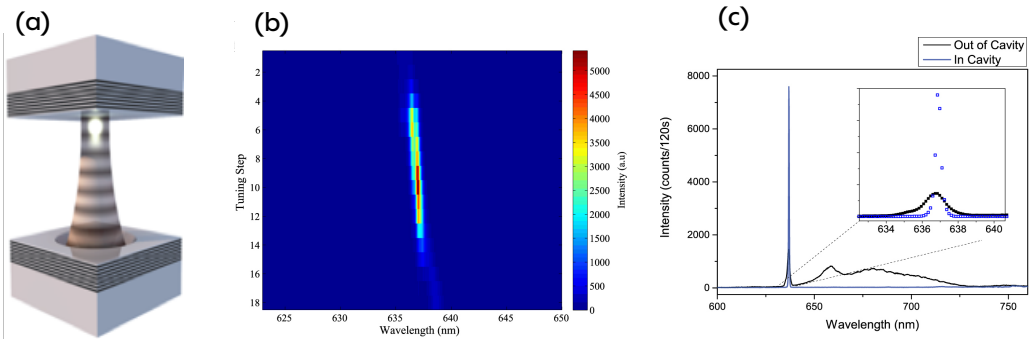

Figure 2.6: **Open-access Fabry-Pèrot cavity: (a)** Schematic diagram of an open-air FP cavity formed by one planar mirror an an opposing concave mirror. An NV centre is embedded in nanodiamond between the mirrors [169]. **(b)** The cavity resonance can be easily yet precisely modified by subtly moving one of the mirrors with a piezoelectric actuator. **(c)** At 77K, the enhanced intensity of ZPl transitions is observed in this cavity structure, with emission from the PSB suppressed. Figure modified and reproduced from [169].

Indeed, open-access FP cavities offer precise tunability via piezoelectric actuators, achieving Purcell enhancements up to F_P=20 [166, 167, 169]. Johnson et al. [169] demonstrated 40% ZPL intensity enhancement at 77 K using a mode volume of V_{mode}=$4.7(\lambda/n)^3$ cavity. Integrating high-quality diamond membranes maintains high finesse ($\mathcal{F}$>10^4) with low-temperature Purcell enhancements [36, 153]. A summary of the key results for NV centres couples to various resonant structures is provided in Table 2.2.

2.4 Strontium Barium Niobate for Electro-Optic Tuning

Strontium barium niobate (SBN) ($Sr_xBa_{1-x}Nb_2O_6$), is a widely studied complex oxide perovskite ferroelectric material known for its high electrooptic and piezoelectric coefficients [173], making it valuable in electrooptic and photorefractive applications. For many integrated photonics applications, fast and efficiently low-

Table 2.2: **Summary of cavity figures of merit and Purcell enhancement for NV centres coupled to a variety of resonant structures. NR: Not Reported. Updated from [32].**

Cavity	Defect	V_{mode} $(\lambda/n)^3)$	Q-Factor	F_P (meas.)	Ref.
Whispering Gallery					
Micro-ring	NV	15	5500	12	[157]
Micro-ring	NV	17-32	4300	12	[172]
Photonic Crystal					
2D-PCC	NV	0.88	3000	70	[147]
2D-PCC	SiV	1.5	400	19	[161]
Nanobeam	NV	1.05	3300	62	[160]
Nanobeam	NV	3.7	1630	7	[158]
Open Cavity					
FIB Milled	NV	4.7	3000	10	[169]
Fibre	NV	NR	NR	13	[36]

power electro-optic modulation of light is essential. With SBNs known extraordinarily high linear electro-optic effect, it is a fantastic candidate material for such applications. In addition, it's strong and highly tuneable electro-optic coefficient make it highly promising for resonant mode tuning of optical waveguides resonators, and for the intended action of the present work, Fabry-Perot cavity tuning.

2.4.0.1 Crystal Structure

The foundational work by Jamieson et al [174] described the ferroelectric tungsten bronze structure of SBN, specifically $Sr_{0.75}Ba_{0.25}Nb_2O_{5.78}$. Using a programmed electronic X-ray automatic diffractometer (PEXRAD) [175], they determined that the structure comprises NbO_6 octahedra forming a network of pentagonal, tetragonal, and triangular channels. The distribution of Sr and Ba within these channels significantly influences the ferroelectric and optical properties. Three interstitial sites are provided by the arrangement of the NbO_6 octrahedra. Trigonal sites are

vacant. The tetragonal A1 sites in Figure 2.7(a) are occupied by Sr atoms, whilst the pentagonal A2 sites are partially occupied by both Sr and Ba atoms [176]. At room temperature, SBN is a *relaxor ferroelectric* with the space group P4bm. Such materials possess a large dielectric constant, large electrorestriction, and broadened phase transitions [177]. This relaxor behaviour arises due to the partial occupancy of the A2 sites which lead to a degree of disorder [178]. A table of the final determined atomic position coordinates is provided in Table 2.3. These coordinates are used later in this thesis in the developing the standard diffraction patterns for XRD and EBSD analysis in Section 6.

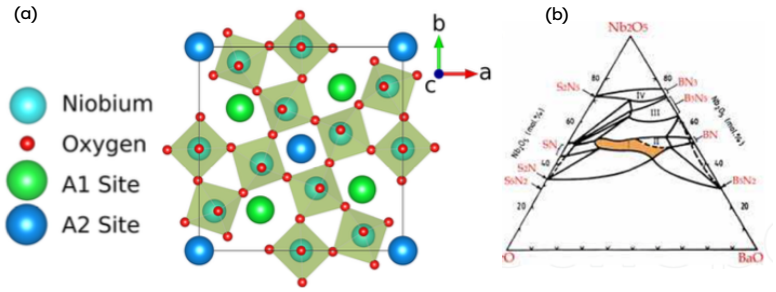

Figure 2.7: **Strontium barium niobate :** (a) crystal structure (figure reproduced from [179]); (b) ternary phase diagram (figure reproduced from [180]).

Table 2.3: **Wykoff position for SBN75, determined experimentally by PEXRAD [174]**

Atom	Pos.	Occ. (%)	x	y	z
Nb(1)	2b	100	0	0.5	0.0236 ± 14
Nb(2)	8d	100	0.07470 ± 6	0.21148 ± 6	0.0089 ± 15
Sr	2a	82.2 ± 1.0	0	0	0.5
0.406Ba/0.594Sr	4c	82.7 ± 0.8	0.17236 ± 8	0.67236 ± 8	0.5069 ± 15
O(1)	8d	100	0.3450 ± 7	0.0049 ± 8	-0.0546 ± 23
O(2)	8d	100	0.1369 ± 7	0.0679 ± 6	0.0663 ± 21
O(3)	4c	100	0.2800 ± 7	0.7800 ± 7	-0.0356 ± 33
O(4)	4c	50	-0.0155 ± 10	0.4845 ± 10	0.5093 ± 92
O(5a)	8d	50	0.3092 ± 16	0.4024 ± 15	0.4795 ± 81
O(5b)	8d	50	0.2792 ± 15	0.4364 ± 26	0.5023 ± 67

The ternary phase diagram [181] (Figure 2.7(b)) suggests that with different mixture ratios of the constituent oxides (SrO, BaO, and Nb_2O_6), different phases may crystalise. If x denotes the percentage concentration of an element, and the compound is represented by $Sr_xBa_{1-x}Nb_2O_6$, when $0.2 \leq x \leq 0.8$. In the region $0.25 \leq x \leq 0.75$ the material crystalizes with a tetragonal tungsten bronze structure [182], where a strong electro-optic effect is known to exist [180]. Podlozhenov et al [183] provided a comprehensive analysis of the structural variations in SBN across the compositional range $0.32 \leq x \leq 0.82$. Their crystallographic studies revealed that increasing Ba content reduces lattice distortions and enhances structural stability, leading to a shift in the ferroelectric-paraelectric phase transition temperature.

The electro-optic response of a crystal is characterised by a tensor of it's individual electro-optic coefficients, known as the Pockels tensor [184]. Each of the components of this tensor describe the displacement of atoms of the crystal in response to an applied electric field. As will be explained further in Section 4.2.3, the tensor of Pockels coefficients for SBN is given by equation 2.12. The r_{42} coefficient has not been widely studied, but the largest reported Pockels coefficient in thin-film form is r_{33}, reported as 844 pm/V [44], whilst the r_{13} coefficient has been reported as high as 47 pm/V [185].

$$r_{SBN} = \begin{pmatrix} 0 & 0 & r_{13} \\ 0 & 0 & r_{13} \\ 0 & 0 & r_{33} \\ 0 & r_{42} & 0 \\ r_{42} & 0 & 0 \\ 0 & 0 & 0 \end{pmatrix} \tag{2.12}$$

Thin-films of SBN have been grown by a variety of methods. Cuniot-Ponsard, et al [186] demonstrated hetero-epitaxial growth of SBN by magnetron sputtering, which is significant since magnetron-sputtering is a very accessible and comparatively low-cost deposition technique. Beskin et al. [179] grew SBN films on $SrTiO_3$ and Si substrates using molecular beam epitaxy (MBE). This approach allowed precise atomic layer control, yielding films with uniform thickness and excellent epitaxial alignment. The integration with Si is significant since it broadens horizons for scalable room temperature electro-optic applications. Schwyn-Thöny et al. [187] pioneered the growth of epitaxial SBN thin films using PLD, demonstrating excellent crystallinity and substrate compatibility. Their work established a framework for optimising deposition parameters, such as laser fluence and substrate temperature. Tayebati et al. [44] later reported a substantial electro-optic coefficient of 844 pm/V in PLD-grown SBN films.

A diamond-based quantum node is required to operate at temperature below 10K to mitigate the mechanisms of inhomogeneous broadening of the NV^- zero-phonon line. When non-centrosymmetric materials cool they often undergo a range of phase-transistions, which can substantially alter their ferroelectric, piezoelectri, dielectric, and electro-optc properties. This does not appear to be the case for SBN, which maintains a tetragonal unit cell structure across a wide temperature range, including cryogenic temperatures. Low-temperature x-ray diffraction studies have confirmed the persistence of this tetragonal symmetry at reduced temperatures [188]. Whilst low-temperature dielectric anomalies have been observed between $15-150$K and $150-300$K [189], high-resolution neutron powder diffraction studies on $Sr_{0.6}Ba_{0.39}Nb_2O_6$ in the temperature range of $10 - 500$ K have indicated that, while there are small changes in the incommensurate modulation of the NbO_6 octahedra at low temperatures, no structural phase transition of the average structure occurs [190]. This suggests that the tetragonal symmetry is retained

even at cryogenic temperatures. Therefore, as SBN is cooled to cryogenic temperatures, it retains its tetragonal crystal symmetry, with no significant structural phase transitions observed, which may indicate that it maintains a large electro-optic response even at cryogenic temperature.

2.4.1 Dielectric Properties

Optical investigations of SBN single crystals have shown the material to be optically uniaxial and negative, with the ordinary refractive index n_o exceeding the extraordinary index n_e [191, 192]. The dielectric function and electronic band structure has been studied using Density Functional Theory (DFT) [193]. In this work, the authors measured the complex dielectric function by spectroscopic ellipsometry (although do not detail which model they used to arrive at this dielectric function result), and compare the spectroscopic data to the dielectric functions predicted by DFT, established for SBN with a projector augmented wave (PAW) method and the Perdew-Burke-Ernzerhof (PBS) pseudopotentials.

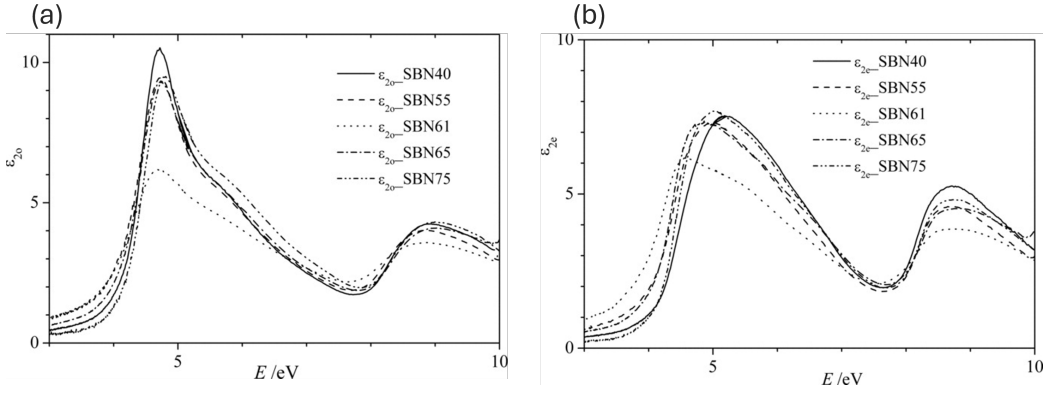

Figure 2.8: **Prediction of the ordinary (a) and extraordinary (b) dielectric functions of SBN by DFT** for a range of SBN compositions [193]. The circle markers reflect the experimental data, whilst the lines reflect the calculated data.

Figure 2.8 shows a comparison between the measured ordinary (a) and extraordinary (b) imaginary component of the dielectric function, and that predicted by

DFT. The dielectric function for both cases is shown to contain two clear absorption bands within the photon energy ranges of $4-6$ eV and $8-10$ eV. The authors attribute the existence of these two spectral bands as being the related to multiple transition mechanisms involving the octahedral NbO_6 groups. The intrinsic band gap is around $3-4$ eV is due to electronic transitions from the valence band to the conduction band, and higher order interband transitions may occur, giving rise to the absorption band at $8-10$ eV.

The UV absorption band (at ~ 4.5 eV) was experimentally studied in depth via optical measurements of thin-film SBN61 in [194]. Using a photon detector, the transmission intensity of light through SBN as a function of wavelength was acquired, and the band gap energy was determined. The authors observed a shift in the absorption edge to lower energies with increasing film thickness which should correspond to a decreasing band gap. The authors claim that calculations based on the well established Tauc formula [195, 196] do not agree with this observation; a result they speculate may be related to "*the existence of ferroelectric domains and structural defects in the films, which violate the translational periodicity the derivation of the formula is based on*".

However, this argument is confusing, since the Tauc formula does not in fact inherently depend on translational periodicity; indeed, the formula was originally proposed for amorphous semiconductors which distinctly lack translational periodicity. Even if the Tauc model did depend on translational periodicity, it isn't clear how a violation of this would result in their reported anomaly. Whilst a break of translational periodicity would result in a violation of Bloch's theorem and a relaxation of momentum conservation, optical absorption would nonetheless still occur, and since the Tauc formula is a phenomenological model relating observations of the optical absorption edge to the band gap energy, it is unclear how the model would fail to match the observed data specifically due to a violation

of translational periodicity. We speculate that the lack of correlation between the absorption shift and band gap energy observed in [197] is more likely due to the complexity of arriving at realistic results when fitting a function with a vast parameter space of dependant variables. Regardless, the authors of this study adopt a model they previously proposed in [197], which is an extension of the generic oscillator approach, which they claim better captures the optical response near the absorption edge compared to standard oscillator models.

While the model in [197] fits the absorption edge well, its accuracy diminishes in the transparent regions of the film and above the first absorption edge. Additionally, the model in [194] neglects the anisotropy of SBN, treating the material as isotropic. Consequently, this model does not fully represent the complex dielectric function, refractive index, and absorption of thin-film SBN. For a thorough assessment of the material's impact on cavity performance, a more accurate and complete fitting process is needed. These issues are addressed in this thesis in Chapter 7 by measuring the optical properties of SBN with an ellipsometer, and fitting the data to a Tauc-Lorenz model (see Section 4.3.1).

2.5 Chapter Summary

In this chapter, the building blocks of a quantum network were explored in detail, with a particular focus on the literature for solid-state quantum networks using NV centres in diamond as a spin-photon network interface. The requirements of the quantum node for achieving efficient interfaces were detailed, including good photon indistinguishability, a scalable fabrication procedure, and device integrability. The role of microcavity structures for enhancing the rate of photon emission into the ZPL was highlighted, and the candidate material for providing cavity tunability, SBN, was described in detail. Thus this chapter provides the key context

within which the present work is set.

3 | Experimental Methods

Throughout the course of this work, numerous experimental methods were employed for thin-film growth, materials characterisation, and cavity mode investigation. These methods are briefly introduced in this section. Whilst Pulsed Laser Deposition, X-Ray Diffraction, Electron Dispersive X-Ray spectroscopy, and Electron Back-Scatter Diffraction spectroscopy, were all performed using commercial hardware solutions, the cavity white light interferometer and polarimeter for electro-optic characterisation were purpose built by the author. Whilst other techniques have been used throughout this thesis, they did not merit a dedicated explanation in this chapter, and will be referred later in the thesis at the appropriate points. On the other hand, this chapter will be frequently referred back to when needed.

3.1 Thin Film Growth by Pulsed Laser Deposition

Epitaxial growth of SBN has been demonstrated by a variety of methods, including RF Sputtering [186], Pulsed Laser Deposition (PLD) [44], and Molecular Beam Epitaxy (MBE) [179]. Whilst RF sputtering is the amongst the easiest and most widely available method for thin film deposition, stoichiometric control is challenging. This presents a fundamental challenge to fabricating SBN75 for high electro-optic tuning capability, where stoichiometric control of the deposited film is crucial. On the other hand, growth by MBE provides superlative stoichiometric control, but the method is technically highly demanding and growth is very slow. PLD provides a happy medium between sputtering and MBE, provide excellent stoichiometric control without the technical demands of MBE growth. Indeed, the strongest measured Pockels coefficient for SBN was ascertained from thin-films

grown by PLD [44].

PLD uses high-energy laser pulses, focussed onto a solid target in a vacuum chamber, to vapourise target atoms to produce a plasma plume which deposits on a heated substrate [198]. When the energetic species in the plasma plume condense on the substrate, they form stable atomic clusters (a process known as nucleation). These adatoms diffuse across the surface, and when they encounter defects or each other, they may form nuclei if the cluster size exceeds a critical threshold. The nature of nucleation i.e. whether it leads to island growth, layer-by-layer growth, or a mixture of both, depends on factors such as the substrate temperature, surface energy, and lattice mismatch. A higher substrate temperature can enhance adatom mobility and promote smoother and more crystalline films. The nucleation process substantially influences the film's microstructure and quality.

Thin films of SBN were grown by Pulsed Laser Deposition onto three different substrate materials: (i) MgO; (ii) $SrTiO_3$; and (iii) $SrTiO_3$ with a 100 nm layer of $SrAl_2O_6$. The MgO and $SrTiO_3$ substrates were chosen since they possess lattice parameters which are closely matched to to c-axis of SBN (c=3.932 nm). In order to epitaxially grow a single crystal material onto a substrate, the strain at the interface between the substrate and the deposited layer caused by lattice mismatch must be minimised. The interfacial strain of SBN and MgO is approximately 6% (Table 3.1), so epitaxial growth is possible albeit with a moderately high strain. On the other hand, the interfacial strain for SBN grown onto $SrTiO_3$ is significantly smaller, at 0.6914%.

For the purposes of this work, it isn't sufficient to simply grow a thin film of SBN onto a substrate. Rather, the SBN needs to be removed from its substrate and integrated into an hybrid diamond-DBR structure. Removing the SBN layer is not trivial - simply grinding away the substrate can cause significant damage to the

Table 3.1: **Table of lattice parameters for SBN and different substrates used in this work.**

Material	a	b	c	Growth Plane	Strain
SBN75	12.482	12.482	3.932		
MgO	4.190	4.190	4.190	c_{SBN}-c_{MgO}	6.1575 %
$SrTiO_3$	3.905	3.905	3.905	c_{SBN}-a_{STO}	0.6914 %
$SrAl_2O_6$	3.7560	3.7560	12.6300	a_{SAl}-a_{STO}	3.8156 %
				c_{SBN}-a_{SAl}	4.6858 %

underlying film. Instead, we propose to release the SBN film by growing it onto a sacrificial layer of strontium aluminate ($SrAl_2O_6$), which is soluble in water. Thus, after growing $SrAl_2O_6$ onto STO, followed by SBN growth, submerging the stack into deionised water will release a freestanding membrane of SBN, which can then be bonded to any arbitrary (but sufficiently smooth) substrate.

The final target material was loaded into a vacuum chamber held at 0.028 mbar, and the chamber was enriched with 20 sccm O_2 at bottle pressure of 20 bar, in order to promote full oxygen richness of the thin-film. The substrate was fixed to a heater to raise the growth temperature, and the target was fixed to a motorised stage allowing the deposition plume to be scanned over the substrate. The target was irradiated with a KrF Excimer 248 nm laser with a voltage of 22 kV and pulse rate of 10 Hz. The laser pulse energy was fixed at 20 mJ using a variable attenuator, and had a spot size of 1×2 mm. The target was scanned over a round area with a 7 mm diameter to promote better homogeneity of the deposited film by ablating regions from the entire target. After characterising the thin-film thickness with a Dektak surface profiler, the deposition rate was found to be approximately 1.4 nm/min. A schematic diagram of the PLD process is shown in Figure 3.1, and the growth parameters are summarised in Table 3.2.

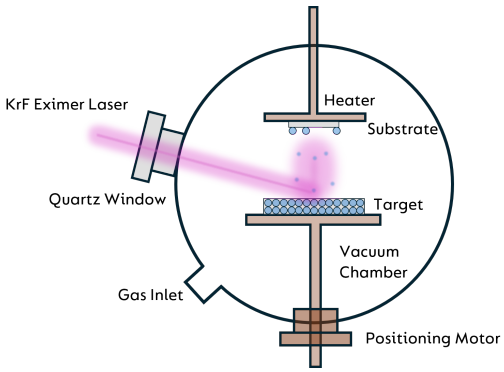

Figure 3.1: **Schematic diagram of the PLD deposition process.** A pulsed laser is focussed through the window of a vacuum chamber onto a sample. The sample can be moved by a positioning motor to ensure uniform ablation. When atoms vapourise from the target surface, they form a plume which nucleate on the sample, which is held above on a heated stage. Gas can be injected in the vacuum chamber for film property engineering.

Table 3.2: **Table of PLD growth parameters**

Chamber Pressure	0.028 mbar
O_2 Flow Rate	20 sccm
O_2 Bottle Pressure	20 bar
Laser Wavelength	248 nm
Laser Voltage	22 kV
Pulse Rate	10 Hz
Pulse Energy	20 mJ
Scan Area	1×2 mm
Beam Diameter	7 mm

3.2 X-Ray Diffraction

X-Ray Diffraction (XRD) is a non-destructive technique used to analyse material properties such as phase composition, crystal structure, and orientation. Crystalline materials consist of small crystallites, each characterised by a specific phase that produces distinct diffraction patterns. By comparing a measured pattern to a reference, these phases can be identified. An X-ray diffractometer generates X-rays using a cathode ray tube, with a detector capturing the diffracted signals

from the sample, which is positioned on a rotatable stage. When X-rays interact with the crystal lattice, they diffract in various directions, and analysing the angles and intensities of these beams provides detailed insights into the material's electron density, lattice planes, crystallinity, microstrain, and defect dislocations.

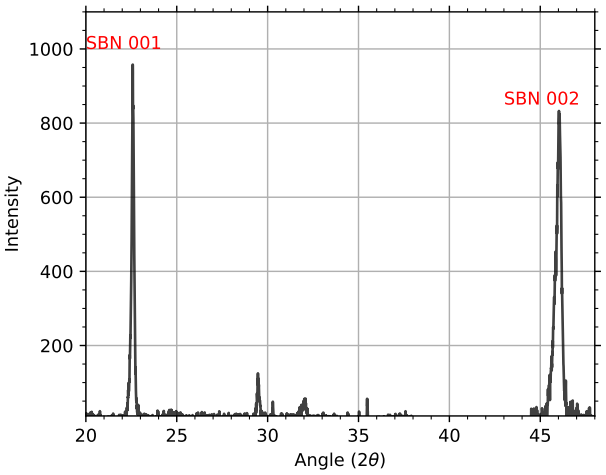

Figure 3.2: **Examplar XRD plot of SBN75** grown onto MgO substrates, shown later in this work. The XRD spectra has been removed from this figure to show only peaks associated with SBN75.

After fitting the broadened XRD peak to an appropriate function (Gaussian, Voigt, or Lorentzian), useful figures of merit can be determined. For example, the interatomic spacing d_{hkl} can be inferred from the fitted peak angle θ as $d_{hkl}{=}\frac{\lambda}{2\sin\theta}$. Here, λ is the $K\alpha$ radiation of the source target used by the XRD system. For a copper source such as used in the present work, this wavelength is $\lambda = 1.540498\mathring{A}$. Knowing the interatomic spacing makes it possible to determine the lattice parameters for a given basis set of Miller indices $\{hkl\}$. For a tetragonal crystal, the interatomic spacing is related to the lattice parameters by:

$$d_{hkl} = \frac{a}{\sqrt{h^2 + k^2}} + \frac{c}{l} \tag{3.1}$$

The crystallite size in the thin film D can be determined from XRD by applying the Scherrer Equation

$$D = \frac{K\lambda}{\beta \cos\theta} \tag{3.2}$$

....where K is the Scherrer numerical constant crystal shape factor (between 0.68 and 2.08, and 0.74 for tetrahedral crystallites with tetragonal symmetry symmetry [199]). β is the line broadening of the domains at FWHM after removing broadening due to the instrument, and is found by determining the FWHM of each XRD spectra peak after fitting. From the crystallite size, the dislocation density δ can be inferred as $\delta{=}1/D^2$.

The microstrain ϵ of a crystalline sample is defined by RMS variations in the lattice parameters across the sample. These variations can be caused by a number of factors, including non-uniform lattice distortions, faulting, dislocations, anti-phase domain boundaries, and grain-surface relaxation. The microstrain can be calculated by considering the percentage ratio of an XRD peak to its position, and is found by observing XRD data by:

$$\epsilon = \frac{\beta}{4\tan\theta} \tag{3.3}$$

The overall crystallinity of the film can be crudely inferred by finding the area under each XRD peak A_{peak} in the dataset to the overall area A_{total}. This provides the crystallinity index $CI{=}\frac{A_{\text{peak}}}{A_{\text{total}}}$.

Equations 3.2 and 3.3 both contain peak broadening terms β, and therefore these equations are only suitable if the peak broadening is dominated by either crystallite size or microstrain. However, it is quite common that the broadening is

caused by a mixture of contributions. A well-established method of addressing this problem is to instead extract these quantities by a Williamson-Hall analysis [200] where these quantities are inferred from extracting a fit to a linear equation constructed by deducing the relationship between the combined contributions to the total peak broadening, and the diffraction angle θ.

The total peak broadening is simply the sum of the broadening terms due to crystallite size and microstrain, i.e. $\beta_{\text{total}}=\beta_{\text{crystallite}}+\beta_{\mu\text{strain}}$. Since $\beta_{\text{crystallite}}=\frac{K\lambda}{D\cos\theta}$ and $\beta_{\mu\text{strain}}=4\epsilon\tan\theta$, the combined peak broadening term is $\beta_{\text{total}}=\frac{K\lambda}{D\cos\theta}+4\epsilon\frac{\sin\theta}{\cos\theta}$. By rearranging this so as to isolate the broadening contributions, a linear equation is formed (Equation 3.4), which can be applied to fit the observations. The slope of this fit gives the microstrain ϵ, whilst the intercept provides the crystallite size D:

$$\beta_{\text{total}}\cos\theta = \epsilon(4\sin\theta) + \frac{K\lambda}{D} \tag{3.4}$$

3.3 Electron Dispersive Spectroscopy

Electron Dispersive Spectroscopy (EDX) is an analytical technique used to determine the elemental composition of materials by detecting characteristic X-rays emitted when a sample is irradiated with a high-energy electron beam. The beam, focused onto the sample by magnetic or electrostatic lenses, interacts with the sample's atoms, causing inner-shell electrons to be ejected. As electrons from higher energy levels fill these vacancies, X-rays unique to each element are emitted. These X-rays are detected by a solid-state detector (Si(Li) or Silicon Drift Detector) positioned near the interaction region and analysed to produce a spectrum that identifies and quantifies the elements present in the sample. The relative concentration of elements is determined by extracting the raw intensity I_k of each element's characteristic X-ray peak using peak fitting methods, such as

Gaussian or Lorentzian functions. To obtain accurate weight percentages, ZAF corrections—accounting for atomic number (Z_k), X-ray absorption (A_k), and fluorescence (F_k)—are applied to calculate the corrected intensity $I'_k = \frac{I_k}{Z_k + A_k + F_k}$. The concentration of each element is then determined as $C_k = \frac{I'_k}{\sum_{i=1}^{n} I'_i}$, and weight percentages are calculated using the atomic mass A_k as $W_k = \frac{C_k A_k}{\sum_{i=1}^{n} (C_i A_i)} \times 100$.

3.4 Electron Backscattered Diffraction

Electron Backscatter Diffraction (EBSD) is a scanning electron microscope (SEM)-based technique used to visualise a sample's microstructure, including phase identification and distribution, grain size, grain boundaries, texture (degree of crystallographic preferred orientation), and local strain variation. A typical EBSD setup (Figure 3.3) involves an electron beam irradiating a tilted sample (typically at 70°) to maximise backscattered electron yield. These electrons interact with the crystal lattice, forming distinct diffraction cones detected by a phosphor screen coupled to a charge-coupled device (CCD), which produces Kikuchi patterns. These patterns contain information about crystal orientation, symmetry, and phase. The Kikuchi bands, corresponding to specific crystallographic planes, are analysed using a Hough transform [201], which identifies band positions and orientations.

The texture of a crystalline material describes the distribution of crystallographic orientations, with random orientations indicating no texture and preferred orientations indicating a certain degree of texture [202]. Kikuchi patterns are stereographically projected onto a two-dimensional plane known as a Wulff net [203] to interpret crystal orientations known as a Wulff net. Pole figures (PFs) are constructed from these projections, plotting the orientations of specific crystallographic directions relative to a fixed sample reference frame. PFs help analyse texture, with highly clustered regions indicating preferred grain orientations and

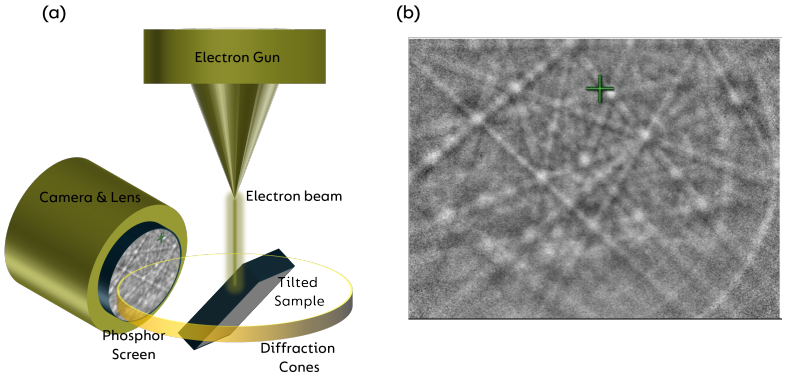

Figure 3.3: **Electron Backscatter Diffraction:** (a) Schematic Diagram of EBSD Hardware. An electrn beam is focussed onto a sample, which is tilted to maximise the interaction volume between the beam and sample. As electrons are inelastically scattered from the sample, they form a diffraction cone and are collected by a phosphor screen. (b) Example Kikuchi pattern of SBN: the backscattered electrons are collected and reconstructed by an appropriate software to unveil crystallographic information.

providing insights into the material's macroscopic properties.

3.5 Spectroscopic Ellipsometry

Ellipsometry is a technique for determining material properties such as refractive index, extinction coefficient, surface roughness, thickness, and crystallinity. It operates by analysing polarised light reflected from a sample and fitting the measured data to a model. The term "spectroscopic" refers to the fact that the technique measures how polarisation changes as a function of wavelength from incident light provided by a broadband incoherent white-light source, enabling deeper insight into the optical and physical properties of materials by subsequent modelling. When polarised light interacts with a material, its polarisation state changes due to the material's optical properties and thickness. By measuring the amplitude ratio Ψ and phase difference δ of the reflected light, optical constants and film characteristics can be inferred. Ellipsometry measures the complex re-

flectance ratio ρ, defined as:

$$\rho = \frac{r_p}{r_s} = \tan \Psi \cdot e^{i\delta} \tag{3.5}$$

Here, r_p and r_s are the reflectance coefficients for the p- and s-polarised components of light, respectively. Ψ represents the amplitude ratio, while δ denotes the phase difference. Changes in δ depend on the angle of incidence and the film's optical thickness, with 180-degree phase shifts occurring near quarter- or half-wavelength thicknesses due to constructive or destructive interference.

The real component of ρ reflects the amplitude ratio of the reflected electric field, revealing information about polarisation and light intensity. The sign of r determines whether interference between parallel and perpendicular components is constructive ($r > 0$) or destructive ($r < 0$). The imaginary component of ρ relates to the extinction coefficient (k), indicating the material's absorption and scattering properties. A positive τ signifies greater absorption or scattering of the parallel component, while a negative τ suggests amplification. Together, these parameters enable detailed characterisation of optical and structural properties, as discussed further in Chapter 7.

3.6 White Light Cavity Spectroscopy

To investigate the cavity response and mode structure, a purpose-built transmission microscope was built (Figure 3.4). A SuperK Fianium supercontinuum light source was focussed into single mode fibre and coupled into the microscope with a translation-mounted fibre coupler. The light was collimated using a 7.5 mm aspheric lens, and guided onto the sample by two steering mirrors, via a rotational variable ND filter wheel to help imaging on a CMOS camera. Prior to focussing

onto the sample, the light is sent via a 90:10 beamsplitter to a CMOS camera, which also images the sample when the white light source on the transmission side is engaged. The sample was mounted on a ThorLabs 3-axis NanoMax300 open-loop piezoactuator sample stage, and the supercontinuum light was focussed onto the sample using a 80X, 0.85 NA infinity-corrected objective lens. After passing through the sample, the laser light was collected and re-collimated with a 20X, 0.40 infinity corrected objective lens, and focussed into a fibre coupler by a 7.5 mm aspheric lens. A flip-mounted mirror in the beam path allows for white light imaging of the sample on the CMOS camera. Another flip-mounted mirror in the collection side allows the light transmitted into the cavities to be focussed into a CMOS camera to image the cavity modes directly. For spectral analysis, the light transmitted through the optical fibre was collimated and focussed onto an Acton SpectraPro 2500i spectrometer with a 1200g/mm Grating, 500mm focal length, and f/6.5 aperture ratio. The practical resolving power is given by the Rayleigh criterion, $d{=}0.61\frac{\lambda}{NA}{=}457.15$ nm. The fabricated cavity features in this work are much larger than the spatial resolution of the microscope, and therefore very visible. The linewidth of the optical cavity modes are designed to be around 1 nm, whilst the spectral resolution of the spectrometer is 0.05 nm. Therefore the spectrometer is more than capable of resolving these cavity modes.

3.7 Measurement of Pockels Coefficients by Polarisation Interferometry

Rigorously determining the Pockels tensor for any material can be a challenging task requiring purpose built optical systems. In principle, certain elements of the Pockels tensor could be deduced via spectroscopic ellipsometry, but practically this is very difficult, since typically the diameter of the incident light beam in

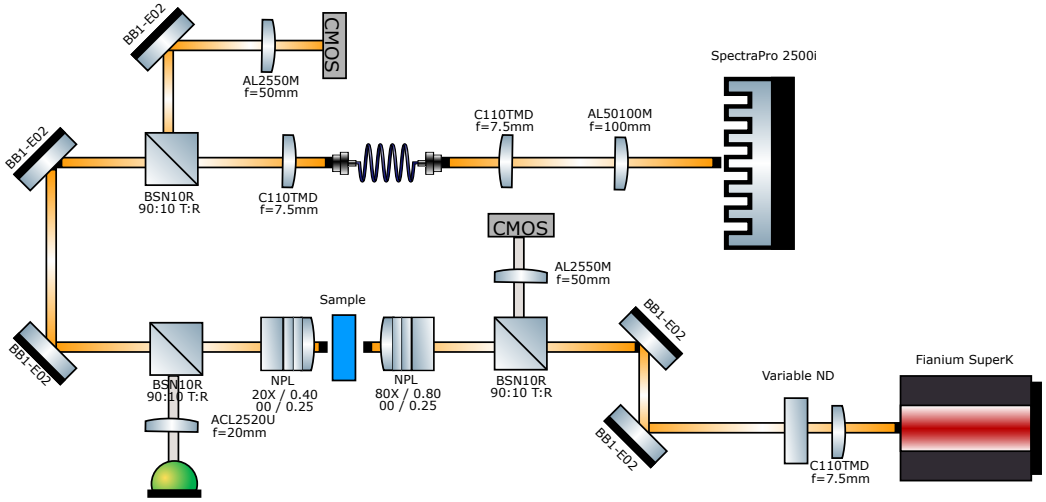

Figure 3.4: **Schematic diagram of transmission microscope for characterising optical response and mode structure of microcavities.** Supercontinuum light is focussed onto a cavity which is supported o n a piezoelectric actuator stage. The light transmitted through the cavity is collected either at a CMOS camera for directly imaging cavity modes, or at a spectrometer for recovering transmitted optical spectra.

most ellipsometers by necessity is much larger than the practical spacing between the electrodes on the material surface. Multiple other approaches have been effectively employed, such as Teng-Man reflectometry [204, 205], transmission measurements [206], prism coupling [207], and polarisation interferometry [42]. In this work we study the effective Pockels coefficient by polarisation interferometry, following the prescription for thin film $BaTiO_3$ detailed in [208].

Whilst it is possible to extract each coefficient of the Pockels tensor by this method, for the practical purpose of this work this is not required, since we are interested only in the Pockels effect experienced along the optic axis. For SBN, this is the coefficients r_{13} and r_{33}, which are inseparable and are jointly experienced along the optic axis. To investigate this, a purpose built polarisation interferometer was built (Figure 3.5). In this method, polarised light incident on a sample is analysed with an analysing polariser.

Electrodes with a spacing of 20 μm were fabricated on SBN thin-films grown on substrates of MgO, $SrTiO_3$, and $SrTiO_3$ with a sacrificial $SrAl_2O_6$ layer. The electrodes were formed lithographically via a bilayer photolithography process. First, PMGI-SF6 photoresist was spun-coat onto each sample at a speed of 4000rpm and acceleration of $10,000$ rpm. After baking at 150° C for 90 seconds, S1813 positive photoresist was spun-coat on top at a speed of 3000 rpm and acceleration of $10,000$ rpm, and baked at 115°for 60 seconds. The electrode pattern was then exposed into the samples with UV radiation (405 nm) using a Polos NanoWriter Advanced direct laser writer, and the photoresist was developed using the base solution MF319 for 60 seconds. Each sample was then coated with 100nm of gold with a 10nm interfacial chrome layer by thermal evaporation in an Edwards Thermal Evaporation bell jar system. The electrodes were finally formed by lifting off the deposited metal in the exposed photoresist region by submersing the sample in Microposit Remover 1165.

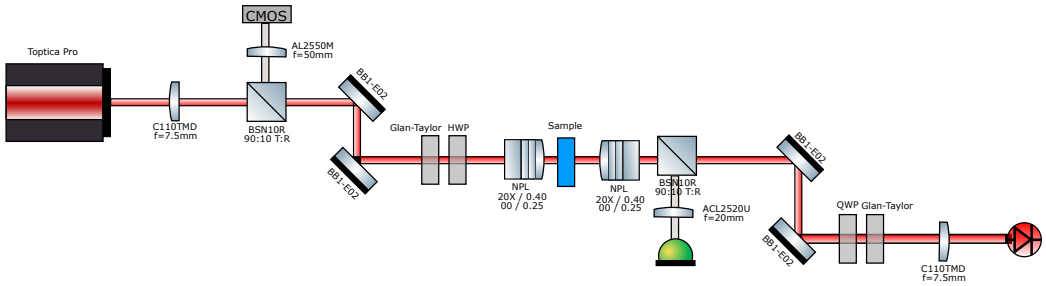

Figure 3.5: **Schematic diagram of polarisation interferometer custom built for measuring the effective Pockels coefficient.** Light from a 637 nm laser is polarised and the incident polarisation angle is set by a half-wave plate. After passing through the sample, the light passes through a quarter wave plate and rotating polarisation analyser, and the effective Pockels coefficient is numerically determined from the transmitted light information.

A Toptica DLC Pro 637 nm tuneable diode laser provides the incident laser light for the sample. A dichroic beamsplitter allows the sample (which is illuminated with a white light LED via a 90:10 beamsplitter) to be imaged on a CMOS

camera whilst blocking the laser light. The incident light is initially polarised with a Glan-Taylor prism, and a half-wave plate on a motorised rotation mount (ThorLabs K10CR2) sets the incident polarisation to the sample. The sample is mounted on an XY translation stage. The incident light is focussed onto the sample, between the electrodes, with a 20X / 0.40 NA objective lens, forming a spot of $FWHM$=$1.22\frac{\lambda}{NA}$=$1.95\ \mu m$. The light transmitted through the sample is then re-collimated with a 10X 0.25 NA objective lens mounted on a z-translation stage. The white light source used for imaging the sample is focussed down the same optics. Since the light transmitted through the SBN film will be slightly elliptically polarised owing to the birefringence of the material, a quarter wave plate and second Glan-Taylor prism, both mounted on motorised stages (ThorLabs ELL14), are iteratively rotated to minimise the transmitted power onto an Si amplified photodetector (ThorLabs FPD510). From the piezoresponse force microscopy measurements in Section 6.5, we know that the saturation voltage for each film is below 10V. Therefore, to align the ferroelectric domains in the thin-films, a DC offset voltage of 10V was applied for 1 minute. Then an alternating voltage V_{ac}=10.0 V_{pp} with a 10V DC offset was applied at a frequency of 20 kHz with a function generator.

3.7.1 Analysis Procedure

The optical components of the electro-optic polarimeter and their impact on the polarisation state of the light is shown in Figure 3.6. The beam passes through a Glan-Taylor prism, polarising it normal to the optical table. A half-wave plate then adjusts the beam's linear polarisation to any desired angle relative to the sample. Upon passing through the sample, where refractive indices are modulated by an electric field, the beam acquires a small ellipticity. This is corrected using a quarter-wave plate aligned 90° to the input polarisation, effectively linearising the

beam and rotating its polarisation by an angle δ. Finally, the beam passes through a rotating analyser (Glan-Taylor prism) at angle θ_a, enabling angle-dependent power measurements. The transmitted power is primarily related to the angle between the two polarisers in the optical path as $P{=}P_{max}\cos^2(\theta_a - \delta)$ [184]. Lenses are used to focus and collimate the beam before the sample and refocus it onto the detector.

Before measurement, the setup is aligned by minimising the detected power using cross-polarised components to ensure linear polarisation through the quarter-wave plate. During the measurement, the quarter-wave plate compensates the modulated ellipticity caused by combined DC and AC electric fields. This results in small polarisation shifts, described by an effective modulation angle δ^*. If δ^* is small, the transmitted power variations ΔP should be proportional to the derivative $dP/d\theta_a$. Therefore, the analyser is rotated combined with lock-in detection and the iterative difference in both transmitted power ΔP and angle $\Delta\theta_a$ are recorded. The lock-in detection is provided by a RedPitaya microcontroller, programmed to function as a lock-in amplifier following [209].

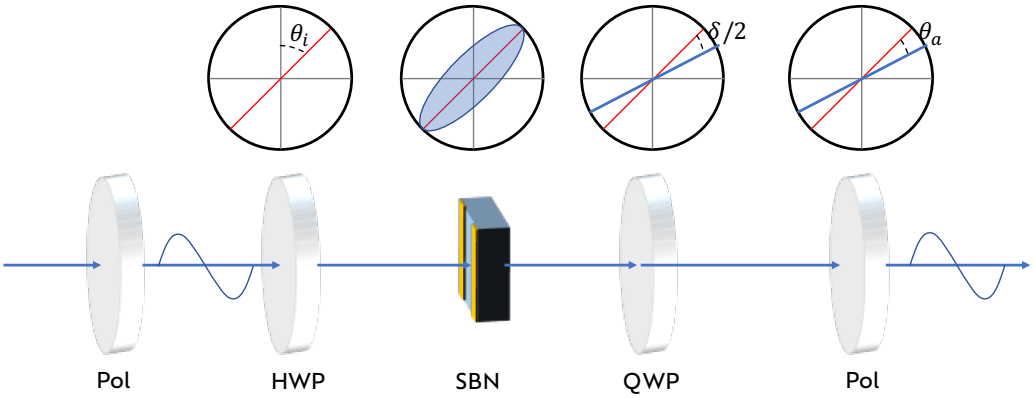

Figure 3.6: **Schematic of electro-optic characterisation of SBN**. As light transits through each component, its polarisation state is modified. This is reflected in the inset figure, and explained further in the main text.

The transmitted power through the sample is fitted to equation 3.6 with the extra fitting coefficients $\theta_{a,off}$ accounting for any misalignment in the analyser angle, and P_{bg} accounting for the finite extinction ratio of the polarising elements.

$$\tilde{P}(\theta_a) \approx P_{max} \cos^2(\theta_a - \theta_{a,off}) + P_{bg} \tag{3.6}$$

The rotation of the polarisation δ in response to an applied field is found by first determining the derivative $dP(\theta_a)/d\theta_a$ of the fitted power, and then fitting this with $\Delta P/P(\theta_a)$ with equation 3.7, whilst accounting for background light contributions with the fitting term A.

$$\frac{\Delta P(\theta_a)}{P(\theta_a)} = \frac{1}{\tilde{P}(\theta_a)} \left(\delta \frac{d\tilde{P}(\theta_a)}{d(\theta_a)} + A \right) \tag{3.7}$$

For practical cavity tuning purposes, an effective Pockels coefficient r_{eff} which accounts for the effective Pockels shift experienced for light transmitted through the film is of interest. For the electric field applied parallel to the $\langle 001 \rangle$ SBN axis, the electro-optic properties depend on the Pockels coefficients r_{13} and r_{33} which define the c-axis Pockels coefficient r_c as:

$$r_{eff} = r_{33} - \left(\frac{n_o}{n_e} \right)^3 r_{13} \tag{3.8}$$

The combined r_{eff} Pockels coefficient is more practically meaningful than its constituent coefficients, since r_{13} and r_{33} are correlated. The effective Pockels coefficient can be determined by equation 3.9 [184, 210].

$$r_{eff} = \frac{2\delta^* \lambda}{\pi n^3 d \nu E_{ac}} \tag{3.9}$$

Here, λ is the wavelength of the incident light (637 nm in this case), n is the extraordinary refractive index value for SBN at wavelength λ determined by ellipsometry; d is the thickness of the SBN layer determined by ellipsometry; $0 \leq \nu \leq 1$ is a coefficient describing the proportion of ferroelectric domains aligned with the optic axis (here ν=0.7 as determined by the EBSD analysis in Section 6.4); and E_{ac} is the applied electric field.

3.8 Chapter Summary

This chapter introduced a variety of experimental methods used in the present work, for material synthesis and characterisation.The thin-film SBN in this work is grown by PLD, and the microstructure is characterised using XRD, EDX, and EBSD. The dielectric properties of the thin-films were characterised using ellipsometry and subsequent modelling, and the electro-optic properties of SBN were measured using a purpose built polarimeter. The cavity optical response was measured using a purpose built white light interferometer. This chapter will be frequently referred back to in later chapters in this thesis.

4 | Background Theory

In this section, the theoretical background of the challenges of producing efficient spin-photon quantum network interfaces is detailed, starting with an exploration of the multiple factors which impede both the quantum coherence and photon indistinguishability. The primary focus of the present work is to enhance the photon emission efficiency of a network node, by placing the emitter within a resonant optical microcavity. Therefore, a brief overview of cavity quantum electrodynamics follows, with a description of how Purcell enhancement can induce substantially more emitted photons suitable for entanglement sharing in a network. Following this background information, the analytic and numerical methods used throughout this thesis for studying the performance of the designed optical microcavities is detailed, covering transfer matrix analysis, Hermite-Gaussian modes. The optical and electro-optic properties of SBN are imperative properties to study analytically since they determine a number of key device design parameters. Therefore, the electro-optic tensor of SBN is derived, and methods for determining the dielectric properties are detailed. Finally, the finite-difference time domain (FDTD) method is briefly introduced. This numerical technique will be used throughout this thesis to make inferences on the impact of the cavity design on intended figures of merit, and also to understand the impact of real-world materials on the performance of the designed cavities.

4.1 Enhancing the Spin-Photon Interface with Optical Microcavities

Entangled states are highly sensitive to noise channels such as amplitude damping, depolarisation, and dephasing, which degrade quantum coherence and entangle-

ment [211]. In NV centres, decoherence arises from mechanisms like two-photon Raman scattering, Orbach processes (T_1 relaxation), spin-spin relaxation (T_2), and spectral inhomogeneity (T_2^*), partially mitigated by Hahn echo sequences [212]. The relaxation rate $1/T_1$ is governed by radiative (τ_{rad}) and non-radiative (τ_{nonrad}) processes, as expressed by $1/T_1 = 1/\tau_{rad} + 1/\tau_{nonrad}$. Efficient entanglement generation relies on device efficiency η, with success probability $P_{success} = \eta^2/2$ [20], where η depends on excitation (η_{exc}), emission (η_{em}), collection (η_{co}), transmission (η_{tr}), and detection (η_{det}) efficiencies [32]. Decoherence from phonons, electronic spins, and nuclear spins limits η_{em}, as vibrational recoil from phonons introduces which-path information, mitigated by operating in the recoil-free Mössbauer-Lamb-Dicke regime. In solid-state systems, η_{em} is tied to the zero-phonon line (ZPL) emissions, $\eta_{em} = \gamma_{ZPL}/\gamma$, determined by the Debye-Waller Factor (DWF). For NV centres, the DWF is low (2-3%), yielding a ZPL branching ratio of 2-4%. This ratio can be significantly enhanced by embedding the emitter in a resonant cavity to exploit the Purcell effect [156], where the cavity Purcell factor F_{cav} boosts the ZPL emission rate γ'_{em} by suppressing phonon sidebands and non-radiative channels.

4.1.1 Free-Space Spontaneous Emission

If an atom is in its excited state with energy E_2, it may spontaneously decay to a lower energy state with energy E_1, and in doing so, release the energy difference between the two states as a photon. The photon has angular frequency ω and energy $\hbar\omega$, such that $E_2 - E_1 = \hbar\omega$, where $\hbar$ is Planck's reduced constant. If the number of atoms in an excited state at a time t is given by $N(t)$, the rate at which N decays is related to the rate of spontaneous emission to a final state f from an initial state i, by:

$$\frac{\partial N(t)}{\partial t} = -A_{if}N(t) \tag{4.1}$$

A_{if} is referred to as the Einstein A coefficient, and is a constant of proportionality. The rate equation can be solved for $N(t)$ to yield $N(t) = N(0)e^{-A_{if}t}{=}N(0)e^{-\gamma_{rad}t}$, where $N(0)$ is the initial number of atoms in the excited state, t is the system time, and γ_{rad} is the radiative decay rate of the transition from one energy eigenstate of a quantum system to a continuum of eigenstates. Consequently, the number of excited states N decays exponentially with time, and after one lifetime, this decreases to 36.8% the original value. The radiative decay rate γ_{rad} is inversely proportional to the lifetime τ_{if}:

$$A_{if} = \gamma_{if} = \frac{1}{\tau_{if}} \tag{4.2}$$

The transition rate in response to a weakly perturbing Hamiltonian H' can be determined by perturbation theory from fermi's Golden Rule. The resulting equality is proportional to the coupling strength between the initial ($|i\rangle$) and final ($|f\rangle$) states of the system (determined by the square of the matrix element of the perturbation $|\langle f|\, H'\, |i\rangle|^2$), and the density of states (DOS) ($\rho(\omega)$). In free space, the transition rate γ^0 is given by:

$$\begin{aligned}\gamma^0 &= \frac{2\pi}{\hbar^2}\left|\langle f|\, H'\, |i\rangle\right|^2 \rho(\omega_0) \\ &= \frac{2\pi}{\hbar^2}\left|M_{if}\right|^2 \rho(\omega_0)\end{aligned}$$

In free space, to determine the photonic DOS, usually a volume V_0 is applied to allow for field quantisation. Consequently, in free space, the photonic DOS is

given by:

$$\rho^0(\omega) = \frac{\omega^2 V_0}{\pi^2 c^3} \tag{4.3}$$

The transition matrix element $M_{if} = \left\langle -\vec{\mu}_{if} \cdot \vec{E}_{\text{vac}} \right\rangle$ is the expectation value of the dipole moment of the transition $\vec{\mu_{if}}$ and the vacuum electric field $\vec{E}_{\text{vac}}$. The amplitude of the transition dipole moment is proportional to the expectation value of the emitter dipole moment $\mu_{if} = \langle \Psi_i | \, \vec{\mu} \, | \Psi_f \rangle$ with respect to the initial Ψ_i and final Ψ_f states.

The vacuum electric field amplitude is:

$$E_{vac} = \sqrt{\frac{\hbar\omega}{2\epsilon_0 V_0}} \hat{e}(\vec{r}_{em}) \tag{4.4}$$

....where $\hat{e}$ denotes a unit vector accounting for polarisation, and $\vec{r}_{em}$ is the specific position of the emitter. Free space vacuum fields have no particular polarisation preference, and therefore to account for the random orientation of the field with respect to the transition dipole, a pre-factor of $1/3$ is introduced to the matrix element, giving:

$$|M_{if}|^2 = \frac{1}{3}\mu_{if}^2 E_{\text{vac}}^2 = \frac{\mu_{if}^2 \hbar\omega}{6\epsilon_0 V_0} \tag{4.5}$$

Consequently, the rate of spontaneous emission in free space is:

$$\gamma^0 = \frac{\mu_{if}^2 \omega_0^3}{3\pi\epsilon_0 \hbar c^3} \tag{4.6}$$

4.1.2 Cavity Enhanced Spontaneous Emission

Placing an emitter within a resonant cavity can significantly enhance the rate of spontaneous emission by increasing the density of photonic states through Purcell enhancement. For NV centres, this improves photon emission into the zero-phonon line, facilitating the generation of indistinguishable photons for entanglement swapping. The confinement of light fields to a smaller mode volume V and enhances coherent coupling $g{=}\left(\frac{\mu_{12}^2\omega}{2\epsilon_0\hbar V}\right)^{1/2}$, which drives deterministic, unitary evolution of the quantum system while preserving coherence. However, practical systems experience non-coherent dynamics, such as cavity-photon decay ($\kappa{=}\omega/Q = \delta\omega$) due to finite mirror reflectivity, and spontaneous photon emission into free space ($\gamma{=}1/(2T_1)$). Strong coupling, characterised by a cooperativity $C{=}\frac{g^2}{\kappa\gamma} > 1$, ensures $g \gg \kappa, \gamma$. For enhancing the photonic density of states in the ZPL for NV centres, strong coupling is not required, and the present work operates in the weak-coupling regime.

The finite lifetime of photonic emission gives rise to an exponentially decaying light field intensity. When a photonic emitter is enclosed within an optical microcavity, the photons bounce back and forth in the cavity, losing some energy via leakage through the mirrors, and decaying exponentially over time (Figure 4.2(a)). Taking the Fourier transform of a decaying exponential envelope gives a Lorentzian function in the frequency domain, and hence in the frequency domain, the cavity fields are described by distinct Lorentzian peaks (Figure 4.2(b)), with with a centre frequency ω_c and a full width half maximum (FWHM) given by the strength of the cavity-photon decay rate κ [213, 214]. Note, in Figure 4.2(b) the mode amplitudes for each peak differ due to a finite discretisation in the finite difference time domain solver used to generate this data. The time-domain electric field resolution is set by the solvers time step, which here is $d_t{=}0.0321$

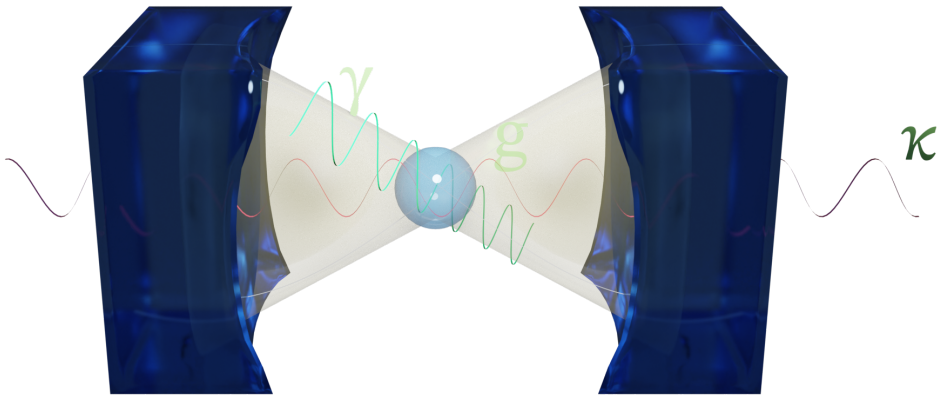

Figure 4.1: **Cavity quantum electrodynamics:** Schematic representation of an emitting atom within a cavity formed by two opposing mirrors. Atomic transitions result in photon emission that couples to cavity modes at a rate γ, while cavity-photon decay occurs at a rate κ.

fs, which sets a lower bound on the precision which can be acquired following a Fourier transform. Therefore, following the Fourier transform, not all of the spectral information for every peak may be perfectly visible.

$$\rho'(\omega_0) = \frac{\kappa/(2\pi)}{(\omega_0 - \omega_c)^2 + (\kappa/2)^2} \tag{4.7}$$

The above Lorentzian transfer function accounts for detuning between the atomic frequency ω_0 and the resonant cavity frequency ω_c. As the cavity photons bounce back and forth, at specific frequencies a pole is found in the transfer function, describing a resonance of the cavity field. This occurs at specific intervals corresponding to the cavity length L: the resonant frequencies ω_m occur at intervals $\omega_m{=}m\pi c/L$. This inter-peak spacing is known as the *free-spectral range* (FSR). The linewidth of the cavity mode is related to the cavity loss rate κ, which broad-

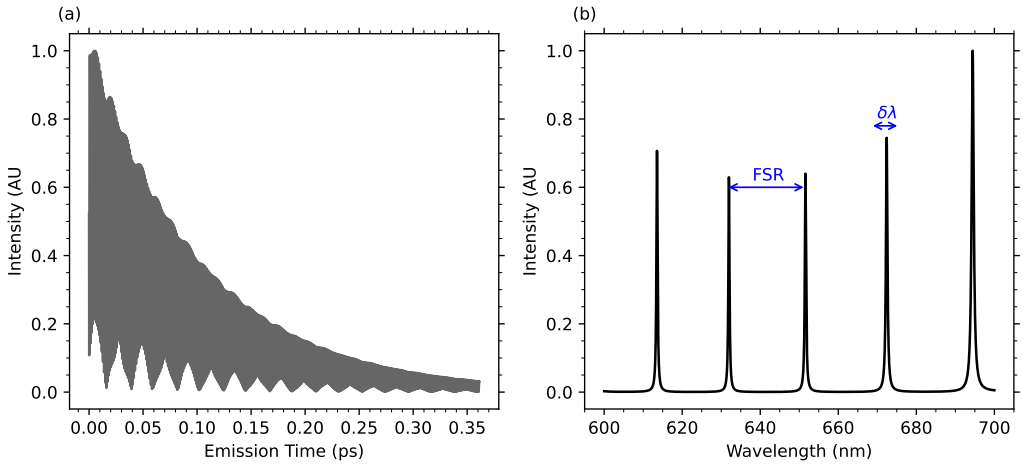

Figure 4.2: **Energy in a cavity:** When a photonic emitter is contained in a cavity, light bounces back and forth between the mirrors over time (a). Due to the finite leakage through the mirrors, the intensity of light decays exponentially. In the frequency domain, this gives rise to distinct modal peaks with a Lorentzian lineshape (b).

ens the Lorentzian peak.

Describing the vacuum electric field inside a cavity may require a slight modification of equation 4.4 to account for the permittivity of the surrounding media of the emitter, ϵ_r^{em}, such that $E_{vac}^{cav} = \frac{\hbar\omega}{2\epsilon_0\epsilon_r V} E(\vec{r}_{em})$. For generality, since the emitter is now placed in a cavity medium, it may have a polarisation $\vec{p}$ preference, and hence the non-dimensional mode function $E(\vec{r})$ must be scaled accordingly. This quantity is normalised such that $|E(\vec{r})|_{\text{max}} = 1$, and is scaled by a factor ζ:

$$\zeta = \frac{\left|\vec{p} \cdot \vec{E}\right|}{|\vec{p}| \cdot \left|\vec{E}\right|} \tag{4.8}$$

For an optimally positioned emitter, the transition matrix element becomes $|\langle f| H' |i\rangle| = \sqrt{\left(\frac{\hbar\omega}{2\epsilon_0\epsilon_r V}\right)}\zeta$, and the rate of spontaneous emission into the cavity γ_{cav} is:

$$\gamma_{cav} = \frac{2\mu_{if}^2 Q}{\hbar\epsilon_0 V} \cdot \frac{(\kappa/2)^2}{(\omega_0 - \omega_c)^2 + (\kappa/2)^2}\zeta \tag{4.9}$$

....where the quality factor Q is the temporal confinement of the cavity mode given by $Q{=}\omega/\kappa$, and the mode volume V is the spatial confinement of the mode. By construction, the mode volume is defined by the energy normalisation condition of the field per photon, E_0. This corresponds to the ratio between the total energy in the mode $U_m{=}1$ and the maximum value of the density of the electronic energy maxima ($\epsilon \left|\boldsymbol{E}_m\right|^2/2$):

$$V = \frac{\int_V \epsilon_r(\boldsymbol{r}) \left|\boldsymbol{E}_m(\boldsymbol{r})\right|^2 + \mu_r(\boldsymbol{r}) \left|\boldsymbol{H}_m(\boldsymbol{r})\right|^2}{\max\left(\epsilon_r(\boldsymbol{r}) \left|\boldsymbol{E}_m(\boldsymbol{r})\right|^2\right)} = \frac{2U_m}{\max\left(\epsilon_r(\boldsymbol{r}) \left|\boldsymbol{E}_m(\boldsymbol{r})\right|^2\right)} \tag{4.10}$$

In practical systems, the construction of the mode volume in Equation 4.10 is an approximation, since it makes assumptions such as Hermiticity, orthonormality, and unphysical boundary conditions. For lossy systems, the mode volume is better described using *quasi-normal modes* [215], but the cavities used in this work are sufficiently low loss that the regular approximation above is appropriate.

The cavity only affects the DOS within a finite solid angle, and so the free-space emission rate is unmodified. The total emission rate in a cavity then can be expressed as $\gamma' = \gamma^0 + \gamma_{cav}$, and the ratio between the cavity modified spontaneous emission to free space is:

$$\frac{\gamma_{cav}}{\gamma^0} = \frac{3\lambda^3}{4\pi^2} \cdot \frac{Q}{V} \cdot \frac{(\kappa/2)^2}{(\omega_0 - \omega_c)^2 + (\kappa/2)^2} \tag{4.11}$$

When the emitter is tuned on resonance with the cavity, the detuning term in eq 4.11 disappears, and the Purcell enhancement is:

$$F_P = \frac{\gamma_{cav}}{\gamma^0} = \frac{3\lambda^3}{4\pi^2} \cdot \frac{Q}{V} \tag{4.12}$$

This is expressed as though the emitter was in vacuum. In reality, the emitter will be within a dielectric medium, and so the Purcell factor must be modified accordingly by the effective optical path length λ/n_{em}:

$$F_P = \zeta^2 \frac{3}{4\pi^2} \left(\frac{\lambda}{n_{\text{em}}}\right)^3 \cdot \frac{Q}{V} \tag{4.13}$$

4.1.2.1 Dipole Placement

This equation for the Purcell factor assumes perfect spatial overlap between the emitter and cavity mode. When this is not perfect, a scaling factor needs to be applied to capture any modal mismatch. For a hybrid-material Fabry-Perot cavity, this can be captured by scaling the electric field at the dipole position E_{em} with the refractive index of the dipole medium n_{em}, and comparing this to the the maximum scaled electric field in the cavity. Therefore, the Purcell enhancement is scaled by a factor $\frac{n_{\text{em}}^2|E_{\text{em}}|^2}{\max(n^2|E|^2)}$. Therefore, the scaled Purcell enhancement is:

$$F_P = \zeta^2 \frac{3}{4\pi^2} \left(\frac{\lambda}{n_{\text{em}}}\right)^3 \cdot \frac{Q}{V} \cdot \frac{n_{\text{em}}^2|E_{\text{em}}|^2}{\max\left(n^2|E|^2\right)} \tag{4.14}$$

This additional scaling factor relates how well the dipole couples with the cavity field in both the longitudinal and transverse directions. For maximum longitudinal mode overlap, the emitter must be placed at a position in the cavity where the electric field is at a maximum. This can be determined analytically by considering the nodes and antinodes of the cavity.

The standing wave profile long the $z-$axis is approximated by $E(z) \propto \sin\left(\frac{q\pi z}{L}\right)$,

where q is the longitudinal mode index and L is the cavity length. The nodes of a cavity are where the electric field component $E(z)$=0. The antinodes are where the cavity field is maximal, and are found where $\frac{q\pi z}{L}=\left(m+\frac{1}{2}\right)\pi$ for $m \in \{0,1,2,....\}$. Therefore, the longitudinal cavity field overlap is maximal so long as the emitter is placed at any one of the cavity antinode locations.

For transverse displacement of the emitter from the cavity field, the cavity mode field decays exponentially from the centre of the cavity beam waist w_o. Therefore, an emitter displaced transversally by $r=\sqrt{x^2+y^2}$ decays proportional to $|E(r)|^2 \propto \exp\left(\frac{-2r^2}{w_o^2}\right)$. So, the cavity scaling factor can be analytically decomposed into:

$$\frac{n_{\text{em}}^2|E_{\text{em}}|^2}{\max\left(n^2|E|^2\right)}=\frac{n_{\text{em}}}{n_{\text{max}}^2}\cdot\sin\left(\frac{q\pi z}{L}\right)\cdot\exp\left(\frac{-2r^2}{w_o^2}\right) \tag{4.15}$$

The impact of even small displacements can be substantial for Purcell enhancement. For example, if the emitter is displaced from the cavity mode at a position r=w_o, the mopde overlap will decay by a factor e^{-2}, corresponding to an 87% drop in Purcell enhancement. It is therefore crucial to have fine positioning accuracy of the emitter position during device fabrication.

4.1.2.2 Cavity Enhanced Branching Ratio

The Purcell enhancement affects both ZPL and PSB emissions, but has no impact on non-radiative decay rates. The free-space ZPL branching ratio ζ_{ZPL}^0 is the Debye-Waller factor (β_0) of the emitter is given by:

$$\gamma_{ZPL}^0=\beta_0=\frac{\gamma_{ZPL}}{\gamma_{rad}}=\frac{\gamma_{ZPL}}{\gamma_{ZPL}+\gamma_{PSB}} \tag{4.16}$$

The presence of the cavity enhances the branching ratio of the emitter by modify-

ing the cavity decay rate. Substituting $\gamma_{ZPL}{=}(1+F_p)$ and $\gamma_{\text{total}}{=}(1+F_p)\gamma_{ZPL}+\gamma_{PSB}$ gives a a cavity enhanced branching ratio β_{cav} of

$$\begin{aligned}\beta_{cav} &= \frac{(1+F_p)\gamma_{ZPL}}{(1+F_p)\gamma_{ZPL}+\gamma_{PSB}} \\ &= \frac{(1+F_p)\gamma_0}{(1+F_p)\gamma_0+(1-\gamma_0)}\end{aligned} \tag{4.17}$$

Thus, embedding an NV centre within an optimised resonant cavity can offer a means to dramatically enhance the efficiency of photon emission in the ZPL, a crucial requirement for developing scalable quantum network nodes.

4.1.3 Hermite-Gaussian Modes

The Fabry-Pérot structures in this work are *plano-convex* structures, formed by enclosing diamond with one flat side and another convex with DBR mirrors, since this structure offers greater lateral field confinement, giving rise to a lower cavity mode volume and a higher cavity-emitter interaction [216]. The field distribution within planar-planar cavities can be simply described by Fresnel coefficients and transfer matrices [217]. However, the field distribution in a plano-convex structure is more complicated due to the Gaussian beam profile induced by the convex mirror. To first order, eigenenergy of the electric field is:

$$\mathcal{E}(r,z) = E_0\frac{w_0}{w(z)}\cdot e^{-ikz}\cdot e^{-\frac{r^2}{w(z)^2}}\cdot e^{-\frac{ikr^2}{2\mathcal{R}(z)}}\cdot e^{i\zeta z} \tag{4.18}$$

.... where $|E_0|$ is the peak amplitude of the Gaussian beam, w_0 is the beam radius at the beam waist, $w(z){=}w_0\sqrt{1+\frac{z^2}{z_R}}$ is the beam radius at position z, where $z_R{=}\frac{\pi w_0^2}{\lambda}$ is the Rayleigh range. $\mathcal{R}(z){=}z+\frac{z_R^2}{z}$ is the wavefront radius of curvature,

$k{=}2\pi/\lambda$ is the wavenumber, and $\zeta(z){=}\tan^{-1}\left(\frac{z}{z_R}\right)$ is the Gouy phase,which is an additional phase occurring in the propagation of Gaussian beams which must be accounted for in the cavity resonance condition design. In equation 4.18, the term $E_0\frac{w_0}{w(z)}$ describes the amplitude reduction along the propagation direction z; e^{-ikz} is a plane wave beam propagation along z; $e^{-\frac{r^2}{w(z)^2}}$ describes the Gaussian profile of the beam, with a spot size $w(z)$; $e^{-\frac{ikr^2}{2\mathcal{R}(z)}}$ is the wavefront radius of curvature at position z; and $e^{i\zeta z}$ is the Gouy phase shift.

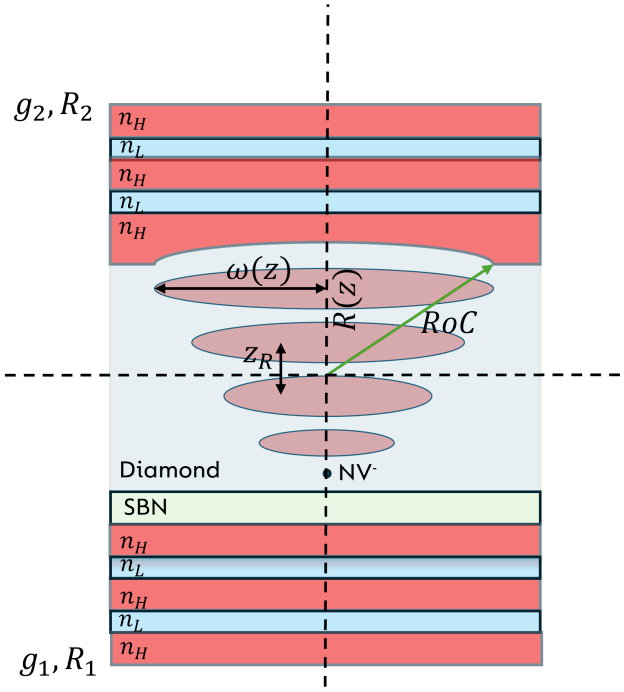

Figure 4.3: **Gaussian beam in a microcavity.** The Fabry-Perot cavity is formed by a plano-convex DBR mirror combination, filled with a diamond:EO material hybrid cavity medium. The convex shape of the diamond top establishes Hermite-Gaussian mode propagation.

Figure 4.3 shows a schematic diagram of a plano-convex optical cavity, and following the approach in [216], a mirror geometric factor $g_i{=}1-L/\mathcal{R}_i$, where L is the length of the cavity. The beam waist w at each mirror is given by:

$$w_1^2 = \frac{\lambda L}{\pi}\sqrt{\frac{g_2}{g_1(1-g_1g_2)}} = \frac{\lambda L}{\pi}\sqrt{\frac{\mathcal{R}-L}{L}}$$
$$w_2^2 = \frac{\lambda L}{\pi}\sqrt{\frac{g_1}{g_2(1-g_1g_2)}} = \frac{\lambda L}{\pi}\sqrt{\frac{\mathcal{R}^2}{L(\mathcal{R}-L)}} \tag{4.19}$$

The cavity is said to be stable if the line segments between the mirrors and their centre of curvature overlap, but with one not lying entirely within the other. Therefore, for a plano-convex cavity to satify the stability criterion, $\mathcal{R} - L > 0$

The Gaussian beam profile detailed above assumes are applicable only to first order. For higher order modes, the paraxial approximation to Helmholtz's equation can be decomposed using the orthogonal set of Hermite-Gaussian modes. Given a mode of order (m, n) in reference to the x and y directions, the electric field amplitude at positions x, y, z may be given by:

$$\mathcal{E}(r,z) = E_0\frac{w_0}{w(z)}\cdot e^{-ikz}\cdot e^{-\frac{x^2+y^2}{w(z)^2}}\cdot e^{-\frac{ik(x^2+y^2)}{2\mathcal{R}(z)}}\cdot e^{i\zeta z(m+n+1)}\cdot H_m\left(\frac{\sqrt{2}x}{w_0}\right)\cdot H_n\left(\frac{\sqrt{2}y}{w_0}\right) \tag{4.20}$$

....where the $H_{m,n}$ terms are the Hermite polynomials. In this instance, the resonance condition of the cavity mode is given by:

$$L = \frac{\lambda}{2n}\left(q + \frac{1}{\pi}(m+n+1)\cos^{-1}\left[\sqrt{\frac{\mathcal{R}-L_0}{\mathcal{R}}}\right]\right) \tag{4.21}$$

....where q is the longitudinal mode index. Higher order Hermite-gaussian modes are typically undesirable, as they induce transverse mode coupling and diffraction loss in the cavity spectrum, deteriorating performance.

Where a cavity exhibits Hermite-Gaussian longitudinal and transverse modes, an effective radius of curvature can be inferred. This describes the curvature of the wavefronts of light oscillating within the cavity, and is related to the distance between the longitudinal and first transverse modes. R_{eff} is found by taking the ratio between the physical length L of the cavity and the beam curvature term containing the difference in resonant wavelengths between the longitudinal and transverse mode δ_{LT} and the wavelength of the cavity modes λ:

$$R_{eff} = \frac{L}{sin^2\left(\frac{2\pi\delta_{LT}}{\lambda}\right)} \tag{4.22}$$

4.1.4 Analytic Theory of Plano-Convex Cavities

Plano-convex cavities can be explored by analytic equations which, whilst not accounting for real-world material peculiarities, do provide a good basis upon which to build initial cavity designs and compare against for cavity analysis. The sharpness of the mode resonance in an FP cavity is described by the finesse

$$F = \frac{\pi}{1 - \sqrt{R_1 R_2}} \tag{4.23}$$

....which depends on the reflectivities R_1 and R_2 of the cavity mirrors. A higher finesse indicates a narrower linewidth of the cavity modes, corresponding to better energy storage and more pronounced resonance effects. The quality factor

$$Q = F(q + q_m) \tag{4.24}$$

....is related to the finesse, and quantifies the energy storage capability of the cavity relative to the energy loss per cycle. It combines the finesse with contributions

from the longitudinal mode index $q{=}\frac{2nL}{\lambda}$ (a measure of the optical path length) and q_m, which accounts for mirror-related losses or other factors. The free-spectral range is related to the cavity length and mode linewidth by

$$\text{FSR} = \frac{\lambda^2}{2nL} \tag{4.25}$$

The normalised mode volume

$$V{=}\frac{\pi\omega_0^2(L+L_m)}{4}\left(\frac{n}{\lambda}\right)^3 \tag{4.26}$$

....is a measure of the spatial confinement of the electromagnetic field in the cavity. It depends on the beam waist ω_0, the cavity length L, the mode-matching length L_m, the refractive index n, and the wavelength λ. A smaller mode volume enhances the interaction between light and matter. Meanwhile, the numerical aperture

$$NA{=}\frac{w_0}{Z_R} \tag{4.27}$$

....describes the focusing or divergence angle of the beam within the cavity. It is the ratio of the beam waist w_0 to the Rayleigh range Z_R, which is a measure of the beam's focus depth. A higher NA implies stronger focusing of light.

A summary table of each cavity parameter for the proposed device of this work is given in Table 4.1. A Purcell enhancement F_P of 50 is ideal since it would allow around two-thirds of photons to be emitted into the ZPL at cryogenic temperatures. The enhanced branching ratio BR with $FP{=}50$ increases an initial Debye-Waller factor DW$=0.04$ by:

$$\begin{aligned} \text{BR} &= \frac{F_P \cdot \text{DW}}{F_P \cdot \text{DW} + (1 - \text{DW})} \\ &= \frac{50 \times 0.04}{50 \times 0.04 + (1 - 0.04)} \\ &= 0.676 \end{aligned} \tag{4.28}$$

So, for a reasonable Purcell factor, 68% of emitted photons can be emitted from the ZPL. The Purcell enhancement is a function of the mode volume and quality factor of the cavity. Implicitely, the smaller the mode volume, the greater the Purcell enhancement. However, since NV centres lack inversion symmetry their charge state is particularly sensitive to surface chemistry effect, and therefore NV's need to be embedded a few μm away from the diamond surface to preserve the charge state stability. This places a lower bound on the cavity mode volume, which in this work, when normalised to the wavelength of interest is V_{norm}=64.

The cavity finesse is set by the mirror reflectivity. A larger finesse would provide a larger quality factor, which in term would provide a greater Purcell enhancement. However, higher finesse cavities are difficult to interact with optically, since the cavity modes are dim due to fewer photons leaving the cavity within an optical isnpection window. A modest foness of F=1200 coupled with a larger cavity supporting q=30 longitudinal modes provides a large quality factor of Q=42000. The cavity photon decay rate κ follows from this quality factor.

The beam waist and Rayleigh range are set by the cavity stability criterion, which in turn establishes the numerical aperture of the cavity. Since a very modest numerical aperture for external collection lenses would be at least $NA > 0.2$ and often much larger, with a cavity NA=0.15 the collection efficiency of cavity photons into external optics is increased with this design.

Table 4.1: **Summary table of plano-convex cavity design parameters from analysis of Hermite-Gaussian modes.**

Parameter	Value
F	1200
Q	42000
κ	70 GHz
q	30
Z_R	4 μm
w_0	580 nm
V	64
NA	0.15
F_p	50

4.1.4.1 Hybrid Cavity performance with Absorbing Media

In the visible spectrum, diamond is highly transparent with a negligible absorption coefficient [218]. When introducing a secondary material into the cavity for resonance tuning, the absorption of that material is an important consideration, since it can have a significantly deleterious effect on the the cavity quality factor by introducing absorptive round trip loss. However, the thickness of the material with respect to the diamond thickness is also important to consider, since the proportion of the cavity mode contained within the tunable layer depends on it's thickness.

The proportion of the cavity mode confined within the absorbing layer is described by the *mode-overlap factor* η, which is the ratio of the optical energy confined in the absorbing layer compared to that contained within the entire cavity. If the diamond layer has thickness d_1 and the absorbing layer has thickness d_2, then the

mode-p factor is:

$$\begin{aligned}\eta &= \frac{\int_{V_{abs}} \epsilon(z) \left|E(z)\right|^2 dz}{\int_V \epsilon(z) \left|E(z)\right|^2 dz} \\ &= \frac{\int_{d_1}^{d_1+d_2} n^2(z) \left|E(z)\right|^2 dz}{\int_0^{d_1+d_2} n^2(z) \left|E(z)\right|^2 dz}\end{aligned} \tag{4.29}$$

....where $\epsilon(z)$ is relative permittivity at position z and $E(z)$ is the electric field distribution along the cavity.

To assess the impact of the absorbing layer on quality factor, it is instructive to consider the case of a planar 1D Fabry-Perot microcavity, with a diamond region bound to an absorbing layer, and surrounded by planar mirrors on each side. Assume a hybrid cavity with layer 1 being the non-absorbing region with refractive index n_1 and thickness d_1, and layer 2 being the absorbing layer with refractive index $n_2 + i\kappa_2$ and thickness κ_2. The standing wave in each layer is sinusoidal for each layer i as $E(z) = E_0 \sin(kn_i z + \phi)$, where k is the wavenumber and ϕ is the induced phase. The total field can therefore be approximated by a sinusoidal function:

$$E(z) = E_0 \sin\left(\frac{\pi z}{d_1 + d_2}\right) \tag{4.30}$$

With this, the mode-overlap factor can be expressed as:

$$\eta = \frac{\int_{d_1}^{d_1+d_2} n^2(z) \sin^2\left(\frac{\pi z}{d_1+d_2}\right) dz}{\int_0^{d_1+d_2} n^2(z) \sin^2\left(\frac{\pi z}{d_1+d_2}\right) dz} \tag{4.31}$$

This can be evaluated analytically. The $\sin^2$ integral has the standard form $\int \sin^2(ax)dx = \frac{x}{2} - \frac{\sin(2ax)}{4a}$, so the numerator of η can be expressed as:

$$\begin{aligned}\text{Numerator} &= n_2^2\left[\frac{d_2}{2} - \frac{\sin\left(\frac{2\pi(d_1+d_2)}{d_1+d_2}\right) - \sin\left(\frac{2\pi d_1}{d_1+d_2}\right)}{4\pi/(d_1+d_2)}\right] \\ &= n_2^2\left[\frac{d_2}{2} - \frac{\sin(2\pi) - \sin\left(\frac{2\pi d_1}{d_1+d_2}\right)}{4\pi/(d_1+d_2)}\right]\end{aligned} \tag{4.32}$$

....and the denominator can be expressed as:

$$\begin{aligned}\text{Denominator} &= n_1^2\left[\frac{d_1}{2} - \frac{\sin\left(\frac{2\pi d_1}{d_1+d_2}\right)}{4\pi/(d_1+d_2)}\right] + n_2^2\left[\frac{d_2}{2} - \frac{\sin\left(\frac{2\pi(d_1+d_2)}{d_1+d_2}\right) - \sin\left(\frac{2\pi d_1}{d_1+d_2}\right)}{4\pi/(d_1+d_2)}\right] \\ &= n_1^2\left[\frac{d_1}{2} - \frac{\sin\left(\frac{2\pi d_1}{d_1+d_2}\right)}{4\pi/(d_1+d_2)}\right] + n_2^2\left[\frac{d_2}{2} - \frac{\sin(2\pi) - \sin\left(\frac{2\pi d_1}{d_1+d_2}\right)}{4\pi/(d_1+d_2)}\right]\end{aligned} \tag{4.33}$$

So, the mode-overlap factor for the 1D Fabry-Perot cavity can be expressed as:

$$\eta = \frac{n_2^2\left[\frac{d_2}{2} - \frac{\sin(2\pi)-\sin\left(\frac{2\pi d_1}{d_1+d_2}\right)}{4\pi/(d_1+d_2)}\right]}{n_1^2\left[\frac{d_1}{2} - \frac{\sin\left(\frac{2\pi d_1}{d_1+d_2}\right)}{4\pi/(d_1+d_2)}\right] + n_2^2\left[\frac{d_2}{2} - \frac{\sin(2\pi)-\sin\left(\frac{2\pi d_1}{d_1+d_2}\right)}{4\pi/(d_1+d_2)}\right]} \tag{4.34}$$

As the mode overlap factor approaches 1, the field becomes increasingly concentrated in the absorbing layer, and the impact of optical absorption becomes more profound. The quality factor of this cavity is determined by the finesse F and the mode index q as $Q{=}Fq$, with the transverse mode index related to the Guoy shift q_m ignored for this analysis since the cavity is a planar structure.

The Finesse must account for the absorption present in the cavity media, since absorption induces a decay of the electric field intensity $I(z)$ governed by the Beer-Lambert law such that $I(z) \propto e^{-2\alpha z}$, where the attenuation constant is related to the extinction coefficient κ by $\alpha{=}\frac{4\pi\kappa}{\lambda}$. So, the round-trip loss due to absorption is:

$$\mathcal{L}_{abs} = 2\alpha L = \frac{8\pi\kappa\eta L}{\lambda} \tag{4.35}$$

The finite reflectance of the DBR mirrors provides a loss pathway for the optical mode also, given by:

$$\mathcal{L}_{mirror} = -\ln(R_1 R_2) \tag{4.36}$$

... where R_1, R_2 are the reflectivities of DBR mirrors 1 and 2. The finesse in the presence of loss can be expressed as:

$$F = \frac{2\pi}{\mathcal{L}_{mirror} + \mathcal{L}_{abs}} = \frac{2\pi}{-\ln(R_1 R_2) + \frac{8\pi\kappa\eta L}{\lambda}} \tag{4.37}$$

So, the quality factor then is:

$$Q = Fq = \frac{2\pi q}{-\ln(R_1 R_2) + \frac{8\pi\kappa\eta L}{\lambda}} \tag{4.38}$$

For a diamond thickness $L{=}4$ μm, the mode overlap factor is shown in Figure 4.4(a) for an increasing absorbing layer thickness. As the absorbing layer thickness increases, more of the optical mode is contained within the absorbing layer, and therefore it's contribution to round trip loss increases. The result on cavity Quality factor for a cavity with $R_1{=}R_2{=}0.999$, and varying absorption layer

thickness and extinction coefficient, is shown in Figure 4.4(b). Naturally, if the absorbing layer thickness is small, the impact on the quality factor and finesse is also small. However, even for very thin absorbing media, if the extinction coefficient is adequately large, there is still a substantially deleterious impact on the quality factor. For this reason, the best known chalcogen based phase change materials are currently insufficient for providing cavity tuning, as was discussed briefly in Section 1.3.1.1, since the extinction coefficient of such materials is typically on the order of 10^0, which would introduce substantial round trip loss. On the other hand, as we show in Section 7.1, strontium barium niobate can be grown to have a very small extinction coefficient of $\sim 10^{-5}$, so the negative impact on the quality factor is expected to be minimal.

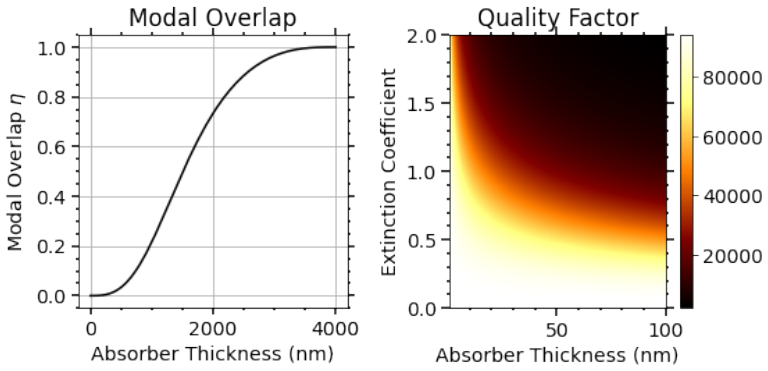

Figure 4.4: **Mode Overlap (a) and Q factor (b) for a hybrid cavity with absorbing media.**

4.1.5 Distributed Bragg Reflector

To create a microcavity, each side of the plano-convex feature must be surrounded with a high reflectivity mirror, such as a distributed Bragg reflector (DBR), which is constructed by stacking alternating layers of dielectric media together, formed by $\lambda/4$ layers of high and low index materials. In this work, the high index layer is chosen to be Ti_2O_2 (n=2.58), while the low index layer is SiO_2 (n=1.46).

Figure 4.5(a) shows a schematic representation of light propagation through a DBR stack. During transit, each boundary layer results in a partial reflection of an incoming electric field, whilst transmitted light is refracted. Electric fields of a wavelength approximately four times greater than the Bragg period optical thickness undergo constructive interference, and a wide range of wavelengths are reflected by the Bragg layers, forming a photonic stop-band Figure 4.5(b).

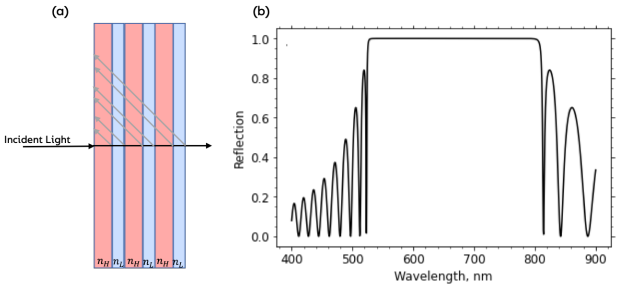

Figure 4.5: **Distributed Bragg Reflector: (a)** A DBR is formed by stacking layers of high-to-low index materials, designed to be a quarter wavelength. As light is incident on the mirror, a portion of the light is reflected, whilst transmitted light is refracted through the mirror. **(b)** Stacking multiple DBR pairs together forms a high-reflectivity photonic stopband.

The propagation and matching matrix formalism detailed above provides a useful means for analysing the reflection and transmission properties of this structure. The system of equations for the DBR is found by considering the scattering and propagation at each interface, i.e. between air and the high index layer, the high-index to low index layer, and the low index layer to air. When light propagates through a media, using an optical transfer matrix approach [217] it can be described by a propagation matrix M_p:

$$M_p = \begin{bmatrix} e^{i\kappa l} & 0 \\ 0 & e^{-i\kappa l} \end{bmatrix} \tag{4.39}$$

On the other hand, when light crosses the boundary of two materials with re-

fractive indices n and n' and with reflection and transmission Fresnel coefficients $\rho{=}\frac{n-n'}{n+n'}$ and $\tau{=}\frac{2}{n+n'}$ respectively, it can be described by a matching matrix M_p:

$$M_m = \begin{bmatrix} 1/\tau & \rho/\tau \\ \rho/\tau & 1/\tau \end{bmatrix} \tag{4.40}$$

With these, the behaviour of light as it passes through a DBR stack with high and low refractive indices is given in Equation 4.41

$$\begin{aligned} \begin{bmatrix} E_{0+} \\ E_{0-} \end{bmatrix} &= M_{\mathrm{m}}^{\mathrm{air/hi}} \begin{bmatrix} E'_{0+} \\ E'_{0-} \end{bmatrix} = M_{\mathrm{m}}^{\mathrm{air/hi}} \left(M_{\mathrm{p}}^{\mathrm{hi}} M_{\mathrm{m}}^{\mathrm{hi/lo}} M_{\mathrm{p}}^{\mathrm{lo}} M_{\mathrm{m}}^{\mathrm{lo/hi}} \right) \begin{bmatrix} E'_{1+} \\ E'_{1-} \end{bmatrix} \\ &= M_{\mathrm{m}}^{\mathrm{air/hi}} \frac{\left(M_{\mathrm{p}}^{\mathrm{hi}} M_{\mathrm{m}}^{\mathrm{hi/lo}} M_{\mathrm{p}}^{\mathrm{lo}} M_{\mathrm{m}}^{\mathrm{lo/hi}} \right)^N}{M_{\mathrm{m}}^{\mathrm{lo/hi}}} M_{\mathrm{m}}^{lo/air} \begin{bmatrix} E'_{N+} \\ 0 \end{bmatrix} \end{aligned} \tag{4.41}$$

The reflectivity of the mirrors is found by first calculating the impedance Z in terms of impermeability η, and then rearranging for Γ in terms of refractive index n. The wave impedance $Z_0{=}\frac{\eta_{hi}^2}{\eta_{lo}^2} Z_1$ and the material impedance $Z_N{=}\frac{\eta_{hi}^2}{\eta_{lo}^2}\eta_{air}$. Therefore, the reflection coefficient Γ is:

$$\Gamma_0 = \frac{Z_0 - \eta_{air}}{Z_0 + \eta_{air}} = \frac{1 - \left(\frac{n_{\mathrm{hi}}}{n_{\mathrm{lo}}}\right)^{2N}}{1 + \left(\frac{n_{\mathrm{hi}}}{n_{\mathrm{lo}}}\right)^{2N}} \tag{4.42}$$

4.1.6 DBR Absorption

When a material such as one of the DBR layers has a non-zero absorbance, it's refractive index takes on an imaginary component given by the extinction coefficient κ, such that $n'{=}n{+}i\kappa$. κ is is related to the absorption coefficient α by $\kappa{=}\frac{\alpha\lambda}{4\pi}$, and

α is related to the measured absorbance A by $\alpha = \frac{2.303A}{d}$, where d is the thickness of the layer. This arises since A is determined by the decay of a transmitted light intensity I compared to an incident intensity I_0 as $A = \log_{10}\left(\frac{I_0}{I}\right)$. Therefore the light intensity I decays with α as $I = I_0 e^{-\alpha d}$.

4.2 Derivation of the Electro-Optic Tensor of SBN

To tune the resonant mode of the optical microcavity, a secondary material needs to be introduced between the diamond membrane and one of the DBR mirrors. As explained in Section 1, one very promising means of achieving cavity tuning is to introduce a strong electro-optic material into the stack, namely strontium barium niobate (SBN). The behaviour of an electro-optic material in response to an applied electric field needs to be carefully considered to understand how best to grow the thin-film and to apply the electric field. This means that the electro-optic tensor for the material must be derived, and the impact of an externally applied electric field on each material axis must be deduced analytically. This information is crucial to not only understanding the viability of a specific electro-optic material for a given application, but also the technical considerations which must be met for the material to function satisfactorily for the desired task. Given the important role these considerations play in the device design, they are described in detail in this section. Here, we describe the tensorial nature of the index ellipsoid of electro-optical materials, and the electro-optic tensor for SBN is analytically deduced for an electric field incident on each principal axis. Finally, the impact of the electric field on arbitrarily oriented electro-optic domains in the thin film is deduced.

4.2.1 Light in Optical Materials

When light propagates in a crystalline material, it interacts with the atomic structure, and the velocity of the light passing through is reduced by a factor related to the materials index of refraction n. In isotropic crystals, light propagates in such a way that its refractive index is uniformly affected regardless of the principal crystal axis, i.e. n_a=n_b=n_c. However, in anisotropic materials, the refractive index is impacted differently, depending on the direction of light with respect to the crystal axes. In a biaxial crystal, all axes affect n differently, so $n_a \neq n_b \neq n_c$. In a uniaxial crystal one of the crystal axes affects the refractive index differently, so n_a=$n_b \neq n_c$. SBN is a uniaxial anisotropic crystal, and therefore contains two ordinary refractive indices n_o ($n_a = n_b = n_o$) and one extraordinary refractive index n_e (n_c=n_e).

The polarisation and incident direction of light with respect to the crystal impacts how it will interact with the crystal lattice. For example, if vertically polarised light travelling along the n_o axes, the phase velocity of light ν_p is affected by the extraordinary component n_e, with ν_p=$\frac{c}{n_e}$. If the light is horizontal in this plane the phase velocity is affected by the ordinary axis i.e. ν_p=$\frac{c}{n_o}$. If light is incident on the optic axis of the crystal, the polarisation doesn't matter, and for both vertical and horizontally polarised light, the phase velocity is ν_p=$\frac{c}{n_o}$. However, if the incident light comes in at an angle θ from the optic axis, the phase velocity is affected by both the ordinary and extraordinary axes depending on the incident angle, i.e. ν_p=$\frac{c}{n(\theta)}$, since the interaction between the light and the crystal is subject to an Euler rotation, and therefore the combined total refractive index can be found from:

$$\frac{1}{n^2(\theta)} = \frac{\cos^2(\theta)}{n_o^2} + \frac{\sin^2(\theta)}{n_e^2} \tag{4.43}$$

To harness the refractive index tunability of an electro-optic material for cavity tuning, it is therefore crucial to carefully consider how light interacts with the EO crystal, and design an integrated photonic device based on this understanding.

4.2.2 Derivation of the Electro-Optic Tensor

Light propagation in anisotropic media is quantitatively described by the optical indicatrix / index ellipsoid [219]. This geometric description can be attained by considering the energy density U of the electromagnetic field $\vec{E}$ with a flux density $\vec{D}{=}\epsilon_0\epsilon\vec{E}$, given by $U_E{=}\frac{\vec{E}\cdot\vec{D}}{2}{=}\frac{1}{2\epsilon_0\epsilon}\vec{D}\cdot\vec{D}$. From the definition of the dot-product, this can be decomposed in terms of individual components:

$$U_E = \frac{1}{2\epsilon_0\epsilon}\cdot\left(\frac{D_x^2}{\epsilon_x}+\frac{D_y^2}{\epsilon_y}+\frac{D_z^2}{\epsilon_z}\right) \tag{4.44}$$

From this, the principal cartesian coordinates can be simply recovered as $x{=}\frac{D_x}{\sqrt{2\epsilon_0 U_E}}$, $y{=}\frac{D_y}{\sqrt{2\epsilon_0 U_E}}$, and $z{=}\frac{D_z}{\sqrt{2\epsilon_0 U_E}}$. The defining equation for the index ellipsoid clearly follows:

$$\frac{x^2}{n_x^2}+\frac{y^2}{n_y^2}+\frac{z^2}{n_z^2}=1 \tag{4.45}$$

The index ellipsoid is the quadratic representation of the impermeability tensor $\boldsymbol{\eta}{=}\epsilon_0\boldsymbol{\epsilon}^{-1}$, i.e. $\sum_{ij}\eta_{ij}x_ix_j{=}1$, with $i,j{=}[1,2,3]$. The expanded impermeability tensor is a 3×3 matrix of the form:

$$\eta_{ij}=\begin{pmatrix}\eta_{11}&\eta_{12}&\eta_{13}\\ \eta_{21}&\eta_{22}&\eta_{23}\\ \eta_{31}&\eta_{32}&\eta_{33}\end{pmatrix} \tag{4.46}$$

To simplify notation, the contracted index Voigt notation is used which maps 2-index pairs to a single index. This maps tensor components in the following way: $\eta_{11} \rightarrow \eta_1$; $\eta_{22} \rightarrow \eta_2$; $\eta_{33} \rightarrow \eta_3$; $\eta_{23}{=}\eta_{32} \rightarrow \eta_4$; $\eta_{13}{=}\eta_{31} \rightarrow \eta_5$; and$\eta_{12}{=}\eta_{21} \rightarrow \eta_6$. So, the tensor can be expressed as:

$$\eta_{ij} = \begin{pmatrix} \eta_1 & \eta_6 & \eta_5 \\ \eta_6 & \eta_2 & \eta_4 \\ \eta_5 & \eta_4 & \eta_3 \end{pmatrix} \tag{4.47}$$

The ability of an electric field to re-distribute charges within a crystal depends on it capacity to overcome the atomic field binding between charged particles. For most materials, this binding energy is typically of order 10^8 V/cm, and therefore an applied field of reasonable intensity is not sufficient to produce an electro-optic effect. However, in certain non-centrosymmetric crystals, this binding may be comparatively weak, and consequently the electro-optic effect may be strong in these materials. In such materials, in the presence of an external electric field, the impermeability tensor is modified by both rotations of the principal axes and stretching and/or squashing of the ellipsoid vertices. Generally, the change of the impermeability tensor with respect to an applied field E can be understood by finding the impermeability tensor with no applied field $\eta_{ij}(0)$, and taking the Taylor expansion for higher order terms:

$$\eta_{ij}(\vec{E}) = \eta_{ij}(0) + \left(\frac{\partial \eta_{ij}}{\partial E_k}\right)_{E=0} E_k + \frac{1}{2}\left(\frac{\partial^2 \eta_{ij}}{\partial E_k E_l}\right)_{E=0} E_k E_l + \cdots \tag{4.48}$$

The first order term in this expansion is known as the *Pockels effect*, and is denoted in Einstein summation conventional shorthand as r_{ijk}, with $r_{ijk}{=}\left(\frac{\partial \eta_{ij}}{\partial E_k}\right)_{E=0}$. The

second order term in this expansion is known as the *Kerr effect*, and describes the quadratic electro-optic response of a material in response to an applied field. This is denoted in shorthand as s_{ijkl}, with $s_{ijkl}=\left(\frac{\partial^2 \eta_{ij}}{\partial E_k \partial E_l}\right)_{E=0}$. So, the change in the impermeability tensor in response to an applied field $\Delta\eta_{ij}=\eta_{ij}(E)-\eta_{ij}(0)$ is:

$$\Delta\eta_{ijk}(\vec{E}) = r_{ijk}E_k + s_{ijkl}E_kE_l \tag{4.49}$$

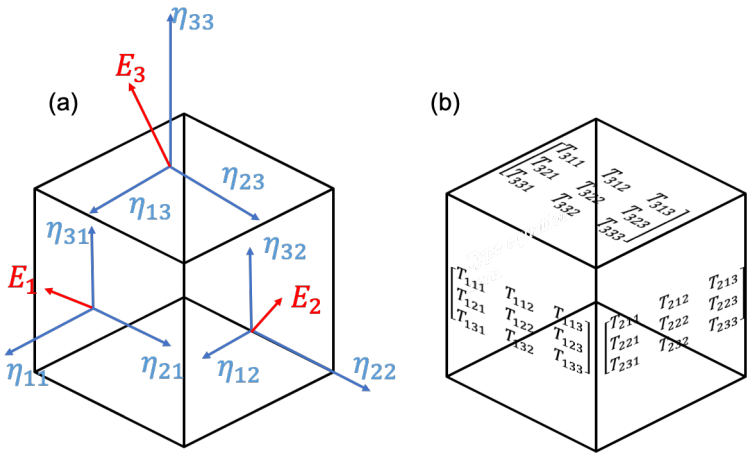

Figure 4.6: **The rank-2 impermeability tensor η interacts with the rank-1 electric field vector (a)**. The linear mapping of the elctric field to the impermeability tensor produces a rank-3 tensor (b), which is the Pockels tensor.

The Pockels coefficients describe the response of the crystal of an optically active material in response to an applied field. In a non-centrosymmetric crystal, the central cation is moved in a direction relative to the crystal axis, by a magnitude measured in pm/V. The Pockels effect is described by a rank-3 tensor, since it linearly connects a second-rank change in the optical properties of the material dielectric response to a first-rank applied electric field 4.6. The tensor order follows directly from the nature of this physical relationship. connecting the electric field E_k to the change in the impermeability η_{ij}. The general form of a rank-3 tensor T_{ijk} for $i \in \{1,2,3\}$ is given in Equation 4.50.

$$T = \left\{ \begin{bmatrix} T_{111} & T_{112} & T_{113} \\ T_{121} & T_{122} & T_{123} \\ T_{131} & T_{132} & T_{133} \end{bmatrix}, \begin{bmatrix} T_{211} & T_{212} & T_{213} \\ T_{221} & T_{222} & T_{223} \\ T_{231} & T_{232} & T_{233} \end{bmatrix}, \begin{bmatrix} T_{311} & T_{312} & T_{313} \\ T_{321} & T_{322} & T_{323} \\ T_{331} & T_{332} & T_{333} \end{bmatrix} \right\} \tag{4.50}$$

A rank-3 tensor therefore contains 27 components, but the impermeability tensor η_{ij} is symmetric, so $\eta_{ij}{=}\eta_{ji}$. Therefore the Pockels tensor r_{ijk} is also symmetric in ij, so $r_{ijk}{=}r_{jik}$, and for each fixed k, the first two indices i, j form a symmetric 3×3 matrix with 6 independent components. Since $k \in \{1, 2, 3\}$, there are 18 independent components of r_{ijk}. With Voigt notation, the rank-3 Pockels tensor can be represented with two components i, j, where $i \in \{1, 2, 3, 4, 5, 6\}, j \in \{1, 2, 3\}$. So, the Pockels tensor can be reduced to a 6×3 matrix which relates the impact of the electric field on each crystal axis:

$$r_{ij} = \begin{pmatrix} r_{11} & r_{12} & r_{13} \\ r_{21} & r_{22} & r_{23} \\ r_{31} & r_{32} & r_{33} \\ r_{41} & r_{42} & r_{43} \\ r_{51} & r_{52} & r_{53} \\ r_{61} & r_{62} & r_{63} \end{pmatrix} \tag{4.51}$$

The Voigt notation contraction can be further applied to the Pockels tensor: $r_{1k}{=}r_{11k}$; $r_{4k}{=}r_{23k}{=}r_{32k}$; $r_{2k}{=}r_{22k}$; $r_{5k}{=}r_{11k}{=}r_{31k}$; $r_{3k}{=}r_{33k}$; and $r_{6k}{=}r_{11k}{=}r_{21k}$. With this, the index ellipsoid in the presence of an applied electric field can be expanded as:

$$\left(\frac{1}{n_x^2} + r_{1k}E_k\right)x^2 + \left(\frac{1}{n_y^2} + r_{2k}E_k\right)y^2 + \left(\frac{1}{n_z^2} + r_{3k}E_k\right)z^2$$
$$+ 2r_{4k}yzE_k + 2r_{5k}xzE_k + 2r_{6k}xyE_k = 1 \tag{4.52}$$

The physical interpretation of this is that the electric field linearly maps to an optical response. The three-vector of the electroc field E_k maps to the change in the optical properties of a material $\Delta\eta_{ij}$ represented by 6 independent components due to symmetry. The Pockels tensor describes how the electric field in direction k modifies the optical response η_{ij} in coordinate space (i, j) as:

$$\Delta\eta_i = \sum_{k=1}^{3} r_{ik}E_k \tag{4.53}$$

This describes a linear relationship between the electric field and its optical response. Hence, despite the fact that the Pockels effect is a non-linear change of the polarisation vector $\vec{P}$ of a material, it is often referred to as a linear electro-optic respoinse with regards to the dielectric permeability and applied field.

It is evident from eq. 4.52 for certain crystal axes and field orientations, the principal axis of the index ellipsoid will be modified. The principal axes themselves then may require a coordinate transformation to yield the change in each component of $\boldsymbol{\eta}$ in the presence of an applied field.

4.2.3 Electro-Optic Response of SBN

SBN is a tetragonal tungsten-bronze crystal in the P4bm point group, with symmetry elements of the space group C_{4h}^2. Consequently, the Pockels tensor for this crystal conveniently reduces to:

$$r_{SBN} = \begin{pmatrix} 0 & 0 & r_{13} \\ 0 & 0 & r_{13} \\ 0 & 0 & r_{33} \\ 0 & r_{42} & 0 \\ r_{42} & 0 & 0 \\ 0 & 0 & 0 \end{pmatrix} \tag{4.54}$$

....where r_{13}=r_{23} and r_{42}=r_{51}. In the literature, it has been shown that the r_{33} component of SBN is extraordinarily high, being measured in thin-film form as r_{33}=844 pm/V [44]. The remaining components are significantly weaker, at r_{13}=47 pm/V and r_{42}=67 pm/V, although are still substantially strong compared to most other electro-optic media. Noting that SBN is a uniaxial material, and therefore n_x=n_y=n_o and n_z=n_e, the expanded index ellipsoid in terms of these components is:

$$\begin{aligned} &\left(\frac{1}{n_x^2} + r_{13}E_z\right)x^2 + \left(\frac{1}{n_y^2} + r_{13}E_z\right)y^2 + \left(\frac{1}{n_z^2} + r_{33}E_z\right)z^2 \\ &+ 2r_{42}yzE_y + 2r_{42}xzE_x = 1 \end{aligned} \tag{4.55}$$

Clearly, different Pockels coefficients can be exploited by applying the electric field along different axes. Doing so, however, causes a modification of the index ellipsoid in different ways.

4.2.3.1 Applying the Electric Field Parallel to z

If an electric field E_z is applied parallel to the z-axis of the SBN thin film, the index ellipsoid reduces to:

$$\left(\frac{1}{n_o^2} + r_{13}E_z\right)x^2 + \left(\frac{1}{n_o^2} + r_{13}E_z\right)y^2 + \left(\frac{1}{n_e^2} + r_{33}E_z\right)z^2 = 1 \tag{4.56}$$

The impermeability tensor then contains updated values:

$$\boldsymbol{\eta} = \begin{pmatrix} \eta_o + r_{13}E_z & 0 & 0 \\ 0 & \eta_o + r_{13}E_z & 0 \\ 0 & 0 & \eta_e + r_{33}E_z \end{pmatrix} \tag{4.57}$$

Conveniently, this modified index ellipsoid is already diagonal, and therefore there is no need to define new principal axes. Applying the differential relation:

$$dn = \frac{1}{2}n^3 d\left(\frac{1}{n^2}\right) \tag{4.58}$$

....the corresponding changes in the refractive indices for each principal component are:

$$n_{x'} = n_o - \frac{1}{2}n_o^3 r_{13}E_z \tag{4.59}$$

$$n_{y'} = n_o - \frac{1}{2}n_o^3 r_{13}E_z \tag{4.60}$$

$$n_{z'} = n_e - \frac{1}{2}n_e^3 r_{33}E_z \tag{4.61}$$

4.2.3.2 Applying the Electric Field Parallel to x

If a field E_x is applied parallel to the x-axis of the principal coordinate system, the index ellipsoid reduces to:

$$\frac{x^2}{n_o^2} + \frac{y^2}{n_o^2} + \frac{z^2}{n_e^2} + 2r_{42}xzE_x = 1 \tag{4.62}$$

Correspondingly, the impermeability tensor is:

$$\boldsymbol{\eta} = \begin{pmatrix} \eta_o & 0 & r_{42}E_x \\ 0 & \eta_o & 0 \\ r_{42}E_x & 0 & \eta_e \end{pmatrix} \tag{4.63}$$

Now the index ellipsoid contains mixed terms, and therefore requires a change of basis to solve the system of equations to interpret the impact of the refractive index components. Using singular value decomposition to achieve this transformation can be quite cumbersome, but since the impact of applying an electric field is seen as a rotation of the index ellipsoid, the principal axis transformation can be more conveniently deduced by applying the Euler rotation matrix R:

$$R = \begin{pmatrix} \cos\theta & -\sin\theta \\ \sin\theta & \cos\theta \end{pmatrix} \tag{4.64}$$

The goal is to determine a new coordinate system (x', y', z') in which the ellipsoid of equation 4.62 contains no mixed terms, i.e. has the form:

$$\frac{x'^2}{n_o^2} + \frac{y'^2}{n_o^2} + \frac{z'^2}{n_e^2} + 2r_{42}xzE_x = 1 \tag{4.65}$$

From inspection it is clear that the y-axis is unmodified, and $y = y'$. Applying the rotation matrix of equation 4.64 to the remaining new axes yields $x = x'\cos\theta - z'\sin\theta$, and $z = x'\sin\theta + z'\cos\theta$. Substituting these terms into equation 4.65

gives:

$$\frac{\left(x'\cos\theta - z'\sin\theta\right)^2}{n_o^2} + \frac{y'^2}{n_o^2} + \frac{\left(x'\sin\theta + z'\cos\theta\right)^2}{n_e^2} + 2r_{42}E_x\left(x'\cos\theta - z'\sin\theta\right)\cdot\left(x'\sin\theta + z'\cos\theta\right) = 1 \tag{4.66}$$

By expanding the brackets and applying the relevant trigonometric identities, equation 4.66 can be re-expressed as:

$$\frac{x'^2\left(1-\sin^2\theta\right) - x'z'\sin 2\theta + z'^2\sin^2\theta}{n_o^2} + \frac{y'^2}{n_o^2} + \frac{x'^2\sin^2\theta + x'z'\sin 2\theta + z'^2\left(1-\sin^2\theta\right)}{n_e^2} + r_{42}E_x\left(x'^2\sin 2\theta + 2x'z'\cos^2\theta - 2x'z'\sin^2\theta - z'^2\sin 2\theta\right) = 1 \tag{4.67}$$

Now, by collecting like terms, a more convenient expression begins to emerge:

$$x'^2\left(\frac{1}{n_o^2} - \frac{\sin^2\theta}{n_o^2} + \frac{\sin^2\theta}{n_e^2} + r_{42}E_x\sin 2\theta\right) + \frac{y'^2}{n_o^2} + z'^2\left(\frac{1}{n_e^2} - \frac{\sin^2\theta}{n_e^2} + \frac{\sin^2\theta}{n_o^2} - r_{42}E_x\sin 2\theta\right) + x'z'\left(\frac{\sin 2\theta}{n_e^2} - \frac{\sin 2\theta}{n_o^2} + 2r_{42}E_x cos^2\theta - 2r_{42}E_x\sin^2\theta\right) = 1 \tag{4.68}$$

This is still quite cumbersome, and the mixed terms are still present. This can be satisfied however by taking an angle θ which enforces that the mixed terms for $x'z'$ vanish (in this case θ=45°), and by applying further the trigonometric identity

for $\tan\theta$:

$$\tan\theta = \frac{\sin\theta}{\cos\theta} = \frac{\sin 2\theta}{1+\cos 2\theta} = \frac{\sin 2\theta}{1-2\sin^2\theta} \tag{4.69}$$

So,

$$\begin{aligned} x'^2\left(\frac{1}{n_o^2} - \frac{2\sin^2\theta}{n_o^2+n_e^2} + r_{42}E_x\sin 2\theta\right) + \frac{y'^2}{n_o^2} + z'^2\left(\frac{1}{n_e^2} - \frac{2\sin^2\theta}{n_o^2+n_e^2} - r_{42}E_x\sin 2\theta\right) \\ = x'^2\left(\frac{1}{n_o^2} + r_{42}E_x\tan\theta\right) + \frac{y'^2}{n_o^2} + z'^2\left(\frac{1}{n_e^2} - r_{42}E_x\tan\theta\right) \end{aligned} \tag{4.70}$$

The angle θ is given by:

$$\tan 2\theta = \frac{2r_{42}E_x}{\frac{1}{n_o^2} - \frac{1}{n_e^2}} \tag{4.71}$$

Finally, by applying the differential relation, the modified refractive indices $n_{x'}$, $n_{y'}$, and $n_{z'}$ are found as:

$$n_{x'} = n_o - \frac{1}{2}n_o^3 r_{42}E_x\tan\theta \tag{4.72}$$

$$n_{y'} = n_0 \tag{4.73}$$

$$n_{z'} = n_e + \frac{1}{2}n_e^3 r_{42}E_x\tan\theta \tag{4.74}$$

With small θ, i.e. $\tan\theta \approx \theta$:

$$n_{x'} \approx n_o - \frac{1}{2}n_o^3 r_{42}E_x\frac{r_{42}E_x}{\frac{1}{n_o^2} - \frac{1}{n_e^2}} = n_o - \frac{1}{2}n_o^3(r_{42}E_x)^2\frac{n_e^2 n_o^2}{n_e^2 - n_o^2} \tag{4.75}$$

$$n_{y'} = n_0 \tag{4.76}$$

$$n_{z'} \approx n_e + \frac{1}{2}n_e^3 r_{42}E_x\frac{r_{42}E_x}{\frac{1}{n_o^2} - \frac{1}{n_e^2}} = n_e + \frac{1}{2}n_e^3(r_{42}E_x)^2\frac{n_e^2 n_o^2}{n_e^2 - n_o^2} \tag{4.77}$$

4.2.3.3 Applying the Electric Field Parallel to y

Similarly, if a field E_y is applied parallel to the y-axis, the index ellipsoid reduces to:

$$\frac{x^2}{n_o^2} + \frac{y^2}{n_o^2} + \frac{z^2}{n_e^2} + 2r_{42}yzE_y = 1 \tag{4.78}$$

.... and the corresponding tensor form is:

$$\boldsymbol{\eta} = \begin{pmatrix} \eta_o & 0 & 0 \\ 0 & \eta_o & r_{42}E_y \\ 0 & r_{42}E_y & \eta_e \end{pmatrix} \tag{4.79}$$

With this, the complete impermeability tensor of the crystal system is found as:

$$\boldsymbol{\eta} = \begin{pmatrix} \eta_o + r_{13}E_z & 0 & r_{42}E_x \\ 0 & \eta_o + r_{13}E_z & r_{42}E_y \\ r_{42}E_x & r_{42}E_y & \eta_e + r_{33}E_z \end{pmatrix} \tag{4.80}$$

For the field applied to the y-axis, the impermeability tensor again contains mixed terms, and hence a coordinate system transform is again required. In the same manner in as for applying the field parallel to the x-axis, the change in refractive index can be found for a field applied parallel to the y-axis as:

$$n_{x'} = n_0 \tag{4.81}$$

$$n_{y'} \approx n_o - \frac{1}{2} n_o^3 r_{42} E_y \frac{r_{42} E_y}{\frac{1}{n_o^2} - \frac{1}{n_e^2}} = n_o - \frac{1}{2} n_o^3 (r_{42} E_y)^2 \frac{n_e^2 n_o^2}{n_e^2 - n_o^2} \tag{4.82}$$

$$n_{z'} \approx n_e + \frac{1}{2} n_e^3 r_{42} E_y \frac{r_{42} E_y}{\frac{1}{n_o^2} - \frac{1}{n_e^2}} = n_e + \frac{1}{2} n_e^3 (r_{42} E_y)^2 \frac{n_e^2 n_o^2}{n_e^2 - n_o^2} \tag{4.83}$$

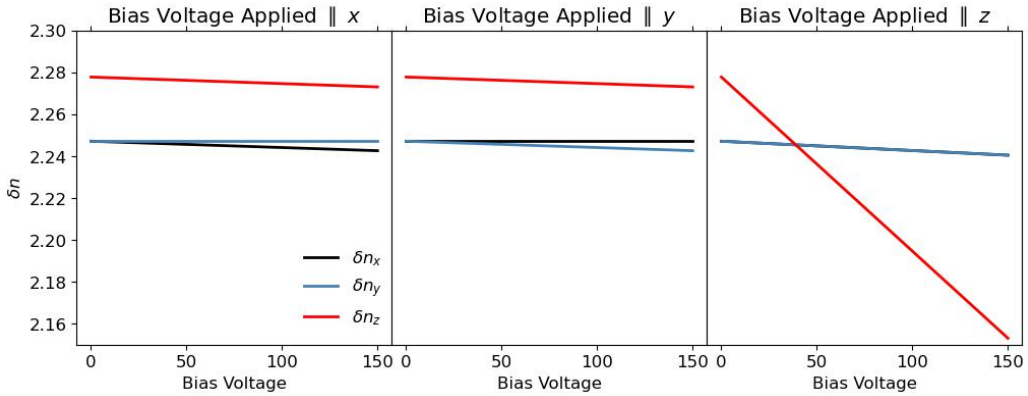

Figure 4.7: **Impact of bias field applied parallel to three different principal axes, x, y, and z.** The strongest change in refractive index is addressed when the bias field is parallel to the optic-axis of the SBN domains.

Clearly the strongest Pockels coefficient is utilised if the electric field is incident upon the z-axis of the thin film. This poses some technological challenges regarding how to deliver the field in this direction, but it is not insurmountable. However, since the extraordinary axis in this material is aligned along the crystal optical axis $\langle 001 \rangle$, as described previously light incident parallel to the optic axis will not experience birefringence, and since the incident light on the microcavities will be in -plane to the z-axis, no electro-optic tuning would be available. This could be solved by growing the SBN thin film along a different crystal orientation, which is challenging but potentially feasible. Conveniently however, as is shown in Section 6.3, for this material a large number of the crystallites are oriented along the

$\langle 310 \rangle$ axis as well as the $\langle 001 \rangle$, which means that sending light along the optic axis will allow for interaction with the strongest Pockels tensor component.

4.2.4 310 Oriented SBN

The optic axis of $\langle 310 \rangle$ oriented domains is rotated by $90°$ with respect to $\langle 001 \rangle$ domains. Therefore the above analysis for the impact of a field applied parallel to each axis still applies, but the frame of optic-axis frame of reference is rotated. To determine the angle between a $\langle 310 \rangle$ oriented domain and each principal axis, we start by constructing unit vectors for each set of Miller indices, $\hat{A}=(h_1, k_1, l_1)$ and $\hat{B}=(h_2, k_2, l_2)$. The dot product of these two unit vectors is related to the angle θ between them by $\hat{A} \cdot \hat{B}= \left|\hat{A}\right| \left|\hat{B}\right| \cos\theta$. Therefore, the angle between the $\langle 310 \rangle$ face and each principal axis can be found by solving for θ. For a tetragonal crystal:

$$\theta = \cos^{-1}\left[\frac{h_1 h_2 + k_1 k_2 + \frac{l_1 l_2}{(c/a)^2}}{\sqrt{h_1^2 + k_1^2 + \frac{l_1^2}{(c/a^2)}} \cdot \sqrt{h_2^2 + k_2^2 + \frac{l_2^2}{(c/a^2)}}}\right] \tag{4.84}$$

The angle difference between a $\langle 310 \rangle$ oriented domain and each principal axis x, y, and z is shown in Table 4.2

Table 4.2: **Angles between $\langle 310 \rangle$ oriented domains and principal axes**

$\boldsymbol{x}$ (001)	$\boldsymbol{y}$ (010)	$\boldsymbol{z}$ (001)
$18.44°$	$71.55°$	$90°$

The existence of a secondary $\langle 310 \rangle$ orientation mitigates the two aforementioned problems of polarisation direction of the material and the difficulty with exciting an electric field along the z-axis, i.e. through the film. Since the $\langle 310 \rangle$ domains are no longer in plane with the lab-frame z-axis, they will experience birefringence upon optical excitation along z. In addition, conveniently, the optic axis of a $\langle 310 \rangle$

oriented domains is fairly close to being perpendicular to the x-axis. Therefore, applying a static field along the x-axis will excite the strongest Pockels coefficient r_{33}.

However, the fact that there are two preferred orientations, with only one of these being optimal, will impact the yield of cavities which can be sufficiently tuned. As shown in Section 6.4, approximately 70% of the SBN domains are oriented along $\langle 310 \rangle$, and therefore for any film bonded to a diamond membrane containing cavities, there is a 30% chance that the SBN tuning layer will not provide sufficient tunability. This may be mitigated however by thin-film growth on different substrates which may promote a much higher probability of $\langle 310 \rangle$ domain growth, such as gadolinium gallium garnate, whose lattice parameters match closely to the a/b lattice parameter of SBN.

4.2.5 Effect of Field Alignment

Since $\langle 310 \rangle$ oriented domains are not perfectly perpendicular to the x-axis, it is sensible to consider the effects of a misalignment in the orientation of the domains with respect to a field applied along the x-axis. Recalling equation 4.48, the impact of misalignment is

$$\eta_{ij}(E\vec{(}\theta)) = \eta_{ij}(0) + \left(\frac{\partial \eta_{ij}}{\partial E_k}\right)_{E=0} E_k \cos\theta + \cdots \tag{4.85}$$

....and the impermeability tensor is:

$$\boldsymbol{\eta} = \begin{pmatrix} \eta_o + r_{13}E_z\cos\theta_z & 0 & r_{42}E_x\cos\theta_x \\ 0 & \eta_o + r_{13}E_z\cos\theta_z & r_{42}E_y\cos\theta_y \\ r_{42}E_x\cos\theta_x & r_{42}E_y\cos\theta_y & \eta_e + r_{33}E_z\cos\theta_z \end{pmatrix} \tag{4.86}$$

Therefore, the differential relation of the refractive index along the z-axis given in equation 4.61 is modified to:

$$n'_z = n_e - \frac{1}{2} n_e^3 r_{33} E_z \cos\theta \tag{4.87}$$

The field alignment angle only affects the magnitude of the delivered field, and does not interact with the core components of the impermeability tensor. Therefore, field misalignment only translates to a lower efficiency of the delivery of the electric field.

4.3 Dielectric Function Models

Once reflectance data has been acquired by ellipsometry, the dielectric function can be inferred by the solution of an appropriate model. There are many different examples of dielectric function models, such as the the Lorentz model [220], the Sellmeier model [221], and the Cauchy model [222]. The choice of which model is most appropriate depends on the material in question and the conditions of the fitting procedure. For example, when fitting only the transparent region of a material, the Sellmeier or Cauchy model may be perfectly adequate to capture the dielectric function. In the presence of free-carrier absorption, the Drude model [223] may be more appropriate. Electric polarisation in the visible/UV region may best be captured by the Lorentz model, or extension to this such as the Tauc-Lorentz model. An exhaustive description of such models is well beyond the scope of this chapter, but an excellent guide can be found in [219]. Each of these different models treat the dielectric function as being described as a harmonic oscillator with various extra terms accounting for phenomena such as behaviour in the absorption edge.

The Lorentz model is generally successful at modelling absorption in thin-films where the absorption is due to some localised effect state [219]. However, if a material contains an absorption term in the band gap, as has been predicted for SBN [193], the Tauc-Lorentz model [195, 196, 224] is well known to capture this behaviour more closely. Therefore this model is chosen for the present study.

4.3.1 Tauc-Lorentz Model

A complete and thorough description of the background of the Tauc-Lorentz model is beyond the scope of this chapter, but the model is very well detailed in [219]. In this chapter, we provide a broader overview of the model background, focusing the outputs of the model for the measured thin-films. The Tauc-Lorentz model regards the dielectric function to be the sum of a real and imaginary component. The real component is denoted as $\epsilon_{r,TL}$, where the subscript TL refers to *Tauc-Lorentz*, whilst the imaginary component is denoted as $\epsilon_{i,TL}$. The imaginary component is actually the sum of the original Lorentz component ϵ_L and the added Tauc component ϵ_T. So, the Tauc-Lorentz complex dielectric function is:

$$\bar{\epsilon} = \epsilon_{r,TL} + \epsilon_{i,TL} = \epsilon_{r,TL} + i(\epsilon_{i,T} + \epsilon_{i,L}) \tag{4.88}$$

The real component of the dielectric function represents the material dispersion and refraction properties, and is derived from the imaginary component via the Kramers-Kronig relations [225, 226]. The imaginary component represents the material absorption, and in the Tauc-Lorentz model it incorporates a Lorentz oscillator and a Tauc gap. The Tauc gap is defined for inter-band transitions above the bandgap as:

$$\epsilon_{i,TL}(E > E_g) = A_T \cdot \left(\frac{E - E_g}{E}\right) \tag{4.89}$$

....where A_T is the Tauc coefficient, E is the photon energy, and E_g is the optical bandgap. The imaginary component gives the response of the material caused only by inter-band absorption, i.e.

$$\epsilon_{i,T}(E < E_g) = 0 \tag{4.90}$$

The Lorentz component of the complex dielectric function is given by:

$$\epsilon_{i,L}(E) = \frac{A_L \cdot E_0 \cdot C \cdot E}{(E^2 - E_0^2)^2 + C^2 \cdot E^2} \tag{4.91}$$

....where A_L is the strength of the $\epsilon_{2,TL}(E)$ peak, C is the peak broadening term, and E_0 is the central peak energy. So, $\epsilon_{i,TL}(E)$ is defined as:

$$\epsilon_{i,TL}(E) = \epsilon_{i,T} \times \epsilon_{i,L} = \begin{cases} \frac{1}{E}\frac{A \cdot E_0 C (E - E_g)^2}{(E^2 - E_0^2)^2 + C^2 \cdot E^2} & E > E_g \\ 0 & E \leq E_g \end{cases} \tag{4.92}$$

....where $A = A_T \times A_L$.

The real part of the dielectric function is derived by applying the Kramer-Kronig relation to ϵ_r:

$$\epsilon_r(E) = \epsilon_r(\infty) + \frac{2}{\pi} P \int_{E_g}^{\infty} \frac{\zeta^2 \cdot \epsilon_i(\zeta)}{\zeta^2 - E^2} d\zeta \tag{4.93}$$

....where P is the Cauchy principal value containing the residues of the integral at poles on the lower half of the complex plane and on the real axis.

4.4 Numerical Analysis by Finite Difference Time Domain Simulation

Analytic methods like transfer matrices and exact solutions to field equations provide a solid foundation for studying cavity performance and design but often oversimplify real-world complexities such as material properties, electric field penetration, and dispersion. These intricacies are better addressed using numerical techniques like finite element and finite-difference time-domain (FDTD) methods. FDTD, a standard for simulating light propagation in physical structures, solves time-dependent Maxwell's equations using central-difference approximations on a discrete grid, known as a Yee cell [227]. This method accounts for material properties, geometric factors, and field leakage through sequential time-stepping. While a detailed exploration of FDTD is beyond this chapter's scope, comprehensive resources are available in [228, 229]. FDTD simulations in this thesis were performed using the Lumerical FDTD software via a setup and post-analysis library purpose built by the author called PyLumerical [230].

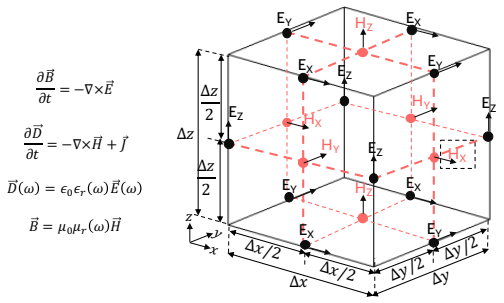

Figure 4.8: **Yee Cell:** The Yee Cell is used to discretise Maxwells equations in space, by placing electric and magnetic fields on a cubic grid, with dimensions specified by meshing resolution.

In FDTD, Maxwell's equations are discretized into finite-difference equations, iteratively solving for electric and magnetic fields until a steady state is reached [228].

The simulation region is divided into Yee cells, where electric field components are computed along the cell edges and magnetic components across the cell faces [227]. Time is discretized into steps of size Δt, ensuring compliance with the Courant-Friedrichs-Lewy condition for numerical stability [231, 232]. After reaching a steady state, time-domain fields are converted to the frequency domain via Fourier transform. Accurate frequency-domain results require long simulation times to prevent distortions like sinc-function artifacts. This poses challenges for high-quality-factor cavities, as detailed in Section 4.4.2, where field decay to near zero can demand impractically long simulations.

4.4.1 Meshing Accuracy

Since the FDTD algorithm discretises the simulation geometry onto a Cartesian mesh, structural variations occurring within any one Yee cell cannot be accounted for, resulting in a stepped permittivity mesh that coincides with the Cartesian one. This may be accounted for by solving Maxwell's integral equations near structural boundaries. For example, the modelling accuracy of curved perfect electrical conductor (PEC) surfaces can be enhanced with the Yu-Mittra method [233], where the contour integral to is reduced to include only the region outside the PEC where the electric field is non-zero (Figure 4.9a). This approach is suitable for simulating structures at radio-frequency and microwave frequencies, but to extend to optical frequencies, the material's dispersion must be taken into account. This is accounted for with Lumerical's conformal meshing approach.

In Figure 4.9b, a convergence plot demonstrates the impact of mesh accuracy refinement on the attained centre wavelength and quality factor from FDTD simulation, for an open-air cavity with radius of curvature $\mathcal{R}$=4 μm, longitudinal mode index q=2, N_p=10, and N_f=6. These parameters are chosen to allow for a convergence test to be conducted within a reasonable execution time. A 'mesh

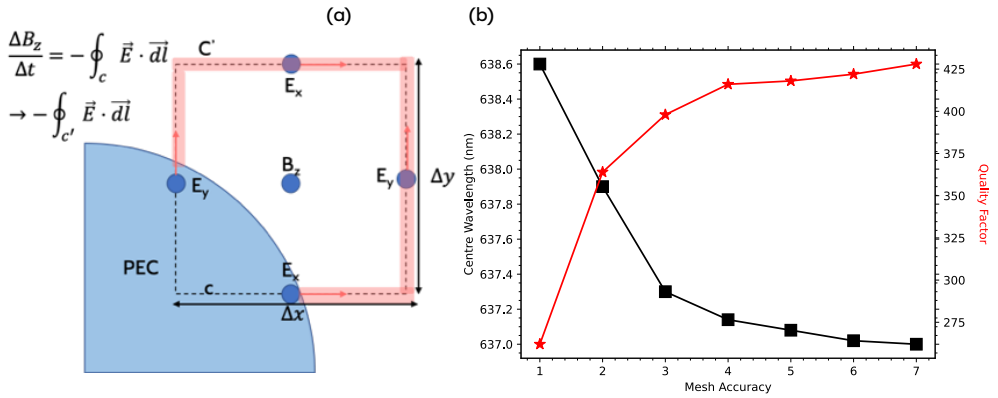

Figure 4.9: **Mesh Accuracy: (a)** The Yu-Metra mesh refinement method reduces the contour integral for the simulation region to include only the region outside a perfect electric conductor (PEC) where the electric field is non-zero. **(b)** Convergence testing the impact of mesh accuracy on centre wavelength and quality factor for a diamond filled cavity of $\mathcal{R}$=4 μm, q=2, N_f=6, N_p=10

accuracy' setting is adjusted from $1-7$, corresponding to a Yee cell size between $10-70$ Yee cells per wavelength. The uncertainties in Table 4.3 are determined by comparing the difference in the calculated figure of merit with respect to the highest possible mesh accuracy setting of 7. Therefore, this represents an artificial computation uncertainty which isn't physically real, but is nonethelss constructive in interpretting FDTD outputas, since it allows for an understanding of the possible range of solutions.

Below a mesh accuracy setting of 3, the Yee cell size is too coarse to sufficiently render the fields with precise enough resolution. At high precision, on the other hand, execution time becomes too long for reasonable simulation. Consequently, for most simulations in this thesis, unless otherwise stated, a mesh accuracy setting of 3 is chosen as a compromise between accuracy and execution time, corresponding to $\sim 0.05\%$ error in centre wavelength estimation.

Table 4.3: **Results of mesh accuracy convergence testing** on a Windows 10 Enteprise system with an AMD Ryzen 9 3905X 16-Core 3.49GHz processor and 64 GB RAM.

Mesh Acc.	Cell Size (nm)	λ_0 (nm)	unc(%)	Q	unc(%)	F_P	unc(%)	Execution Time (mins)
1	41.8	638.60	0.250	262	48.12	4.25	43.75	1.00
2	27.2	637.90	0.140	364	16.16	5.74	14.39	2.78
3	19.5	637.30	0.050	398	7.26	6.12	8.00	15.35
4	15.2	637.14	0.020	416	2.84	6.37	4.00	24.95
5	12.5	637.08	0.010	418	2.37	6.57	0.91	41.98
6	10.6	637.02	0.003	422	1.41	6.58	0.76	81.04
7	9.2	637.00	0.000	428	0.00	6.63	0.00	130.37

4.4.2 Quality Factor Determination

The quality factor (Q) of a resonant cavity in FDTD simulations is typically determined via Fourier transformation of the electromagnetic field, measuring the resonance frequency ω_0 and its full width at half maximum FWHM, $\delta\omega$, with $Q{=}\omega_0/\delta\omega$. While straightforward for low-Q cavities, where fields decay fully within the simulated time, high-Q cavities require alternative methods since $\delta\omega \sim 1/T_{\text{sim}}$ limits precision.

For high-Q cavities, Q is derived from the decay envelope of the time-domain signal $E(t) = e^{-t(\alpha - i\omega_0)}$, where $\alpha{=}\omega_0/2Q$. The envelope slope m is obtained by fitting $\log|E(t)|{=}mt$, leading to $Q{=}\frac{-\omega_0 \log e}{2m}$. Figure 4.10 illustrates the frequency domain transmission spectrum of a diamond cavity ($\mathcal{R}{=}8\mu m$, $q = 15$), showing fundamental and transverse modes. These modes are identified by observing the electric field profile at each associated wavelength, which correspond to Hermite-Gaussian modes of varying order (as demonstrated in Section 5.4.1). The fundamental mode for ω_0 is isolated with a Guassian filter, aiding Q estimation. However, due to mode interference, filter artefacts, and envelope-signal separation [234] still remain. To mitigate these, a convergence test is always con-

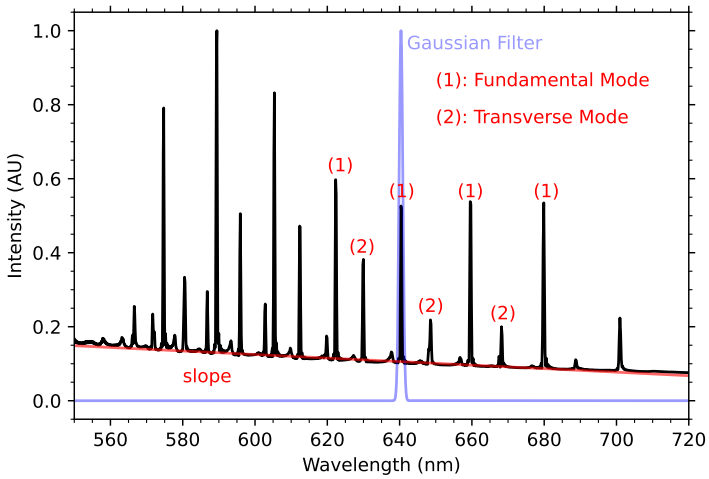

Figure 4.10: **Frequency domain transmission spectrum:** Following Fourier transformation, the time domain spectrum is visualised in the frequency domain, revealing a number of fundamental (2) and transverse (1) modes. The quality factor is found by determining the slope of this spectrum, and the applying a Gaussian peak filter to the fundamental mode of interest to extracting the resonant wavelength.

ducted when calculating Q over increasing portions of the time-domain data.

4.4.3 Calculating Cavity Mode Volume

The mode volume integral of Equation 4.10 can be computed directly, but is computationally very expensive due to its four-dimensional matrix space. However, this complexity can be significantly reduced by exploiting the cylindrical symmetry of the Gaussian modes [235], thereby transforming the integral to a double-integral in two-dimensions:

$$V_{2D} = \frac{\int_0^{r_{max}} \int_{z_{min}}^{z_{max}} 2\pi r \int \epsilon(\mathbf{r},\mathbf{z}) \left|E(\mathbf{r},\mathbf{z})\right|^2 dzdr}{\max(\epsilon(\mathbf{r},\mathbf{z}) \left|E(\mathbf{r},\mathbf{z})\right|^2)} \tag{4.94}$$

....where dz and dr denote the size of the mesh cells. As such, the mode volume calculation can be discretised to the Yee cell. To account for two-fold symmetry

of the dipole emitter, frequency-domain monitors are placed along the x-z and y-z axes, and the average field intensity taken from both monitors is used for the mode volume calculation. A comparison between the simulated mode volume for 3D and 2D integration is provided in table 4.4 as the number of cavity modes is increased from 1 to 7. It can be seen that the 2D integration tracks the full 3D solution with minimal error:

Table 4.4: **Comparison between mode volume calculations with 2D and 3D integrals**

q	$V_{3D}\ (\lambda/n)^3$	$V_{2D}\ (\lambda/n)^3$	unc(%)
1	0.98	0.974	0.93
2	1.41	1.39	1.22
3	2.46	2.46	0.74
4	2.97	2.93	1.15
5	4.05	4.01	0.99
6	4.55	4.50	2.43
7	4.97	4.82	3.1

4.4.4 FDTD Simulation of Diamond:SBN Microcavity

To study the impact of modifying the refractive index of an SBN layer when it is hybridised with a diamond monolithic cavity, an FDTD simulation with a mesh accuracy of 3 was constructed which considered each material as ideal dielectrics, but with a modified refractive index of the SBN layer. The impact of this shifting index on the centre wavelength of the microcavity is shown in Figure 4.11, for a monolithic diamond cavity with longitudinal mode index q=30, radius of curvature $\mathcal{R}$=8 μm, and a 300 nm thick layer of SBN stacked between the diamond and the planar mirror. An electrode bias voltage was assumed to range between 0-100 V, and the refractive index of the SBN layer was correspondingly adjusted based on the theoretical change. The cavity resonance is seen to blue-shift from $\sim$637.1 nm to $\sim$636.6 nm. This constitutes approximately 2.4% of the intended free spec-

tral range of the final cavity device, although this tunability range can of course be improved further by applying higher bias voltages. The grey shaped confidence band in this plot represents the computational uncertainty in the wavelength due to the finite meshing, with uncertainties given in Tables 4.3 and 4.4

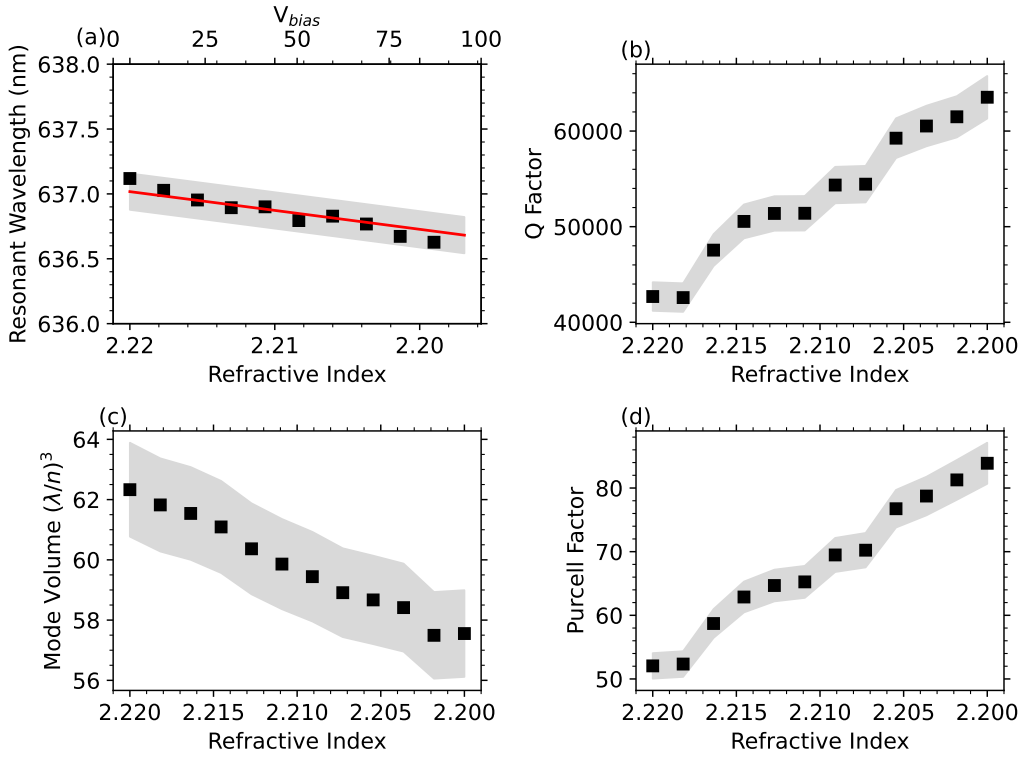

Figure 4.11: **Impact of SBN tuning on cavity figures of merit:** With the application of an electric field the SBN refractive index decreases linearly. This induces a linear blue shifting of the resonant wavelength (a). During SBN tuning, both the Purcell factor (b) and quality factor (d) increases. This is due to the corresponding decrease in mode volume (c).

In addition to the potential impact on the centre wavelength, the effect of the tuning layer on cavity quality factor, Purcell factor, and mode volume are also studied by FDTD simulation. As the cavity resonance is tuned, the Purcell factor is actually substantially improved, 52.26 to 87.14 (Figure 4.11a) due to the reduced mode volume (Figure 4.11b) induced by the optical path length modification dur-

ing tuning. Correspondingly, the cavity quality factor is dramatically enhanced from 42883 to 65461. These results strongly indicate that the cavity resonance mode can be readily tuned in practice when bonding a strong electro-optic material between the diamond and featured mirror, with little degradation to the cavity figures of merit. The simulated FDTD results align well with expected analytic solutions, and therefore provide a strong motivation for pursuing this approach as a cavity tuning method.

4.4.5 Modelling Real World Parameters in FDTD

The true power of FDTD simulation lies in its capacity to model the impact of real-world material properties, such as surface roughness, dispersion, and absorption. Throughout this thesis, each constituent element of the cavity device will be characterised experimentally, and those experimental properties will be provided to the FDTD model to build an understanding of each material's impact on cavity performance. Here we brioefly introduce how surface roughness and material optical properties are provided to an FDTD simulation.

4.4.5.1 Modelling Surface Roughness

The impact of a rough layer on the quality factor would be to provide a path for scattering, which increases round-trip loss and reduces quality factor, since Q is limited by round-trip loss as $Q{=}\frac{2\pi nL}{\lambda L_{RT}}$, and therefore the scattering losses S are proportional to $S \propto \left(\frac{4\pi\sigma}{\lambda}\right)^2$. With physical surface roughness data acquired, one could in principal load the acquired dataset as a material directly into FDTD simulation. However, this is not an optimal approach, since the material resolution may not align well with the capabilities of FDTD. It is better to create an artificially rough surface layer with boundaries informed by the surface roughness measurements. This can be created by constructing the correlation function of the

Hurst exponent:

$$H = \mathbb{E}\left[\frac{R(n)}{S(n)}\right] = Cn^H \tag{4.95}$$

This is defined as $n \to \infty$, where n is the range of observations of the dataset; $R(n)$ is the range of the first n cumulative deviations from the mean; $S(n)$ is the series of the first n deviations; and C is a constant parameter. The surface roughness can be simulated by creating a matrix of uniform random numbers in k space, removing high frequency components, and then converting back to real space. The parameters of the correlation function of the Hurst exponent are randomly sampled in this way, where:

$$\langle H(r)H(r+\delta)\rangle = \sigma^2 e^{-\left(\frac{\delta}{l_c}\right)^2} \tag{4.96}$$

....where H is the Hurst exponent; δ is a positional variation parameter; σ is the RMS roughness; and L_c. Based on the measured surface roughness of the SBN, an artificially rough layer is created, and then fed into the FDTD simulation. Once this layer is defined, it can be added to the FDTD simulation as a rough layer with either ideal or modelled optical parameters.

When simulating the rough layer with a finite difference solver, first an artificially rough layer is created from the above corellation function, and an ordinary structure with a rough top layer is created. To capture the optical impact of the roughness, it is crucial to set an appropriate mesh size. Since the smallest avergae surface roughness expected is around 700 pm, the mesh should reflect this. However, meshing the entire structure with such a fine mesh would be computationally intractavble. Instead, an extra mesh with much greater refinement can be added to cover only the top rough layer. Meanwhile, a coarser mesh can still be applied to

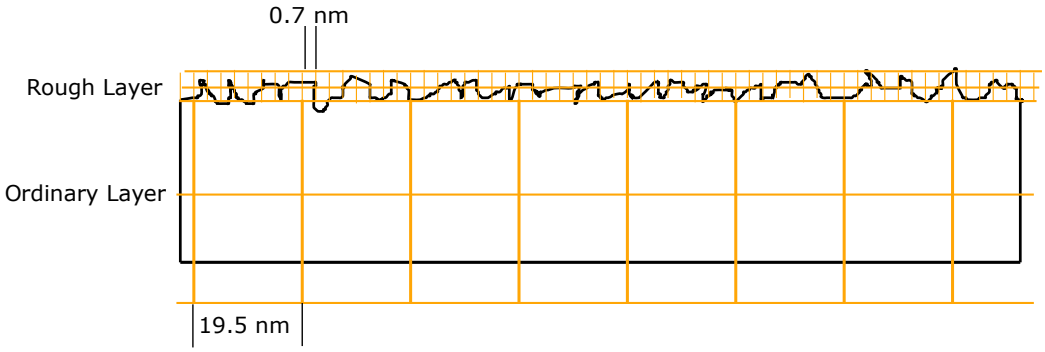

Figure 4.12: **Refined meshing for surface roughness:** For the majority of the simulated structure, a fairly coarse mesh is suitable enough to capture optical performance. However, to capture the effects of surface roughness, a much finer mesh in the rough layer is needed.

the rest of the structure (Figure 4.12).

4.4.5.2 Modelling Optical Properties

If a materials refractive index and extinction coefficient (n and k) data is experimentally known, this set of data can be used to build a material model using any dielectric model of choice. For the practical application of the cavity, only the transparrent region of the SBN films is of concern, and therefore the Lorentz model confined to the bandwidth of interest is sufficient to capture the dispersive and absorptive behaviour of this material. In Chapter 5, experimental data for the DBR coatings is also added as a material property in FDTD simulation.

4.5 Chapter Summary

In this chapter, we explored the theoretical principles underlying the development of efficient spin-photon quantum network interfaces, focusing on enhancing photon emission efficiency through resonant optical microcavities. We detailed the challenges posed by quantum decoherence and photon indistinguishability, em-

phasizing the role of Purcell enhancement in increasing zero-phonon line (ZPL) emissions for entanglement applications. The analytic tools of transfer matrix analysis and Hermite-Gaussian modes were presented alongside the numerical technique of finite-difference time-domain (FDTD) simulation to evaluate cavity performance. Additionally, the electro-optic properties of Strontium Barium Niobate (SBN) were examined, with a focus on its tensorial behavior under applied electric fields and its integration as a tuning mechanism for microcavities. Together, this provides an analytic foundation for the coming chapters in this thesis.

5 | Microcavity Fabrication

In this chapter, the fabrication of monolithic microcavities in diamond by focussed ion beam milling is detailed, alongside optical characterisations of the cavity following DBR mirror coating. The microcavities were fabricated into 10 μm thick, single crystal, electronic grade diamond membranes and coated with DBR mirrors for prototyping. Their optical properties were measured using a purpose built transmission microscope, and the optical response was compared to analytic and numeric models. The cavity arrays exhibited strong and repeatable cavity longitudinal cavity modes with accompanying transverse modes. The measured cavity finesse was only around 10% what was expected, but this is explained following a thorough characterisation of the DBR mirror coatings: high absorption in the TiO_2 DBR layer negatively impacted the mirror reflectivity and therefore the cavity finesse. Therefore with better coatings, it is expected that the cavities should readily reach their full potential.

5.1 Cavity Formation by Focussed Ion Beam Milling

A number of different approaches of fabricating convex/concave cavity features for Fabry-Pèrot structures are well established in literature, including nanoimprint lithography [236, 237], polymer reflow [238–242], and focussed ion beam (FIB) milling [243]. The latter is a well developed process in the photonic nanomaterials group (PNG) at Oxford University, and therefore is the primary emphasis of this thesis. In this approach, a beam of Ga^+ ions is emitted and accelerated from a cone source focussed onto the sample by electrostatic lenses. The high energy of the incident ions causes a small number of atoms from the diamond to be sputtered off the surface. In this work, the Zeiss Crossbeam 540 Analytic SEM/FIB is em-

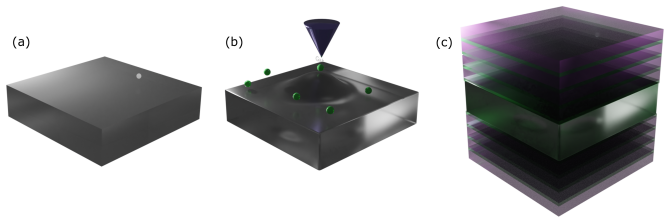

Figure 5.1: **Cavity fabrication procedure.**(a) A 10 μm thick diamond membrane is prepared for milling by cleaning, sticking to an SEM stub, and coating; (b) The diamond surface is bombarded with Ga^+ ions using a focused ion beam, to form convex cavity features; (c) The featured diamond is coated each side with DBR mirrors, made of SiO_2 and TiO_2 layers grown by ion assisted E-beam evaporation.

ployed for milling. To mill away the diamond in such a way as to produce a cavity feature, a predefined map of FIB dwell times at each location is programmed into the FIB, in a structure known as a 'stream file'.

5.1.1 Stream File Development

The stream file is a set of coordinates governing the milling procedure. It contains three columns of data - x- and y- positional coordinates, and a z coordinate which relates to the FIB dose, i.e. the amount time the FIB stays at each x-y position to deliver a desired charge. The intended field-of-view of the FIB during the milling of each cavity is discretised into x and y coordinates, and the intended depth of the features is initially designed as a positional coordinate z, which will later be translated into a charge dose.

To design the cavity geometry, it is sufficient to define the z-coordinates from a cross-section of the cavity (Figure 5.2) and transform the cartesian grid into polar coordinates. To begin, the width of the cavity feature W_{feat} is related to a desired radius of curvature r and feature depth d by $W_{feat} = 2\sqrt{r \cdot d - d^2}$. The total

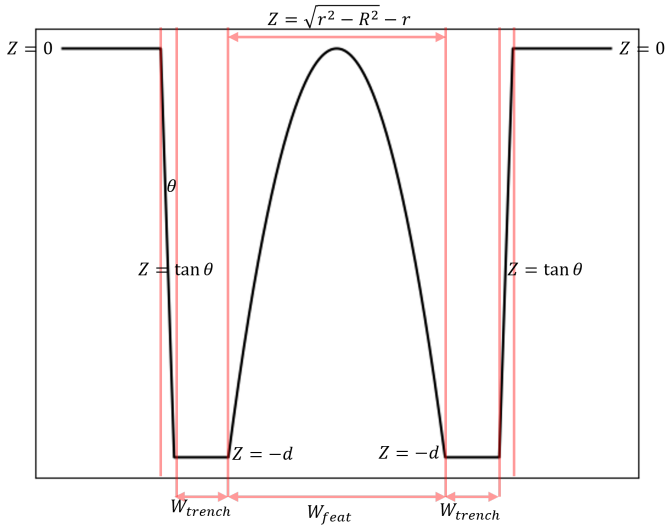

Figure 5.2: **Cross-section of cavity design feature.** The desired geometry is determined analytically and a mesh grid of geometric values is determined computationally, ready to be programmed into the FIB.

width of the cavity W_{cavity}, is defined to include space for a 'trench' region at the minimum of the feature depth, and is set to be $W_{cavity} = 1.5 \cdot W_{feat}$. Therefore, the width of the trench feature W_{trench} is $W_{trench} = .5(W_{cavity} - W_{feat})$.

The 3D cartesian grid is first defined by creating an array of x- and y- coordinates between some minimum (xy_{min}) and maximum (xy_{max}) values, defined as:

$$-\left(\frac{W_{feat}}{2} + W_{trench}\right) - c \leq xy \leq \left(\frac{W_{feat}}{2} + W_{trench}\right) + c \qquad (5.1)$$

.... where c is some constant to account for the region outside of the cavity area. A linearly spaced array of dimension n of x- and y- coordinates is defined between xy_{min} and xy_{max}. Therefore the x and y arrays are defined as:

$$x = \left[xy_{min}, xy_{min} + \frac{xy_{max} - xy_{min}}{n-1}, xy_{min} + 2 \cdot \frac{xy_{max} - xy_{min}}{n-1}, \cdots, xy_{max} \right] = [x_1, x_2, \cdots, x_n] \tag{5.2}$$

$$y = \left[xy_{min}, xy_{min} + \frac{xy_{max} - xy_{min}}{n-1}, xy_{min} + 2 \cdot \frac{xy_{max} - xy_{min}}{n-1}, \cdots, xy_{max} \right] = [y_1, y_2, \cdots, y_n] \tag{5.3}$$

An $n \times n$ grid of coordinates for x and y is then filled with coordinate values, such that:

$$X = \begin{bmatrix} x_1 & x_2 & \cdots & x_n \\ x_1 & x_2 & \cdots & x_n \\ \vdots & \vdots & \ddots & \vdots \\ x_1 & x_2 & \cdots & x_n \end{bmatrix} \qquad Y = \begin{bmatrix} y_1 & y_2 & \cdots & y_n \\ y_1 & y_2 & \cdots & y_n \\ \vdots & \vdots & \ddots & \vdots \\ y_1 & y_2 & \cdots & y_n \end{bmatrix}$$

This cartesian space is then converted to a polar coordinate system defined by a grid $R{=}\sqrt{X^2 + Y^2}$. The Z grid of coordinates relates the depth of the cavity feature at each radial point in R. The value of each element in the grid of Z coordinates dependant on position R can be seen in the cross sectional profile of a cavity design in Figure 5.2. Note the sloped path between $Z{=}-d$ and $Z{=}0$: this is to assist any etching which may be done on the cavity feature, to prevent over or under etching in the corners.

5.1.1.1 Relating Cavity Depth to FIB Dose

To relate the Z-coordinates to the physical ablation achievable by the FIB, the intended milled depth at each point needs to be related to the amount of material which can be sputtered away. The volume of the grid in the z-axis V_z is defined by multiplying each element $z \in Z$ weighted by the grid mesh discretisation factor δ_{xy}=$x_1 - x_0$:

$$V_z^i = z_i \cdot (\delta xy)^2 \tag{5.4}$$

The amount of charge required at each grid point is determined by the sputter rate R of the FIB, i.e. the rate at which material which is sputtered from the sample surface:

$$q_z = V_z \cdot R = V_z \cdot \frac{M}{\rho N_A e^-} \cdot S j_p \tag{5.5}$$

The sputter rate is determined by the molar weight M of the target (kg/mol),the density ρ of diamond (kg/m^3), the electron charge e^-=1.6×10^{-19} C, the sputtering yield S (atoms/ion), which is an empirically determined factor for each FIB and sample material, and the primary ion current density j_p (A/m^2). In equation 5.5, $N_A = 6.022 \times 10^{-23}$ atoms per mole is the Avogadro number. With this the dwell time required at each grid point for the FIB to deliver the required dose for a given beam current I_{beam} is:

$$t_{dwell} = \frac{q_z}{I_{beam}} \tag{5.6}$$

5.1.1.2 Redeposition Mitigation

Redeposition is a common problem encountered during FIB milling. This is a problem where material which has been sputtered away from the surface can be redeposited onto or indeed into the surface, which distorts the resulting feature from the designed pattern. To mitigate this, the combined matrix of coordinates and dwell times were randomised by permuting the 3-dimensional grid so that the ion beam randomly sampled discrete regions of the defined grid.

5.1.2 Milling Parameter Optimisation

The sputter rate of the diamond membrane when irradiated by the FIB needs to be determined in order to correctly define the stream file. To determine this, the sputter yield of the FIB must be found. A single crystal diamond sample was ablated under the FIB for a varying incident beam current. In the Zeiss Crossbeam-540, the FIB acceleration voltage is fixed at 30 kV, and therefore the beam current was varied instead of the more common approach of varying the acceleration voltage. The milling beam diameter of the focussed ion beam is a fixed quantity, at 10 nm, and the resolution of the beam positioning for the Zeiss Crossbeam 540 is 0.1 nm. After irradiation, the depth and lateral dimensions of the milled rectangular trenches were determined by optical profilometry, and the sputter yield S was calculated as [244]:

$$S = \frac{l_1 l_2 z e}{N_i I t} \tag{5.7}$$

....where l_1 and l_2 are the lengths and widths of the rectangle, z is the depth of the trench, $e = 1.602 \times 10^{-19}$ C is the electron charge, I is the incident beam current, and t is the total sputter time. N_i is the the average atomic volume, and

for diamond, $N_i = 5.67 \times 10^{-24}$ cm^3/at [245].

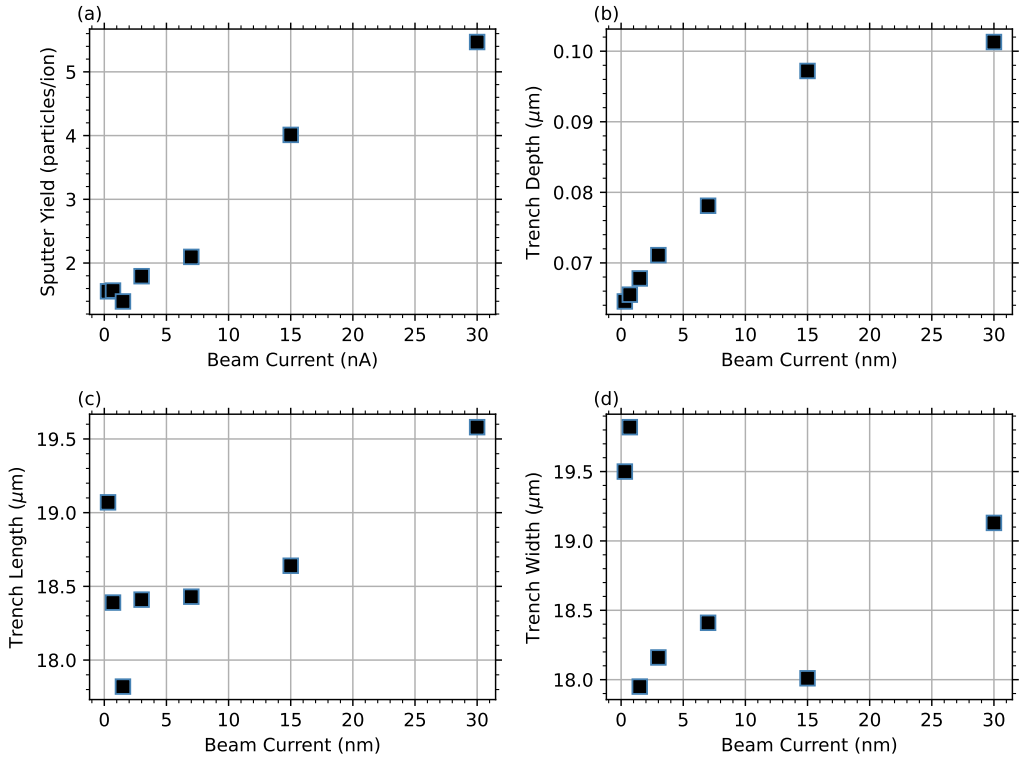

Figure 5.3: **Impact of FIB beam current on diamond sputtering.** (a) Sputter yield of diamond irradiated with Ga^+ ions from a Zeiss Crossbeam 514 FIB at 30keV, with varying incident beam current. (b) depth of milled trench; (c) length of milled trench; (d) width of milled trench

Figure 5.3(a) displays the measured sputter yield of diamond monotonically increasing with respect to the applied beam current. The length and width of the trench (Figure 5.3(b) and (c) respectively) were both intended to be 18 μm, and broadly sustain this across each beam current. On the other hand, the trench depth increases proportionally to the incident beam beam current before plateauing after 15 nA, since higher beam currents appear to cause damage to the diamond surface rather than milling much deeper. Therefore, a beam current of 7 nA is chosen for the FIB milling of the cavities, with a sputter yield of 2.2 particles/ion.

5.2 $10\ \mu m$ Diamond Membrane Surface Roughness

Prior to milling, the surface roughness of the 10μm HiQuTe diamond membranes were characterised by optical profilometry. The quality of the diamond surface is very important for the successful adhesion of DBR mirrors, since thin-films tend not to bond well to rough surfaces. A rough surface may also inhibit the cavity optical response by adding scattering pathways for light.

5.2.1 Membrane Surface Profile

The HiQuTe membranes are formed by polishing CVD grown diamond plates from an initial thickness of several hundred μm down to 10μm, using a polishing wheel infused with a combination of olive oil and diamond dust (a method known as scaif polishing). This results in a naturally rough surface due to polishing damage leaving sp-2 carbon on the surface, and creating sub-surface damage of typically a few μm [246]. Surface level sp-2 carbon can be chemical etched away using a tri-acid boiling method [247], whilst sub-surface damage can be plasma etched by reactive ion species [246, 248, 249]. Figure 5.4 shows the typical surface of the HiQuTe membranes, obtained by a Microxam-800 surface mapping profilometer in Phase Scanning Interference (PSI) mode, with a $100X$ objective lens. The diagonal striations are the sp-2 carbon caused by the polishing process. Alongside this, there is evident debris among all the diamond surfaces, since polishing is a dirty process, and the manufacturers do not clean the final membrane product. Cleaning membranes is very challenging due to handling, but can be achieved by a piranha acid process.

Nonetheless, in regions without substantial debris, the RMS roughness (Rsq) of the membranes is sub-nm (Table 5.1), which is more than sufficiently smooth for

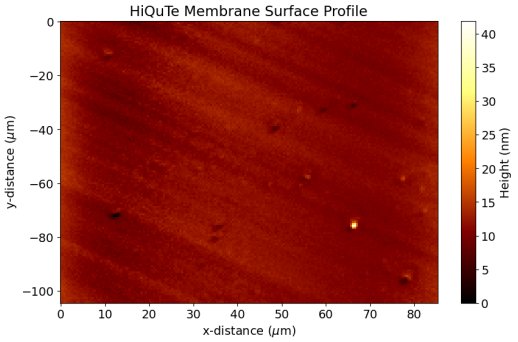

Figure 5.4: **Surface profile of 10 μm diamond membranes, obtained via optical profilometry.** The diamond membranes are initially very dirty due to residue from the polishing process. Therefore, surface defects remain. However, the diamond itself shows sub-nm smoothness.

device integration and cavity performance.

Table 5.1: **Statistical information of diamond membrane surface obtained from optical profilometry.**

Average Value (nm)	22.93
RMS Roughness (Sq) (nm)	0.773
RMS (grain-wise) (nm)	0.773
Mean Roughness (Sa) (nm)	0.622
Skew (Ssk) (nm)	0.1466
Excess Kurtosis (nm)	-0.1324

5.2.2 Membrane Mounting and Milling

The membrane was mounted by hand using a pick-and-place vacuum tool onto a 100 μm thick fused-silica cover slip mount which contained a laser machined hole providing for optical access both sides of the membrane. The membrane was secured onto the cover slip with nail varnish, and mounted onto a scanning electron microscope (SEM) stub with silver dag (Figure 5.5(a)). To prevent sample charging under the SEM, the membrane was sputter coated with a 4 nm layer of chromium which was chemically etched away after milling.

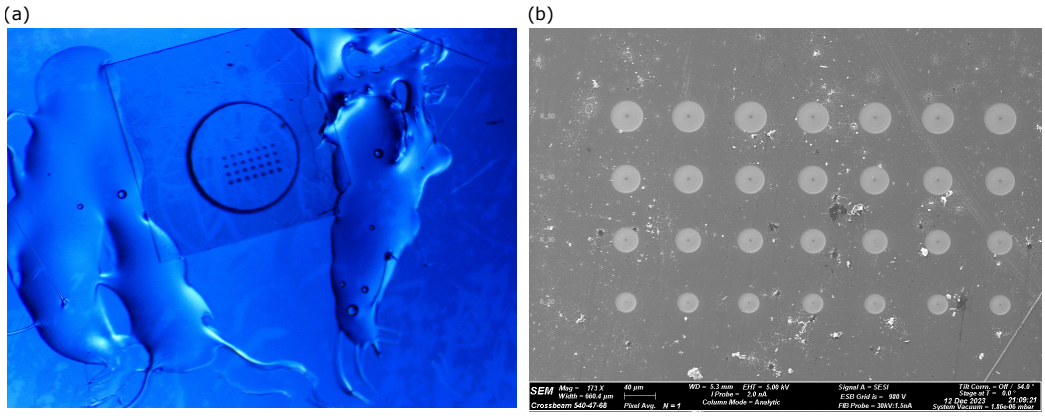

Figure 5.5: **Cavity formation in 30μm membrane** (a) Widefield image of mounted membrane with cavity features; (b) SEM image of microcavity array FIB milled into diamond membrane.

Arrays of cavities of radii of curvatures of 10μm, 20μm, 30μm, 40μm, 50μm, 55μm, 95μm, 120μm, 250μm, and 310μm were milled into 1 mm^2, 10 μm thick electronic grade diamond membrane provided by HiQuTe-Diamond (Figure 5.5(b)).

5.2.3 Cavity Physical Characterisation

Figure 5.6(a) shows an SEM image of a cavity feature formed in a 10μm membrane by FIB milling, with a beam current of 7 nA and 10 repeated milling doses. There is an evident steep trenching effect as desired, and a convex feature in the centre of the cavity structure. To assess the surface roughness of the cavity features, each cavity was analysed using a Microxam-800 surface mapping profilometer. A 3D profile of the cavity feature in (a) can be seen in Figure 5.6(b), and a cross section of this profile is plotted in Figure 5.6(c).The intended depth of the cavity features is around 325 nm.

The surface roughness is found by fitting a polynomial function to the cross-sectional profile, and assessing the root mean square deviation from the fitted line. The results for cavity features etched between 50μm to 300μm are displayed

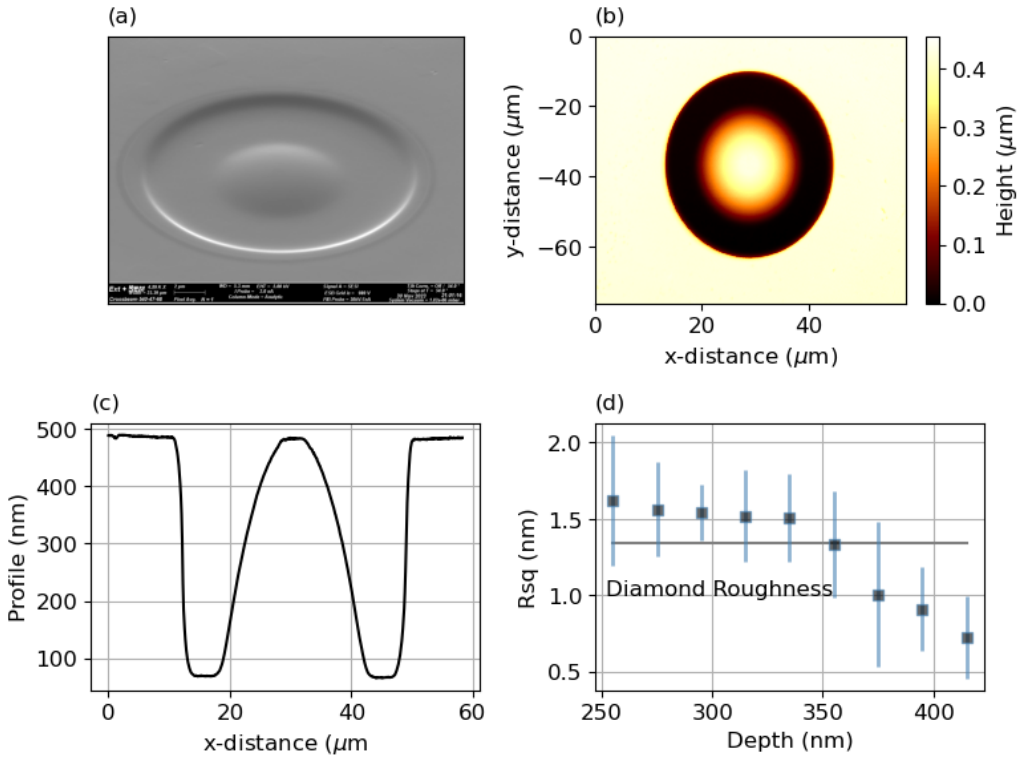

Figure 5.6: **Physical characterisation of cavity features:** (a) SEM image of FIB milled cavity feature in diamond membrane; (b) 3D optical profile of cavity feature; (c) cross-sectional cavity profile; (d) the polishing effect of the FIB can be observed as cavity radius of curvature increases

in Figure 5.6(d). Importantly, achieving sub-nanometer cavity surface roughness does not require a super-polished diamond membrane a-priori. The FIB can provide a polishing effect itself due to the strong dependance of the sputter rate with the angle of incidence of the beam [250–252]. Initially, the surface roughness of the smaller radii features exceeds the natural diamond roughness due to inhomogeneous sputtering of the deposited Cr layer on the diamond surface. However, above 150 nm the cavity features become much smoother than the original membrane roughness, approaching an average roughness of around 500 pm.

5.2.4 DBR Coating

After the cavity features were milled, the diamond membranes were coated in DBR layers consisting of SiO_2 for the low-index layer and TiO_2 for the high index layer. The coatings were deposited by the Thin-Film Facility at Oxford University, by argon ion beam assisted (IBAD) electron beam deposition, in an Edwards E500 bell jar system under vacuum. 13 layers were deposited on each side of the membrane, with the TiO_2 being both the interface layer with the diamond, and the top layer to air, such that the layer stack was [TiO_2, SiO_2, TiO_2, SiO_2, TiO_2, SiO_2, TiO_2, SiO_2, TiO_2, SiO_2, TiO_2, SiO_2, TiO_2]. The deposition system growth parameters for the TiO_2 and SiO_2 layers are detailed in Table 5.2

Table 5.2: **Table of parameters for DBR growth in IBAD E-Beam deposition system.**

Layer	Current	IBAD Pressure	Chamber Pressure	Rate
TiO_2	120 mA	2.5×10^{-4} mbar	1.6×10^{-4} mbar	0.1-0.5 nm/s
SiO_2	40 mA	2.5×10^{-4} mbar	1.6×10^{-4} mbar	0.1-0.5 nm/s

In principle, this should result in a DBR reflectivity of 99.80% and transmittivity of 0.2% at 637 nm. Of course, a higher reflectivity is more desirable, but with each deposited DBR layer, any imperfections in purity and absorption compound, and therefore negatively affect the final reflectivity. A highly optimised coating process is therefore required for very high quality cavities, which must be outsourced. It is therefore useful to work with lower quality coatings for initial prototyping.

5.2.5 Optical Characterisation

To investigate the cavity response and mode structure, a purpose-built transmission microscope was built, as detailed in Section 3.6 (Figure 3.4). The optical response of the cavity features is shown in Figure 5.8(a) cavity radii of curvature

varying between 10 μm to 310 μm. The strong dominant peaks in the spectra are the longitudinal mode of the cavities, and it is interesting to note that the centre frequency of each peak is reasonably stable and impervious to the changing radius of curvature, implying a fairly stable fabrication procedure across each cavity.

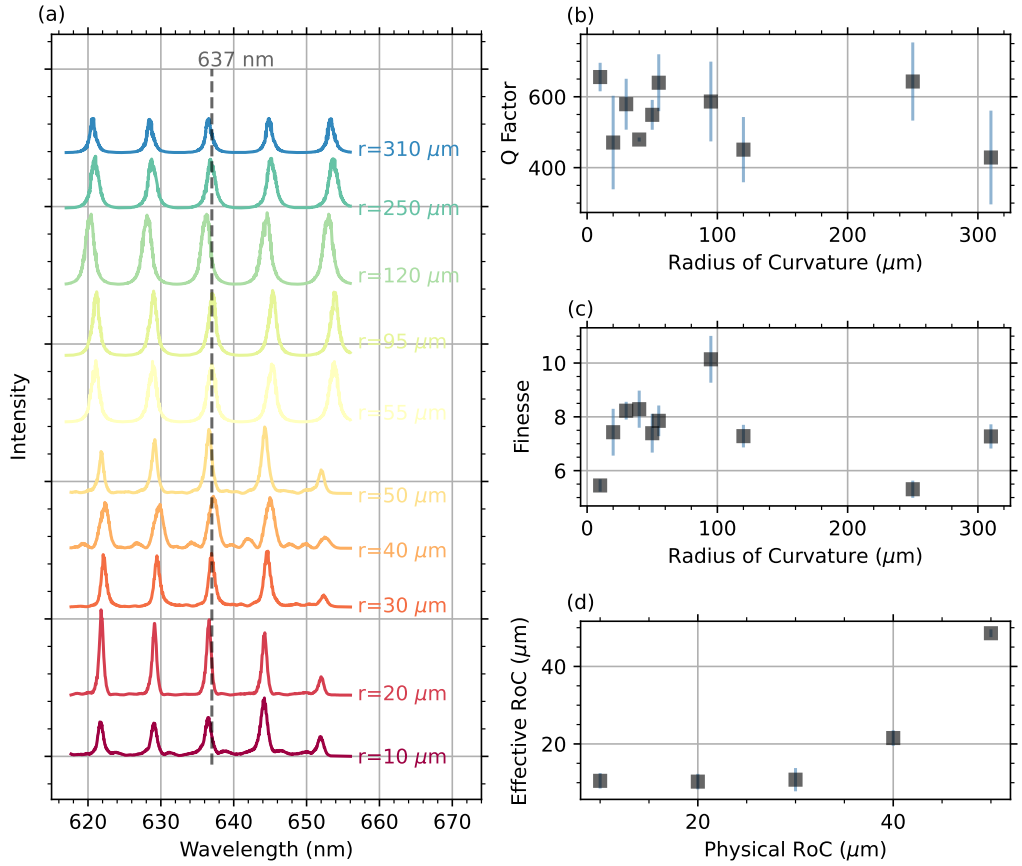

Figure 5.7: **Optical response of optical microcavities of radii of curvature between 10 - 310 μm milled into 10 μm diamond membranes:** (a) Sample optical spectra of each cavity radii of curvature; (b) Extracted average quality factor; (c) Extracted average finesse; (d) Effective radius of curvature, determined by evaluating difference between longitudinal first transverse mode positions.

The measured average quality factor Q for each cavity radius of curvature is shown in Figure 5.8(b). This is found by taking the ratio of the peak centre frequency ω_0 to the full-width half-maximum (FWHM) of the peak $\delta\omega$, i.e. $Q{=}\omega_0/\delta\omega$.

There is no apparent strong dependancy between the radius of curvature and the measured quality factor, which suggests that the Q-Factor is dominated by the cavity finesse, which itself is dominated by the reflectivity of the mirrors on each side of the diamond.

The lower than expected Q-Factor corresponds with the measured cavity finesse, which is found by taking the ratio between the wavelength FWHM of each longitudinal peak $\delta\lambda$ and the free-spectral range FSR, i.e. $F{=}\delta\lambda/FSR$. The finesse is determined by the reflectivity of the mirrors and absorption processes. Assuming no absorption, the finesse calculated as $F{=}\frac{\pi}{\sqrt{1-R1R2}}$. The thin film coatings deposited here were designed to possess a reflectivity of 97%, and therefore the expected finesse of the cavity is $F{=}105$. Unfortunately, for these cavities the measured finesse is found to be around only 10% of what was designed for the cavity geometry and DBR coating, at around $F{=}10$. The cavity Q-factor depends on the finesse, since $Q{=}F(q+q_m)$, and hence the Q-Factor is correspondingly diminished. The reason for this lower than expected finesse is investigated in detail in Section 5.3.

Despite the lower than expected finesse, a mode structure containing both longitudinal and transverse modes are visible in some of the cavity spectra, albeit vaguely. In Figure 5.8(a), the mode structure of a 55μm radius of curvature cavity is shown. The dominant peaks are the clearly visible longitudinal Hermite-Gaussian modes, corresponding to the simulated $HG00$ modes in Figure 5.8(b). A number of features are evident in the remaining spectra. By fitting the resonance condition for a Hermite-Gaussian mode (equation 4.21) to this spectra, as detailed in Section 4, the features observed in the spectra overlap precisely with the transverse modes $HG01$, $HG11$, and $HG21$.

Each cavity radii of curvature appears to admit these HG modes, and therefore

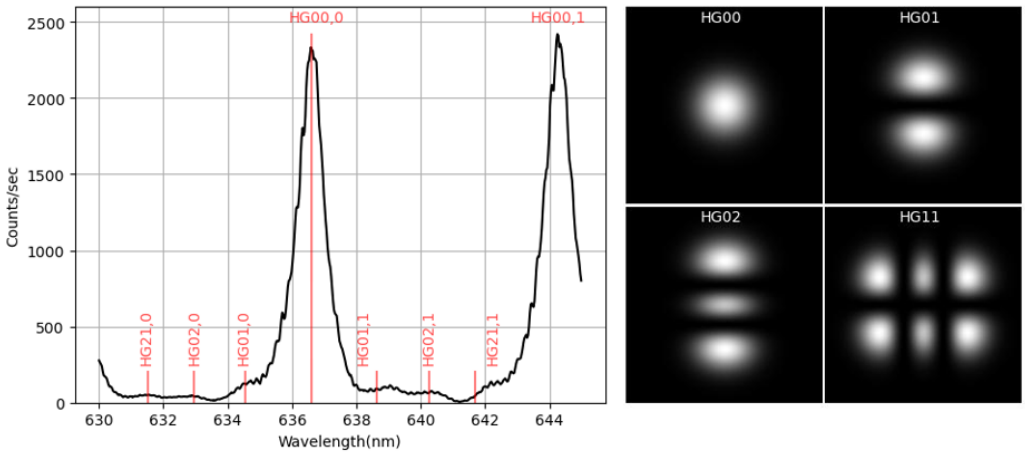

Figure 5.8: **Cavity mode structure:** (a) Observed cavity modes for 50μm radius cavity, showing strong longitudinal modes and weak transverse modes; (b) simulated profiles of Hermite-Gaussian modes corresponding to weakly observed modes.

it is possible to infer the effective radius of curvature R_{eff} for each cavity (Figure 5.7(d)). R_{eff} is found by taking the ratio between the physical length L of the cavity (10 μm in this case) and the beam curvature term containing the difference in resonant lengths between the longitudinal and transverse mode, as given in Equation 4.22. In Figure 5.7(d), the effective radius of curvature is slightly smaller than the physical radius, although it does appear to steeply increase with larger physical radii. At the smallest physical radius of curvature of 10μm, the effective radius is 10.135μm, and the effective radius seems to approach this value as a lower limit. Indeed the cavity stability criterion places a lower bound on the effective radius of curvature for light to be confined within the cavity, as detailed in Section 4.

The centre wavelength of each cavity is stable around a region close to the design resonance wavelength of 637 nm (Figure 5.9), implying a uniform membrane thickness, uniform DBR deposition, and a stable FIB milling procedure. The average centre wavelength is slightly lower than the design wavelength, at 636.65

nm, but this can be easily compensated in further fabrication iterations.

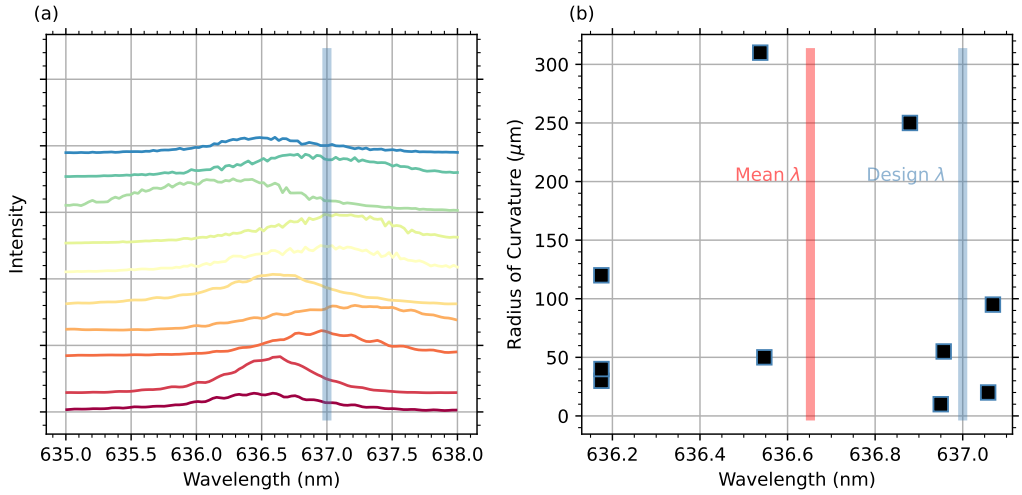

Figure 5.9: **Variation in cavity wavelength for different radii of curvature cavities:** (a) Cavity spectra; (b) resonant wavelength. For each radius of curvature cavity, the measured centre wavelength is quite stable, varying within 0.8 nm.

5.3 Investigation of DBR Mirror Performance

The discrepancy between the designed cavity finesse and the measured value can be attributed to the quality of the DBR mirror coatings. The process of depositing DBR coatings with high reflectivity and low absorption is delicate and requires specialised deposition systems. Any deviation in the deposition process can significantly impact the quality of the DBR mirrors. As a result, such coatings are typically applied by specialised industrial partners, such as Layertec or Manx Precision Optics. In this study, the mirrors were deposited by the Oxford University Thin-Film Facility.

Using the transfer matrix approach described in Section 4.1.5, we can estimate the expected transmission and reflection spectra of the DBR coatings based on the number of layers deposited on the planar and featured sides of the diamond.

For the 13-layer structure fabricated on each side of the diamond, the expected minimum transmission coefficient is 0.0002, the maximum reflection coefficient is 0.97, and the stop-bandwidth is 185 nm (Figure 5.10).

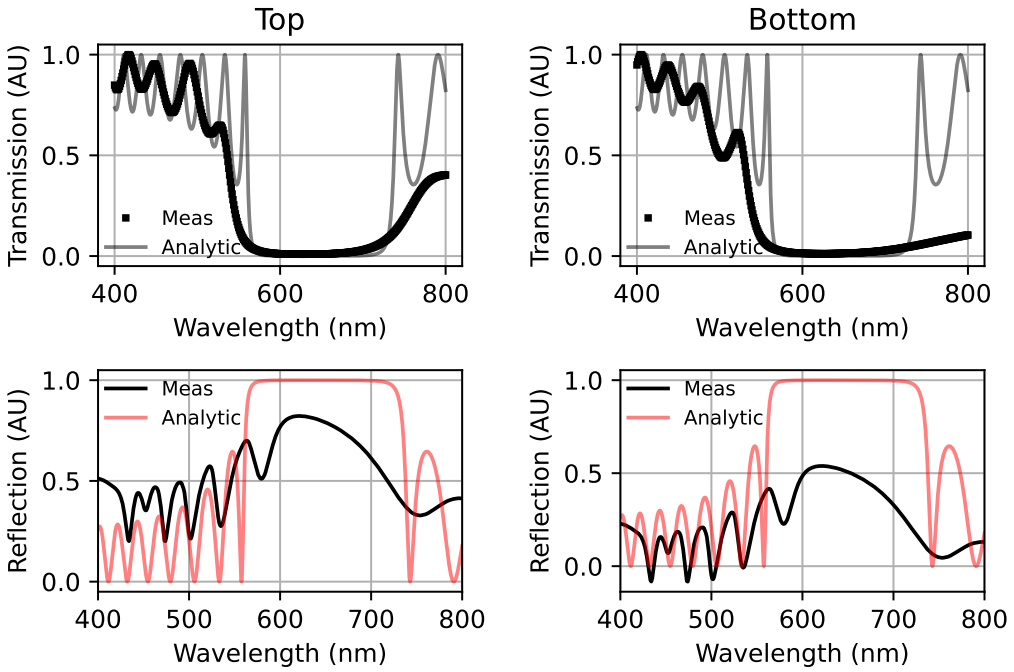

Figure 5.10: **Reflection and transmission profiles of the DBR coatings on the top and bottom sides of the HiQuTe diamond membrane.** Whilst transmission through the DBR stack is close to what is expected, the DBR reflection data differs significantly, explaining the diminished cavity performance.

The actual transmission and reflection spectra were measured using a spectrophotometer on SiO_2 test pieces placed in the deposition chamber. These measured spectra were compared with the expected spectra, as shown in Figure 5.10. Prior to acquiring the transmission and reflection date for these samples, calibration transmission and reflection spectra were acquired. First, 100% light transmission was acquired by allowing the spectrophotometer light source to irradiate the detector with no sample in place. Then 0% light transmission was acquired by placing a 'black standard' (a black material which fully absorbs the transmitted

light) in the optical path, and acquiring data across the entire spectral range. The sample transmission data was then found by placing the DBR sample in the beam path. To calibrate the reflection data, 100% reflection was found by placing a 'white standard' (a white material which is highly reflective) in the reflected beam path and measuring the reflected light. The 0% reflection was found by placing no object in the beam path and acquiring data across the entire spectral range. The sample reflection data was then acquired by placing the DBR mirrors in the sample reflected light path.

The transmission spectra for both the top and bottom DBR mirrors match closely with the theoretical expectations in terms of their absolute values in the stopband, although deviate at the stopband edge and passband, possibly due to dispersion effects not being accounted for in the modelling. However, the reflection spectra show significant deviation from the ideal case in both the stopband and passband. This result was consistently observed using both an ellipsometer and a reflection probe. While the transmission coefficient aligns with expectations, the reflection coefficient differs notably. At 637 nm, the reflection coefficients for the top and bottom mirrors are measured to be $R_{\text{top}} = 0.8225$ and R_{bottom}=0.5389, respectively.

The reduced cavity finesse can now be explained more clearly, given that the finesse is related to the reflection coefficients by the formula $F=\frac{\pi}{1-\sqrt{R_{\text{top}}R_{\text{bottom}}}}$. With the measured reflection coefficients, the calculated finesse is found to be F=9.399, which is in good agreement with the measured cavity finesse.

Table 5.3: **Measured Transmission and Reflection Coefficients for the Top and Bottom DBR Coatings of the Optical Microcavity at 637 nm.**

	Expected	Top	Bottom
Transmission	0.00021	0.00879	0.01181
Reflection	0.9700	0.8225	0.5389

In addition to the significant deviation in the magnitude of the reflection spectra, there is no clear stopband, and its centre appears to be blue-shifted. Both the attenuation and blue-shifting of the stopband suggest that absorption and thickness inhomogeneities in the mirrors may be contributing to the reduced reflection performance. These factors can be quantified and incorporated into the transfer matrix model for further analysis.

The homogeneity of the mirror thickness can be assessed using cross-sectional SEM imaging of the DBR mirrors. The DBR test sample was mounted in a Zeiss Crossbeam 540 SEM/FIB, and a trench was milled into the mirror using FIB. The trench was initially milled with a beam current of 1.5 nA for rough milling, and then polished at a lower beam current of 300 pA to improve imaging resolution. The layer stack is shown in Figure 5.11(a). While the TiO_2 layer appears fairly uniform in thickness, the SiO_2 layer shows significant variation. This variation could account for the observed blue-shifting of the reflection stopband but would likely have only a minor impact on the intensity reduction.

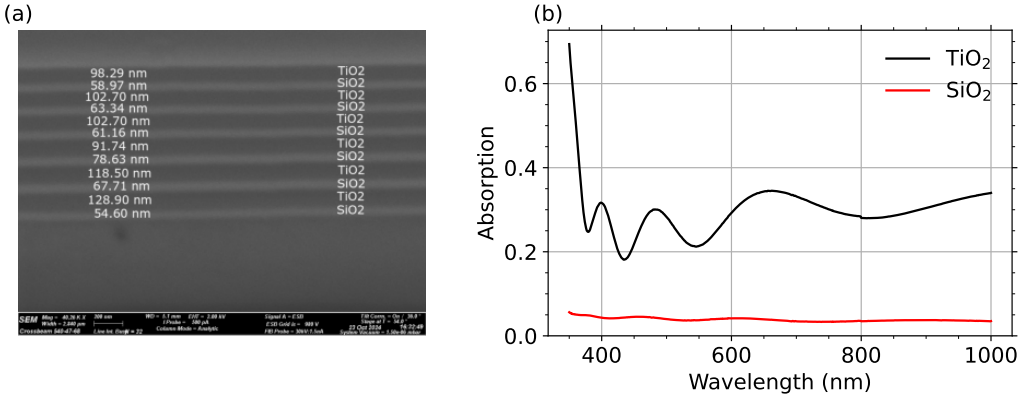

Figure 5.11: **(a) Thickness and (b) absorption of the TiO_2 and SiO_2 DBR mirror layers, measured by spectrophotometry.** The thickness variation of the SiO_2 is significantly larger than that of the TiO_2 layer. However, the absorption of the TiO_2 layer is substantial, and the dominating cause of loss.

The absorption spectra for the TiO_2 and SiO_2 layers were measured using separate

test pieces of each material. The absorption spectra, shown in Figure 5.11(b), reveal that while SiO_2 exhibits low absorption, TiO_2 is highly absorbent. It is well known that TiO_2 can lose oxygen during deposition, which is often desirable for creating oxygen vacancies [253, 254]. In the case of e-beam evaporation, TiO_2 films may lose oxygen due to excessive deposition energy or re-sputtering effects. The argon plasma used during deposition could also contribute to oxygen vacancies, particularly when impurities such as carbon are present, which can form volatile compounds like CO_2. We hypothesize that the enhanced absorption in the TiO_2 layer may be due to carbon contamination in the deposition chamber, with some carbon atoms being incorporated into the TiO_2, thereby increasing its absorption. The measured absorption spectra are consistent with those of carbon-implanted TiO_2 films reported in [255].

By incorporating both the layer thicknesses and the absorption spectra into the transfer matrix model, we can account for the real-world imperfections in the DBR coatings. The absorption introduces a complex component to the refractive index of both TiO_2 and SiO_2 layers $n'=n+i\kappa$, as detailed in Section 4.1.6. Using the absorbance data obtained by spectrophotometry and the layer thicknesses from SEM, we can calculate the transmission and reflection spectra of the DBR coatings using the transfer matrix model with an absorption term. The predicted spectra are compared to the measured spectra in Figure 5.12.

By incorporating the measured thickness inhomogeneities and absorption properties into the transfer matrix model, the predicted spectra closely match the experimentally measured spectra in the photonic stopband. There are further deviations from the simulated spectra in the passband, likely caused by interdiffusion, where the refractive index gradually changes near interfaces due to diffusion or surface roughness, affecting performance outside the stop band more strongly. This is challenging to experimentally characterise and analytically simulate, and since the

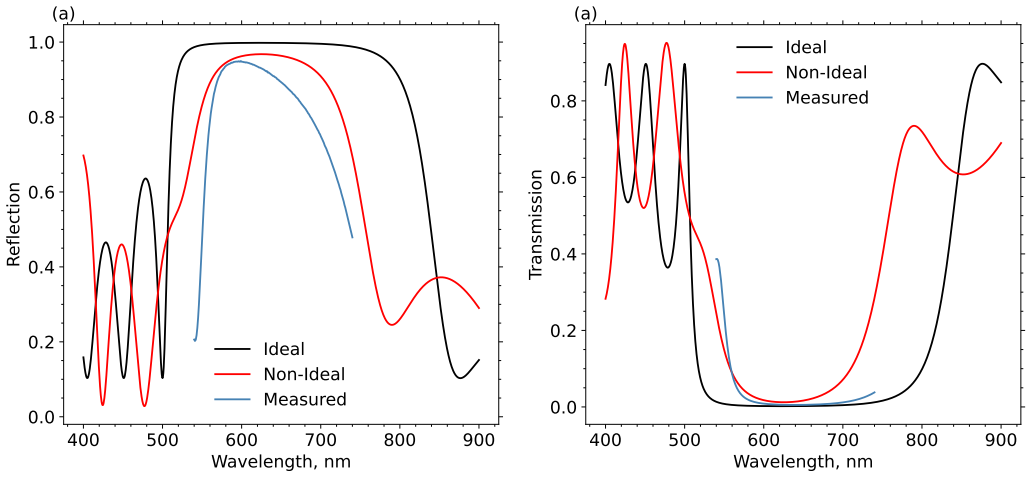

Figure 5.12: **Comparison between the expected and measured DBR reflection (a) and transmission (b) coefficients.** Incorporating the thickness variation of each layer and the absorption spectrum provides a much more detailed model of the DBR layers, and sheds light on the cause of diminished cavity performance.

breadth and height of the stopband is of primary interest, this effect is neglected in this analysis.

5.4 Feedback from FDTD Simulation

The physical parameters of the monolithic cavities were incorporated into an FDTD model in order to cross-validate the acquired spectra with what may be theoretically expected, and to gain valuable information about the expected Purcell enhancement and collection efficiency of each cavity geometry. These simulations were performed using the Lumerical FDTD software with *PyLumerical*, a substantive Python wrapper class developed by the author for creating the simulation and analysing the results [230]. To establish the simulation, the diamond is taken as an ideal, non-dispersive material of constant refractive index n=2.41. It is useful to compare between an ideal case for the DBR mirror coatings and the real-world impact of the measured thickness variations and absorption. Therefore

the DBR mirrors are considered initially in their ideal case, but subsequently the measured layer thicknesses and absorption are accounted for.

5.4.1 Cavity Electric Fields and Optical Spectra

The measured cavity fields of the 10μm HiQuTe membrane were compared with an FDTD model which incorporated the measured membrane thickness, average thickness variation of each DBR layer and the measured absorption coefficients. By placing a power monitor at the top of the cavity feature, the cavity mode profile can be extracted for each peak in the cavity spectrum (left hand side of Figure 5.13)

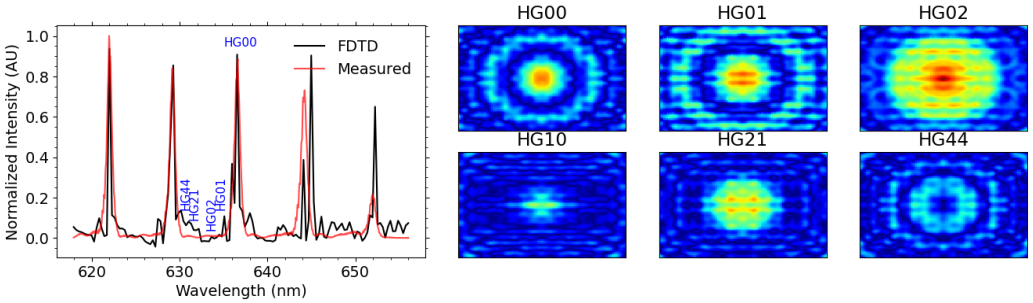

Figure 5.13: **Comparison of measured spectra vs FDTD**. On the left-hand side is a comparison between the measured cavity spectra and that simulated by FDTD methods. Aside this are the mode profiles for each FDTD peak.

A comparison of this model for the 90μm radius of curvature cavities is shown in Figure 5.13. Encouragingly, the simulated response overlaps very closely to that which was measured, indicating the completeness of the model, and therefore that the impact of each material has been well characterised for its impact on cavity performance. The peak data of the measured and the simulated cavity spectra were fit to a Lorentzian function, and the Q-factor, FSR, and finesse were compared. This comparison is shown in Table 5.4. It is clear that the simulated and measured figures of merit very closely match one another. Therefore it is legitimate to make

inferences on potential cavity enhancement based on this model.

Table 5.4: **Comparison between the figures of merit for measured and simulated cavities.**

	Measured	FDTD
Q	866	914
FSR	7.426	7.270
$\delta\lambda$	0.735	0.704
F	10.10	10.33

In the FDTD simulation, since the cavity dimensions are fairly large and the inclusion of modelled dispersive materials is computationally highly resource intensive, a smaller grid mesh had to be chosen to allow the simulation to run in a tractable time. The grid size δ was set to be $1/20$ of the shortest wavelength (615 nm) in each region, using a conformally refining mesh [233]. A summary table of the mesh grid dimensions for each cavity region is given in Table 5.5. Based on the results of the impact of the meshing accuracy on the cavity figures of merit, an approximate uncertainty in the centre wavelength and quality factor for this FDTD simulation is 0.81% and 15% respectively.

Table 5.5: **Summary of grid meshing parameters used in the FDTD simulation of the optical microcavities**

Meshing Method	Conformal
λ_{min}	615 nm
λ_{eff}	255.6 nm
Δ_{xy} TiO_2	14.50 nm
Δ_{xy} SiO_2	21.21 nm
Δ_{xy} Diamond	12.78 nm
Δ_{xy} SBN	13.91 nm

The simulated spectra to some extent can illuminate the measured transverse mode structure, although since the simulated finesse is intentionally low, it is again difficult to observe the spectra in detail. This problem is compounded by the mesh

resolution, which was by necessity fairly coarse because the computational overhead of the inclusion of the measured materials in the simulation can quickly make the simulation for practical purposes intractable with fine meshing. However, encouragingly the transverse mode spectra overlaps the spectra inferred from the measured data shown in Figure 5.8.

5.4.2 Cavity Enhancement

Without an emitter in the cavity, it isn't possible to directly measure the cavity Purcell factor. But based on the measured physical and optical properties of the cavity, it is possible to infer the expected enhancement both analytically and by numerical investigation. This is a crucial part of the device design process, since the fabrication procedure is very labour intensive, and it is therefore imperative to confidently infer the expected cavity enhancement.

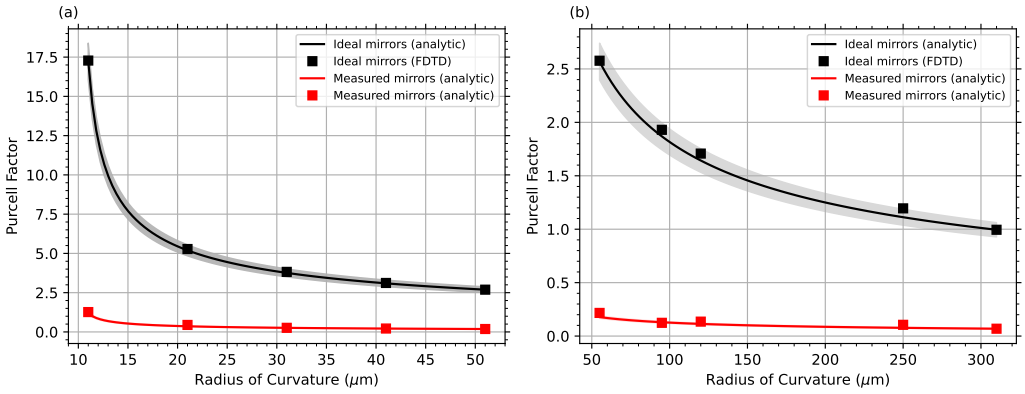

Figure 5.14: **Analytic and numeric calculation of Purcell factor:** (a) for smaller and (b) larger radii of curvature cavities. For the larger radius of curvature cavities, the expected Purcell enhancement is fairly low, even in the ideal scenario of lossless DBR coatings. On the other hand, by shrinking the cavity mode volume by reducing the radius of curvature, the expected Purcell enhancement can be quite significant.

For the larger radius of curvature cavities, given the fairly thick membrane of

10μm, the mode volume is quite large at between $98.50(n/\lambda)^3$ for $10\mu m$ radius of curvature cavities, and $2067.29(n/\lambda)^3$ for the $313\mu m$ RoC cavities. Therefore the Purcell enhancement is expected to be fairly low, even in the ideal scenario of lossless DBR coatings. This would be improved substantially by opting for higher reflectivity DBR coatings of course, and indeed the intended membrane thickness of the final device is between 3-5 μm, which would substantially improve the enhancement.

The results of the FDTD simulation Purcell factor simulation is shown in Figure 5.14 for smaller (a) and larger(b) radius of curvature cavities. In each case, the ideal case is shown in black, whilst the cavity objects with the modelled materials based on the acquired information in this chapter is shown in red. The black confidence interval in each plot represents the uncertainty in the estimate of the Purcell factor based on earlier testing. The uncertainty in the red dataset from modelled materials is too small to see in the figure.

Table 5.6: **Table of Inferred Purcell Factor and Branching Ratio**

Materials	Ideal	Modelled
FP	17.5	1.27
BR	0.3505	0.0256

Even in the ideal scenario, the larger radii of curvature cavities produce modest Purcell enhancement due to the large mode volume. However, the smaller radius can provide more substantive cavity enhancement. In the ideal scenario with low reflectivity mirrors, the Purcell enhancement could reach around 17.45, whilst even with the absorbent coatings observed in this chapter, a maximum Purcell enhancement of 1.27 is numerically extracted. In the ideal scenario, this translate to a branching ratio (BR) enhancement of the Debye-Waller Factor $DWF \approx 3\%$ for a typical NV centre of $BR{=}\frac{Fp \cdot DWF}{DWF \cdot Fp + (1-DWF)} \approx 35.05\%$. Therefore, the rate at which entanglement could be generated, with all other factors held constant,

could be enhanced by a factor of 32%. In the non-ideal case, the low Purcell enhancement of 1.27 would provide a branching ratio of 2.56%. Therefore, in future work it is vital to work with higher quality optical DBR coatings to realise sufficient cavity enhancement. These results are summarised in Table 5.6.

5.5 Chapter Summary

In this chapter, the fabrication of microcavity features in thin diamond membranes by focussed ion beam milling was reported, along with it's subsequent surface characterisation. After coating the cavities with DBR mirrors formed of SiO_2 and TiO_2, the optical response of the cavities was characterised with a purpose built spectroscopic microscope. Whilst cavity modes very evidently visible, the inferred finesse was around only 10% what was expected. From further study, it was found that the mirror deposition environment inhibited the growth of high finesse mirrors, and the deposition system and approach of the Thin-Film Facility at Oxford requires repair. Therefore, with better mirrors, it is expected that the cavity finesse should meet the design expectation. In the process of investigating the cause of the lower than expected cavity performance, a good design workflow and set of experimental characterisation and theoretical validations was established. In future work, the DBR coatings should be either outsourced to a coating manufacturer whom can ensure low absorption and uniform thickness, or the mirrors deposited in-house could be improved.

6 | Thin-Film Growth of SBN by PLD

In the present work, thin-films of strontium barium niobate were grown epitaxially onto a variety of substrates by Pulsed Laser Deposition (PLD). For initial prototyping, the thin-films were grown onto MgO substrates, and their microstructure was thoroughly characterised using a variety of techniques including X-Ray Diffraction (XRD), optical profilometry, Electron Dispersive Spectroscopy (EDX), and Electron-Backscatter Diffraction (EBSD). The final goal is to integrate these thin-films onto diamond membrane cavities, so it is necessary to find a way to remove the substrate of the thin-film. Here we propose that this can be achieved by growing the SBN film onto a sacrificial layer of strontium aluminate on strontium titanate. This section details the preparation of the PLD targets, the EO thin-film growth, microstructure characterisation, and the release of freestanding membranes of SBN.

6.1 Fabricating the Ceramic Target Material

To grow a thin film by PLD, a pulsed laser vaporises atoms of the surface of a target material, which then become energetically drawn to a substrate, whereupon the atoms nucleate [198]. The strong EO phase of $Sr_xBa_{1-x}Nb_2O_6$ is present when the $x \in [0.2, 0.8]$[180], and the strongest reported EO coefficient in thin-film form has been seen when x=0.75 [44]. Since control of the material stoichiometry is required, the PLD targets need to be fabricated from powders. Therefore, the targets were fabricated by mixing, pressing, and sintering powders of $SrCO_3$, $BaCO_3$, and Nb_2O_6.

To achieve the desired ratio of constituent powders, the required molar concentration of each powder mixture was calculated. Based on the molecular weights

of the constituent powders given in Table 6.1, the relative concentration of each powder for a desired ratio is calculated, and also shown in Table 6.1.

Table 6.1: **Molar Concentration of SBN target Powders**

Compound	Molar Weight	Concentration	Total Molar Conc.
$SrCO_3$	147.6300	0.75	110.7225
$BaCO_3$	197.3400	0.25	49.3350
Nb_2O_6	265.8100	1.00	265.8100

For a desired total powder amount, for a desired Sr:Ba ratio of 0.75:0.25, the required percentage of each constituent powder by weight was calculated, as shown in Table 6.2. Based on this, the required powder weight was measured on a digital scale and poured into a shared container.

Table 6.2: **Mixed quantities of each target powder**

x	Compound	g/mol	%wt	grams
0.75	$SrCO_3$	110.7225	25.9993	3.120
	$BaCO_3$	49.3350	11.5846	1.392
	Nb_2O_6	265.81	62.4161	7.488

To each powder mixture, polyvinyl buterate (PVB) dissolved in hot ethanol was added at 1.5% of the total final weight, to act as a binding agent. Since the powders are carbonates which will burn off when heated, the final powder weight is the sum of the non-carbonate products in Table 6.3. Therefore, 0.175 g of PVB was added to the mixture.

Table 6.3: **Weights of powders after with carbon burned off**

compound	grams
Sr	2.1550
Ba	1.1236
Nb_2O_6	8.7192

The combined powders were milled by mechanical agitation with yttria stabilised zirconia milling media for several hours to provide a heterogeneous mixture, and

the added ethanol was evaporated in an Erlenmeyer flask rotating in a hot bath of DI water until only the powders remained. The powder was ground with a mortar and pestle, and filtered through a very fine, lab-grade sieve to produce very small granules.

With the powder prepared, the targets were prepared with a two step sintering process. First, the powders were mechanically pressed into 10 mm diameter 3 mm thick pellets by placing the powder into a die cast and hydraulically pressing. Each target was then sintered in a Carbolite sintering furnace. To remove the carbonates, the furnace temperature was ramped to 600°C at a rate of 25°C/min, and held at this temperature for one hour. Next, the furnace temperature was ramped to 900°C at a rate of 5°C/min, and held for 7 hours. To provide better heterogeneity, the resulting target was ground down again using a mortar and pestle, and then sieved, mechanically pressed, and re-sintered, this time ramping at 10°C/min up to 600°C, holding for 1 hour, and then ramping 3°C/min to the final sintering temperature. For the PLD growth the final sinter temperature was 1350°C, held for a duration of 48 hours.

6.1.1 Compaction Pressure

The compaction pressure set at the hydraulic press when pressing targets for thin-film growth is an important consideration, since it impacts the density and porosity the target. These are important factors which may impact the quality, efficiency, and consistency of the resulting thin films. A higher density target can ensure a more uniform material composition, and therefore more consistent ablation [198]. More consistent ablation provides a more consistent flux of material onto the substrate, leading to more uniform thin films with desired stoichiometry and thickness. The target density can also influence the density of the deposited film. A denser target tends to produce films with fewer voids and a more compact

structure, which may provide better electrical properties and higher mechanical strength.

A more porous target material can lead to uneven ablation, faster target degradation, and fracture during the deposition process. More porous targets are more likely to trap gases or impurities within their structure, which can be released during ablation, contaminating the deposited film. In addition, the target porosity can affect the laser-material interaction, potentially leading to non-uniform plume formation, which may result in non-uniform deposition rates, and varying and compositions. Consequently, in targets with significant porosity, differential ablation rates can occur where certain components ablate more easily than others, making it challenging to maintain the stoichiometry of complex oxide films.

The density and porosity of the ceramic targets were determined by the method of Archimedes. Archimedes principle states that a body at rest in a fluid is acted upon by an upward pushing force, known as the buoyant force F_b. This force is directly equal to the weight of the fluid which the body displaces, and if the body is completely submerged, the fluid volume displaced is equal to the volume of the liquid. Formally, $F_b = -\rho g V$, where ρ is the fluid density, g is the acceleration due to gravity, and V is the fluid volume.

The target density is found by first weighing it when dry, giving the targets dry mass M_{dry}, and the submersing the target in water until saturated and measuring it's wet weight W_{wet}. Since the target experiences the buoyant force F_b, its apparent weight is reduced. Meanwhile, the volume V of the sample is calculated using the difference between the dry and wet weights. The dry weight is simply the weight of the pellet when it is dry, but the wet weight is found by accounting for the impact of the water $M_{wet} = M_{afterboilinwater} - M_{afterboil} + M_{dry}$. Therefore the volume is calculated as $V = \frac{M_{dry} - M_{water}}{\rho_{water} - \rho_{air}}$. The density of the pellet

is found by relating the dry mass of the target to the density of water and air as $\rho{=}M_{dry} \cdot \frac{\rho_{water}-\rho_{air}}{M_{dry}-M_{water}} + \rho_{air}$. The pellet porosity is found by relating the pellet mass to the density of water as $\phi_{open}{=}\frac{(M_{afterboil}-M_{dry})/\rho_{water}}{V} \times 100$.

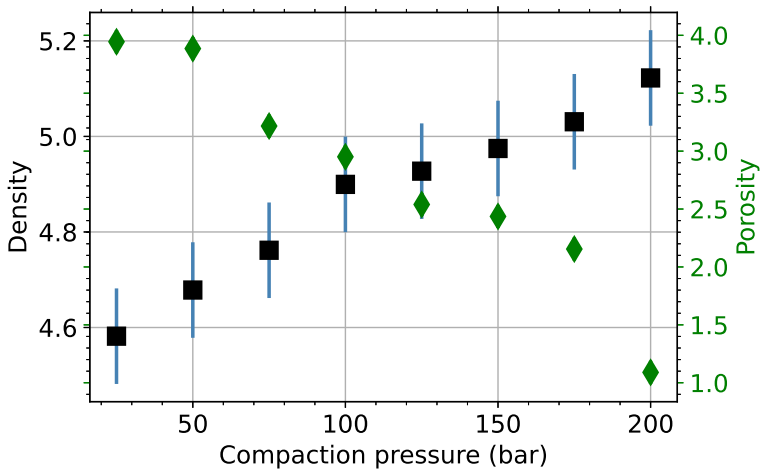

Figure 6.1: **Density and porosity of SBN PLD targets**. The targets were submerged in water and the porosity and density of each target as a function of compaction pressure was determined by the method of Archimedes.

The porosity and density of the sintered pellets were measured by Archimedes method for targets pressed at pressure between 25-200 bar. As the compaction pressure increases, the density increases roughly linearly, whilst the porosity precipitously declines polynomially. However, at target pressures above 150 bar, structural defects were seen to commonly occur and the integrity of the target was diminished. Therefore it is desirable to not exceed this pressure.

6.1.2 Composition

The compaction pressure of the target influences the target elemental composition, since a higher compaction pressure leads to denser packing of the powder particles, and a reduced porosity. This can help minimise the loss of volatile elements during sintering because there are fewer pathways for gases to escape. Conversely,

lower compaction pressures result in higher initial porosity, increasing the risk of volatilisation of elements such as strontium and barium oxides during sintering. This can alter the stoichiometry of the final material. In addition dense packing from higher compaction pressures enhances contact between particles, promoting solid-state diffusion during sintering. This can lead to more uniform elemental distribution and better incorporation of elements into the desired phase.

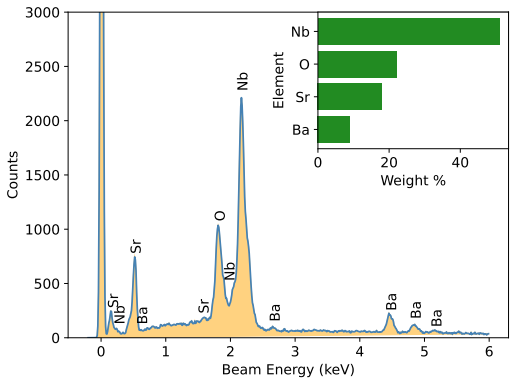

Figure 6.2: **EDX spectra of SBN target compacted at 150 Bar and sintered for 48 hours.** Multiple species are evident at increasing beam energy, whilst the carbon coating used for imaging is ignored in the analysis. Inset: Target composition by weight percentage.

To evaluate the composition of the target ceramic as a function of both compaction pressure and sintering temperature, the targets measured in a Zeiss Evo Scanning Electron Microscope (SEM) and studied via Electron Dispersive X-Ray Spectroscopy (EDX). The background of this measurement technique is detailed in Section 3.3. An exemplary x-ray spectra of the target is shown in Figure 6.2 for incident beam energies up to 6 keV. In the inset figure, the atomic percentage of each constituent element for this dataset is shown.

The impact of compaction pressure on the target composition is show in Figure 6.3, by weight percentage (a), atomic percentage (b), and relative ratio between Sr and Ba (c). As the compaction pressure is increased, the constituent

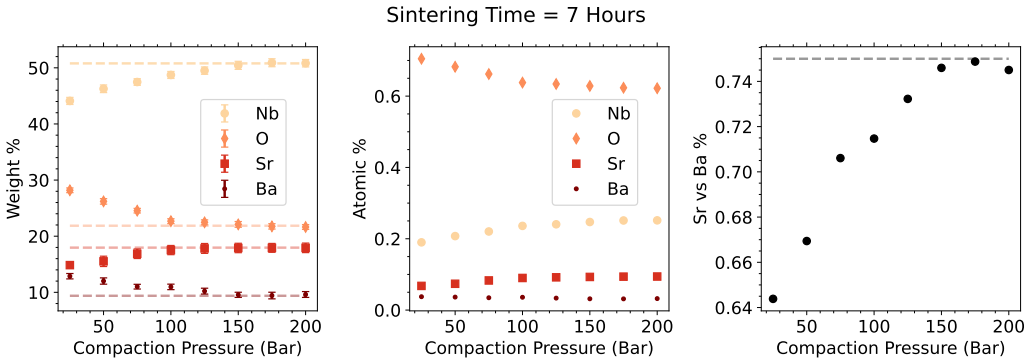

Figure 6.3: **Summary of extracted composition of SBN targets sintered at 1350C for 7 hours with a variety of compaction pressures**. (a) Weight % of each constituent element, extracted from the EDX spectra. (b) Corresponding atomic percentage of each constituent element. (c) Ratio of strontium to barium as a function of compaction pressure.

elemental ratios asymptotically reach a steady-state value. The desired Sr:Ba ratio of $0.75 : 0.25$ is reached when the compaction pressure is 175 bar. However as noted earlier, at this pressure the target structure degraded. Therefore a slightly lower compaction pressure of 150 bar is chosen for the final target, with very little deviation from the desired ratio.

6.1.3 Impact of Sintering Temperature and Duration

In addition to the compaction pressure, the sintering temperature and duration can play a significant role in determining the elemental composition of the target, as well as structural components such as grain sizes. In choosing an appropriate sintering temperature, it is important to avoid heating the powder above its melting point, since doing so would drastically alter the target composition. The melting points of each constituent powder in the target is given in Table 6.4. Although the melting point of $BaCO_3$ is low, when mixed with the other powder the overall melting point is much higher. Nonetheless, the low melting point of $BaCO_3$may result in a trade-off between grain size and elemental composition.

Table 6.4: **Melting points of SBN target constituent powders**

Compound	Melting Point ($^{\circ}C$)
$SrCO_3$	1494
$BaCO_3$	811
Nb_2O_6	1512
$Sr_xBa_{1-x}Nb_2O_6$	1480 - 1500

For the present work, a sintering temperature of 1350 °C was chosen which sinters the powders without melting the combination. When sintering for too brief a period, the powders may only diffuse on the surface, leading to less homogeneity, smaller grains, and mechanical weakness. On the other hand, sintering for too long may lead to coarse grains and and weak pellets. Initially the powders were sintered (for the second sintering run) for 7 hours. Figure 6.4(a) shows an SEM image of the surface of a pellet sintered for this time. It is visibly evident that the target has not properly densified and bonded. On the other hand, a target sintered for 48 hours is shown in Figure 6.4(b). It is clear that this target has more fully densified. Therefore the sintering time of the targets in this work was chosen to be 48 hours.

(a) 7 Hours Sintering

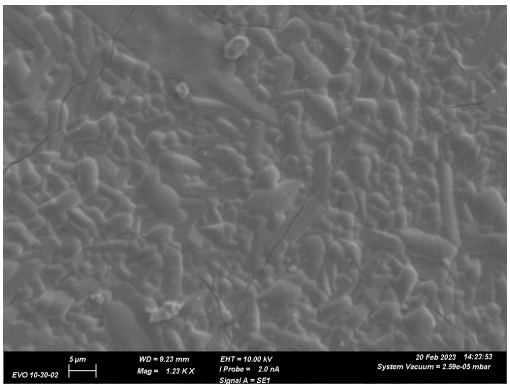

(b) 48 Hours Sintering

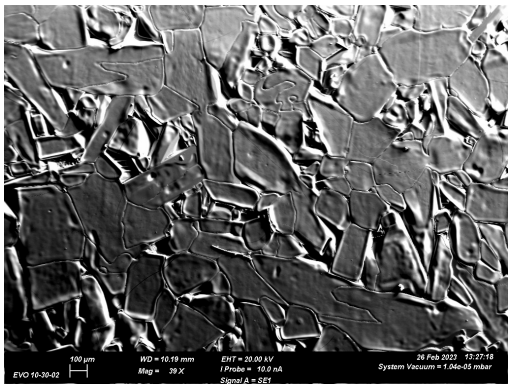

Figure 6.4: **SEM image of SBN target surfaces sintered for :** (a) 7 hours; (b) 48 hours. In (a) the target has not properly densified and bonded, but in (b) the target is more densified. Note the SEM scale of (a) is smaller than (b) in order to full see the finer, non-bonded structure, which is not present in (b).

Importantly, the sintering time does not appreciably affect the elemental composition of the target, as measured by EDX. A comparison of the target compositions is provided in Table 6.5. The invariance of the composition with sintering time suggests that the constituent components are not volatilising or reducing/oxidising during the sintering process.

Table 6.5: **Composition of SBN targets sintered for** 7 **and** 48 **hours**

	7 hours		48 hours	
Element	Weight %	Atomic %	Weight %	Atomic %
Nb	48.05	23.34	50.70	25.67
O	23.22	65.45	21.13	62.15
Sr	12.82	6.60	12.81	6.88
Ba	13.91	4.57	15.45	5.29

6.1.4 Grain Analysis by Electron Backscatter Diffraction

The grain boundaries and microtexture of the SBN target sintered for 48 hours was analysed by EBSD using a Zeiss Merlin SEM fitted with an Oxford Instruments EBSD system consisting of a phosphorescence screen and CMOS camera. The incident electron beam acceleration voltage was set to 30 kV at a beam current of 2 nA. Prior to the analysis, the SBN target was polished using progressively finer sandpaper and ultimately diamond infused polishing disks. This smooth surface was essential for observing the lattice planes of the target. When the incident X-Ray diffracts through the crystalline sample, inelastically scattered electrons are collected by a phosphor screen, and the crystal information is reconstructed (as detailed in Section 3.4). The Zeiss Merlin EBSD uses a proprietary Oxford Instruments software package which performs the necessary Hough transforms, stereographic projections, orientation interpolations, etc. The user must program in crystal information, including lattice parameters, crystal symmetry, atom site locations, and atom occupancy, from which the empirical crystal information can

be determined.

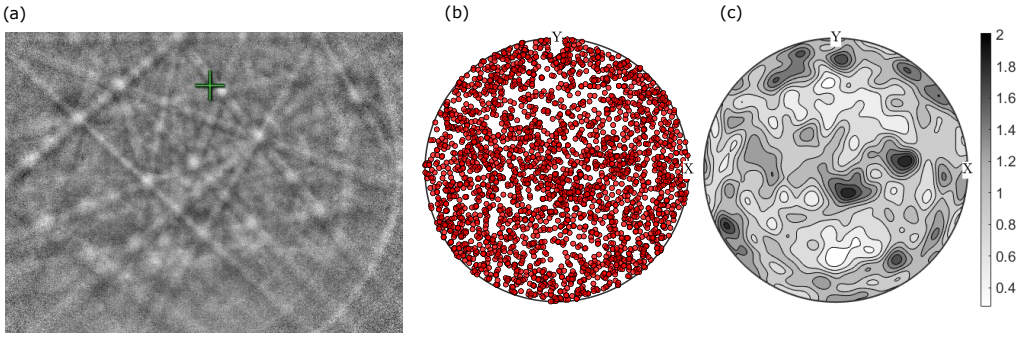

Figure 6.5: **EBSD analysis of SBN75 target:** (a) Kikuchi pattern, displaying strong lattice bands; (b) Pole figure projected along $\langle 001 \rangle$ axis, showing polycrystallinity with no texture; (c) Pole density figure shows no texture either, confirming polycrystalline nature of target/.

In Figure 6.5(a), the reconstructed Kikuchi pattern observed by the EBSD detector is shown, displaying strong lattice bands. The pole figure acquired for the SBN target is shown in Figure 6.5(b), with respect to a $\langle 001 \rangle$ plane. Each point shows an individual pole found, and it is clear that the target is highly polycrystalline with no texture, as expected. Figure 6.5(c) shows the density of poles across the figure, which corroborates the observation of polycrystallinity.

In Figure 6.6(a), an inverse pole map with respect to the z-axis (IPF-Z) is shown for the target. The variations in colour indicate a range of crystallographic orientations in the grains, demonstrating the polycrystallinity of the ceramic. A uniform colour across many grains would suggest a texture or preferred orientation, but the diversity in colour implies a more random orientation distribution. The black regions represent non-indexed orientations, which could not be resolved. This could be due to due to the roughness of the SBN target, but since the target was highly polished in preparation for the analysis, this is perhaps not the most likely explanation. Rather, it is more likely that this is the result of lattice distortions occurring near the grain boundaries which obscure the diffraction pattern. Alternatively, this

could indicate the presence of amorphous phases, since non-crystalline regions in ceramics often do not produce distinct diffraction patterns.

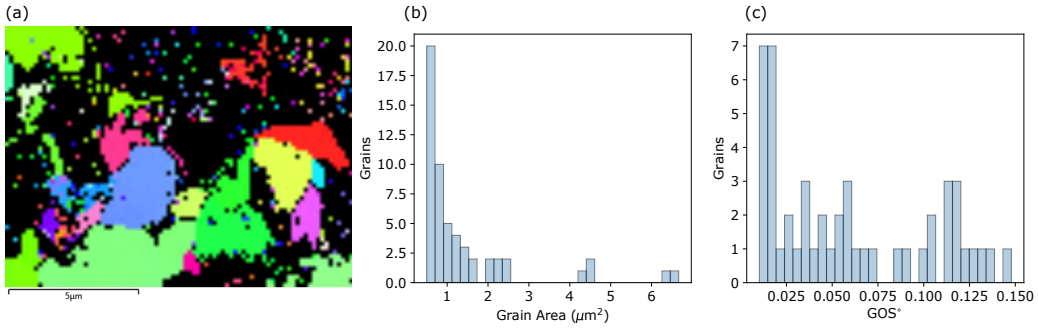

Figure 6.6: **EBSD analysis of SBN target grains:** (a) Inverse pole map with respect to the z-axis (IPF-Z) is shown for the target. The variations in colour indicate a range of crystallographic orientations in the grains, demonstrating the polycrystallinity of the ceramic.The black regions represent non-indexed orientations, which could not be resolved.(b) histogram of the grain areas (μm^2) based on the observed EBSD orientation data is provided. The strong bias toward smaller/medium sized grain areas suggests that the target is structurally hard. (c) grain orientation spread (GOS) is concentrated below $0.05°$, suggesting that the majority of the grains have minimal internal strain.

In Figure6.6(b), a histogram of the grain areas (μm^2) based on the observed EBSD orientation data is provided. A grain boundary in this analysis is defined as standard [256] where neighbouring pixels are misoriented with respect to each other's Euler angles by $\geq 10°$. The preponderance of the grain areas are between $0.5-1.25$ μm^2, whilst some grains are in excess of 6 μm^2. The strong bias toward smaller/medium sized grain areas suggests that the target is structurally quite hard, and therefore likely to withstand the energetic sputtering process of PLD.

Meanwhile, the grain orientation spread (GOS) is concentrated below $0.05°$ (Figure6.6(c)), which signifies that the majority of the grains have minimal internal strain. This is desirable in ceramics as it indicates that the grains are largely strain-free, which enhances mechanical stability and reduces the likelihood of cracking under stress. The combination of small/medium size grain areas and low GOS

suggests that the sintering and recrystallization processes have been effective, producing a predominantly strain-free microstructure.

6.2 Growth of Epitaxial Strontium Barium Niobate by Pulsed Laser Deposition

6.2.1 Substrates

In this work, the SBN thin film was grown onto two different substrates: MgO and $SrTiO_3$, which were chosen for their relatively close lattice parameter match to SBN 3.1. MgO was initially chosen as a prototyping substrate since it was this substrate on which the large Pockels coefficient of 844 pm/V was originally measured [44]. However, due to the large misfit strain between SBN and MgO, it may not be the most optimum choice of substrate, and $SrTiO_3$ may provide thin-film SBN with better microstructural properties.

6.2.1.1 Growth of SBN onto $SrAl_2O_6$

To develop a tunable monolithic cavity, the goal is to integrate the SBN layer on a diamond substrate. This is challenging however, due to the large lattice parameter mismatch between diamond and the c-axis of SBN (Table 6.6). At $\sim 10\%$ interfacial strain, epitaxial growth is unfavourable.

SBN can grow epitaxially onto substrates of MgO and $SrTiO_3$, however, due to the typically large dimensions of such substrates, this cannot be integrated with the final device directly. Chemically etching away the substrate can be challenging, and therefore a means of producing a freestanding membrane of SBN is highly desirable. We propose to achieve this by growing the SBN thin film onto a $SrTiO_3$ substrate which possesses a sacrificial $SrAl_2O_6$ grown by ablating a powder pressed

Table 6.6: **Comparison of lattice parameters for SBN and various substrates.** Epitaxial growth of SBN onto diamond is challenging due to the large interfacial strain, but growth onto MgO or $SrTiO_3$ is possible.

Material	Lattice Param (nm)	Strain (%)
SBN	3.932	
Diamond	3.567	10.23
MgO	4.213	6.70
$SrTiO_3$	3.905	0.69
$SrAl_2O_6$	3.756	4.69

target by PLD. It is known that this material can grow well onto $SrTiO_3$ substrates, and since it is soluble in water [257], if a new material is grown epitaxially on top, submerging the device in DI water could produce freestanding membranes of SBN.

A freestanding membrane of SBN can then be transferred to the diamond membrane and directly bonded. This bonding process could be achieved by cleaning both the diamond and SBN membranes, enriching them with O_2 plasma, and then placing both membranes in DI water. Since the membranes have been enriched with oxygen, they will become hydrophillic, so subsequently bringing both membranes into contact with one another would cause them to form a capilliary bond, which can be hardened to a covalent bond by subsequent annealing.

6.2.1.2 Growth Models

The c-axis lattice parameter of SBN is close to the lattice parameters of both MgO and $SrTiO_3$. Therefore SBN can grow epitaxially on these substrates. However, since $a_{SBN} >> a_{STO/MgO}$, a-axis SBN cannot be grown epitaxially onto these substrates, and therefore the substrates favour c-axis growth. As detailed in [258] the relationships between lattice parameters of SBN and MgO/STO are:

$$|a_{MgO/STO}| \approx |c_{SBN}|$$
$$|a_{MgO/STO}|^2 + (3|c_{MgO/STO}|)^2 \approx |c_{SBN}|^2 \quad (6.1)$$

c_{SBN} grown onto a- or b-oriented MgO or $SrTiO_3$ tilts at an eigen-angle of $\tan^{-1}\frac{1}{3} = 18.4°$ away from the interface, whilst c_{SBN} grown on c-oriented MgO or $SrTiO_3$ tilt $18.4°$ in-plane to the interface. Therefore SBN grows in the manner of a unit cell.

6.3 Microstructure Characterisation by X-Ray Diffraction

X-Ray Diffraction (XRD) is a powerful technique for studying the crystalline properties and microstructure materials. As detailed in Section 3.2, by this method the lattice parameters, crystallite size, microstrain, dislocation density, and crystallinity can all be studied by irradiating a sample with X-rays and analysing the resulting spectra for a given material. In this work, the Empyrean XRD was employed to make 2θ measurements.

6.3.1 Data Fitting and Structure Refinement

Analysis of the acquired intensity values with respect to diffraction angle can be a cumbersome process requiring careful treatment, involving four steps: (i) the data must be pre-processed to properly identify the peak positions; (ii) the shape of each peak must be identified (e.g. Lorentzian or Gaussian); (iii) an appropriate fitting model must be chosen; and (iv) a least squares fitting algorithm must be

applied to the data to extract quantities of interest. Whilst there are specialised XRD analysis software packages which can facilitate this treatment, such as the industry standard X'pert High Score, it is often necessary to treat the peaks manually. In the present work, the complexity of the dataset made the manual approach necessary, and therefore the data was processed using OriginPro. The individual steps are detailed in the subsequent subsections.

6.3.1.1 Pre-Processing

Before fitting the peak data, the peaks in the dataset must be properly isolated. First, the baseline of the data must be corrected. The intensity data contains background data which includes noise and drift, and which must be subtracted before analysing the peaks. To remove the baseline, the background data was fitted with an asymmetric least squares smoothing algorithm [259] and subtracted from the original data. Next, the data was smoothed with a Savitzky-Golay filter algorithm [260] to reduce noise without distorting the peaks.

Finally, the peaks in the dataset were matched with reference material patterns to index the individual peaks and provide phase and orientation information on the respective materials. For the substrate materials MgO and $SrTiO_3$, and the interfacial $SrAl_2O_6$, matching the peak positions is simple since there are well-known reference patterns available in material databases. For SBN however, this is more complex since the reference intensity data is highly dependent on the ratio of Sr:Ba. To circumvent this problem, it is possible to simulate a diffraction pattern using the Vesta software based on atomic positions attained by density functional theory (DFT) [183]. With this, the peak position matching was optimised using Rietveld refinement [261].

6.3.1.2 Peak Fitting

Each peak in the acquired intensity data possess unique characteristics. Some peaks are found to be Lorentzian in nature, some Gaussian, and some Voigt. Others are found to a convolution of two peaks, typically two Gaussians. These situations are generally found when the $K\alpha_1$ and $K\alpha_2$ peaks overlap. To mitigate this problem, a double-Gaussian was fitted to the data and the peaks were separated by Fourier deconvolution. With each peak shape identified and separated, the individual peaks were fitted to their respective fitting models using a Levenberg-Marquardt [262, 263] least-squares fitting algorithm.

6.3.2 XRD Analysis

The temperature at which a thin-film material is grown can profoundly impact the nucleation and crystallinity. At higher temperatures, atoms on the substrate surface are much more free to move and diffuse than at lower temperatures. This allows the deposited material to order itself into energetically favourable sites on the substrate surface, promoting better epitaxial growth and single crystallinity. On the other hand, at lower temperatures polycrystallinity is more likely to emerge due to increased nucleation density.

The role of the growth temperature on the crystallinity of SBN was studied by growing SBN onto MgO substrates at chamber temperatures of ($300°$C, $500°$C, $700°$C), and $900°$C, and evaluating the peak formation in 2θ XRD. The resulting XRD intensity data for each temperature is shown in Figure 6.7. At lower temperatures ($300°$C, $500°$C, and $700°$C), the SBN thin-film appears to posses multiple different crystal phases, and no particular strong dominant phase. However, by $900°$C, the thin film clearly favours a strong $\langle 001 \rangle$ orientation, whilst the other phases are suppressed.

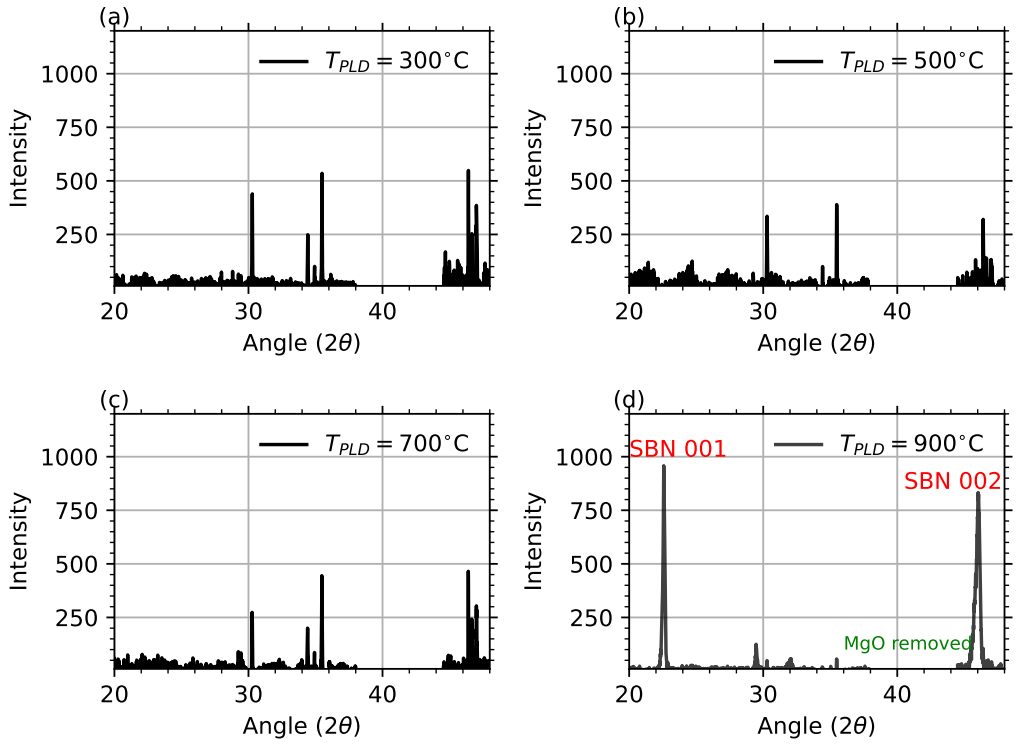

Figure 6.7: **Comparison of XRD spectra for SBN grown by PLD** onto MgO substrates at temperatures of 300°C, 500°C, 700°C, and 900°C. The MgO spectra has been removed for clarity.

6.3.2.1 Microstructure Figures of Merit

Each peak found in Figure 6.7 was fit to the appropriate functions, and we attempted to deduce microstructural figures of merit as detailed in Section 3.2. However, we found that the peak broadening was dependent on both crystallite size and microstrain, making it impossible to discern these quantities by simple peak fitting, and therefore a Williamson-Hall analysis (as detailed in Section 3.2) was performed. Williamson-Hall plots for SBN grown onto MgO at increasing chamber temperatures is shown in Figure 6.8. The error bars in these plots are found by determining the error in each broadening term due to the sample and the instrument itself. In (a)-(c), the gradient of the slope is slightly increasing which

implies a small degree of tensile strain, where the film is stretching to match the MgO lattice during epitaxial growth. However, in (d) the strain becomes compressive at the higher growth temperature of $900°C$, which implies that the film is becoming epitaxially compressed to match the substrate.

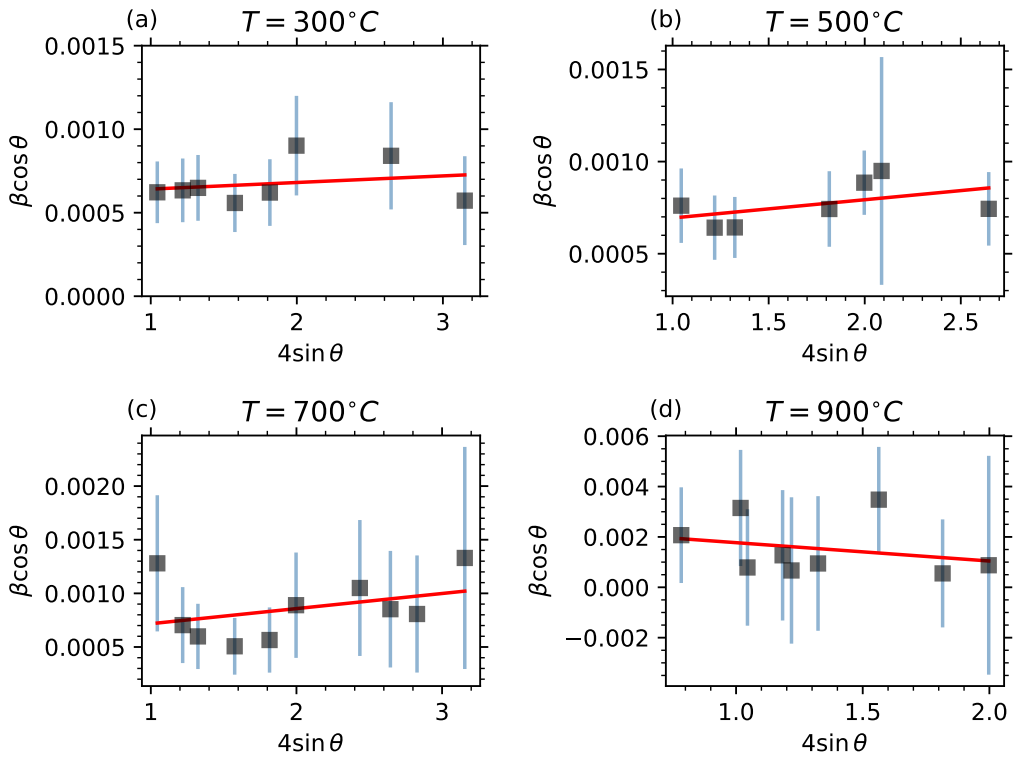

Figure 6.8: **Williamson-Hall Plot for SBN grown onto MgO:** at (a) 300°C; (b) 500°C; (c) 700°C; and (d) 900°C. The slight positive gradient in (a-c) indicates tensile strain in the film, whilst the negative gradient of the fitted line in (d) indicates compressive strain.

Whilst generally capturing the trend, the linear fits in Figure 6.8 are not perfect, with low goodness-of-fit metrics such as the R^2 value. The fitted coefficients are displayed in Table 6.7. This indicates that the peak-broadening, strain, and crystallite size are not necessarily perfectly captured by the assumptions of the Williamson-Hall plot. This can be due to further mixed broadening mechanism such as non-uniform strain or anisotropic stress; anisotropic crystallites; or

stacked defects, and therefore a deep understanding of each mechanism would be required to reduce the uncertainty further. Operationally however, within the limitations of the method, the approximate results it yields are sufficient for making inferences about the impact of the film on the full device fabrication process.

Table 6.7: **Coefficients of linear fits of the Williamson-Hall data for SBN grown on MgO.**

T_{growth}	Intercept	Slope	R^2
$300°C$	$6.01859E{-}4 \pm 1.34786E{-}4$	$3.94817E{-}5 \pm 6.84517E{-}5$	0.05253
$500°C$	$5.94761E{-}4 \pm 1.43151E{-}4$	$9.91021E{-}5 \pm 7.90185E{-}5$	0.2393
$700°C$	$5.7633E{-}4 \pm 2.75205E{-}4$	$1.41029E{-}4 \pm 1.29761E{-}4$	0.12865
$900°C$	0.00248 ± 0.00148	$-6.0821E{-}4 \pm 0.0013$	0.03978

By this method, the crystallite size and microstrain were found for SBN grown onto MgO substrates for each growth temperature. Since the dislocation density depends on crystallite size, this quantity was also deduced for each growth temperature. The impact of the growth temperature of the crystallinity of the thin-film was determined by integrating the peak spectra with respect to the total spectra for each growth temperature, as described in Section 3.2.

Figure 6.9 shows the crystallite size (a) microstrain (b) dislocation density (c) and crystallinity index (d) of thin-film SBN grown onto MgO at temperatures increasing from $300°$ C to $900°$ C. As the temperature increases, the dislocation density can be seen to decrease exponentially as the film crystallises. In the same manner, as the temperature increases, the microstrain is seen to increase due to the enhanced crystallinity of the thin-film. The dislocation density at the final sintering temperature of $900°C$ is on the order of 10^{12} m^{-2}, which is fairly large, indicative of the lattice mismatch between SBN and MgO. The nature of these defects could be studied in greater detail using an SEM based technique known as electron channeling contrast imaging (ECCI) [264], but gathering such data for thin ferroelectric films is very challenging due to the large interaction volume

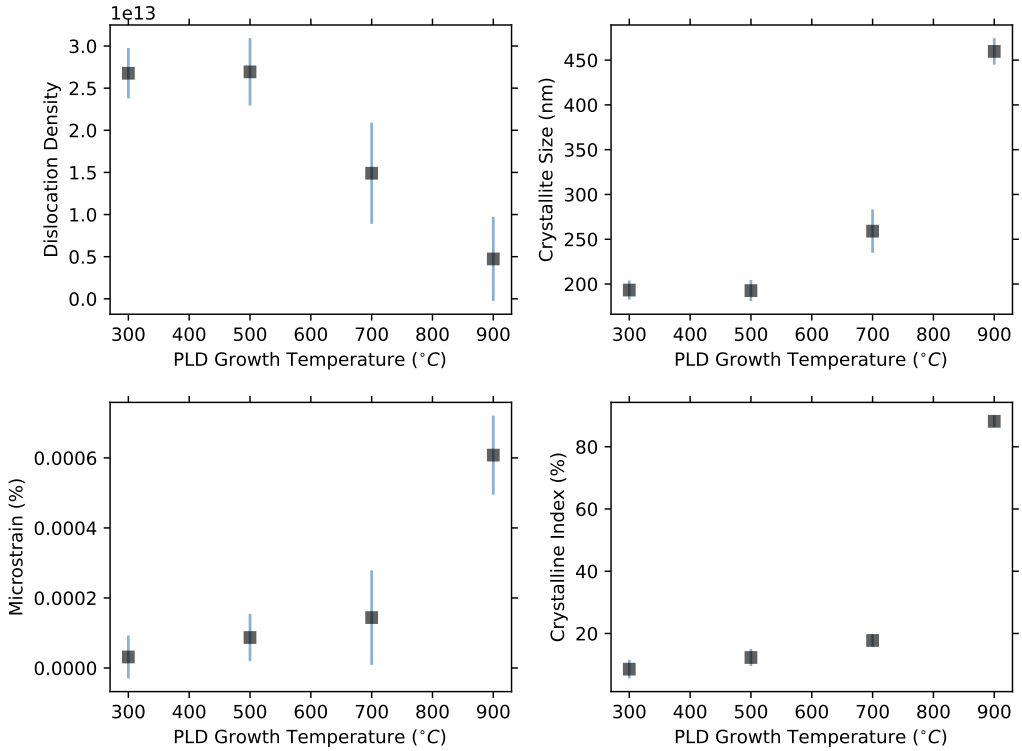

Figure 6.9: **Figures of Merit of SBN thin film extracted by XRD**, as a function of growth temperature: (a) crystallite size; (b) microstrain; (c) dislocation density; (d) crystallinity index.

of the SEM compared to the thin film depth. Regardless, a defect density of the order seen for the $900°C$ film is not uncommon or disqualifying for thin-film materials. FInally, as the temperature increases, the crystallinity index does also, to a maximum value of 88%, therefore indicating a decently crystalline material. This can likely be improved further by a subsequent thermal anneal in oxygen.

Table 6.8: **Lattice parameters of SBN grown on MgO at $900°$C**

d ($\mathring{A}$)	a ($\mathring{A}$)	b ($\mathring{A}$)	c ($\mathring{A}$)
3.93254	12.48211	12.48211	3.93254

6.3.3 SBN75 Grown onto $SrTiO_3$

After determining the growth temperature required for thin-film nucleation using MgO substrates, our attention turned to growing a thin-film on a structure compatible with cavity integration, i.e. a $SrTiO_3$ substrate with a $SrAl_2O_6$ interfacial layer. Just as for growth on MgO, a strong $\langle 001 \rangle$ peak is present, but this time much narrower due to to a closer lattice match. Figure 6.10 shows a comparison of the $\langle 001 \rangle$ SBN peak grown onto the three different substrates. The left-hand plot shows the real peak 2θ positions, which have been shifted in the right-hand plot to overlap one another to show a clear comparison between peaks.

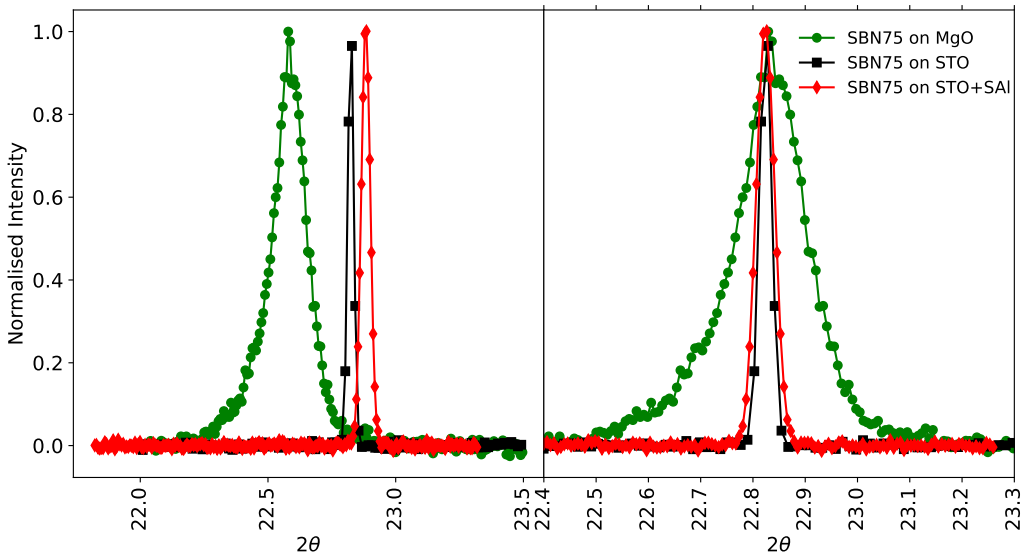

Figure 6.10: **Comparison of the SBN 001 peak when grown on MgO and on STO**, along with the STO 001 peak. SBN grown onto $SrTiO_3$ and the sacrificial layer possess much narrower linewidths than that grown on MgO, since the lattice parameters of SBN and STO are more closely matched than SBN-MgO (Table 3.1).

In comparison to the SBN $\langle 001 \rangle$ peak grown onto MgO, the SBN peak grown onto $SrTiO_3$ and the sacrificial layer possess much narrower linewidths, since the lattice parameters of SBN and STO are more closely matched than SBN-MgO

(Table 3.1). Indeed, the microstrain for thin films grown on STO and STO+SAl is correspondingly lower than growth on MgO. Despite the narrower peak broadening however, the crystallite size of these films is smaller than for those grown on MgO. This may be a consequence of several factors: for example, the strong lattice match of SBN to STO may actually lead to significant epitaxial strain in the early stage of growth, inhibiting the coalescence of crystallites into larger domains as the film relieves strain through mechanisms such as misfit dislocations [198]. On MgO on the other hand, the weaker lattice match may allow for relaxation far more easily through strain relaxation mechanisms such as defects. Other factors may be at play such as the substrate surface energy, island growth dynamics, and chemical interactions, which are beyond the necessary scope of the present work, but would be an interesting avenue of further study.

Table 6.9: **Comparison of XRD figures of merit for SBN grown on MgO, STO, and STO+SAl**

Substrate	2θ Peak Centre (deg)	FWHM (deg)	D (nm)	ϵ (%)
MgO (900°C)	22.57928	0.14700	459.69	0.00060
STO	22.82857	0.02872	232.16	0.000297
STO + SAl	22.8354	0.04237	157.26	0.000439

6.3.4 3-Axis XRD (ϕ-Scans)

X-ray diffraction (XRD) analysis confirms that the SBN thin films exhibit near-single-crystal quality, with a prominent $\langle 001 \rangle$ peak indicating a strong preferential orientation. However, it is well-documented that SBN may also support a secondary $\langle 310 \rangle$ orientation. Due to the inherent crystal symmetry, this secondary orientation cannot be observed in the standard 2θ XRD spectra obtained using a simple spinning goniometer. Identification of such secondary orientations require a ϕ-scan along multiple axes. Due to the long a-axis of SBN compared to it's c-axis, this presented a significant challenge for the Empyrean X-Ray Diffrac-

tometer used in this work, as it could not be directed along the necessary crystal planes to achieve an adequate signal-to-noise ratio. Consequently, the ϕ-scans obtained with the available hardware were insufficient to conclusively determine the presence of a secondary orientation.

6.4 Electron Backscatter Diffraction

Since it was not possible to acquire 3D XRD information, EBSD was employed as an alternative method for crystallographic analysis. EBSD offers the additional advantage of providing precise orientation maps across the entire sample, enabling both the quantification of $\langle 001 \rangle$ and $\langle 310 \rangle$-oriented domains and the spatial identification of their distribution within the film. However, the application of EBSD to thin-film ferroelectric materials such as SBN presents several technical challenges:

- **Interaction Volume:** The SBN thin films used in this study are approximately 100 nm thick, whereas the interaction volume of the electron beam with the sample is significantly larger. This discrepancy poses a challenge for acquiring EBSD data, as a considerable fraction of the backscattered electrons may originate from the substrate rather than the thin film, potentially complicating the interpretation of the data.
- **Pseudosymmetry:** Pseudosymmetry is a phenomenon frequently encountered in perovskite materials, where the atomic arrangement appears to approximate a higher symmetry than that of the true underlying space group [265]. This can cause significant complications in the interpretation of EBSD data, as the resulting diffraction patterns may yield multiple possible solutions instead of a single, definitive solution, making the indexing of crystallographic orientations more challenging.

Both these limitations were surmountable by carefully considering the interaction of the SEM with the SBN surface and the symmetry operations on the point group of SBN. The mitigation of these problems is detailed in the following subsections.

6.4.0.1 Interaction Volume

When an electron beam interacts with a material, the interaction occurs within a defined volume, which depends on several factors. The size of this interaction volume is determined by the atomic number of the material, as higher atomic numbers absorb more electrons and thus have smaller interaction volumes. It is also influenced by the acceleration voltage of the electron beam, with higher voltages allowing deeper penetration into the material, and by the angle of incidence, where greater angles result in smaller interaction volumes.

For the SBN thin films studied in this work, which are only a few hundred nanometers thick and deposited on a 500 μm-thick MgO substrate, it is important to ensure that only the backscattered electrons originating from the SBN layer are included in the analysis, whilst eliminating substrate electrons. This requirement sets an upper bound on the acceleration voltage and beam current of the SEM, and a balance between signal-to-noise ratio and backscattered electron (BSE) signal origin must be found. To determine this, a Monte Carlo simulation of electron trajectories was conducted to model the interaction of the electron beam with the material. The results for acceleration voltages of 5 kV and 30 kV are displayed in Figure 6.11.

EBSD is primarily a surface-level sensitive technique, and analyses crystalline information from the top $10-50$ nm of a material [266]. Whilst at high acceleration voltages the electron beam penetrates deeper, the generated Kikuchi pattern is formed from a shallow subset of backscattered electrons which originate from a shallow region near the surface, since the Kikuchi pattern is formed only by

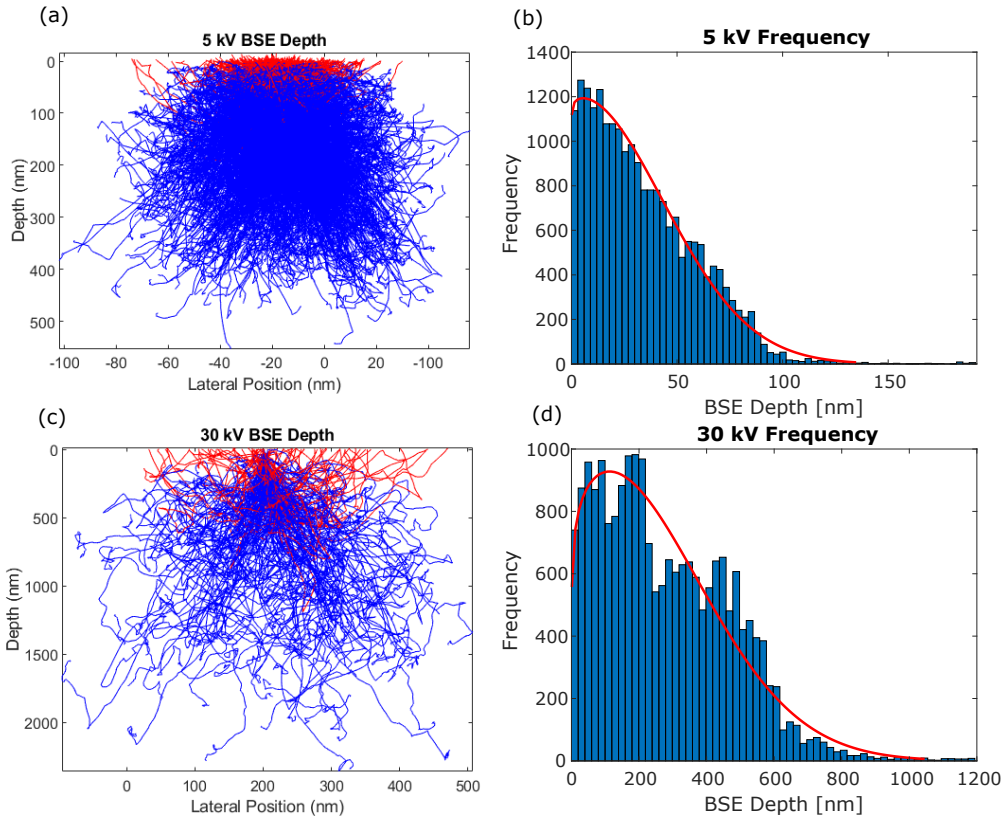

Figure 6.11: **Monte-Carlo simulation of electron beam interaction with the SBN thin film at acceleration voltages of 5kV and 30kV**. The red paths in (a) and (c) denote backscattered electrons, while the blue trajectories represent incident electrons from the SEM. (b) and (d) show the frequency of backscattered trajectories with respect to depth.

inelastically backscattered electrons which undergo coherent, channeling interactions with the crystal planes near the surface. These interactions only produce well-defined patterns if the electrons exit the crystal with relatively low angular spread and energy loss, which strongly favours electrons emerging from the near-surface region. However, elastically scattered electrons do not contribute usefully to Kikuchi band formation because they lack the inelastic interaction needed to initiate the channeling process that produces the patterns. Instead, they can contribute a diffuse background noise signal, which can reduce the contrast of the

Kikuchi bands. Therefore, even though the Kikuchi pattern formation is primarily a surface-level technique, if many electrons are backscattered from deeper into the sample, resolving the Kikuchi can be problematic.

This scenario cana rise at higher acceleration voltages, such as 30 kV, where the incident beam penetrates deep into the substrate, and correspondingly many of the elastically backscattered electrons may emerge from the substrate, which would corrupt the subsequent orientation analysis. On the other hand, at 5 kV comparatively few electrons are backscattered from the substrate. Therefore, to successfully acquire enough backscattered electrons from the SBN film rather than the substrate, the acceleration voltage was set to 5 kV with a beam current of 10 nA.

6.4.0.2 Pseudosymmetry

Figure 6.12(a) shows an inverse pole figure Z-map for SBN grown onto MgO. In this data, the AzTec indexing software is unable to discern between these $\langle 001 \rangle$ and $\langle 310 \rangle$ indices, as reflected in the two colouring schemes, red and green. Each pixel in the figure represents a unique orientation, but these do not overlap well with the band-contrast image (Figure 6.12(b)),implying that there are two overlapping phases. Therefore, a pseudosymmetry axis complicates the analysis, since the measured spectral pattern possess two solutions instead of one unique solution. This must be accounted for before the indexing software can successfully identify the orientations.

The presence of a pseudosymmetry axis in SBN has not been previously been documented in the literature, to the best of our knowledge, but is predictable from first principles, since SBNs space group is a lower symmetry subgroup. From the group theory of the SBN crystal structure, the P$\bar{4}$bm space group is a subgroup of the higher-symmetry group P4/mmm. P4/mmm is a high-symmetry,

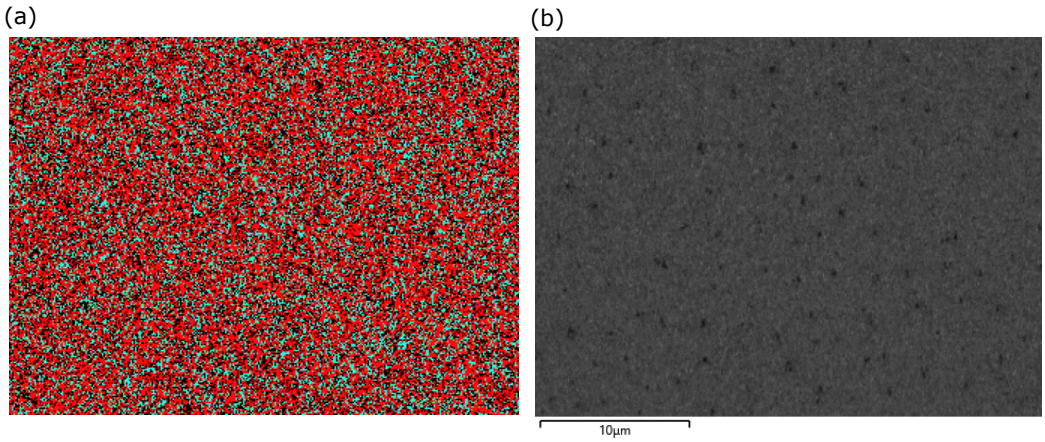

Figure 6.12: **EBSD map of SBN on MgO:** (a) IPF Z-map without pseudosymmetry correction. The indexing software is unable to discern between these $\langle 001 \rangle$ and $\langle 310 \rangle$ indices, as reflected in the two colouring schemes, red and green.(b) the orientations in the IPF-Z map do not overlap with the band contrast image, implying an axis of pseudosymmetry.

centrosymmetric space group with the point group 4/mmm, including inversion, mirror planes, and higher-order symmetry operations. On the other hand, P4bm is a lower symmetry, non-centrosymmetric subgroup, derived by removing inversion symmetry and certain mirror planes. It has the point group 4mm, retaining the fourfold axis and polar characteristics. During the thin-film growth at high temperature, the higher-symmetry P4/mmm may actually be the correct symmetry, but as the film cools, SBN relaxes into a stable tetragonal P4bm symmetry at room temperature [182] due to slight distortions.

To define the axis of pseudosymmetry, it is necessary to investigate the symmetry operations of both the 4mm and 4/mmm point groups, and determine which symmetry axes are common. This can be achieved by observing the character tables for the irreducible representations of each group. Both groups share the fourfold rotational symmetry C_4 along the c-axis, whilst inversion symmetry and some mirror planes are lost in the 4mm group. Therefore, the pseudosymmetry axis is the c-axis, $\langle 001 \rangle$. This correction can be compensated for in the index-

ing software, and with this the true IPFZ figure is found (Figure 6.13(b)), which maps the Kikuchi bands in Figure 6.13(a) to indexed orientations. Now the indexing displays unique solutions, with red pixels indicating a $\langle 001 \rangle$ phase and green pixels representing $\langle 310 \rangle$.

In Figure 6.13(c), an Inverse Pole Figure (IPF) of the data is displayed. While the pole figure plots the crystal direction relative to sample axes, the inverse pole figure plots the sample direction relative to crystal axes. This is more useful for visualising grain orientations, since it shows that the sample's reference axes are oriented with respect to the crystal lattice, and indicate which crystallographic direction is parallel to the specified sample direction, providing insight into the orientation of grains relative to the sample geometry.

A further highly useful property of the IPF is the ability to discern the orientation distribution function (ODF) which provides information on the density of crystallites arranged in specific orientations. In Figure 6.13(d) the frequency of domain orientations is shown. There is evidently a large frequency of both $\langle 001 \rangle$ and $\langle 310 \rangle$ orientations present over an area of 2.5 mm^2, with a preference for $\langle 310 \rangle$ oriented grains. Since the SBN film is not a perfect single crystal, there is a small frequency of other orientations present, namely $\langle 410 \rangle$ and $\langle 516 \rangle$. However, these are dwarfed by the high density of $\langle 001 \rangle$ and $\langle 310 \rangle$ oriented domains. A summary of the frequency of each orientation is provided in Table 6.10. The strong preference for $\langle 310 \rangle$ is extremely promising for both the delivery of an external electric field to the thin film and for the birefringence of light incident along the crystal c-axis, as described in Section 4.2.

Whilst the preference for $\langle 310 \rangle$ oriented growth is encouraging, it isn't necessarily a given, and a reasonable frequency of domains will still be inaccessible in the proposed cavity architecture. In future work, it is possible that the thin-film growth

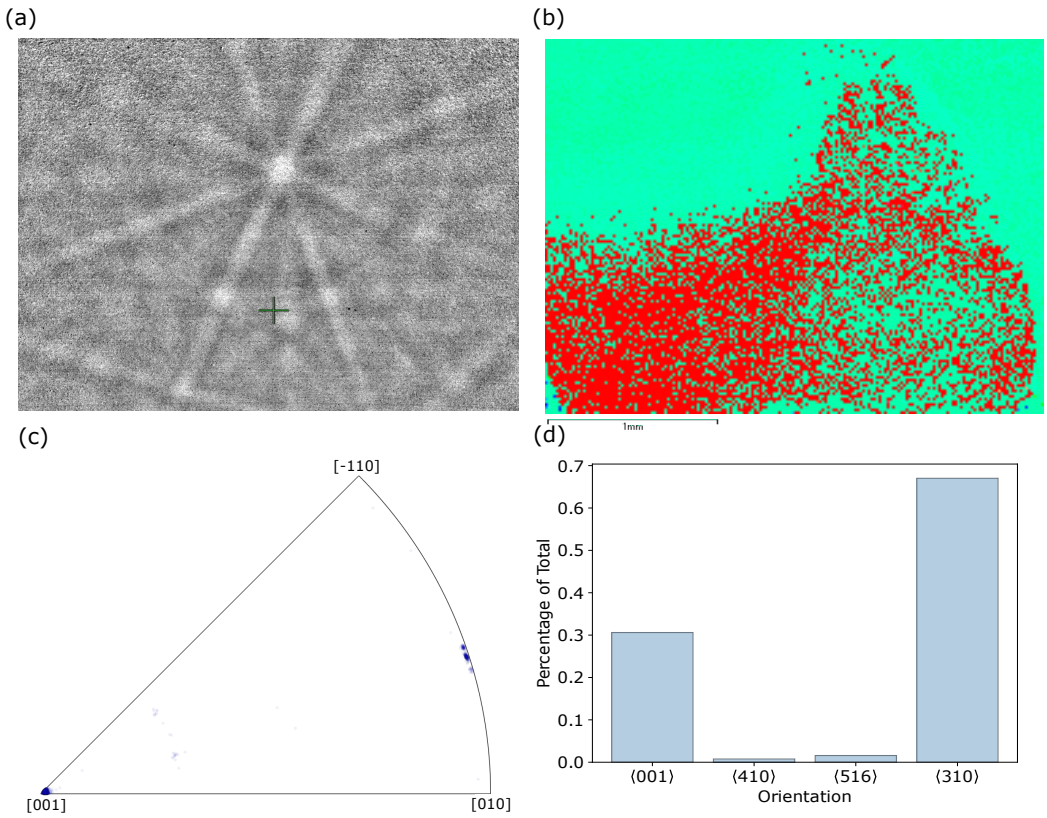

Figure 6.13: **EBSD of SBN75 thin-film grown onto MgO:** (a) EBSD Kikuchi pattern showing a strong $\langle 310 \rangle$ centre orientation; (b) Inverse pole map in the z-axis, mapping grain orientations to a z-axis IPF, The green grains are $\langle 310 \rangle$ oriented, and the red grains are $\langle 001 \rangle$ oriented; (c) Upper inverse pole figure displaying a density of $\langle 310 \rangle$, $\langle 001 \rangle$, $\langle 410 \rangle$ and $\langle 516 \rangle$ grains; (d) Normalised histogram of grain orientations

could be encouraged to substantially suppress $\langle 001 \rangle$ growth. One potential means to achieve this would be to carefully select the substrate surface termination to encourage one orientation over another. Another means could be grow on novel substrates such as gadolinium gallium garnet, which have a principal axis closely matched to the a-axis of SBN.

Table 6.10: **Summary frequency of domain orientations**

Orientation	Frequency (%)
$\langle 001 \rangle$	30.61
$\langle 410 \rangle$	0.78
$\langle 516 \rangle$	1.58
$\langle 310 \rangle$	67.02

6.5 Observation of Ferroelectricity by Piezoresponse Force Microscopy

It is well established that SBN when in the tetragonal tungsten bronze phase is a relaxor ferroelectric, and therefore it is prudent to determine the degree to which the grown thin film can be polarised by an externally applied field, since this is a strong indicator of the successful growth of the thin-film with desirable optoelectric properties. More importantly, in a ferroelectric film with multiple domains, varying orientations of the ferroelectric domains will result in the bias electric field having a different affect on differently oriented domains

Ferroelectricity can be measured directly in thin-film materials using the piezoresponse force microscopy (PFM) technique, in which an atomic force microscopy (AFM) probe is brought into proximity with the sample film and biased with an AC electric field to induce deformation in the sample film via the converse piezoelectric effect (CPE) [267]. When the probe is brought into contact with a ferroelectric material, the sample becomes deformed proportionally to the magnitude of its piezoelectric tensor components. The magnitude of the piezoresponse force induced by the bias field can be detected with a lock-in detection scheme.

The polarisability of SBN in the presence of an externally applied electric field deposited on MgO, $SrTiO_3$+ $SrAl_2O_6$ and diamond is shown in Figures 6.14,6.15,

and 6.16 respectively. In each figure, a bias voltage is applied to the sample at a magnitude of $1V$, $5V$, and $10V$ moving left to right on the figure. The AFM tip is scanned across an area of 5μm^2 and the phase response is plotted.

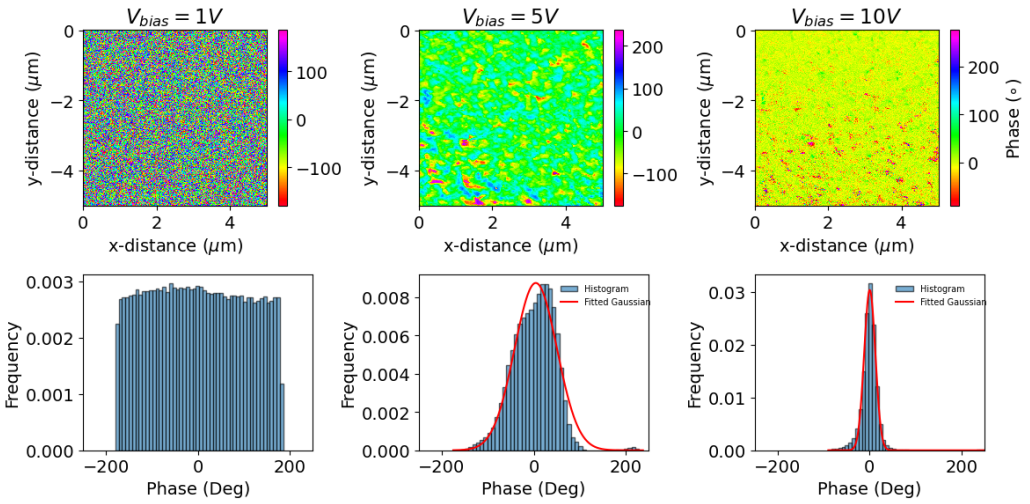

Figure 6.14: **Piezoresponse Force Microscopy (PFM) mapping of SBN on MgO.** At a 1V bias, the ferroelectric domains are randomly oriented, but as the bias voltage increases to 5V and 10V, the ferroelectric domains are become strongly aligned. The histograms in the bottom half show the distribution of ferroelectric domain phase orientations in response to each applied bias voltage.

For SBN grown onto an MgO substrate, at a 1V bias, the ferroelectric domains are randomly oriented (Figure 6.14). However, as the bias voltage increases to 5V and 10V evident regions where the ferroelectric domains are aligned become apparent. The histograms in the bottom half of Figure 6.14 show the distribution of ferroelectric domain phase orientations in response to each applied bias voltage. With increasing voltage, the collective orientation moves from being evenly randomly distributed, to tightly oriented in a common phase orientation.

The phase histograms for the SBN grown onto MgO and STO+SAl are summarised in Table 6.11. For SBN grown onto MgO, it takes a higher bias voltage to pole the domains compared to SBN grown onto STO+SAl, and therefore the

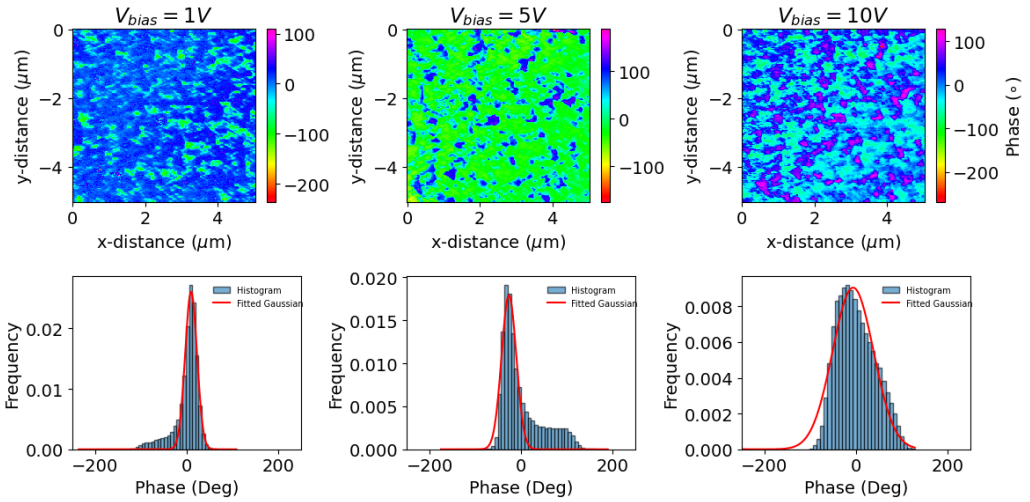

Figure 6.15: **Piezoresponse Force Microscopy (PFM) mapping of SBN on STO+SAl.** The ferroelectric domains are already quite well aligned at a bias voltage of 1V. At higher voltages, the phase behaviour becomes more complicated suggesting a more dynamic response possibly due to interfacial effects.

phase distribution is uniform for V_{bias}=1 V. At low bias ($5V$), the phase amplitude is low (0.009), and the distribution's mean value is high (4.302), with large standard deviation σ (46.179) and FWHM (108.743). This indicates a broad distribution of phase values with a relatively weak response. At higher bias ($10V$), the amplitude increases significantly to 0.030, and the distribution becomes sharper (reduced σ and FWHM). The mean value also decreases sharply to 0.208, suggesting a transition in domain behavior or alignment. On the other hand, for SBN grown onto STO+SAl, at $1V$, the amplitude is 0.026, with a mean phase of 10.060. The standard deviation (σ) and FWHM indicate a moderately narrow distribution. At $5V$, the mean phase shifts strongly negative (-26.824), the amplitude decreases to 0.018, and the spread (σ and FWHM) increases. This suggests a redistribution of domain orientations with weaker overall alignment. At $10V$, the mean returns closer to zero (-6.285), with a sharp drop in amplitude to 0.009 and a large spread (σ=44.800, FWHM=105.496), implying a highly disordered

or mixed domain state.

The film grown onto MgO exhibits a more pronounced amplitude increase with voltage than STO+SAl, suggesting stronger domain polarisation response to higher fields. It also shows narrowing of the distribution (smaller σ and FWHM) with increased bias, indicating improved domain alignment or polarisation uniformity. The film grown onto STO+SAl demonstrates more complex behaviour, with the distribution widening and the mean shifting significantly, suggesting a more dynamic or less stable response. The sign and magnitude of the mean phase vary significantly between samples and voltages, reflecting differences in domain orientation and material-specific ferroelectric properties. These results suggest that SBN grown onto MgO responds more uniformly to increasing bias, while SBN grown on STO+SAl exhibits more complex domain dynamics, possibly due to interface or domain interaction effects.

Table 6.11: **Summary of the ferroelectric domain orientation histograms observed by PFM for SBN grown onto MgO and STO+SAl.**

Sample	V_{bias}	Amp	Mean	σ	FWHM
MgO	$1V$				
	$5V$	0.009	4.302	46.179	108.743
	$10V$	0.030	0.208	12.145	28.600
STO+SAl	1V	0.026	10.060	12.994	30.598
	5V	0.018	-26.824	16.131	37.986
	10V	0.009	-6.285	44.800	105.496

Since the intention of the final application is to incorporate a thin-film of SBN onto a diamond membrane, it is worthwhile considering the quality of the thin film when grown directly onto diamond. Therefore SBN was also grown onto a single crystal electronic grade piece of bulk diamond, provided by element6. When measuring the microstructure and optical characteristics of the deposited thin film, it was not possible to acquire reliable data. PFM is not so limited by

the small size of the diamond chip, and therefore it is useful to consider whether a ferroelectric effect is found in the film deposited on diamond.

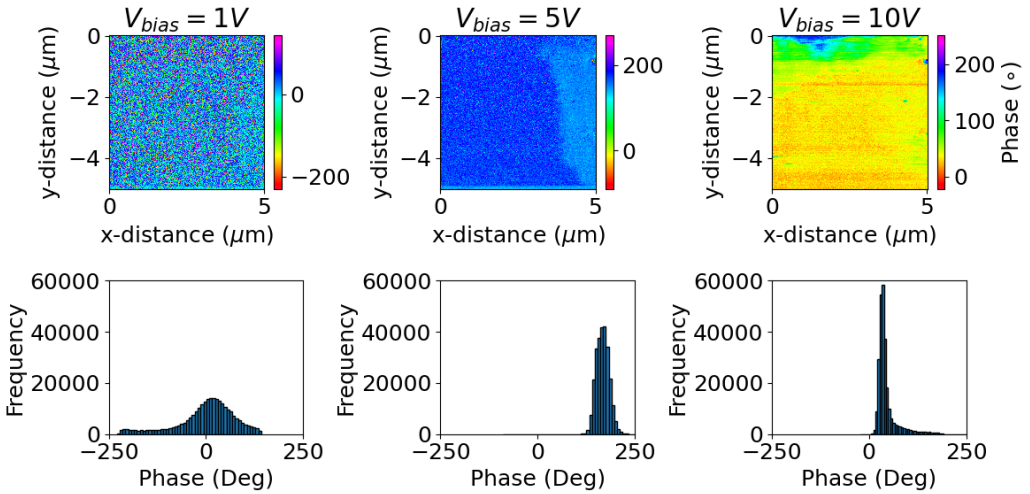

Figure 6.16: **Piezoresponse Force Microscopy (PFM) mapping of SBN on Diamond.** The apparent alignment of domains at higher bias voltages is an artefact of tip-sample charging, and is not revealing of a ferroelectric response.

Figure 6.16 shows a phase map for SBN grown onto diamond. Although at first glance it may appear that there is a strong polarisability of the thin film, but the apparent phase change here is not due to a ferroelectric effect. Rather, this is an an artefact due to the charge interaction between the AFM probe and the sample. Indeed, consistent with the microstructural and optical measurements of SBN grown onto diamond, there does not appear to be a ferroelectric effect in this film.

Figure 6.17 shows a hysteresis curve of the phase response for each thin-film sample, in the 'on-field' and 'off-field' states. The on-field state of the piezoelectric response is measured when a DC bias field (in addition to the AC driving voltage) is applied to the material, directly influencing the orientation of the ferroelectric domains. Domains aligned with the field will switch or stabilise their polarisation direction, altering the piezoelectric response phase. This can reveal information about switching dynamics and coercive fields. On the other hand, the off-field

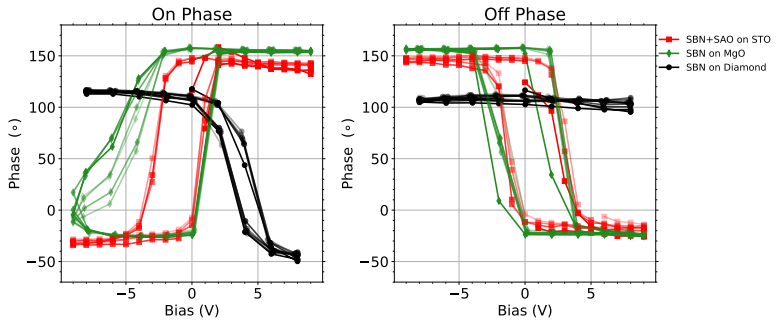

Figure 6.17: **Piezoresponse Force Microscopy (PFM) measurement of SBN on various substrates.** Induced phase hysteresis curve in (a) 'On-state' and (b) 'off-state'. The coercive and saturation voltages can be found from these hysteresis curves. In the on-state, SBN grown on diamond has an apparent hysteresis. However, this is not present in the off-state, suggesting that the observed domain alignment is an artefact of the tip-sample interaction, not ferroelectricity.

State is the phase of the piezoelectric response when no external DC bias field is applied, but only the AC driving voltage is present. The phase corresponds to the material's inherent polarisation state without external bias influence, and reflects the natural polarisation direction of the domains after a switching or poling event. This helps to indicate the the stable remanent polarisation state of the material, and distinguish between real poling effects, and a response which is due to tip-sample interactions. Since there is no remanent response for diamond in the off-field state, the apparent effect seen in the on-field state is likely an artefact of a tip-sample interaction.

PFM does not extract directly the polarisation field of the materials ferroelectric domains: rather, it extracts epiphenomena which arise as a result of the ferroelectric behaviour, such as hysteretic phase switching. From this, it is possible to deduce a number of important parameters such as saturation field and coercive field.

The coercive, saturation, and remanent voltages and electric fields for SBN grown onto MgO and STO+SAl, obtained by PFM, are given in Table 6.12. The coercive

Table 6.12: **Coercive, saturation, and remanent field of SBN grown onto MgO and STO+SAl, observed by PFM**

Substrate	V_{coerc}	E_{coerc}	V_{sat}	E_{sat}	V_{rem}	E_{rem}
MgO	1.0 V	10 MV/m	2.25 V	22.5 MV/m	6.5 V	65 MV/m
STO+SAl	0.5 V	5 MV/m	2.0 V	20 MV/m	2.75 V	27.5 MV/m

field for MgO is twice as high as that for STO+SAl, indicating that it requires a higher electric field to switch the polarisation. This could imply stronger domain pinning or larger energy barriers for domain switching in the MgO sample, potentially due to interactions at the interface. The saturation field values are relatively close, suggesting that both substrates allow the domains to fully polarise under similar electric field strengths. However, MgO requires a slightly higher field to reach saturation, consistent with the higher coercive field. The remanent field (after the external voltage is removed) is significantly higher for MgO, indicating much stronger polarisation retention. This suggests that SBN grown on MgO has more stable domains or better polarisation locking compared to STO+SAl. All voltage values for MgO are higher than for STO+SAl, reflecting the overall stronger polarisation retention and higher energy barriers associated with the MgO substrate. The large V_{rem} for MgO (6.5 V) compared to STO+SAl (2.75 V) could point to substrate-induced effects, such as strain or stronger interfacial bonding.

The MgO substrate enhances the stability and strength of ferroelectric domains in SBN, as seen in the higher E_{coerc}, E_{sat}, and E_{rem} values. This suggests it may be a better choice for applications requiring robust and stable ferroelectric properties, and the MgO sample may be more favourable to allowing a higher electro-optic coefficient than the STO+SAl film. On the other hand, the STO+SAl substrate, with lower fields, indicates easier polarization switching, which might be advantageous for applications requiring low-power operation or rapid domain switching.

6.6 Surface Roughness

The surface roughness of the SBN thin-film is a crucial fabrication parameter which must be considered, since a rough layer may have a profound impact on the optical properties of the microcavity. The surface roughness for the SBN thin-films was measured by optical profilometry, and after mean plane subtraction was found to be below 1 nm (R_{Sq}=0.9306 nm and R_{Sa}=0.7436 nm). A summary table of the measured surface roughness is provided in Table 6.13

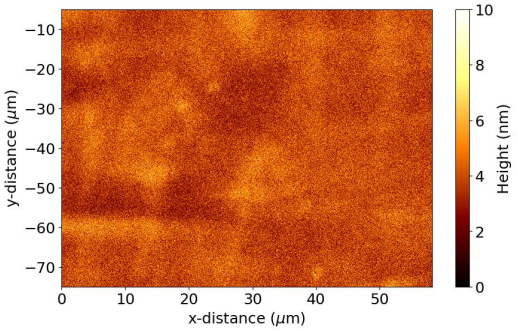

Figure 6.18: **SBN:75 on MgO surface roughness measured by optical profilometry.** Whilst the maximum peak height is around 10 nm, root mean square roughness is sub-nm, and so the thin-film has promise for further device integration.

Table 6.13: **Surface roughness of SBN75 on MgO substrate**

Parameter	Value
Average Value	4.118 nm
RMS Roughness (Sq)	0.9306 nm
Mean Roughness (Sa)	0.7436 nm

6.6.1 Impact of Roughness on Cavity Quality Factor

To assess the impact of a rough surface on the performance of an optical microcavity, it is not resource efficient to do so by physical experiment. Rather it is more prudent to feed real-world information from measured samples into an appropriate

model. Therefore, the FDTD method was applied to assess the impact of an artificially rough surface with the roughness parameters determined experimentally above. An artificially rough surface was therefore numerically generated by the correlation function method detailed in Section 4.4.5.1 (Figure 6.19(a)), and provided as a surface layer in FDTD simulation. Figure 6.19(b) shows a comparison between the resonant cavity wavelength of a monolithic microcavity with an ideal SBN layer, one with rough numerical layer corresponding to the measured surface roughness in Figure 6.18, and one more with a very large surface roughness of Sa=35 nm to demonstrate the extreme case of surface roughness. To reduce computation time, the cavity longitudinal mode index was kept small at $q = 6$. The other cavity parameters used in this simulation are shown in Table 6.14

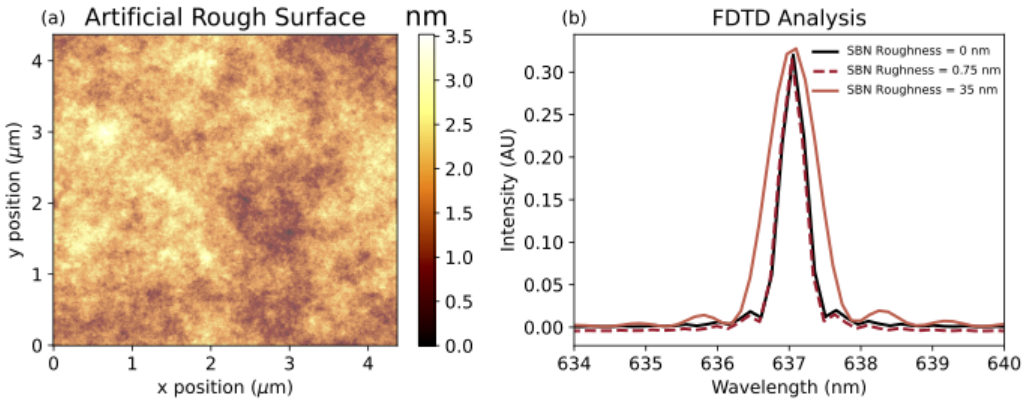

Figure 6.19: **Impact of surface roughness on cavity modes:** (a) An artificially rough surface was generated by a correlation function and provided to the FDTD software. (b) The impact of this layer on the cavity fundamental mode was assessed by FDTD simulation.

In the FDTD simulation, the quality factor of the resonant mode of the cavity with an ideal SBN layer Q=3600, while adding a layer with roughness Sa=750 pm and 35 pm yielded Q=3551 and Q=3067 respectively. Since a surface roughness of 750 pm is quite small, the impact on the cavity was correspondingly negligible at a reduction of 1.36%, corresponding to an additional round trip loss of approxi-

Table 6.14: **Cavity parameters used in FDTD simulation of impact of surface roughness on cavity mode.**

Parameter	Value
q	6
Radius of Curvature	$3\mu m$
N # Featured Mirrors	11
No # Planar Mirrors	16
SBN thickness	325 nm
Mesh Accuracy	3
Average Roughness (rms)	35 nm

mately 0.022%. Even in the highly unlikely scenario of a substantially rough SBN layer of 35 nm, the reduction in Q factor is approximately 25%, corresponding to an enhanced round trip loss of 0.48%, which would be practically a manageable tolerance. These FDTD results are summaries in Table 6.15

Table 6.15: **Summary of the impact of artificially rough layers of SBN on quality factor of a cavity mode.**

Roughness (nm)	Q Factor	Q Factor Reduction	Round Trip Loss
0	3600		
0.75	3551	1.36%	0.022%
35	3067	25%	0.48%

6.7 Chapter Summary

In this chapter, we detailed the growth of SBN thin films onto a variety of substrates by Pulsed Laser Deposition. The growth conditions of the ceramic target materials are important factors for the grown film and were therefore carefully considered and characterised. The microstructure of the SBN thin-films was characterised by XRD and the impact of substrate choice on the microstructure was studied, revealing that compared to thin-film growth on MgO substrates, growth onto $SrTiO_3$ provides lower microstrain and dislocation density and smaller crys-

tallites. Meanwhile growth onto $SrTiO_3$ with an interfacial layer of $SrAl_2O_6$ also provides improvements in these figures of merit compared to MgO.

Through EBSD, the domain orientation of the grown thin-films was studied, revealing preference for growth in the $\langle 310 \rangle$ orientation over $\langle 001 \rangle$. This is a crucial factor for the proposed cavity tuning architecture. This preference can be improved further by pre-treating the substrate with a TiO_2 layer.

By PFM, we demonstrated that the thin films grown onto MgO and $SrTiO_3$ + $SrAl_2O_6$ possess an intrinsic polarisation consistent with ferroelectricity, and we characterised polarisability and ferroelectric domain size. Unfortunately, growing directly onto a diamond plate does not appear to yield a film with this property. The surface roughness of the grown thin-films were shown to be sub-nm, and the potential impact of the measured surface roughness on cavity performance was studied by FDTD simulation, and was found to be negligible.

7 | Optical and Electro-Optical Characterisation of SBN Thin-Films

The optical properties of electro-optic thin films are key to understanding both their tunability by external electric fields and the influence of their integration on the overall optical performance of a cavity. In Chapter 4.2, we derived the electro-optic tensor for SBN and demonstrated how the application of an external electric field modifies the index ellipsoid. To fully comprehend the films grown in this project, it is essential to populate the impermeability tensor with accurate values for the ordinary and extraordinary refractive indices. Additionally, since cavity photons oscillate and decay with time constants proportional to the losses in cavity materials, it is critical for materials incorporated into the device to exhibit minimal loss at the operational wavelength. This first part of this section details the measurement of both refractive indices and absorption coefficients for SBN.

In the second part of this section, the effective electro-optic coefficient for the SBN thin-film is reported following measurement on a purpose built polarisation interferometer. Consistent with the strong Pockels effect observed in literature, we extract a Pockels coefficient of 399 pm/V, 436 pm/V, and 318 pm/V for SBN grown onto MgO, $SrTiO_3$, and $SrTiO_3$ + an $SrAl_2O_6$ sacrificial layer respectively. With this, the complete FDTD model reflecting the real-world materials is constructed to predict the cavity tunability for this material.

7.1 Spectroscopic Ellipsometry of SBN Thin Films

The complex reflectance of SBN thin films grown on MgO, $SrTiO_3$, and $SrTiO_3$ with a $SrAl_2O_6$ sacrificial layer is plotted in Figure 7.1 for wavelengths between

200-1650 nm. In Figure 7.1(a), the reflectance spectra does suggest the presence of an absorption edge at lower wavelengths, corroborating a prediction in the literature [193]. The observed absorption edge possesses an elongated tail, which may be explained by first principles studies conducted on $Ba_{0.5}Sr_{0.5}TiO_3$ [268], which suggested that the presence of an absorption edge with a tail implies localised defect states which are at least in part responsible for the absorption.

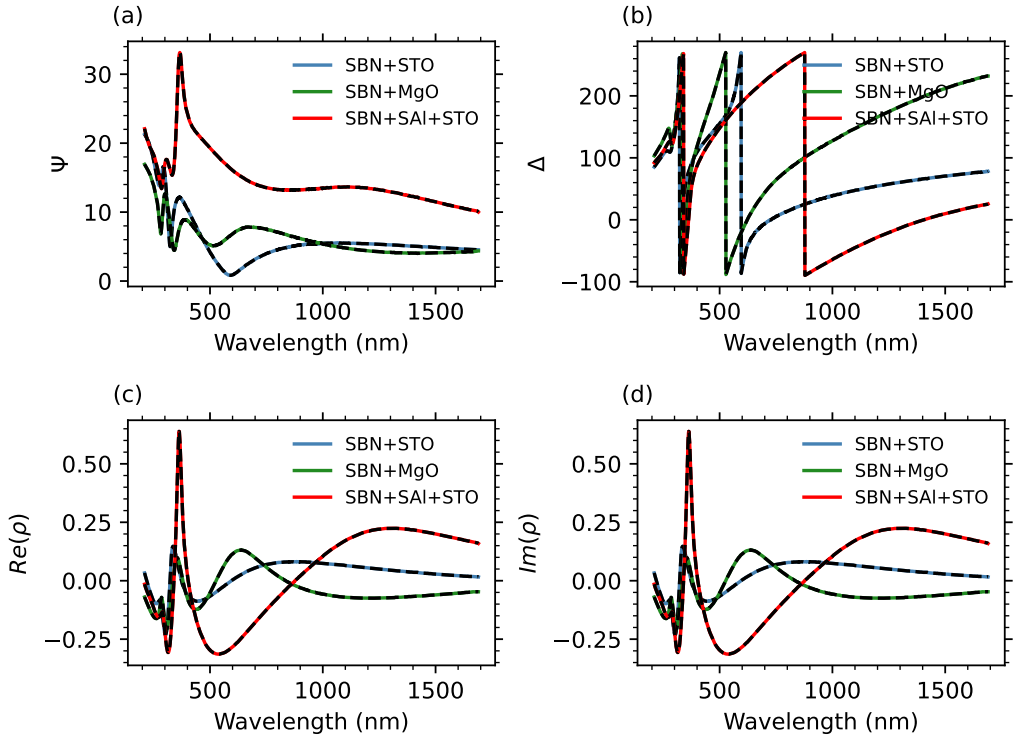

Figure 7.1: **Complex reflectance of SBN thin-films measured by ellipsometry:** (a) Amplitude coefficient; (b) phase shift; (c) real component of the complex reflectance; (d) imaginary component of the complex reflectance. The black dashed lines in each plot are the fitted data from the Tauc-Lorentz model.

These data give extra vindication for the choice of the Tauc-Lorentz model, which was developed specifically to calculate the band gap unambiguously in the presence of defect state absorption [195, 196]. Although the model was initially developed with amorphous semiconductors in mind, it can be employed when-

ever interband absorption is not the only absorption source, as was demonstrated in [269].

Figure 7.1 shows the amplitude coefficient Ψ (a), phase component $\Delta(b)$, and real (c) and imaginary (d) components of the complex reflectance ρ, for SBN grown onto MgO, $SrTiO_3$, and $SrTiO_3$ with a sacrificial layer. In each plot, black dashed lines show the result of the data fit to the Tauc-Lorentz model. Thin-films grown onto MgO and $SrTiO_3$ possess very close optical characteristics, with the harmonic response of films grown on $SrTiO_3$ slightly leading (in terms of phase response) those grown on MgO. On the other hand, the oscillation of the film grown on a sacrificial layer substantially lags behind the other other substrates

The Tauc-Lorentz model is a model of the dielectric function and not directly the complex reflectance. The two quantities are related though, since in ellipsometric data, the s- and p- reflected light components are given by Equation 7.2, where $\theta_{i,t}$ are the incident and transmitted angles respectively, and $n{=}\sqrt{\epsilon}$. Therefore the components of the complex reflectance can be found in terms of the dielectric model.

$$r_s = \frac{n_1 \cos\theta_i - n_2 \cos\theta_t}{n_1 \cos\theta_i + n_2 \cos\theta_t} \tag{7.1}$$

$$r_s = \frac{n_2 \cos\theta_i - n_1 \cos\theta_t}{n_2 \cos\theta_i + n_1 \cos\theta_t} \tag{7.2}$$

For each thin-film measured, the data fitting was performed using the CompleteEase software, standard to the Wolfram M-2000 ellipsometer. For SBN grown onto $SrTiO_3$ and MgO substrates, the thin film material was represented as infinitely deep $SrTiO_3$ and MgO respectively with optical parameter well defined by a standard dielectric model library. The SBN layer was defined as a effec-

tive medium described by a Tauc-Lorentz oscillator, and with surface roughness and film thickness included. For the SBN grown onto $SrTiO_3$ with a sacrificial $SrAl_2O_6$ layer, the secondary layer was modelled as a simple Cauchy material. Since the $SrAl_2O_6$ layer likely has it's own absorption edge which would be defined properly with the Tauc-Lorentz model, for practical purposes, attempting to fit a model with two Tauc-Lorentz oscillators can be extremely cumbersome, and since the absorption edge of this material is not of interest here, it is appropriate to consider the material to be a generic oscillator.

Table 7.1: **Fitted parameter from the Tauc-Lorentz model applied to SBN thin films**

Material	MSE	ϵ_∞	E_g
SBN + $SrTiO_3$	1.2461	4.4944 ± 0.0472	3.938 ± 0.001
SBN + MgO	0.7175	4.4521 ± 0.0658	3.896 ± 0.001
SBN + $SrTiO_3$ + $SrAl_2O_6$	1.2254	4.8026 ± 0.0622	3.589 ± 0.001

To refine the fit of the model, thickness and surface roughness were included as variable parameters, and both thickness non-uniformity and depolarisation data were included.

In Figure 7.2, the modelled components of the complex dielectric function for each thin-film is shown as a function of photon energy. The complex component ϵ_2 (Figure 7.2(b)) clearly demonstrates a long absorption tail at energies above 4 eV and indeed appear very close to one another up to energies of 5 eV, and therefore the band-gap energies are correspondingly close to one another at 3.938 eV and 3.896 eV for films grown onto $SrTiO_3$ and MgO respectively (Table 7.1). For the SBN grown onto the sacrificial layer however, the absorption edge and band-gap is shifted to 3.58 eV.

The real component of the dielectric function is represented by ϵ_∞ in Table 7.1, and expresses the high-frequency dielectric constant excluding contributions from

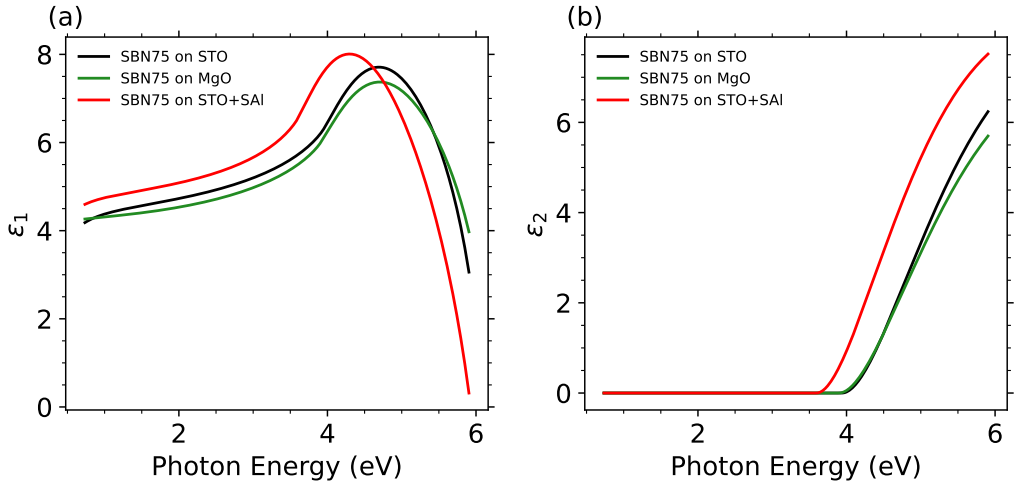

Figure 7.2: **Dielectric function of SBN thin films:** (a) Real component ϵ_1; (b) Imaginary component ϵ_2. The real component ϵ_1 (a) is related to the complex component by the Kramers-Kronig relations. The complex component ϵ_2 (b) demonstrates a long absorption tail at energies above 4 eV. Photon energies of SBN films grown on MgO and STO are close to one another up to energies of 5 eV, but for SBN grown onto SAL+STO, the absorption edge and band-gap is shifted to 3.58 eV.

free carriers and lattice vibrations. Since the imaginary and real components of ϵ are related by the Kramers-Kronig relations, the absorption edge in Figure 7.2(b) is reflected by broad peak in the real component (Figure 7.2(a)).

For inclusion as a tuneable material in optical microcavities, the refractive index and extinction coefficient are very important quantities. These quantities are shown in Figure 7.3 for each thin-film, but here the presentation of the analysis is confined to the primarily transparent region of interest (although the initial fitting was conducted over a region including the absorption edge.) SBN grown onto $SrTiO_3$ demonstrates negative uniaxial birefringence, corroborating earlier optical studies in the literature [191, 192]. However, the SBN grown onto MgO here is shown to be positive uniaxial. This is likely due to the misfit strain of the interface revealed by XRD analysis in Chapter 6.3.2. Meanwhile, thin-films grown

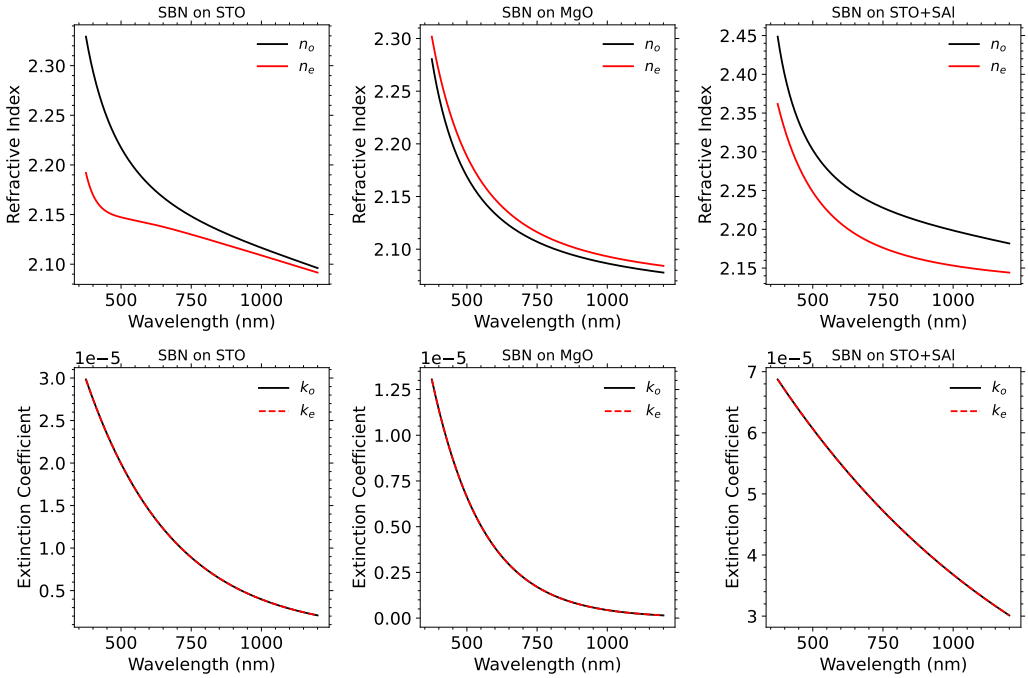

Figure 7.3: **Comparison of refractive index and extinction coefficients for SBN grown on different substrates**. SBN grown onto $SrTiO_3$ demonstrates negative uniaxial birefringence, but on MgO here is positive uniaxial, likely due to the misfit strain. Thin-films grown onto the sacrificial layer are negative uniaxial with a slightly higher refractive index. The extinction coefficient for all substrates is of the order 10^{-5}.

onto the sacrificial layer remain negative uniaxial with a slightly higher refractive index. For all substrates, the extinction coefficient is of the order 10^{-5}, making the material highly suitable for integration into an optical microcavity.

7.1.1 FDTD Simulation with Modelled SBN

The measured refractive index and extinction coefficient for the SBN grown onto $SrTiO_3$ and $SrAl_2O_6$ were included into the FDTD model of the optical microcavities to asses the potential impact of the SBN layer on the cavity performance. A highly absorbing material will inhibit the cavity quality factor since the round trip photon loss would inhibit temporal mode confinement. Therefore it is important

to consider what the impact would be of any absorption on the cavity performance.

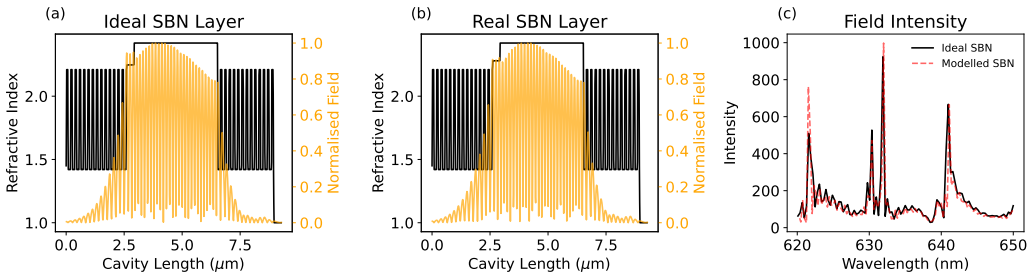

Figure 7.4: **FDTD analysis of impact of SBN on cavity fields:** (a) Impact of an ideal dielectric SBN layer on cavity field profile - the field intensity in the ideal SBN layer is marginally larger than that in the SBN layer possessing the refractive index and extinction coefficients of the SBN thin-film grown onto $SrTiO_3$ (b). In (c), there is a comparison of impact of ideal and measured SBN layers on cavity resonance peaks, which is clearly minimal.

Figure 7.4(a) shows the normalised field intensity simulated by the FDTD method, in a 8μm radius of curvature cavity with longitudinal index q=30 and an SBN layer represented as an ideal dielectric. In this model, the dipole source sits at an anti-node at the centre of the diamond, and the cavity is enclosed by ideal DBR mirrors. The field intensity in the ideal SBN layer is marginally larger than that in the SBN layer possessing the refractive index and extinction coefficients of the SBN thin-film grown onto $SrTiO_3$ (Figure 7.4(b)). In the ideal case, the normalised field intensity maxima in the SBN layer is 0.9492, whereas in real case, it is 0.9188. Correspondingly, the SBN layer has much smaller impact on the cavity resonance modes compared to the ideal case (Figure 7.4(c)). The inclusion of the measured SBN layer also reveals minimal impact on the quality factor and Purcell factor (Table 7.2). The SBN layer here is modelled as being 100 nm thick since this was the measured thickness of the grown film. Ideally, the SBN layer would be thicker, up to 1 μm, since this would allow provide a larger quality factor (since Q depends on the number of longitudinal modes supported within the cavity, which depends on cavity length) whilst having a small impact on the

mode volume. However, in practice, growing such thick SBN layers would require rather a long growth time, with a growth rate of approximately 1 nm per minute. Therefore, for the present work a compromise of film thicknesses of 100 nm was chosen.

Table 7.2: **Table of cavity figures of merit for the ideal and real SBN materials modelled in FDTD simulation.**

SBN Layer	Q-Factor	Purcell Factor
Ideal	40289	49.527
Modelled	39871	47.219

7.2 Measurement of Pockels Coefficients by Polarisation Interferometry

Following the procedure in Section 3.7, the effective Pockels coefficients (r_{eff}) for SBN films grown on MgO, STO, and STO+SAl substrates were measured using polarisation interferometry. The transmitted power, varying sinusoidally with the polarimeter analyser angle, was fitted using Equation 3.6. Exemplary data for SBN on MgO is shown in Figure 7.5(a), with a high fit quality (R^2=0.999). The normalised transmitted power change, $\Delta P/P$, increases linearly with bias voltage, confirming the linear electro-optic effect (Figure 7.5(b)).

The polarisation rotation δ under applied fields was extracted by differentiating $P(\theta_a)$ and fitting $\Delta P/P$ using Equation 3.7, accounting for background contributions with a term A. The modulated power was fitted using P=$P_{max}\cos^2(\theta_a - \theta_{a,off})+P_{BG}$. Results for SBN on (a) MgO, (b) STO, and (c) STO+SAl are shown in Figure 7.6. In each case the derivative decreases polynomially due to the cosinusoidally varying power term in the denominator of Equation 3.7. The slope and peak magnitude of the fits are related to the rotation δ of the polarisation as

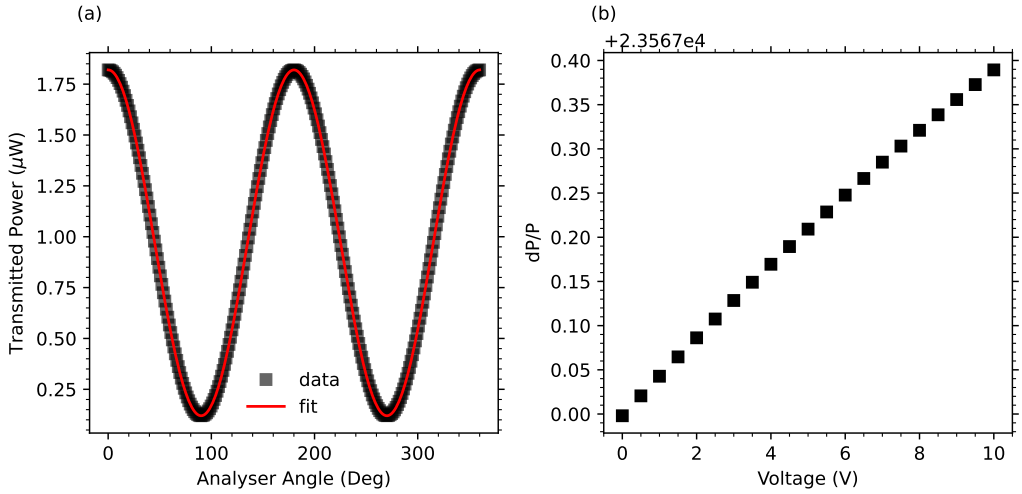

Figure 7.5: **Optical power transmission through SBN:** (a) As thye analyser angle is rotated through $360°$, the detected powervaries sinusoidally; (b) Normalised power transmission vs. bias voltage. The increase in this power transmission confirms the presence of a Pockels effect.

the light passes through the SBN sample, which relates to the effective Pockels coefficient, determined by Equation 3.9.

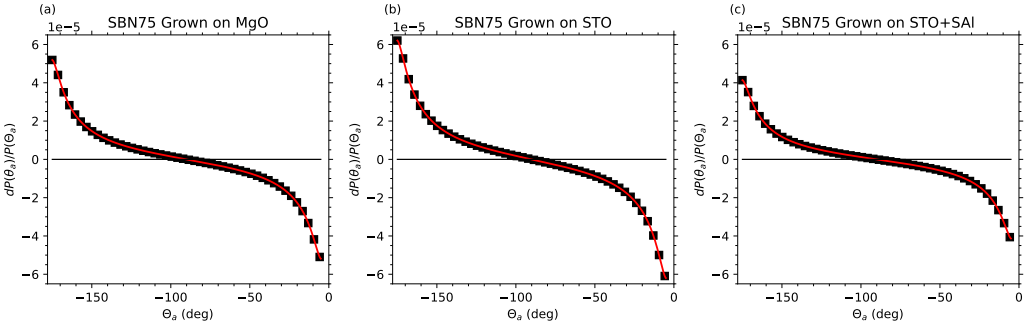

Figure 7.6: **Fitted power differential with respect to analyser angle.** For SBN grown onto (a) MgO; (b) STO; (c) STO+SAl, the fit to the differential power reveals the magnitude of the effective Pockels coefficient (see main text).

A table summarising the δ and background A values extracted from the fitting procedure, as well as the resulting r_{eff} values, is provided in Table 7.3. The largest Pockels coefficient of r_{eff}=436 pm/V was observed for SBN grown onto STO,

whilst SBN grown onto MgO was slightly lower at r_{eff}=399 pm/V. The lowest Pockels coefficient was observed on the hybrid STO+SAl substrate, at r_{eff}=318 pm/V. These values are smaller than the r_{33}=844 pm/V observed in [270], although this is not a fair comparison since we are inferring an effective Pockels coefficient combining two tensor components, r_{33} and r_{13} as opposed to just the r_{33} coefficient. A more fair comparison is with the r_{eff}=387 pm/V for SBN grown onto STO by RF sputtering, recently reported in [271]. The PLD growth in this work provides a substantially higher electro-optic effect.

Table 7.3: **Measured Pockels Coefficients for SBN films.**

Substrate	δ	A	r_{eff} (pm/V)
MgO	25.1×10^{-5}	1.19×10^{-12}	399
STO	36.0×10^{-5}	1.00×10^{-12}	436
STO+SAl	20.0×10^{-5}	1.24×10^{-12}	318

The incident angle θ_i set by the halfwave plate also plays an important role. Figure 7.7 shows the impact of θ_i on r_{eff} for each thin film sample. When the incident polarisation varies the observed Pockels coefficient correspondingly varies, with a peak r_{eff} observed at 90° and a minimum r_{eff} seen at 0°. The average effective Pockels coefficients for each thin-film device were 181.19 pm/V, 182.40 pm/V, and 139.62 pm/V for SBN grown on MgO, STO, and STO+SAl respectively.

7.2.1 Feedback from FDTD Simulation

With a measured effective Pockels coefficient for the SBN membrane, the expected effect on cavity performance and tunability can be remodelled. An FDTD model was built using the simulation parameters summarised in Table 7.4, whilst manually varying the set ideal refractive index of the SBN layer according to the expected shift in refractive index for a given bias voltage. For the cavity design, the electrodes are spaced by d=6μm, and therefore a bias voltage of $0 \leq V \leq 400$

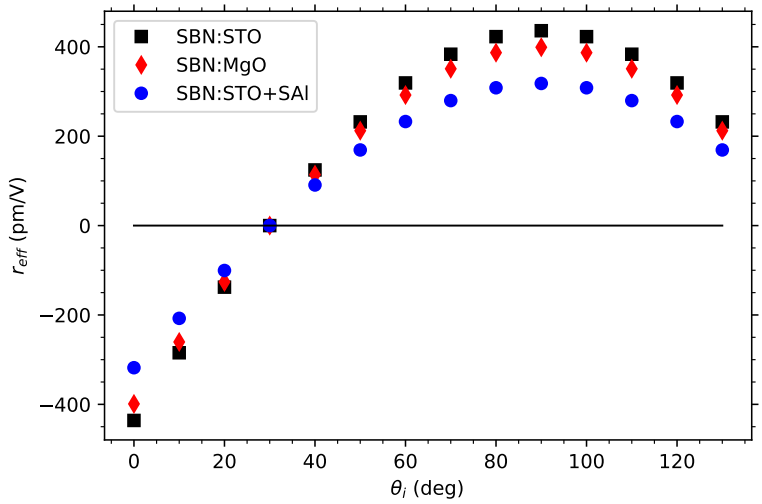

Figure 7.7: **Dependence of the Pockels effect on incident polarisation angle.** As the incident polarisation angle is modified, the alignment of the incident field with the ferroelectric domains of the SBN film is changed. There is therefore an ideal incident angle of transmission.

V relates to a bias electric field $E{=}V/d$ of $0 \leq E \leq 70 \times 10^6$ V/m. The materials in this simulation are set to be ideal dielectrics, since any dispersion and absorption should have a negligible impact on the wavelength tunability range.

Table 7.4: **Parameters of FDTD simulation for wavelength tuning with SBN**

Length	4 μm
RoC	8 μm
q	30
Nf	11
Np	16
MeshAcc	3

Figure 7.8 shows the results of the FDTD simulation for each thin-film sample. Over a bias voltage range of 400 V, the resonant wavelength is predicted to be substantially tunable, by 3.644 nm for SBN grown onto STO, 3.318 nm for SBN grown onto MgO, and 2.612 nm for SBN grown onto STO + SAl. Since the intended free-spectral range of this cavity is $FSR{=}\frac{\lambda^2}{2nL}{=}21.05$ nm for a cavity

of length L=4μm, with a bias voltage of 400 V, the cavity could in principal be wavelength tuned 15.764% of an FSR for SBN grown on MgO, 17.315% for STO, and 12.411% for STO+SAl, which is more than sufficient for practical application. Of course, growing SBN with even higher effective Pockels coefficients would enhance this tunability range even further. A summary table of the expected wavelength shift for a maximum bias voltage of 400 V is provided in Table 7.5.

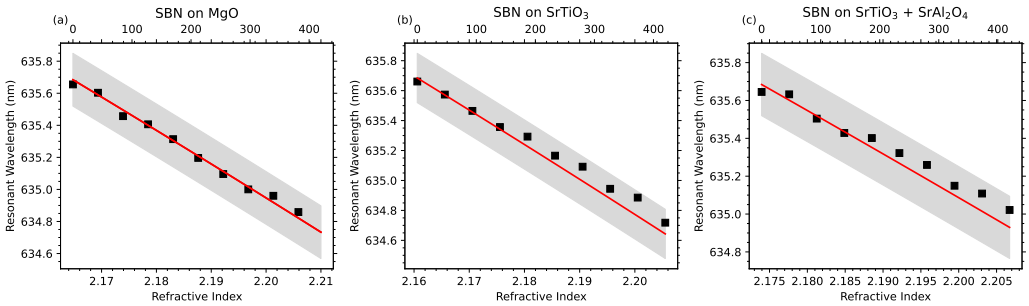

Figure 7.8: **FDTD analysis of SBN tunability:** Based on the magnitude of the effective Pockels coefficients r_{eff}, the SBN tunability of thin films grown onto substrates of (a) $SrTiO_3$; and (b) MgO, with a bias voltage of up to V_{bias}=100 V. The resonant wavelength is predicted to be substantially tunable, by 3.644 nm for SBN grown onto STO, 3.318 nm for SBN grown onto MgO, and 2.612 nm for SBN grown onto STO + SAl.

Table 7.5: **Wavelength shift and tunability as a percentage of free-spectral range**

Sample	$\Delta\lambda$ (nm)	$\%$ of FSR
MgO	3.318	15.764%
STO	3.644	17.315%
STO+SAl	2.612	12.411%

7.3 Chapter Summary

In this chapter, we detailed the dielectric and electro-optic properties of SBN thin films grown onto MgO, $SrTiO_3$, and $SrTiO_3$ with a sacrificial $SrAl_2O_6$. From an

investigation by spectroscopic ellipsometry and thorough subsequent modelling using a Tauc-Lorentz approach, the optical properties of the thin-films were determined. The band gap energy of SBN grown on the sacrificial layer was found to be slightly lower than for films grown onto MgO or $SrTiO_3$, with a correspondingly red shifted absorption edge. Unlike previous observations in the literature, the uniaxial birefringence of SBN was shown, and was found to be negative for SBN grown onto $SrTiO_3$ and $SrTiO_3$ plus the sacrificial layer, but was found to be positive for SBN grown onto MgO, likely due to the large interface misfit strain. For each film, the extinction coefficient was found to be around 10^{-5}, making the film is highly suitable for integration into an optical microcavity, since its impact on round trip photon loss will be minimal. This is confirmed by FDTD simulation.

The electro-optic properties of each film were determined by polarisation interferometry, using a purpose-built optical system. Since only the effective Pockels coefficient is of interest for the present work, the Pockels tensor analysis was limited to this quantity only, and substantial r_{eff} coefficients were found for each film. Using the determined electro-optic coefficients, an FDTD model was built to investigate the wavelength tunability range for each film based on the know shift in refractive index. This revealed the possibility of substantial frequency tuning with each thin film. These characterisations complete the development of each individual constituent component of the intended final cavity device.

8 | Conclusions

Rapid progress towards achieving fault tolerant quantum computation is being made, and significant breakthroughs in quantum sensing and secure communications are continuing to come to fruition. A separate significant challenge remains to connect distant quantum processors over a quantum network. Diamond is a highly promising substrate for quantum network nodes, since it possesses a very low nuclear spin environment ensuring a noise free environment for quantum states, a variety of defect centres which can act as artificial atoms capable of quantum processing, and an optical interface allowing easy integration into optical communication networks. The NV defect centre in diamond is highly promising as a qubit candidate for quantum technology, and can be deterministically created in electronic-grade diamond by a novel laser writing process. However, the NV centre nascently has a poor spin-photon interface for quantum networks due to a low Debye-Waller factor.

To ensure the the NV centre can generate photons suitable for entanglement efficiently, it is necessary to couple the defect to the eigenmode of an optical microcavity. In the present work, we presented prototype results for the first monolithic microcavities in diamond for this purpose. The monolithic structure, combined with the ability to deterministically place a high-density of NV centres with high positional accuracy in diamond, makes substantial progress toward developing a scalable quantum network node based on NV centres. Tuning the resonant mode of a monolithic cavity is a substantial challenge, but progress towards a solution in this work by synthesising a membrane of a very strong electro-optic material which can be bonded to the diamond, and provide resonant wavelength tuning by modifying the optical path length of the cavity in situ with an applied electric field.

8.1 Summary of Research Achievements

This work demonstrated the **first prototypes of monolithic Fabry-Pérot cavities** in diamond using focused ion beam (FIB) milling to fabricate hemispherical features in 10μm membranes. DBR mirrors were deposited on these cavities, and the mode structure was probed by optical spectroscopy using a purpose built white light interferometer. While the DBR coating quality presented a limit to the achievable cavity finesse, the prototype structures revealed a stable longitudinal mode structure across a variety of radii of curvature cavities, which even with low reflectivity mirrors would provide a reasonable Purcell enhancement. This work provides a solid base for further optimisation. Indeed, with improved DBR coatings, the potential Purcell enhancement for embedded emitters could be substantial.

We proposed a **novel means of tuning the resonant mode** of these cavities using SBN, an extraordinarily strong electro-optic material. We derived the electro-optic tensor for this material and used this to inform device design considerations and we grew the material by pulsed laser deposition. We rigorously characterised the microstructure of SBN using techniques such as XRD and EBSD. To the best of our knowledge, our EBSD analysis and observation of the pseudosymmetry is the first analysis of its kind for this material, and reveals a strong $\langle 310 \rangle$ electro-optic domain growth axis. We also proposed a growth platform for producing releasable freestanding membranes of SBN by growing the films onto a sacrificial layer of strontium aluminate. This has the potential to open up platform independent photonic device integration for SBN thin-films.

In addition to the microstructural characterisation, **optical and electro-optical properties were studied for SBN** grown onto MgO, STO, and STO+SAl. We

improved on analyses of the dielectric function previously reported in literature by building a Tauc-Lorentz model and fitting this to complex reflectance data acquired by ellipsometry. An impact assessment of the dielectric properties of the SBN thin-films on potential cavity performance was undertaken, using the modelled optical properties of the SBN layers. In addition, using a purpose built polarimeter, we extracted high effective Pockels coefficient values for each thin-film.

Throughout the thesis, we endeavoured to build a complete model of the cavity devices by FDTD simulation using the real-world measured material parameters, in order to understand the impact of each constituent component in the cavity device design. With this insight, it is possible to isolate the effect of each element of the design and make specific improvements and optimisations in future work.

8.2 Current Status of the Technology

The work presented in this thesis contributes to overcoming some of the major technical barriers to realising efficient and scalable quantum network nodes. The aim of this work was to first identify how to fabricate monolithic microcavities, and crucially how best to allow for resonant mode tuning. With this achieved, the aim was to study each constituent component of the cavity design to build a rigorous understanding of each element. Some challenges remain, however. First, with each element of the design well characterised, further progress on DBR coating needs to be made. Second, the constituent elements of the cavity design need to be brought together to the final device. Finally, the scalability of the proposed fabrication methods, particularly FIB milling, requires further exploration. Despite these challenges, the synthesis of a very strong electro-optic tuning material, and the observance of cavity modes in monolithic structures, are significant steps

forward in the development of quantum optical devices.

8.3 Potential Impact

The enhanced coupling efficiencies and spectral tuning capabilities which will emerge from the cavities in this work improve the feasibility of long-distance quantum communication using NV centres in diamond, and offer the prospect of a substantial increase in the branching ratio of the NV centre. Due to anomalously high absorption in one of the DBR layers in the prototype cavities in this work, we infer a Purcell enhancement of 1.27 leading to an enhanced branching ratio of 2.56%. However, without the absorbance issue but with still low reflectivity mirrors, we infer that a Purcell enhancement of 17.45 is possible leading to an enhanced branching ratio of 35%. With substantially better DBR coatings available commercially, we expect the enhancement in branching ratio to be considerably higher again.

The techniques developed in this work could contribute to broader advancements in integrated photonics, including quantum information processing and hybrid quantum-classical devices. SBN is an extraordinarily strong electro-optic material, and we have discussed how freestanding membranes of this material can be synthesised and bonded to other substrates. This opens the door to substrate independent, highly tunable layers which can be readily integrated into a variety of optical platforms. In addition, since SBN retains its crystal symmetry at low temperature, we predict that the high Pockels effect should remain in cryogenic environments, making this material well suited to a variety of quantum optical applications.

In addition to extraordinary linear electro-optic and piezoelectric responses, SBNs tetragonal tungsten bronze crystal structure contains many vacant sites, allowing

it to be doped with a wide range of dopants such as rare earth and transition metals, allowing for many interesting optoelectronic applications such as frequency conversion. Introducing rare earth dopants into SBN could allow the material to operate as a quantum memory with a highly tunable interface.

8.4 Proposals for Future Work

Building on the foundation laid in this thesis, the following areas are proposed for future research. Most importantly, the prototype cavities in this work were limited by an anomalously high absorption in the TiO_2 DBR layer, which we attribute to contamination. With better DBR coatings, the performance of these cavities is expected to be substantially improved. With improved cavities in thin membranes, the SBN layer grown on the sacrificial SAl layer should be released and bonded to the planar side of the diamond membrane, and the full cavity device should be fabricated and integrated, with embedded NV centres. With this, integration into a quantum network via entanglement protocols can be explored.

Whilst FIB milling of the cavity features is an effective and highly controllable method, questions remain as to whether the process can inhibit device performance by the implantation of Ga^+ ions into the diamond membrane from the ion beam, and therefore it is prudent to investigate other methods of cavity formation. Another promising approach is to define the cavity features lithographically using a positive photoresist reflow method.

Further optimisations of the SBN thin-film can be made. Whilst we report a substantial effective Pockels coefficient between 318 to 436 pm/V, with refined growth and subsequent annealing procedure, we may be able to enhance this further, reducing the power requirement for tuning the cavity mode. In addition, whilst we observed around 70% of EO domains were oriented in the desirable

$\langle 310 \rangle$ orientation, we may be able to encourage further orientation by introducing other surface layer to the substrate during SBN growth. Whilst we characterised the room temperature Pockels coefficient, it would be highly useful and novel to study this as a function of decreasing temperature, down to the operation cryogenic temperatures. Indeed, studying the effects of operational conditions on the entire cavity performance would be prudent.

8.5 Final Remarks

The research presented in this thesis bridges critical gaps in the development of quantum optical devices, advancing the realisation of scalable quantum networks. By addressing fabrication, material, and integration challenges, this work contributes to the broader goal of harnessing quantum technologies for transformative applications in communication, computation, and sensing. While challenges remain, the methods and insights developed here pave the way for future innovations in this rapidly evolving field.

Bibliography

1. Feynman, R. P. in *Feynman and Computation* 133–153 (CRC Press, 2018).
2. Lloyd, S. Universal Quantum Simulators. *Science,* 1073–1078 (1996).
3. Shor, P. W. *Algorithms for quantum computation: discrete logarithms and factoring* in *Proc. - Annu. IEEE Symp. Found. Comput. Sci. FOCS* (1994), 124–134.
4. Bennett, C. H. & Brassard, G. *Quantum cryptography: Public key distribution and coin tossing* in *Proc. IEEE/ACS Int. Conf. Comput. Syst. Appl. AICCSA* **175** (1984), 8.
5. Ekert, A. K. Quantum Cryptography Based on Bell's Theorem. *Phys. Rev. Lett.* **67,** 661 (1991).
6. Aharonov, D. & Ben-Or, M. Fault-Tolerant Quantum Computation with Constant Error Rate. *SICOMP* (2008).
7. Knill, E., Laflamme, R. & Zurek, W. H. Resilient Quantum Computation. *Science* **279,** 342–345 (1998).
8. Kitaev, A. Y. Fault-Tolerant Quantum Computation by Anyons. *Ann. Phys.* **303,** 2–30 (2003).
9. Shor, P. W. *Fault-Tolerant Quantum Computation* in *Proceedings of 37th Conference on Foundations of Computer Science* (1996), 56–65.
10. Wehner, S., Elkouss, D. & Hanson, R. Quantum Internet: A Vision for the Road Ahead. *Science* **362** (2018).
11. Kimble, H. J. The Quantum Internet. *Nature* **453,** 1023–1030 (2008).
12. Monroe, C., Meekhof, D. M., King, B. E., Itano, W. M. & Wineland, D. J. Demonstration of a Fundamental Quantum Logic Gate. *Phys. Rev. Lett* **75,** 4714–4717 (1995).

13. Duan, L.-M., Lukin, M. D., Cirac, J. I. & Zoller, P. Long-Distance Quantum Communication With Atomic Ensembles and Linear Optics. *Nature* **414,** 413–418 (2001).

14. Briegel, H.-J., Dür, W., Cirac, J. I. & Zoller, P. Quantum Repeaters: The Role of Imperfect Local Operations in Quantum Communication. *Phys. Rev. Lett.* **81,** 5932–5935 (1998).

15. Azuma, K., Tamaki, K. & Lo, H.-K. All-Photonic Quantum Repeaters. *Nat. Commun.* **6,** 1–7 (2015).

16. Balasubramanian, G. *et al.* Ultralong Spin Coherence Time in Isotopically Engineered Diamond. *Nat. Mater.* **8,** 383–387 (2009).

17. Bar-Gill, N., Pham, L. M., Jarmola, A., Budker, D. & Walsworth, R. L. Solid-State Electronic Spin Coherence Time Approaching One Second. *Nat. Comms* **4,** 1–6 (2013).

18. Maurer, P. C. *et al.* Room-Temperature Quantum Bit Memory Exceeding One Second. *Science* **336,** 1283–1286 (2012).

19. Yang, S. *et al.* High-Fidelity Transfer and Storage of Photon States in a Single Nuclear Spin. *Nat. Photonics* **10,** 507–511 (2016).

20. Barrett, S. D. & Kok, P. Efficient High-Fidelity Quantum Computation Using Matter Qubits and Linear Optics. *Phys. Rev. A* **71** (2005).

21. Bergeron, L. *et al.* Silicon-Integrated Telecommunications Photon-Spin Interface. *PRX Quantum* **1,** 020301 (2020).

22. Higginbottom, D. B. *et al.* Optical observation of single spins in silicon. *Nature* **607,** 266–270 (2022).

23. Dhaliah, D., Xiong, Y., Sipahigil, A., Griffin, S. M. & Hautier, G. First-principles study of the T center in silicon. *Phys. Rev. Mater.* **6,** L053201 (2022).

24. Castelletto, S. & Boretti, A. Silicon carbide color centers for quantum applications. *Journal of Physics: Photonics* **2,** 022001 (2020).
25. Arakawa, Y. & Holmes, M. J. Progress in Quantum-Dot Single Photon Sources for Quantum Information Technologies: A Broad Spectrum Overview. *Applied Physics Reviews* **7,** 021309 (2020).
26. Stern, H. L. *et al.* A quantum coherent spin in hexagonal boron nitride at ambient conditions. *Nature Materials* **23,** 1379–1385 (2024).
27. Tittel, W., Afzelius, M., Kinos, A., Rippe, L. & Walther, A. Quantum Networks Using Rare-Earth Ions. *arXiv:2501.06110* (2025).
28. Rahmouni, A. *et al.* Entangled photon pair generation in an integrated SiC platform. *Light - Science and Applications* **13,** 110 (2024).
29. Chen, Y.-C. *et al.* Laser Writing of Coherent Colour Centres in Diamond. *Nat. Photonics* **11,** 77–80 (2017).
30. Chen, Y.-C. *et al.* Laser Writing of Individual Nitrogen-Vacancy Defects in Diamond with Near-Unity Yield. *Optica* **6,** 662–667 (2019).
31. Janitz, E. *et al.* Fabry-Perot microcavity for diamond-based photonics. *Phys. Rev. A* **92,** 043844 (2015).
32. Johnson, S., Dolan, P. R. & Smith, J. M. Diamond Photonics for Distributed Quantum Networks. *Prog. Quantum. Electron.* **55,** 129–165 (2017).
33. Janitz, E., Bhaskar, M. K. & Childress, L. Cavity Quantum Electrodynamics With Color Centers in Diamond. *Optica* **7** (2020).
34. Ruf, M., Weaver, M. J., van Dam, S. B. & Hanson, R. Resonant Excitation and Purcell Enhancement of Coherent Nitrogen-Vacancy Centers Coupled to a Fabry-Perot Microcavity. *Phys. Rev. A* **15** (2021).
35. Bogdanovic, S. *et al.* Robust Nano-Fabrication of an Integrated Platform for Spin Control in a Tunable Microcavity. *APL Photonics* **2** (2017).

36. Bogdanovic, S. *et al.* Design and Low-Temperature Characterization of a Tunable Microcavity for Diamond-Based Quantum Networks. *Appl. Phys. Lett.* **110,** 171103 (2017).
37. Herrmann, Y. *et al.* Coherent Coupling of a Diamond Tin-Vacancy Center to a Tunable Open Microcavity. *arXiv:2311.08456v1* (2023).
38. Herrmann, Y. *et al.* Coherent Coupling of a Diamond Tin-Vacancy Center to a Tunable Open Microcavity. *Physical Review X* **14** (2024).
39. Wuttig, M. & Yamada, N. Phase-change materials for rewriteable data storage. *Nature Materials* **6,** 824–832 (2007).
40. Delaney, M., Zeimpekis, I., Lawson, D., Hewak, D. W. & Muskens, O. L. A New Family of Ultralow Loss Reversible Phase-Change Materials for Photonic Integrated Circuits: Sb2S3 and Sb2Se3. *Adv. Funct. Mater.* **30,** 2002447 (2020).
41. *Electro-optic Materials on Silicon* https://research.ibm.com/projects/electro-optic-materials-on-silicon. Accessed: 2024-12-28.
42. Abel, S. *et al.* Large Pockels Effect in Micro- And Nanostructured Barium Titanate Integrated on Silicon. *Nat. Mater.* **18,** 42–47 (2019).
43. Abel, S. *et al.* A strong electro-optically active lead-free ferroelectric integrated on silicon. *Nat Commun* **4,** 1671 (2013).
44. Tayebati, P., Trivedi, D. & Tabat, M. Pulsed laser deposition of SBN:75 thin films with electro-optic coefficient of 844 pm/V. *Applied Physics Letters* **69,** 1023–1025 (1996).
45. Kómár, P. *et al.* A quantum network of clocks. *Nature Physics* **10,** 582–587 (2014).
46. Broadbent, A., Fitzsimons, J. & Kashefi, E. *Universal blind quantum computation* in *2009 50th annual IEEE symposium on foundations of computer science* (2009), 517–526.

47. Wootters, W. K. & Zurek, W. H. A single quantum cannot be cloned. *Nature* **299,** 802–803 (1982).

48. Bell, J. S. On the Einstein Podolsky Rosen Paradox. *Phys. Phys. Fiz.* **1,** 195–200 (1964).

49. Clauser, J. F., Horne, M. A., Shimony, A. & Holt, R. A. Proposed Experiment to Test Local Hidden-Variable Theories. *Phys. Rev. Lett* **23,** 880 (1969).

50. Bell, J. *Introduction to the Hidden Variable Questions. In" Foundations of Quantum Mechanics."(ed. B. D'Espagnat), Course 49* 1972.

51. Clauser, J. F. & Horne, M. A. Experimental Consequences of Objective Local Theories. *Phys. Rev. D* **10,** 526 (1974).

52. Einstein, A., Podolsky, B. & Rosen, N. Can Quantum-Mechanical Description of Physical Reality Be Considered Complete? *Phys. Rev.* **47,** 777–780 (1935).

53. Wu, C. S. & Shaknov, I. The Angular Correlation of Scattered Annihilation Radiation. *Phys. Rev.* **77,** 136–136 (1950).

54. Freedman, S. J. & Clauser, J. F. Experimental Test of Local Hidden-Variable Theories. *Phys. Rev. Lett.* **28,** 938–941 (1972).

55. Aspect, A., Grangier, P. & Roger, G. Experimental Tests of Realistic Local Theories via Bell's Theorem. *Phys. Rev. Lett.* **47,** 460–463 (1981).

56. Aspect, A., Grangier, P. & Roger, G. Experimental Realization of Einstein-Podolsky-Rosen-Bohm Gedankenexperiment: A New Violation of Bell's Inequalities. *Phys. Rev. Lett.* **49,** 91–94 (1982).

57. Aspect, A., Dalibard, J. & Roger, G. Experimental Test of Bell's Inequalities Using Time-Varying Analyzers. *Phys. Rev. Lett.* **49,** 1804–1807 (1982).

58. Kwiat, P. G. *et al.* New High-Intensity Source of Polarization-Entangled Photon Pairs. *Phys. Rev. Lett.* **75,** 4337–4341 (1995).

59. Weihs, G., Jennewein, T., Simon, C., Weinfurter, H. & Zeilinger, A. Violation of Bell's Inequality Under Strict Einstein Locality Conditions. *Phys. Rev. Lett.* **81,** 5039–5043 (1998).

60. Rowe, M. A. *et al.* Experimental Violation of a Bell's Inequality With Efficient Detection. *Nature* **409,** 791–794 (2001).

61. Hensen, B. *et al.* Loophole-Free Bell Inequality Violation Using Electron Spins Separated by 1.3 Kilometres. *Nature* **526,** 682–6 (2015).

62. Giustina, M. *et al.* Significant-Loophole-Free Test of Bell's Theorem With Entangled Photons. *Phys. Rev. Lett.* **115,** 250401 (2015).

63. Shalm, L. K. *et al.* Strong Loophole-Free Test of Local Realism. *Phys. Rev. Lett.* **115,** 250402 (2015).

64. Shih, Y. & Alley, C. O. New Type of Einstein-Podolsky-Rosen-Bohm Experiment Using Pairs of Light Quanta Produced by Optical Parametric Down Conversion. *Phys. Rev. Lett* **61,** 2921 (1988).

65. Ou, Z. Y. & Mandel, L. Violation of Bell's Inequality and Classical Probability in a Two-Photon Correlation Experiment. *Phys. Rev. Lett.* **61,** 50–53 (1988).

66. Klyshko, D. N., Penin, A. N. & Polkovnikov, B. F. Parametric Luminescence and Light Scattering by Polaritons. *J. Exp. Theor. Phys.* **11,** 5 (1970).

67. Burnham, D. C. & Weinberg, D. L. Observation of Simultaneity in Parametric Production of Optical Photon Pairs. *Phys. Rev. Lett.* **25,** 84–87 (1970).

68. Greenberger, D. M., Horne, M., Zeilinger, A. & Żukowski, M. Bell Theorem Without Inequalities for Two Particles. II. Inefficient Detectors. *Phys. Rev. A* **78,** 022111 (2008).

69. Cirac, J. I. & Zoller, P. Preparation of Macroscopic Superpositions in Many-Atom Systems. *Phys. Rev. A* **50,** R2799–R2802 (1994).

70. Pellizzari, T., Gardiner, S. A., Cirac, J. I. & Zoller, P. Decoherence, Continuous Observation, and Quantum Computing: A Cavity QED Model. *Phys. Rev. Lett* **75,** 3788–3791 (1995).

71. Turchette, Q. A., Hood, C. J., Lange, W., Mabuchi, H. & Kimble, H. J. Measurement of Conditional Phase Shifts for Quantum Logic. *Phys. Rev. Lett* **75,** 4710–4713 (1995).

72. Hagley, E. *et al.* Generation of Einstein-Podolsky-Rosen Pairs of Atoms. *Phys. Rev. Lett* **79,** 1–5 (1997).

73. Maître, X. *et al.* Quantum Memory With a Single Photon in a Cavity. *Phys. Rev. Lett* **79,** 769–772 (1997).

74. Walther, H. Experiments on Cavity Quantum Electrodynamics. *Phys. Rep.* **219,** 263–281 (1992).

75. Thompson, R. J., Rempe, G. & Kimble, H. J. Observation of Normal-Mode Splitting for an Atom in an Optical Cavity. *Phys. Rev. Lett.* **68,** 1132–1135 (1992).

76. Cirac, J. I. & Zoller, P. Quantum Computations With Cold Trapped Ions. *Phys. Rev. Lett* **74,** 4091–4094 (1995).

77. King, B. E. *et al.* Cooling the Collective Motion of Trapped Ions to Initialize a Quantum Register. *Phys. Rev. Lett* **81,** 1525–1528 (1998).

78. Poyatos, J. F., Cirac, J. I. & Zoller, P. Quantum Gates With "Hot" Trapped Ions. *Phys. Rev. Lett* **81,** 1322–1325 (1998).

79. Feng, X.-L., Zhang, Z.-M., Li, X.-D., Gong, S.-Q. & Xu, Z.-Z. Entangling Distant Atoms by Interference of Polarized Photons. *Phys. Rev. Lett.* **90,** 217902 (2003).

80. Lim, Y. L., Beige, A. & Kwek, L. C. Repeat-Until-Success Linear Optics Distributed Quantum Computing. *Phys. Rev. Lett.* **95,** 030505 (2005).

81. Benjamin, S. C., Eisert, J. & Stace, T. M. Optical Generation of Matter Qubit Graph States. *New J. Phys.* **7,** 194–194 (2005).

82. Akopian, N. *et al.* Entangled Photon Pairs From Semiconductor Quantum Dots. *Phys. Rev. Lett.* **96,** 130501 (2006).

83. Hu, C. Y., Young, A., O'Brien, J. L., Munro, W. J. & Rarity, J. G. Giant Optical Faraday Rotation Induced by a Single-Electron Spin in a Quantum Dot: Applications to Entangling Remote Spins via a Single Photon. *Phys. Rev. B* **78,** 085307 (2008).

84. Cabrillo, C., Cirac, J. I., García-Fernández, P. & Zoller, P. Creation of Entangled States of Distant Atoms by Interference. *Phys. Rev. A* **59,** 1025–1033 (1999).

85. Benjamin, S., Lovett, B. & Smith, J. Prospects for Measurement-Based Quantum Computing With Solid State Spins. *Laser Photonics Rev.* **3,** 556–574 (2009).

86. Benjamin, S. C., Browne, D. E., Fitzsimons, J. & Morton, J. J. L. Brokered Graph-State Quantum Computation. *New J. Phys.* **8,** 141–141 (2006).

87. Raussendorf, R. & Briegel, H. J. A One-Way Quantum Computer. *Phys. Rev. Lett* **86,** 5188–5191 (2001).

88. Briegel, H. J., Browne, D. E., Dür, W., Raussendorf, R. & Van den Nest, M. Measurement-Based Quantum Computation. *Nat. Phys* **5,** 19–26 (2009).

89. Hein, M., Eisert, J. & Briegel, H. J. Multiparty Entanglement in Graph States. *Phys. Rev. A* **69,** 062311 (2004).

90. Briegel, H. J. & Raussendorf, R. Persistent Entanglement in Arrays of Interacting Particles. *Phys. Rev. Lett* **86,** 910 (2001).

91. Briegel, H. J. in *Compendium of Quantum Physics* (eds Greenberger, D., Hentschel, K. & Weinhert, F.) 96–105 (Springer, Berlin, Heidelberg, 2009).

92. Hurst, D. L., Joanesarson, K. B., Iles-Smith, J., Mork, J. & Kok, P. Generating Maximal Entanglement between Spectrally Distinct Solid-State Emitters. *Phys Rev Lett* **123,** 023603 (2019).

93. Callus, E. & Kok, P. Cumulative generation of maximal entanglement between spectrally distinct qubits using squeezed light. *Physical Review A* **104,** 052407 (2021).

94. Bennett, C. H. *et al.* Purification of Noisy Entanglement and Faithful Teleportation via Noisy Channels. *Phys. Rev. Lett.* **76,** 722–725 (1996).

95. Vedral, V. *Introduction to Quantum Information Science* (Oxford University Press on Demand, 2006).

96. Wilde, M. M. *Quantum Information Theory* (Cambridge University Press, 2013).

97. Pan, J.-W., Simon, C., Brukner, Č. & Zeilinger, A. Entanglement Purification for Quantum Communication. *Nature* **410,** 1067–1070 (2001).

98. Bennett, C. H. *et al.* Teleporting an Unknown Quantum State via Dual Classical and Einstein-Podolsky-Rosen Channels. *Phys. Rev. Lett.* **70,** 1895–1899 (1993).

99. Zukowski, M., Zeilinger, A., Horne, M. A. & Ekert, A. K. " Event-Ready-Detectors" Bell Experiment via Entanglement Swapping. *Phys. Rev. Lett* **71** (1993).

100. Lukin, M. D. Colloquium: Trapping and Manipulating Photon States in Atomic Ensembles. *Rev. Mod. Phys.* **75,** 457–472 (2003).

101. Tittel, W. *et al.* Photon-Echo Quantum Memory in Solid State Systems. *Laser Photonics Rev.* **4,** 244–267 (2010).

102. Hammerer, K., Sørensen, A. S. & Polzik, E. S. Quantum Interface Between Light and Atomic Ensembles. *Rev. Mod. Phys.* **82,** 1041–1093 (2010).

103. Morton, J. J. *et al.* Solid-State Quantum Memory Using the 31 P Nuclear Spin. *Nature* **455,** 1085–1088 (2008).

104. Lvovsky, A. I., Sanders, B. C. & Tittel, W. Optical Quantum Memory. *Nat. Photonics* **3,** 706–714 (2009).

105. Brown, B. J., Loss, D., Pachos, J. K., Self, C. N. & Wootton, J. R. Quantum Memories at Finite Temperature. *Rev. Mod. Phys.* **88** (2016).

106. Heshami, K. *et al.* Quantum Memories: Emerging Applications and Recent Advances. *J. Mod. Opt* **63,** 2005–2028 (2016).

107. Chou, C. W. *et al.* Measurement-Induced Entanglement for Excitation Stored in Remote Atomic Ensembles. *Nature* **438,** 828–832 (2005).

108. Moehring, D. L. *et al.* Entanglement of Single-Atom Quantum Bits at a Distance. *Nature* **449,** 68–71 (2007).

109. Zoller, P. *et al.* Quantum Information Processing and Communication. *Eur. Phys. J. D* **36,** 203–228 (2005).

110. Ritter, S. *et al.* An Elementary Quantum Network of Single Atoms in Optical Cavities. *Nature* **484,** 195–200 (2012).

111. Pfaff, W. *et al.* Demonstration of Entanglement-by-Measurement of Solid-State Qubits. *Nat. Phys* **9,** 29–33 (2012).

112. Bernien, H. *et al.* Heralded Entanglement Between Solid-State Qubits Separated by Three Metres. *Nature* **497,** 86–90 (2013).

113. Pfaff, W. *et al.* Unconditional Quantum Teleportation Between Distant Solid-State Quantum Bits. *Science* **345,** 532–535 (2014).

114. Kalb, N. *et al.* Entanglement Distillation Between Solid-State Quantum Network Nodes. *Science* **356,** 928–932 (2017).

115. Pompili, M. *et al.* Realization of a Multinode Quantum Network of Remote Solid-State Qubits. *Science* **372,** 259–264 (2021).

116. Kalb, N., Humphreys, P. C., Slim, J. J. & Hanson, R. Dephasing Mechanisms of Diamond-Based Nuclear-Spin Memories for Quantum Networks. *Phys. Rev. A* **97** (2018).

117. Stolk, A. J. *et al.* Metropolitan-scale heralded entanglement of solid- state qubits. *Science Advances* **10** (2024).

118. Humphreys, P. C. *et al.* Deterministic Delivery of Remote Entanglement on a Quantum Network. *Nature* **558,** 268–273 (2018).

119. Hofmann, J. *et al.* Heralded Entanglement Between Widely Separated Atoms. *Science* **337,** 72–75 (2012).

120. Stephenson, L. *et al.* High-Rate, High-Fidelity Entanglement of Qubits Across an Elementary Quantum Network. *Phys. Rev. Lett* **124,** 110501 (2020).

121. Delteil, A. *et al.* Generation of Heralded Entanglement Between Distant Hole Spins. *Nat. Phys.* **12,** 218–223 (2016).

122. Stockill, R. *et al.* Phase-Tuned Entangled State Generation Between Distant Spin Qubits. *Physical Rev. Lett.* **119,** 010503 (2017).

123. DiVincenzo, D. P. The Physical Implementation of Quantum Computation. *Fortschritte der Phys.* **48,** 771–783 (2000).

124. Robledo, L. *et al.* High-Fidelity Projective Read-Out of a Solid-State Spin Quantum Register. *Nature* **477,** 574–578 (2011).

125. Loretz, M., Pezzagna, S., Meijer, J. & Degen, C. Nanoscale Nuclear Magnetic Resonance with a 1.9-nm-Deep Nitrogen-Vacancy Sensor. *Appl. Phys. Lett.* **104,** 033102 (2014).

126. Shinada, T., Okamoto, S., Kobayashi, T. & Ohdomari, I. Enhancing Semiconductor Device Performance Using Ordered Dopant Arrays. *Nature* **437,** 1128–1131 (2005).

127. Schnitzler, W. *et al.* Deterministic Ultracold Ion Source Targeting the Heisenberg Limit. *Phys. Rev. Lett.* **102,** 070501 (2009).

128. Lea-wilsonf, M., Lomer, J. N. & Van Wyk, J. Electron Spin Resonance of the R4/W6 Defect in Irradiated Diamond. *Philos. Mag. B* **72,** 81–89 (1995).

129. Naydenov, B. *et al.* Dynamical Decoupling of a Single-Electron Spin at Room Temperature. *Phys. Rev. B* **83,** 081201 (2011).

130. Yamamoto, T. *et al.* Extending Spin Coherence Times of Diamond Qubits by High-Temperature Annealing. *Phys. Rev. B* **88,** 075206 (2013).

131. Deák, P., Aradi, B., Kaviani, M., Frauenheim, T. & Gali, A. Formation of NV Centers in Diamond: A Theoretical Study Based on Calculated Transitions and Migration of Nitrogen and Vacancy Related Defects. *Phys. Rev. B* **89,** 075203 (2014).

132. Fu, K.-M., Santori, C., Barclay, P. & Beausoleil, R. Conversion of Neutral Nitrogen-Vacancy Centers to Negatively Charged Nitrogen-Vacancy Centers Through Selective Oxidation. *Appl. Phys. Lett.* **96,** 121907 (2010).

133. Orwa, J. *et al.* Engineering of Nitrogen-Vacancy Color Centers in High Purity Diamond by Ion Implantation and Annealing. *J. Appl. Phys.* **109,** 083530 (2011).

134. Van Dam, S. B. *et al.* Optical Coherence of Diamond Nitrogen-Vacancy Centers Formed by Ion Implantation and Annealing. *Phys. Rev. B* **99,** 161203 (2019).

135. Ruf, M. *et al.* Optically Coherent Nitrogen-Vacancy Centers in Micrometer-Thin Etched Diamond Membranes. *Nano Lett* **19,** 3987–3992 (2019).

136. Ohno, K. *et al.* Three-Dimensional Localization of Spins in Diamond using 12C Implantation. *Appl. Phys. Lett.* **105,** 052406 (2014).

137. Ohno, K. *et al.* Engineering Shallow Spins in Diamond with Nitrogen Delta-Doping. *Appl. Phys. Lett.* **101,** 082413 (2012).

138. McLellan, C. A. *et al.* Patterned Formation of Highly Coherent Nitrogen-Vacancy Centers Using a Focused Electron Irradiation Technique. *Nano Lett.* **16,** 2450–2454 (2016).

139. Kirkpatrick, A. R. *et al.* Deterministic Laser-Writing of Nitrogen-Vacancy Centres in High Purity Diamond. *In Preparation.*

140. Cheng, X. *et al.* Laser Activation of Single Group-IV Colour Centres in Diamond. *Nat. Commun.* **16** (2025).

141. Stephen, C. J. *et al.* Deep Three-Dimensional Solid-State Qubit Arrays with Long-Lived Spin Coherence. *Phys. Rev. Appl.* **12,** 064005 (2019).

142. Nemoto, K. *et al.* Photonic Architecture for Scalable Quantum Information Processing in Diamond. *Phys. Rev. X* **4,** 031022 (2014).

143. Greentree, A. D. *et al.* Critical Components for Diamond-Based Quantum Coherent Devices. *J. Condens. Matter Phys.* **18,** S825 (2006).

144. Schröder, T. *et al.* Quantum Nanophotonics in Diamond. *JOSA B* **33,** B65–B83 (2016).

145. Fairchild, B. A. *et al.* Fabrication of Ultrathin Single-Crystal Diamond Membranes. *Adv. Mater.* **20,** 4793–4798 (2008).

146. Riedel, D. *et al.* Deterministic Enhancement of Coherent Photon Generation From a Nitrogen-Vacancy Center in Ultrapure Diamond. *Phys. Rev. X* **7,** 031040 (2017).

147. Faraon, A., Santori, C., Huang, Z., Acosta, V. M. & Beausoleil, R. G. Coupling of Nitrogen-Vacancy Centers to Photonic Crystal Cavities in Monocrystalline Diamond. *Phys. Rev. Lett* **109,** 033604 (2012).

148. Maletinsky, P. *et al.* A Robust Scanning Diamond Sensor for Nanoscale Imaging With Single Nitrogen-Vacancy Centres. *Nat. Nanotechnol* **7,** 320–324 (2012).

149. Ovartchaiyapong, P., Pascal, L. M. A., Myers, B. A., Lauria, P. & Bleszynski Jayich, A. C. High Quality Factor Single-Crystal Diamond Mechanical Resonators. *Appl. Phys. Lett.* **101,** 163505 (2012).

150. Pomorski, M., Caylar, B. & Bergonzo, P. Super-Thin Single Crystal Diamond Membrane Radiation Detectors. *Appl. Phys. Lett.* **103,** 112106 (2013).

151. Teissier, J., Barfuss, A., Appel, P., Neu, E. & Maletinsky, P. Strain Coupling of a Nitrogen-Vacancy Center Spin to a Diamond Mechanical Oscillator. *Phys. Rev. Lett* **113** (2014).

152. Tao, Y. & Degen, C. Facile Fabrication of Single-Crystal-Diamond Nanostructures With Ultrahigh Aspect Ratio. *Adv Mater* **25,** 3962–7 (2013).

153. Janitz, E. *et al.* Fabry-Perot Microcavity for Diamond-Based Photonics. *Phys. Rev. A* **92,** 043844 (2015).

154. Bogdanović, S. *et al.* Robust Nano-Fabrication of an Integrated Platform for Spin Control in a Tunable Microcavity. *APL Photonics* **2** (2017).

155. Høy Jensen, R. *et al.* Cavity-Enhanced Photon Emission From a Single Germanium-Vacancy Center in a Diamond Membrane. *Phys. Rev. Applied* **13,** 064016 (2020).

156. Purcell, E. M. Proceedings of the American Physical Society. *Phys. Rev.* **69,** 674–674 (1946).

157. Faraon, A., Barclay, P. E., Santori, C., Fu, K.-M. C. & Beausoleil, R. G. Resonant Enhancement of the Zero-Phonon Emission From a Colour Centre in a Diamond Cavity. *Nat. Photonics* **5,** 301–305 (2011).

158. Hausmann, B. J. M. *et al.* Coupling of NV Centers to Photonic Crystal Nanobeams in Diamond. *Nano Lett.* **13,** 5791–5796 (2013).

159. Lee, J. C. *et al.* Deterministic Coupling of Delta-Doped Nitrogen Vacancy Centers to a Nanobeam Photonic Crystal Cavity. *Appl. Phys. Lett.* **105,** 261101 (2014).

160. Li, L. *et al.* Coherent Spin Control of a Nanocavity-Enhanced Qubit in Diamond. *Nat. Comms* **6,** 1–7 (2015).

161. Riedrich-Möller, J. *et al.* Nanoimplantation and Purcell Enhancement of Single Nitrogen-Vacancy Centers in Photonic Crystal Cavities in Diamond. *Appl. Phys. Lett.* **106,** 221103 (2015).

162. Englund, D. *et al.* Deterministic Coupling of a Single Nitrogen Vacancy Center to a Photonic Crystal Cavity. *Nano Lett.* **10,** 3922–3926 (2010).

163. Wolters, J. *et al.* Enhancement of the Zero Phonon Line Emission From a Single Nitrogen Vacancy Center in a Nanodiamond via Coupling to a Photonic Crystal Cavity. *Appl. Phys. Lett.* **97,** 141108 (2010).

164. Barclay, P. E., Fu, K.-M. C., Santori, C., Faraon, A. & Beausoleil, R. G. Hybrid Nanocavity Resonant Enhancement of Color Center Emission in Diamond. *Phys. Rev. X* **1,** 011007 (2011).

165. Van der Sar, T. *et al.* Deterministic Nanoassembly of a Coupled Quantum Emitter–Photonic Crystal Cavity System. *Appl. Phys. Lett.* **98,** 193103 (2011).

166. Hunger, D. *et al.* A Fiber Fabry–Perot Cavity With High Finesse. *New J. Phys.* **12,** 065038 (2010).

167. Kaupp, H. *et al.* Scaling Laws of the Cavity Enhancement for Nitrogen-Vacancy Centers in Diamond. *Phys. Rev. A* **88,** 053812 (2013).

168. Albrecht, R., Bommer, A., Deutsch, C., Reichel, J. & Becher, C. Coupling of a Single Nitrogen-Vacancy Center in Diamond to a Fiber-Based Microcavity. *Phys. Rev. Lett.* **110,** 243602 (2013).

169. Johnson, S. *et al.* Tunable Cavity Coupling of the Zero Phonon Line of a Nitrogen-Vacancy Defect in Diamond. *New J. Phys.* **17,** 122003 (2015).

170. Hauf, M. *et al.* Chemical control of the charge state of nitrogen-vacancy centers in diamond. *Physical Review B—Condensed Matter and Materials Physics* **83,** 081304 (2011).

171. Bluvstein, D., Zhang, Z. & Jayich, A. C. B. Identifying and mitigating charge instabilities in shallow diamond nitrogen-vacancy centers. *Physical review letters* **122,** 076101 (2019).

172. Faraon, A. *et al.* Quantum Photonic Devices in Single-Crystal Diamond. *New J. Phys.* **15,** 025010 (2013).

173. Neurgaonkar, R., Oliver, J. & Cross, L. Ferroelectric properties of tetragonal tungsten bronze single crystals. *Ferroelectrics* **56,** 31–36 (1984).

174. Jamieson, P., Abrahams, S. & Bernstein, J. Ferroelectric Tungsten Bronze-Type Crystal Structures. I. Barium Strontium Niobate Ba0. 27Sr0. 75Nb2O5. 78. *J. Chem. Phys.* **48,** 5048–5057 (1968).

175. Abrahams, S. Programmed Electronic X-Ray Automatic Diffractometer. *Review of Scientific Instruments* **33,** 973–977 (1962).

176. Chernaya, T., Maksimov, B., Volk, T., Ivleva, L. & Simonov, V. Atomic structure of Sr 0.75 Ba 0.25 Nb 2 O 6 single crystal and composition-structure-property relation in (Sr, Ba) Nb 2 O 6 solid solutions. *Physics of the Solid State* **42,** 1716–1721 (2000).

177. Yang, W., Fang, F. & Fang, D.-N. in *Comprehensive Structural Integrity* (eds Milne, I., Ritchie, R. & Karihaloo, B.) 645–686 (Pergamon, Oxford, 2003).

178. Chakrabarti, A. & Bera, J. Structure and ferroelectric properties of BaBi3. 8M0.2 (Ti3.8Nb0.2) O15 (M=Mg, Ca, Sr and Ba) ceramics. *Physica B: Condensed Matter* **406,** 2891–2897 (2011).

179. Beskin, I. M., Kwon, S., Posadas, A. B., Kim, M. J. & Demkov, A. A. Growth and Structure of Strong Pockels Material Strontium Barium Nio-

bate on SrTiO3 and Si by Molecular Beam Epitaxy. *Advanced Photonics Research* **2** (2021).

180. Cuniot-Ponsard, M. in *Ferroelectrics-Material Aspects* (IntechOpen, 2011).
181. Carruthers, J. & Grasso, M. Phase Equilibria Relations in the Ternary System BaO-SrO-Nb2 O 5. *Journal of The Electrochemical Society* **117,** 1426 (1970).
182. Jamieson, P., Abrahams, S. & Bernstein, J. Ferroelectric tungsten bronze-type crystal structures. I. Barium strontium niobate Ba0. 27Sr0. 75Nb2O5. 78. *The Journal of Chemical Physics* **48,** 5048–5057 (1968).
183. Podlozhenov, S. *et al.* Structure of strontium barium niobate $Sr_xBa_{1-x}Nb_2O_6$ (SBN) in the composition range $0.32 \leq x \leq 0.82$. *Acta Crystallographica Section B Structural Science* **62,** 960–965 (2006).
184. Yariv, A. & Yeh, P. *Optical Waves in Crystals* (Wiley New York, 1984).
185. Ducharme, S., Feinberg, J. & Neurgaonkar, R. Electrooptic and piezoelectric measurements in photorefractive barium titanate and strontium barium niobate. *IEEE Journal of Quantum Electronics* **23,** 2116–2121 (1987).
186. Cuniot-Ponsard, M., Desvignes, J. M., Ea-Kim, B. & Leroy, E. Radio frequency magnetron sputtering deposition of hetero-epitaxial strontium barium niobate thin films (SrxBa1-xNb2O6). *Journal of Applied Physics* **93,** 1718–1724 (2003).
187. Schwyn Thony, S., Youden, K. E., Harris, J. S. & Hesselink, L. Growth of epitaxial strontium barium niobate thin films by pulsed laser deposition. *Applied Physics Letters* **65,** 2018–2020 (1994).
188. Qadri, S. B., Bellotti, J. A., Garzarella, A. & Wu, D. H. Anisotropic thermal expansion of strontium barium niobate. *Applied physics letters* **86** (2005).

189. J. M. Povoa, R. G. & Bhalla, A. S. Low temperature dielectric relaxation phenomena in relaxor ferroelectric strontium barium niobate single crystals. *Ferroelectrics* **158,** 283–288 (1994).

190. Schefer, J. *et al.* Structural properties of $\mathrm{Sr_{0.61}Ba_{0.39}Nb_2O_6}$ in the temperature range $10 - -500\ \mathrm{K}$ investigated by high-resolution neutron powder diffraction and specific heat measurements. *Phys. Rev. B* **74,** 134103 (2006).

191. Kip, D. *et al.* Refractive Indices of Sr0.61Ba0.39Nb2O6 Single Crystals. *Physica Status Solidi (a)* **154,** K5–K7 (1996).

192. Woike, T. *et al.* Refractive Indices of Congruently Melting Sr0.61 Ba0.39 Nb2 O6. *physica status solidi (a)* **186,** R13–R15 (2001).

193. Andriyevsky, B. *et al.* Electronic and Optical Properties of Strontium Barium Niobate Single Crystals. *Ferroelectrics* **426,** 194–205 (2012).

194. Shirokov, V. B., Pavlenko, A. V., Stryukov, D. V. & Revinskii, Y. V. Optical Properties of Barium Strontium Niobate SBN61 Films. *Physics of the Solid State* **60,** 1005–1010 (2018).

195. Tauc, J. Optical properties and electronic structure of amorphous Ge and Si. *Materials Research Bulletin* **3,** 37–46 (1968).

196. Tauc, J. in *Optical Properties of Solids: Papers from the NATO Advanced Study Institute on Optical Properties of Solids Held August 7–20, 1966, at Freiburg, Germany* (eds Nudelman, S. & Mitra, S. S.) 123–136 (Springer US, Boston, MA, 1969).

197. Shirokov, V. B. Approximation of a transmission spectrum of MgO by a damped oscillator with relaxation. *Optics and Spectroscopy* **112,** 135–137 (2012).

198. Chrisey, D. B. & Hubler, G. K. Pulsed Laser Deposition of Thin Films. *Handbook of Laser Technology and Applications* (2003).

199. Langford, J. I. & Wilson, A. J. C. Scherrer after sixty years: A survey and some new results in the determination of crystallite size. *Journal of Applied Crystallography* **11,** 102–113 (1978).

200. Williamson, G. & Hall, W. X-ray line broadening from filed aluminium and wolfram. *Acta metallurgica* **1,** 22–31 (1953).

201. Hough, P. V. *Method and means for recognizing complex patterns* US Patent 3,069,654. 1962.

202. Engler, O. & Randle, V. (*Introduction to texture analysis : macrotexture, microtexture, and orientation mapping* 2nd ed. eng (CRC Press, Boca Raton, 2010).

203. Wulff, G. 1. Untersuchungen im Gebiete der optischen Eigenschaften isomorpher Krystalle. *Zeitschrift für Kristallographie-Crystalline Materials* **36,** 1–28 (1902).

204. Teng, C. & Man, H. Simple reflection technique for measuring the electro-optic coefficient of poled polymers. *Applied Physics Letters* **56,** 1734–1736 (1990).

205. Schildkraut, J. S. Determination of the electrooptic coefficient of a poled polymer film. *Applied optics* **29,** 2839–2841 (1990).

206. Johnston, A. R. & Weingart, J. Determination of the low-frequency linear electro-optic effect in tetragonal BaTiO 3. *JOSA* **55,** 828–834 (1965).

207. Hunsperger, R. G. *et al. Integrated optics* (Springer, 1995).

208. Abel, S. *Electro-optic photonic devices based on epitaxial barium titanate thin films on silicon* Thesis (2015).

209. Stimpson, G. A., Skilbeck, M. S., Patel, R. L., Green, B. L. & Morley, G. W. An open-source high-frequency lock-in amplifier. *Review of Scientific Instruments* **90,** 094701 (2019).

210. Reitze, D. *et al.* Electro-optic properties of single crystalline ferroelectric thin films. *Applied physics letters* **63,** 596–598 (1993).

211. Nielsen, M. A. & Chuang, I. *Quantum Computation and Quantum Information* (American Association of Physics Teachers, 2002).

212. Hahn, E. L. Spin Echoes. *Phys. Rev.* **80,** 580–594 (1950).

213. Ujihara, K. Decay rate dependence of the spontaneous emission pattern from an atom in an optical microcavity. *Optics communications* **101,** 179–184 (1993).

214. Romeira, B. & Fiore, A. Purcell effect in the stimulated and spontaneous emission rates of nanoscale semiconductor lasers. *IEEE Journal of Quantum Electronics* **54,** 1–12 (2018).

215. Kristensen, P. T., Van Vlack, C. & Hughes, S. Generalized effective mode volume for leaky optical cavities. *Optics letters* **37,** 1649–1651 (2012).

216. Brooker, G. *Modern Classical Optics* (Oxford University Press, 2003).

217. Hect, E. *Optics* 4th ed. (Addison Wesley, 2002).

218. Phillip, H. R. & Taft, E. A. Kramers-Kronig Analysis of Reflectance Data for Diamond. *Phys. Rev.* **136,** A1445–A1448 (1964).

219. Fujiwara, H. *Spectroscopic Ellipsometry: Principles and Applications* (John Wiley & Sons, 2007).

220. Lorentz, H. *The theory of electrons and its applications to the phenomena of light and radiant heat* (Leipzig : B.G. Teubner ; New York : G.E. Stechert, 1916).

221. Sellmeier, W. Ueber die durch die Aetherschwingungen erregten Mitschwingungen der Körpertheilchen und deren Rückwirkung auf die ersteren, besonders zur Erklärung der Dispersion und ihrer Anomalien. *Ann. Phys.* **223,** 525–554 (1872).

222. Cauchy, A.-L. Sur la réfraction et la réflexion de la lumière. *Bulletin de Ferussae* **14,** 6–10 (1831).

223. Drude, P. *The Theory of Optics* (Longmans, 1925).

224. Jellison Jr, G. & Modine, F. Parameterization of the optical functions of amorphous materials in the interband region. *App. Phys. Lett.* **69,** 371–373 (1996).

225. De L. Kronig, R. On the Theory of Dispersion of X-Rays. *J. Opt. Soc. Am.* **12,** 547–557 (1926).

226. Kramers, H. A. *La diffusion de la lumiere par les atomes* in *Atti Cong. Intern. Fisica (Transactions of Volta Centenary Congress) Como* **2** (1927), 545–557.

227. Yee, K. Numerical Solution of Initial Boundary Value Problems Involving Maxwell's Equations in Isotropic Media. *IEEE Trans. Antennas Propag.* **14,** 302–307 (1966).

228. Sullivan, D. M. *Electromagnetic Simulation Using the FDTD Method* (John Wiley & Sons, 2013).

229. Wartak, M. S. in *Computational Photonics: An Introduction with MATLAB* 262–287 (Cambridge University Press, 2013).

230. *PyLumerical - A Wrapper Library for Lumerical FDTD* https://github.com/png-materials-ox/PyLumerical.

231. Courant, R., Friedrichs, K. & Lewy, H. Über die Partiellen Differenzengleichungen der Mathematischen Physik. *Math. Ann.* **100,** 32–74 (1928).

232. Courant, R., Friedrichs, K. & Lewy, H. On the Partial Difference Equations of Mathematical Physics. *IBM J. Res. Dev.* **11,** 215–234 (1967).

233. Yu, W. & Mittra, R. A Conformal Finite Difference Time Domain Technique for Modeling Curved Dielectric Surfaces. *IEEE Microw. Wirel. Compon. Lett.* **11,** 25–27 (2001).

234. Boriskin, A. V., Boriskina, S. V., Rolland, A., Sauleau, R. & Nosich, A. I. Test of the FDTD Accuracy in the Analysis of the Scattering Resonances Associated with High-Q Whispering-Gallery Modes of a Circular Cylinder. *J. Opt. Soc. Am. B* **25,** 1169–1173 (2008).

235. Fox, M. *Quantum Optics: An Introduction* (OUP Oxford, 2006).

236. Wang, X. *et al.* High resolution 3D NanoImprint technology: Template fabrication, application in Fabry-Perot filter array based optical nanospectrometers. *Microelectronic Engineering* **110,** 44–51 (2013).

237. Nguyen, D. T. *et al.* 3D nanoimprint for NIR Fabry-Perot filter arrays: fabrication, characterization and comparison of different cavity designs. *Applied Nanoscience* **6,** 1127–1135 (2016).

238. Lee, C., Choi, H., Gu, E., Dawson, M. & Murphy, H. Fabrication and characterization of diamond micro-optics. *Diamond and Related Materials* **15,** 725–728 (2006).

239. Ruffieux, P. *et al.* Two step process for the fabrication of diffraction limited concave microlens arrays. *Opt. Express* **16** (2008).

240. Liu, H. *et al.* Large radius of curvature micro-lenses on single crystal diamond for application in monolithic diamond Raman lasers. *Diamond and Related Materials* **65,** 37–41 (2016).

241. Zhu, T. F. *et al.* Fabrication of diamond microlenses by chemical reflow method. *Opt Express* **25,** 1185–1192 (2017).

242. Liang, Y. *et al.* Fabrication of concave microlenses on a diamond by a spin coating process. *Opt Express* **28,** 9320–9326 (2020).

243. Trichet, A. A. P., Dolan, P. R., Coles, D. M., Hughes, G. M. & Smith, J. M. Topographic control of open-access microcavities at the nanometer scale. *Opt. Express* **23,** 17205–17216 (2015).

244. Guzmán de la Mata, B., Dowsett, M. & Twitchen, D. Sputter yields in diamond bombarded by ultra low energy ions. *Applied Surface Science* **252.** Proceedings of the Fifteenth International Conference on Secondary Ion Mass Spectrometry, 6444–6447 (2006).

245. Singh, J. *Semiconductor Devices: An Introduction* International ed., 54 (1994).

246. Schuelke, T. & Grotjohn, T. A. Diamond polishing. *Diamond and Related Materials* **32,** 17–26 (2013).

247. Smith, G. F. Mixed perchloric, sulfuric and phosphoric acids and their applications in analysis. *(No Title)* (1942).

248. Tatsumi, N., Harano, K., Ito, T. & Sumiya, H. Polishing mechanism and surface damage analysis of type IIa single crystal diamond processed by mechanical and chemical polishing methods. *Diamond and Related Materials* **63.** 9th International Conference on New Diamond and Nano Carbons NDNC 2015, 80–85 (2016).

249. Hsieh, C.-H., Tsai, H.-Y., Lai, H.-T. & Lin, H.-Y. *Comparison between mechanical method and chemical-assisted mechanical method for CVD diamond film polishing* in *Nano- and Microtechnology: Materials, Processes, Packaging, and Systems* (eds Sood, D. K., Malshe, A. P. & Maeda, R.) **4936** (SPIE, 2002), 337–344.

250. Frost, F. *et al.* Ion beam assisted smoothing of optical surfaces. *Applied Physics A* **78,** 651–654 (2004).

251. Frost, F. *et al.* Large area smoothing of surfaces by ion bombardment: fundamentals and applications. *Journal of Physics: Condensed Matter* **21,** 224026 (2009).

252. Trichet, A. A., Dolan, P. R., Coles, D. M., Hughes, G. M. & Smith, J. M. Topographic control of open-access microcavities at the nanometer scale. *Optics express* **23,** 17205–17216 (2015).

253. Mesoudy, A. E. *et al.* Band gap narrowing induced by oxygen vacancies in reactively sputtered TiO2 thin films. *Thin Solid Films* **769,** 139737 (2023).

254. Foo, C. *et al.* Characterisation of oxygen defects and nitrogen impurities in TiO2 photocatalysts using variable-temperature X-ray powder diffraction. *Nature Communications* **12,** 661 (2021).

255. Impellizzeri, G. *et al.* C ion-implanted TiO2 thin film for photocatalytic applications. *Journal of Applied Physics* **117,** 105308 (2015).

256. Radle, V. *Microtexture Determination and its Applications* (The Institute of Materials, 1992).

257. Lu, D. *et al.* Synthesis of freestanding single-crystal perovskite films and heterostructures by etching of sacrificial water-soluble layers. *Nature Materials* **15,** 1255–1260 (2016).

258. Su, D., Infortuna, A., Muralt, P., Setter, N. & Cantoni, M. Transmission-electron-microscopy study of quasi-epitaxial tungsten-bronze (Sr2.5 Ba2.5 Nb10 O30) thin film on perovskite (SrTiO3) single crystal. *Journal of Materials Research* **22,** 157–163 (2011).

259. Eilers, P. H. & Boelens, H. F. Baseline correction with asymmetric least squares smoothing. *Leiden University Medical Centre Report* (2005).

260. Savitzky, A. & Golay, M. J. E. Smoothing and Differentiation of Data by Simplified Least Squares Procedures. *Analytical Chemistry* **36,** 1627–1639 (1964).

261. Rietveld, H. M. A profile refinement method for nuclear and magnetic structures. *Journal of Applied Crystallography* **2,** 65–71 (1969).

262. Levenberg, K. A method for the solution of certain non-linear problems in least squares. *Quarterly of applied mathematics* **2,** 164–168 (1944).

263. Marquardt, D. W. An Algorithm for Least-Squares Estimation of Nonlinear Parameters. *Journal of the Society for Industrial and Applied Mathematics* **11,** 431–441 (1963).

264. Wilkinson, A. J. & Hirsch, P. B. Electron diffraction based techniques in scanning electron microscopy of bulk materials. *Micron* **28,** 279–308 (1997).

265. Glaser, R. *Symmetry, spectroscopy, and crystallography : the structural nexus* eng (Wiley-VCH, Weinheim, 2015).

266. Randle, V. *Microtexture determination and its applications* (CRC Press, 2023).

267. Güthner, P. & Dransfeld, K. Local poling of ferroelectric polymers by scanning force microscopy. *Applied Physics Letters* **61,** 1137–1139 (1992).

268. Longo, E. *et al.* Density functional theory calculation of the electronic structure of $\mathrm{Ba_{0.5}Sr_{0.5}TiO_3}$: Photoluminescent properties and structural disorder. *Phys. Rev. B* **69,** 125115 (2004).

269. Price, J., Hung, P., Rhoad, T., Foran, B. & Diebold, A. Spectroscopic ellipsometry characterization of HfxSiyOz films using the Cody–Lorentz parameterized model. *Applied Physics Letters* **85,** 1701–1703 (2004).

270. Trivedi, D., Tayebati, P. & Tabat, M. Measurement of Large Electro-Optic Coefficients in Thin Films of Strontium Barium Niobate (Sr0. 6Ba0. 4Nb2O6). *Appl. Phys. Lett.* **68,** 3227–3229 (1996).

271. Christensen, A. *et al.* Electro-optic effect in thin film strontium barium niobate (SBN) grown by RF magnetron sputtering on SrTiO3 substrates. *Journal of Applied Physics* **136** (2024).